Biochemical reconstitution of human autophagy initiation

Dissertation
for the award of the degree
“Doctor rerum naturalium”
of the Georg-August-Universität Göttingen

within the doctoral program
“Biomolecules: Structure - Function - Dynamics”
of the Göttingen Graduate Center for
Molecular Biosciences, Neurosciences and Biophysics (GGNB)

submitted by
Anh N.M. Nguyen
from Binh Minh, Vietnam
Göttingen, 2023

Members of the Thesis Advisory Committee

Dr. Alex Faesen (Supervisor, 1st reviewer)
Research Group Biochemistry of Signal Dynamics
Max Planck Institute for Multidisciplinary Sciences, Göttingen, Germany

Prof. Dr. Michael Thumm (2nd reviewer)
Department of Cellular Biochemistry
University Medical Center Göttingen, Germany

Prof. Dr. Marina Rodnina
Department of Physical Biochemistry
Max Planck Institute for Multidisciplinary Sciences, Göttingen, Germany

Further members of the Examination Board

Prof. Dr. Reinhard Jahn
Department of Neurobiology
Max Planck Institute for Multidisciplinary Sciences, Göttingen, Germany

Dr. Alexander Stein
Research Group Membrane Protein Biochemistry
Max Planck Institute for Multidisciplinary Sciences, Göttingen, Germany

Prof. Dr. Rubén Fernández-Busnadiego
Institute for Neuropathology
University Medical Center Göttingen, Germany

Date of oral examination: 25/04/2023

AFFIDAVIT

I hereby declare that the presented thesis entitled “Biochemical reconstitution of human autophagy initiation” has been written independently and with no other sources and aids than quoted.

The results of this thesis were communicated in the following preprint:

Metamorphic proteins at the basis of human autophagy initiation and lipid transfer.

Nguyen A*, Lugarini F*, David C, Hosnani P, Knotkova B, Patel A, Parfentev I, Friedrich A, Urlaub H, Meinecke M, Stork B and Faesen AC (#).

* These authors contributed equally to this work

Correspondence author

The preprint is under revision.

Part of the Materials and Methods section in this thesis (from section 2.7 to 2.22) is taken from the Materials and Methods section of the above preprint.

Summary

Autophagy is a tightly regulated process that eukaryotic cells use as a major survival mechanism to reallocate nutrients to essential processes in adverse conditions such as nutrient or energy deprivation. Autophagy is characterized by the formation of a phagophore, a double membrane organelle that matures into an autophagosome to capture damaged or surplus materials in the cytosol and deliver them to the lysosome for degradation and recycling. Yet, how the autophagosome is generated *de novo* remains a long-standing question in biology. Research in the last decades has suggested that autophagosome biogenesis requires the transfer of lipids from the endoplasmic reticulum (ER) to the nascent autophagosome (phagophore), which happens at the membrane contact site (MCS) between the two organelles. Several core autophagy initiation complexes and a lipid transfer machinery are recruited to the MCS to modulate autophagic membrane formation and elongation. However, profound questions remain: How does the MCS assemble at the right place and time? Is there a regulatory mechanism? How is lipid transfer modulated to support phagophore elongation? Answering these questions would provide fundamental insight into the mechanisms of autophagosome biogenesis. In this thesis, biochemical reconstitution is used as a reductionist approach to address these questions. One of the main challenges of this approach is the production of recombinant proteins. Here, we meet this challenge by purifying almost all full-length proteins of the core autophagy initiation complexes (ULK1 complex, PI3K complex 1, ATG9) and the lipid transfer unit (ATG2-WIPI4). Interestingly, we were able to reconstitute a seven-subunit autophagy initiation super-complex and found that a three-subunit complex of ATG9-ATG13-ATG101 serves as a core complex for the assembly of other four subunits, including ULK1, FIP200, ATG14L, and BECN1. Data from our lab also shows that ATG13 and ATG101 are metamorphic proteins, and their metamorphoses result in an incredibly slow self-assembly of the core complex. The slow assembly of the core complex thus acts as a rate-limiting step in the assembly of the super-complex and raises the possibility of a regulatory mechanism for on-demand assembly of the super-complex upon autophagy induction. Moreover, I found that the core complex also interacts with the lipid transfer unit, ATG2-WIPI4, to form a five-protein subcomplex. ATG2-WIPI4 was previously found to tether membranes and mediate lipid transfer at the MCS. Surprisingly, the lipid transfer efficiency of the lipid transfer unit can be significantly enhanced by both ATG9 and ATG13-ATG101 of the core complex. In summary, our findings pave the way for mechanistic models that explain how autophagosome biogenesis is regulated in space and time and how the co-incidence of the different functional complexes supports autophagosome expansion.

Table of Contents

Abbreviations

AIM	Atg8-interacting motif
AMPK	adenosine monophosphate-activated protein kinase
ATG	autophagy-related
ATP	adenosine triphosphate
Aβ	amyloid-β
BSA	bovine serum albumin
COPII	coat protein complex II
ddH_2O	double-distilled water
DLS	dynamic light scattering
E.coli	*Escherichia coli*
ER	endoplasmic reticulum
ERES	endoplasmic reticulum exit site
ERGIC	ER-Golgi intermediate compartment
GABARAB	gamma-aminobutyric acid receptor-associated protein
GFP	green flourescent protein
GOI	gene of interest
GST	glutathione s-transferase
GUVs	giant unilamellar vesicles
Hepes	4-(2-hydroxyethyl)-1-piperazineethanesulfonic acid
HORMA domain	Hop1, Rev7 and Mad2 domain
IDRs	intrinsically disordered regions
IM	isolation membrane
kDa	kilo Dalton
LB	lysogeny broth
LIR	LC3-interacting region
LTPs	lipid transfer proteins
LUVs	large unilamellar vesicles
MBP	maltose binding protein
mCherry	monomeric Cherry
MCS	membrane contact site
MP	mass photometry
mTOR	mammalian/mechanistic target of rapamycin
MW	molecular weight
OD_{600}	optical density at a wavelength of 600 nm
PAS	pre-autophagosomal structure
PBS	phosphate buffered saline

PCR	polymerase chain reaction
PE	phosphatidylethanolamine
PI	phosphatidylinositol, PtdIns
PI(3,5)P_2	phosphatidylinositol 3-phosphate
PI3K-C1	the class III PI3K complex 1
PI3K-C2	the class III PI3K complex 2
PI3P	phosphatidylinositol 3-phosphate
PLs	proteoliposomes
PMSF	phenylmethane sulfonyl fluoride
PROPPINs	β-propellers that bind PtdIns
rpm	rounds per minute
S. cerevisiae	*Saccharomyces cerevisiae*
SARs	selective autophagy receptors
SDS-PAGE	SDS-polyacrylamide gel electrophoresis
SF	stain-free
S. pombe	*Schizosaccharomyces pombe*
UPS	ubiquitin-proteasome system
v/v	volume per volume
w/v	weight per volume
WIPI	WD-40 repeat containing protein that interacts with PtdIns
XL-MS	cross-linking mass spectrometry

List of Tables

List of Figures

1. Introduction

Living cells are constantly growing, dividing, and responding to their environment. Despite that, cells continuously make mistakes. Some are inherited or acquired, while others occur because of inefficient or erroneous metabolic processes. Therefore, a variety of self-regulating quality control mechanisms are required to maintain cellular homeostasis and prevent permanent damage. Eukaryotic cells have two major quality control systems responsible for the degradation of proteins and organelles: the ubiquitin-proteasome system (UPS) and autophagy. Through many sophisticated sets of feedback control, these two degradative systems not only balance protein synthesis with the breakdown of dysfunctional proteins and organelles, but also maintain amino acid pools and energy balance by recycling the degraded components. Though autophagy has historically received less attention than the UPS, advances in autophagy molecular genetics have led to a renaissance of interest in the last few decades with many surprising insights about its regulation and functions. This thesis aims to contribute more insights into the current understanding of autophagy using biochemical reconstitution as a research tool. In this introduction, current literature regarding the autophagy process is discussed, followed by specific aims that target some knowledge gaps in the field.

1.1. Autophagy: the basics

Daily laboratory activities routinely generate a lot of waste. The waste is usually classified into different categories depending on some common characteristics that make the downstream recycling processes less complicated. The waste is then delivered to its corresponding waste processing systems for recycling or disposal. We perceive this process as routine, but could you imagine what would happen if the waste recycling and disposal system did not exist? Undeniably, laboratories would be filled with waste and become unusable in a short period of time. This would also apply to any household, company, or society.

Therefore, a waste recycling system is necessary for any entity, whether it is as large as a society or as small as a single cell.

Autophagy is a cellular recycling system that is comparable to our daily waste recycling system in many ways. Cells, like humans, create "waste" in the form of broken organelles or protein aggregates. Cellular waste is gathered and transported to the lysosomes (analogous to the recycling facilities) for breakdown. The process was initially described by Ashford and Porter (1962) as a mechanism that facilitates the breakdown of cytoplasmic materials. The mechanism then got its name, “autophagy” (Greek words for self-eating, “phagy” meaning eat, and “auto” meaning self) by Christian de Duve in 1963, when he described autophagy as a process by which a cell engulfs a portion of its cytosolic content for lysosomal degradation. It then took another 30 years before the key molecular players in the process were identified. The discovery of conserved autophagy-related genes by different groups studying the process in yeast is another foundation of current autophagy understanding (Tsukada and Ohsumi, 1993, Thumm et al., 1994, Baba et al., 1994, Feldwisch et al., 1995). Their contributions transformed the field into an exciting research topic in life science. Since then, autophagy research has been focused on gaining a comprehensive knowledge of the molecular process as well as its regulation and function. Today, autophagy is generally referred to as an evolutionary conserved process responsible for maintaining homeostasis in the cell by degrading and recycling aggregated intracellular proteins, macromolecules, or dysfunctional organelles.

1.1.1. Different types of autophagy

In mammalian cells, there are three primary types of autophagy: macroautophagy, microautophagy, and chaperone-mediated autophagy (Figure 1.1). Despite their mechanistic differences, all three result in cargo delivery to the lysosome for degradation and recycling.

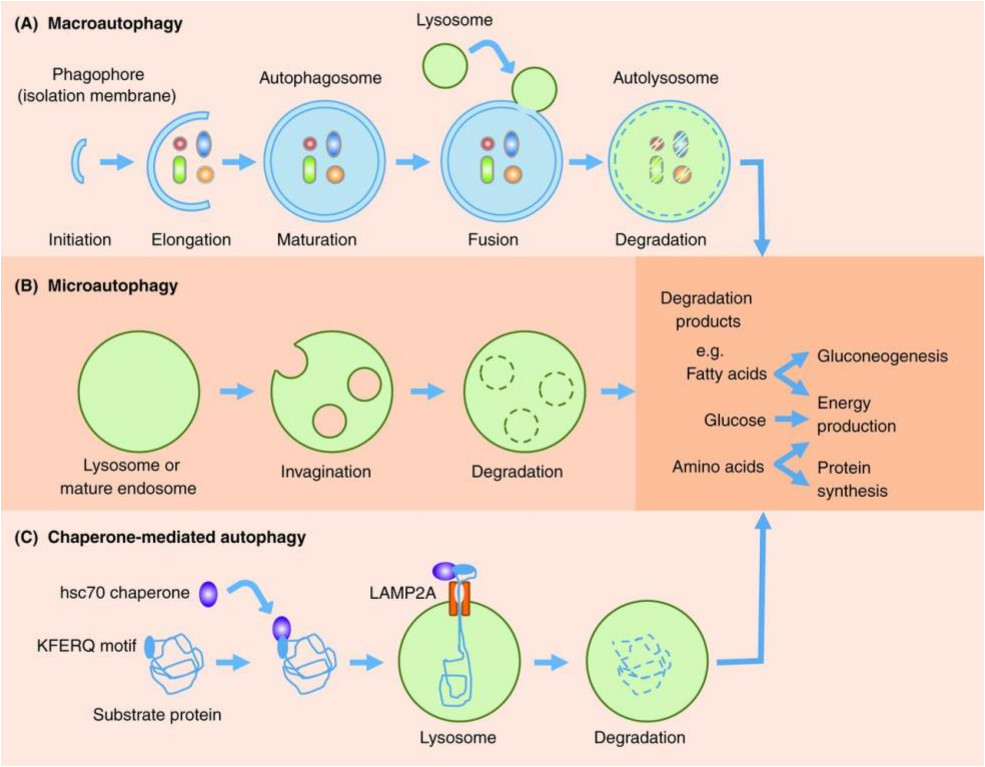

Figure 1.1. A schematic illustration of the three main types of autophagy: Macroautophagy, Microautophagy and Chaperon-mediated autophagy (CMA). A) In macroautophagy, dysfunctional proteins and organelles are selectively or non-selectively captured by the autophagosome and delivered to the lysosome. B) In microautophagy, a small portion of cytosolic content is directly engulfed by the lysosome by inward invagination. C) In chaperon-mediated autophagy, substrates containing the KFERQ motif are recognized and translocated across the lysosomal membrane thanks to molecular chaperones HSC70 and lysosome-associated membrane protein-2A (LAMP2A). Degradation products, e.g. fatty acids, glucose, and amino acids, can be reused by the cells. Figure taken from Ding and Choi (2015).

Macroautophagy is the most common type of autophagy in cells and will be simply referred to as autophagy in this thesis. Since it is a mechanism to maintain cellular homeostasis, autophagy is tightly regulated. Basal autophagy takes place during normal physiological conditions, while inducible autophagy occurs in response to different types of stimuli, including starvation, growth factor deprivation, infection, or hypoxia (Kroemer et al., 2010). Autophagy requires the *de novo* formation of a cup-shaped membrane called a phagophore (also known as an isolation membrane - IM) (Mizushima et al., 2011, Wen and Klionsky, 2016). The phagophore then elongates to sequester a portion of cytosolic content and mature into an enclosed vesicle called an autophagosome. The autophagosome is a special vesicle with a lumen sealed by a double bilayer membrane rather than a single bilayer membrane like most other cellular vesicles. The outer membrane of the autophagosome then fuses with the lysosome to form a hybrid lytic organelle called an autolysosome. Subsequently, the resident hydrolases within the autolysosome breakdown the luminal materials, including the inner membrane of the autophagosome. Lastly, the molecular building blocks resulting from the breakdown can then be transported back into the cytosol for reuse in various cellular functions such as energy production or protein synthesis (Yorimitsu and Klionsky, 2005)(Figure 1.1). Autophagy was previously described as a non-selective process; however, it can also be selective for different types of targeted cargo. This is again analogous to the waste classification system we use in our daily lives, where each type of waste is assigned a label for subsequent recycling or disposal. Some examples are mitophagy, pexophagy and ERphagy which selectively degrade the mitochondria, peroxisomes, and endoplasmic reticulum (ER), respectively (Ashrafi and Schwarz, 2013, Hutchins et al., 1999, Nakatogawa and Mochida, 2015) (Figure 1.2). Each type of selective autophagy is specific for the cargo it degrades and therefore requires specific receptors for cargo recognition. These receptors are called selective autophagy receptors (SARs) which tag specific cargos for selective degradation by engaging the targeted cargos with the core autophagy machinery, enabling the autophagosomes to develop and encapsulate the cargos (Gatica et al., 2018) (Figure 1.2). Through their conserved motifs, namely LC3-interacting region (LIR) in mammals and Atg8-interacting motif (AIM) in yeast, SARs bind to the LC3/GABARAP protein family (or Atg8 protein family in yeast), which resides on the phagophore (Noda et al., 2010) (Figure 1.2). In either route (selective or non-selective), the clearance of cellular components is important for maintaining homeostasis, protecting cells from potential hazards, and allowing regeneration of building blocks for constructing new cytosolic components.

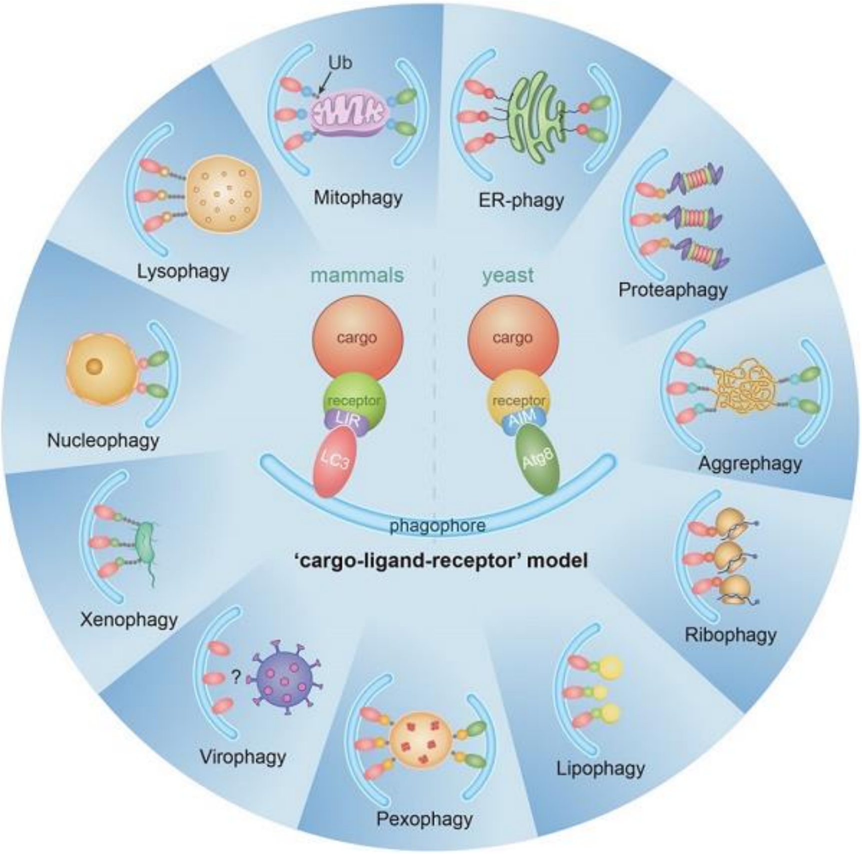

Figure 1.2. Several types of selective autophagy in mammalian and yeast cells. Selective autophagy is named based on the cargo it degrades. The cargo is recruited to the autophagosome by the binding of selective autophagy receptors (SARs) to the lipidated LC3 in mammals or Atg8 in yeast, at the respective LC3-interacting region (LIR) or Atg8-interacting motif (AIM). Figure taken from Li et al. (2021b).

Microautophagy is the lesser-known type of autophagy, which was named by Christian de Duve (de Duve and Wattiaux, 1966). In the 1980s, the process was observed mainly in isolated rat liver, in which the lysosomes were able to ingest different types of cytosolic materials such as ovalbumin, lysozyme, and ferritin (Marzella et al., 1981, Ahlberg et al., 1982, Ahlberg and Glaumann, 1985). Much of the new insight into microautophagy was obtained from yeast due to its large vacuole and the straightforward manipulation of its genetics (Uttenweiler and Mayer, 2008). The process is now defined as a direct internalization of cargos to be degraded by the lysosome (in mammals) or the vacuole (in yeast and plants) (Schuck, 2020) (Figure 1.1). During microautophagy, the lysosomal/vacuolar membrane is randomly invaginated into autophagic tubes to enclose a portion of the cytosol. The forming structures are then ingested into the lysosome/vacuolar lumen, where they are subsequently degraded (Muller et al., 2000). Like autophagy, microautophagy can be selective or non-selective, and occurs in vegetative conditions as well as in the presence of stresses such as starvation or metabolic stress (Schuck, 2020). The term “micro” is, however, obsolete since studies in yeast have shown that it can target cellular structures of many sizes, including large structures such as the mitochondria (Campbell and Thorsness, 1998) or the ER (Schuck et al., 2014).

Chaperone-mediated autophagy (CMA) is the third main type of autophagy that has only been found in higher eukaryotes and does not rely on vesicle formation, unlike macro- and microautophagy. Instead, targeted cargos are transported directly across the lysosomal membrane through an active protein translocation mechanism (Figure 1.1). CMA-cargo contains a KFERQ-like motif, which is recognized by the heat shock cognate protein (HSC70; also known as HSPA8) in the cytosol (Dice, 1990). The cargo-HSC70 complex is then targeted to the lysosome through their binding to lysosome-associated membrane protein type 2A (LAMP2A) (Chiang et al., 1989, Cuervo and Dice, 1996). In some cases, other co-factors or covalent modifications are also required for the binding of the cargo-HSC70 complex to LAMP2A (Ferreira et al., 2015, Quintavalle et al., 2014). Once bound, LAMP2A oligomerizes, followed by a series of sophisticated mechanisms to unfold the protein before translocating it into the luminal side of the lysosome. Lysosomal HSC70 is then responsible for the uptake of the peptide in the lumen, followed by its degradation and recycling back into the cytosol (Bandyopadhyay et al., 2008). CMA, therefore, serves as a quality control mechanism for cytosolic misfolding or damaged proteins. It is also upregulated in prolonged starvation conditions to assist the cell in dealing with metabolic stress (Orenstein and Cuervo, 2010).

1.1.2. Autophagy and diseases

Regardless of the types, autophagy is a crucial pathway to maintain homeostasis of the cell in normal physiological conditions as well as a major survival mechanism in the presence of different cellular stresses such as nutrient deprivation, infection, protein aggregation, etc. Therefore, dysregulation of autophagy has been shown to be closely related to the pathogenesis of many diseases (Mizushima et al., 2008). Here, I would like to briefly summarize the role of autophagy in cancer and neurodegenerative diseases, which are two of the most clinically challenging diseases, to highlight the importance of autophagy research regarding its therapeutic implications.

In cancer, autophagy is widely regarded as a “double-edged” sword that can act as a tumor suppressor or a tumor promoter (Chavez-Dominguez et al., 2020). In the early stages of tumorigenesis, autophagy serves as a tumor-suppressive mechanism by turning over damaged cytosolic materials, organelles, or aggregated proteins, thereby preventing the spread of damage, including DNA alterations. However, in the later stages, it may promote cancer growth and dissemination by recycling metabolites in cancer cells to maintain their extremely demanding metabolism and serving as a housekeeper for cancer cells in response to anti-cancer therapy (Yang and Klionsky, 2020). Many core *ATG* (autophagy-related) genes have been discovered to have recurring genetic alterations in cancer. For instance, *BECN1* is one of the earliest and best examples of an *ATG* gene acting as a tumor suppressor. Monoallelic deletion of *BECN1* has been found in up to 40%-75% of the cases of breast cancer and ovarian cancer (Aita et al., 1999). By restoring *BECN1* expression, autophagy was restored in breast cancer cell lines, and their proliferation and tumorigenesis were suppressed (Liang et al., 1999). Similarly, frameshift mutations in other core *ATG* genes such as *ATG2B*, *ATG5*, *ATG9*, and *ATG12* have been linked to over 25% of gastric and colorectal cancers because those mutants typically led to the proteins’ loss of functions and consequently dysfunctional autophagy (Kang et al., 2009). Aside from the direct involvement of the *ATG* genes, the antitumor role of autophagy is accredited by the fact that some tumor suppressors, including TP53/p53, PTEN, DAPK, TSC1-TSC2, and STK11/LBK1 promote autophagy (Lorin et al., 2013, Mrakovcic and Frohlich, 2018). Conversely, once a tumor develops, autophagy is very effective in assisting tumor survival and promoting metastasis by eliminating cancer cells’ stresses. In their microenvironment, cancer cells deal with different types of stresses, such as hypoxic, genotoxic, and oxidative stress, which are greatly alleviated by upregulating autophagy. Inhibition of autophagy in these cells promotes cell death, highlighting the vital role of autophagy in promoting tumorigenesis and metastasis (Kocaturk et al., 2019, White, 2012). For example, deletion of core autophagy genes such as *ATG7*, *ATG12*, or *LC3* in later stages of cancer has been shown to inhibit the survival of breast cancer stem cells (Cufi et al., 2011, Maycotte et al., 2015). Nonetheless, determining whether autophagy is pro- or anti-cancer at different stages remains difficult because observations differ between different cancer types and their respective environments. Therefore, further research into the detailed molecular mechanisms of autophagy and associated pathways is critical for developing new anti-cancer therapies based on autophagy modulation.

Autophagy is also linked to many neurodegenerative diseases since it is vital for neuronal homeostasis by removing toxic substances that cause neuronal death and gradual loss of cognitive function (Tooze and Schiavo, 2008). Increasing evidence indicates that inactivation of the lysosomal system led to the accumulation of autophagosomes in brain cells of patients suffering from a variety of neurodegenerative disorders, including Alzheimer's disease (Nixon and Cataldo, 2006) , Parkinson's disease (Kabuta et al., 2008), and Huntington's disease (Sarkar et al., 2007). Such accumulations are caused by defects in autophagosome clearance rather than autophagy induction, suggesting that modulating the late phases of autophagy could be a potential therapeutic approach. The pathogenesis of Alzheimer's disease, for example, is attributed to the accumulation of aggregated amyloid-β (Aβ) peptide and intracellular hyperphosphorylated microtubule-associated protein tau (MAPT) (Nixon, 2007). This is presumably due to a defect in autophagosome-lysosome fusion and maturation. Furthermore, most neurodegenerative disorders are associated with defects in mitophagy and CMA. However, detailed interpretation of the molecular mechanism is difficult because some core *ATG* genes are involved in multiple other processes besides canonical autophagy, and their mutation frequency varies substantially between diseases (Yang and Klionsky, 2020). In comparison with cancer, the role of autophagy in neurodegenerative diseases seems to be even more enigmatic, with relevant preclinical research trailing far behind. Thus, much work is still needed to unravel the pathogenic characteristics of autophagy.

The role of autophagy in diseases is far from exhaustive with just the two examples mentioned above because it is also involved in many more diseases, such as inflammatory, infectious diseases, obesity, diabetes, etc. Although there is still controversy and many unanswered questions regarding its exact molecular mechanism and role in each case, autophagy research has developed rapidly in the last few decades and provided significant impacts on animal and human health-related problems. Thus, further investigation into the intricacy of autophagy's processes and its internal or external regulators would be valuable for the future development of novel therapies that take advantage of autophagy modulation.

1.2. The hierarchy of the core autophagy initiation machinery

Autophagy is a highly conserved catabolic process that requires the well-orchestrated activities of many components to ensure its progression. Central to this cycle are more than 40 conserved autophagy-related (ATG) proteins, which cooperatively function in defined hierarchies, usually in multi-protein complexes (Mizushima et al., 2011). Among them, 18 core ATG proteins have been classified into six functional groups according to their involvement in different steps of autophagy: 1) the ULK1/2 kinase complex (Atg1 in yeast), 2) the class III PI3K complex 1 (PI3K-C1), 3) phosphatidylinositol 3-phosphate (PI3P) binding proteins, 4 and 5) two ubiquitin-like conjugation systems of ATG12 and LC3II (Atg12 and Atg8), and 6) ATG9 (Atg9) vesicles. Hierarchical analysis in yeast and mammalian systems has revealed that these functional groups are sequentially recruited to the site of autophagosome formation to perform their functions (Suzuki et al., 2007, Itakura and Mizushima, 2010). In recent years, increasing efforts have been put into defining the mechanistic detail of each step in the pathway and elucidating the functional roles of the core ATG proteins. In brief, autophagy can be divided into four distinct phases: initiation, expansion, maturation, and fusion-degradation, which correspond to the life cycle of an autophagosome (Figure 1.3). The ULK1 complex, the PI3K-C1, and ATG9 vesicles are among the first that are recruited to the autophagy initiation site and involved in the early stages of autophagy. In yeast, the initiation site is termed PAS (pre-autophagosomal structure, also known as phagophore assembly site), which locates near the vacuole. In mammals, it is unknown whether the PAS equivalent exists because autophagy seems to be initiated at multiple sites in the cytosol. However, the most well-known site of mammalian autophagy initiation is the “omegasome”, which is an Ω-shaped sub-domain of the ER enriched in phosphatidylinositol 3-phosphate (PI3P) and marked with PI3P-binding protein, DFCP1 (Axe et al., 2008, Suzuki and Ohsumi, 2010). The first membrane building blocks required for PAS/omegasome nucleation are hypothesized to come from ATG9 vesicles (Sawa-Makarska et al., 2020, Yamamoto et al., 2012). When autophagy is induced, the ULK1 complex and PI3K-C1 are subsequently activated, which generates and enriches PI3P on the nucleated membrane. PI3P is an important phospholipid, required for the recruitment of downstream PI3P-binding effectors, which in turn recruit the lipid transfer unit ATG2-WIPI4 (Atg2-Atg18) and two conjugation systems of LC3 (Atg8 in yeast). Lipid transfer unit is required for phagophore expansion, whereas LC3/Atg8 is required for phagophore membrane maturation and cargo recruitment through the SARs (Nakatogawa, 2020). Figure 1.3 provides an overview of these steps, and the following sections will discuss each functional group in more detail with regards to the mammalian systems. Comparisons to the well-studied yeast system will also be discussed where relevant.

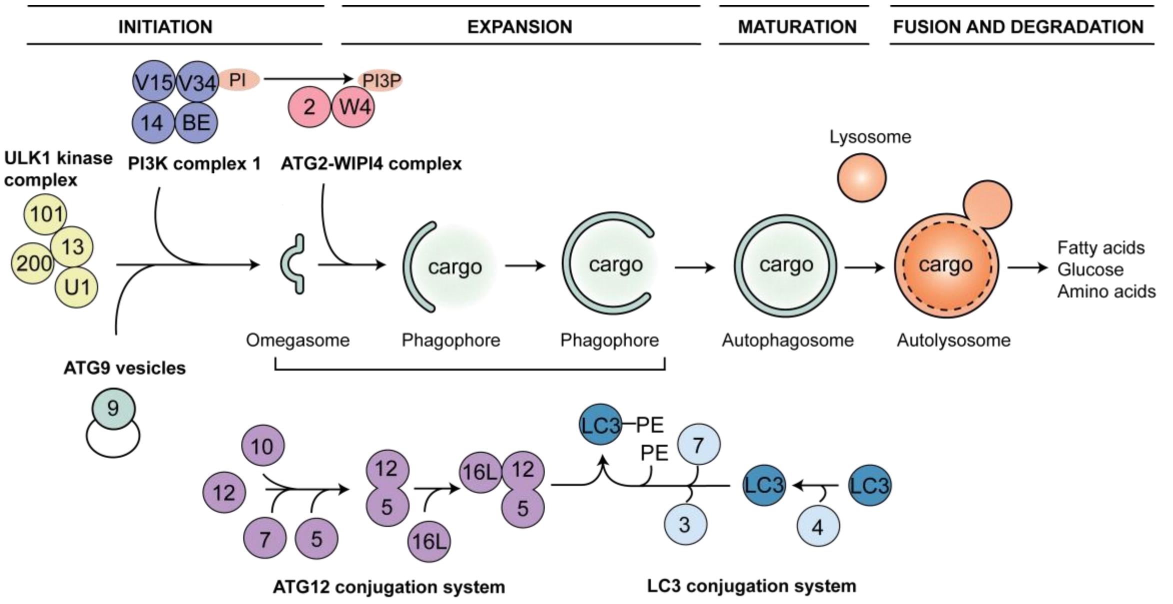

Figure 1.3. A schematic drawing of the four steps in the mammalian autophagy pathway. Six functional groups are targeted to the initiation site (omegasome) in a hierarchical manner. ATG9 vesicles are supposed to provide the initial membranes. ULK1 is the most upstream kinase that localizes to the omegasome, followed by an activation of the PI3K-C1, a lipid kinase complex that converts PI into PI3P. WIPI4 is an adaptor protein that binds to PI3P and forms a complex with ATG2. The ATG2-WIPI4 complex is a lipid transfer unit that mediates lipid transfer from the ER to the phagophore for its expansion. The maturation of the phagophore involves two conjugation systems that conjugate LC3 into the phagophore. LC3 is required for the scaffolding of the phagophore membrane and the binding of selective autophagy receptors (SARs). The phagophore expands, engulfs cytosolic cargo, and matures into the autophagosome. The autophagosme eventually fuses with the lysosome, where the internal content is degraded and recycled.

1.2.1. Upstream regulators of autophagy

As a major source of recycled metabolites, autophagy needs to be turned on efficiently and promptly in critical situations such as low ATP or nitrogen levels and amino acid deprivation. Besides being extensively induced during stress, it must also be effectively suppressed to baseline levels under normal physiological conditions to prevent excessive intracellular digestion. Unsurprisingly, it is regulated by both the mammalian/mechanistic target of rapamycin (mTOR) signaling pathway, which senses the cell's nutritional status, and the adenosine monophosphate-activated protein kinase (AMPK) pathway, which senses the cell's energy level (Sarkar et al., 2007, Ganley et al., 2009, Hosokawa et al., 2009a, Kim et al., 2011b). Both pathways directly regulate the ULK1 kinase complex (Atg1 in yeast), the most upstream stress-sensing component in the core autophagy machinery (Petherick et al., 2015, Zachari and Ganley, 2017).

mTOR is a 289-kDa serine-threonine kinase of the PI3K- related kinase (PIKK) protein family. As the name implies, mTOR is inhibited by rapamycin (sirolimus), an anti-fungal macrolide produced by *Streptomyces hygroscopicus* (Seto, 2012). The protein is also the key catalytic component of both the mTOR complex 1 (mTORC1) and complex 2 (mTORC2). The inhibitory effect of mTORC1 in autophagy is extensively characterized, while that of mTORC2 is less well-understood, partly because of its indirect effects in autophagy (Saxton and Sabatini, 2017). In nutrient-rich conditions, mTORC1 negatively regulates autophagy by actively phosphorylating ULK1 at S757, inhibiting its ability to form a complex with AMPK. Furthermore, it has been demonstrated that mTORC1-mediated phosphorylation of ATG13, a component of the ULK1 complex, contributes to the inhibition of the ULK1 complex (Jung et al., 2009). When cellular energy is limited, AMPK is activated and mTORC1 is inactivated by AMPK to relieve the S757 phosphorylation, resulting in the ULK1-AMPK interaction. Once bound, AMPK phosphorylates ULK1 at S317 and S777, leading to ULK1 activation and consequently autophagy induction (Figure 1.4) (Kim et al., 2011a, Saxton and Sabatini, 2017). However, it is noteworthy that the phosphorylation sites of AMPK on ULK1 are not well-conserved across species, thus further research is required to determine whether they represent an AMPK recognition motif (Scott et al., 2002). Moreover, inhibiting mTORC1 by rapamycin treatment or amino-acid deprivation is sufficient for ULK1 activation independent of AMPK. However, the coordination between AMPK and mTORC1 is still important to ensure that autophagy is not excessively activated unless in severe conditions (Kim et al., 2011a). Under moderate glucose limitation and adequate amino acid supply, for example, it is more advantageous for the cell to upregulate metabolism rather than induce autophagy. Hence, AMPK can enhance the activity of metabolic enzymes through phosphorylation but not completely inhibit mTORC1, thus minimizing autophagy initiation beyond basal levels.

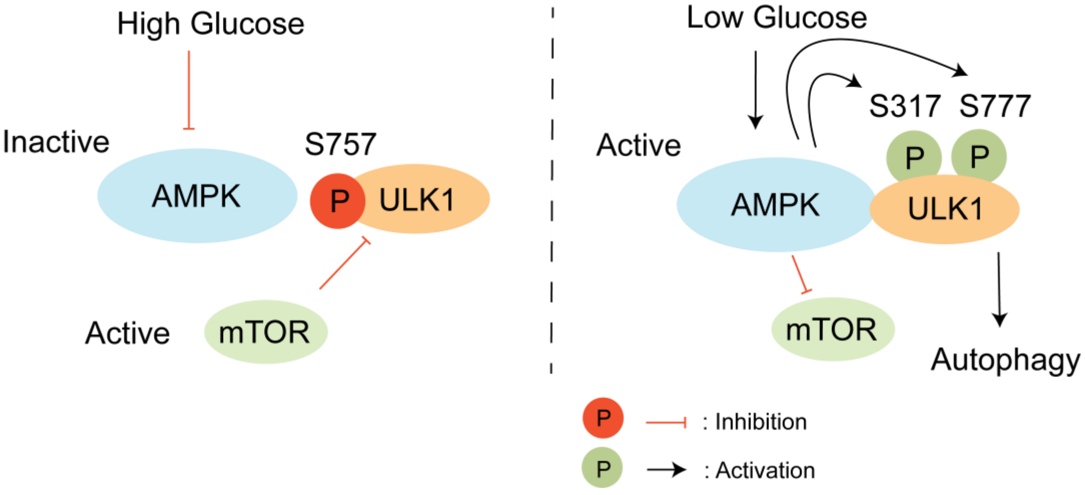

Figure 1.4. The role of AMPK and mTOR in regulation of autophagy through ULK1 activation and inactivation. Left: When cells have sufficient glucose, AMPK is inactive and mTOR is active. Through the phosphorylation of S757 on ULK1, active mTOR inactivates ULK1 and prevents it from interacting with AMPK. Autophagy is not initiated. Right: When glucose levels are low, AMPK is activated. Activated AMPK inhibits mTOR and frees ULK1 from mTOR inhibition. Phosphorylation of ULK1 at S757 is decreased, and the protein can interact with and be phosphorylated by AMPK on S317 and S777. When ULK1 is phosphorylated, it becomes active and initiates autophagy.

1.2.2. The ULK1 kinase complex

As described above, the ULK1 (Atg1 in yeast) complex is the primary kinase complex and the most upstream sensor in autophagy that receives the signal from the upstream signaling pathways and transmits it to the downstream autophagy cascades (Suzuki et al., 2007, Itakura and Mizushima, 2010). Specifically, its primary functions are to recruit ATG9/Atg9 vesicles, leading to the nucleation of the autophagic membrane (Suzuki et al., 2015b, Sekito et al., 2009), and to activate the class 3 PI3K complex 1 at the site of autophagosome biogenesis to promote PI3P production (Russell et al., 2013, Park et al., 2016). The role of ATG9 vesicles and the class 3 PI3K complex 1 will be discussed in detail in Section 1.2.3 and Section 1.2.4, respectively.

The mammalian ULK1 complex consists of four protein components: ULK1 (unc-51-like kinase 1) or its paralogues (ULK2 to ULK4), FIP200 (focal adhesion kinase (FAK)-family interacting protein of 200 kDa, also known as RB1CC1), ATG13, and ATG101 (Ganley et al., 2009, Hosokawa et al., 2009b) (Figure 1.5).

ULK1 and ULK2 have redundant roles in canonical autophagy since it requires a double knockout of *ULK1* and *ULK2* to completely block starvation-induced autophagy (Lee and Tournier, 2011, Yan et al., 1999, Cheong et al., 2011). The yeast Atg1 complex consists of Atg1, Atg13, Atg17, Atg29, and Atg31. Atg1 and Atg13 are orthologs of the mammalian ULK1 and ATG13, respectively. The functional counterpart of Atg17 is FIP200 in mammals, whereas Atg29 and Atg31 have no orthologs in the mammalian complex, and the counterpart of mammalian ATG101 does not exist in budding yeast (Cheong et al., 2008) (Figure 1.5).

ULK1 (Atg1 in yeast) is a 112 kDa protein consisting of a conserved serine-threonine kinase domain at its N-terminal and a conserved EAT (early autophagy targeting) domain at its C-terminal, which are separated by a serine-proline-rich disordered region (Yan et al., 1998). *In vitro*, the EAT domain of ULK1/Atg1 binds directly to membranes with a strong preference for high curvatures, thus acting as a curvature sensor for the complex (Chan et al., 2009, Ragusa et al., 2012). In addition, the domain is also required for ATG13/Atg13 interaction and autophagy induction (Stjepanovic et al., 2014, Fujioka et al., 2014, Yeh et al., 2011, Chan et al., 2009). However, it is unclear whether the interactions are mutually exclusive. Meanwhile, various regulatory phosphorylation occurs in the middle serine-proline-rich region (Egan et al., 2011). Within this region, there are also conserved LIR/AIM motifs, which allow direct binding of ULK1/Atg1 to LC3/GABARAP/Atg8 family proteins (Figure 1.5) (Kraft et al., 2012, Alemu et al., 2012). These interactions suggest other roles for ULK1/Atg1, since LC3/Atg8 is dispensable for ULK1/Atg1 kinase activity (Kraft et al., 2012). For example, these interactions are proposed to be involved in autophagosome maturation and/or self-targeting of the complex to the inner membrane of the autophagosome for degradation as negative feedback for autophagy (Kraft et al., 2012). Lastly, despite being one of the most appealing targets in the autophagy cascades, the kinase domain of ULK1 is less well characterized, partly due to difficulties in protein purification. Recently, Lazarus et al. (2015) reported a crystal structure of the ULK1 kinase domain bound to its inhibitor. The structure reveals a typical eukaryotic kinase with a positively charged loop between N and C terminal lobes, which may be involved in the regulation of kinase activity. Indeed, the authors showed that autophosphorylation at T180 in the loop is essential for the regulation of ULK1 kinase activity. Multiple ULK1 substrates have also been identified, either within the ULK1 complex (multiple sites on FIP200, ATG13, and two sites, S11 and S203 on ATG101) or in components of the downstream PI3K-C1 (three sites on BECN1, one site at S249 on VPS34, and one site at S29 on ATG14L) (Egan et al., 2015, Baskaran et al., 2014, Russell et al., 2013). However, the functional consequences of these phosphorylation sites remain elusive, except for a few phosphorylation sites on BECN1 and ATG14L that are important for the activation of the PI3K-C1. These sites will be discussed in Section 1.2.4.

The role of the three other proteins in the ULK1 complex is poorly characterized compared to ULK1. FIP200 is a large protein (1594 amino acid residues) with no clear sequence homolog in yeast, although it does contain an Atg11 homology region and is generally referred to as a functional equivalent of Atg17 and Atg11 in *S. cerevisiae* (Hara and Mizushima, 2009). The protein consists of an N-terminal scaffolding domain, a long coiled-coil (CC) region (residues 860−1391) in the middle, and a C-terminal Atg11-like “Claw” domain (Shi et al., 2020b, Turco et al., 2019) (Figure 1.5 C). In comparison with ULK1, FIP200 has many more interaction partners either within or outside of the autophagy cascades, such as Pyk2, FAK, ActA, p53, TSC1, ASK1 and TRAF2, suggesting its roles in various cellular pathways (Chen et al., 2016). Nevertheless, although it is established as a four-component complex, the basis of subunit interactions within the ULK1 complex is still unclear because there is still conflicting evidence regarding whether ULK1 interacts directly with FIP200 (Ganley et al., 2009) or indirectly through ATG13 (Shi et al., 2020b). Meanwhile, several studies agree that ATG13 is the central component of the complex that recruits and serves as a linker for the remaining subunits (Hosokawa et al., 2009a, Suzuki et al., 2015a, Hieke et al., 2015). Moreover, although understanding of FIP200 as a scaffolding protein is limited, analogies can be drawn from Atg17 in yeast. For intance, Ragusa et al. (2012) reported the crystal structure of the Atg1 subcomplex consisting of Atg17, Atg29, and Atg31 in *Lachancea thermotolerans*, showing that Atg17 adopts an S-shaped dimer, with Atg31 and Atg29 bound to the inner side of each Atg17 crescent (Figure 1.5 B). The authors also propose a model in which the Atg17-Atg29-Atg31 complex induces Atg9 vesicles' tethering upon the engagement of Atg1 and Atg13, implying the scaffolding functions of Atg17 in positioning Atg9 vesicles for their fusion into the autophagic membrane (Ragusa et al., 2012). As an Atg17 counterpart, FIP200 can also act as a scaffolding factor in a similar fashion; however, the model requires further validation both *in vitro* and in cells.

Recent crystal structures of the human or *S. pombe* ATG13-ATG101/Atg13-Atg101 subcomplex reveal that they are two HORMA (Hop/Rev7/Mad2) domain-containing proteins (Qi et al., 2015, Suzuki et al., 2015a). While ATG13 consists of an N-terminal HORMA domain followed by a long C-terminal intrinsically disordered region (IDR), ATG101 is mainly made up of a HORMA domain. The IDR of ATG13 contains binding regions for both ULK1 and FIP200, while the HORMA domain forms a heterodimer with ATG101 (Figure 1.5 A). Park et al. (2016) showed that ATG14L binds to the HORMA domain region of ATG13, though they did not investigate whether the interaction is mutually exclusive with ATG101. The interaction is proven to be crucial for the recruitment and activation of the PI3K-C1 through ULK1-dependent phosphorylation of ATG14L. In yeast, the HORMA domain of Atg13 was also found to interact with both Atg14L and Atg9 (Suzuki et al., 2015b, Jao et al., 2013). Additionally, ATG13 also contains a short membrane binding motif at its N-terminal, preceding the HORMA domain, which is required for the protein's translocation to the autophagosome initiation site (Karanasios et al., 2013). Mutation of the motif impairs ATG13 localization to the initiation site, thus inhibiting autophagic flux upon autophagy induction by rapamycin treatment (Wallot-Hieke et al., 2018). Surprisingly, the IDR region of yeast Atg13 also serves as a link between two Atg17-Atg29-Atg31 complexes by binding to two distinct regions on Atg17. Multiple repeats of the interactions lead to the assembly of supramolecular Atg1 complex, recruitment of Atg9 vesicles through its interaction with Atg13, and consequently autophagy induction (Yamamoto et al., 2016). It has been postulated that the higher-order assembly of such supramolecular complexes induces liquid-liquid phase separation to generate a liquid-like biomolecular condensate, which in this case is the PAS (Fujioka et al., 2020). The authors could also reproduce the liquid-like Atg1 droplets *in vitro* using purified proteins and showed that it is tethered to giant unilamellar vesicles (GUVs) containing Vac8 (a vacuolar membrane protein) due to the interaction between Vac8 and Atg13. This *in vitro* observation mimics the PAS formation near the vacuole in cells. Function-wise, a liquid-like PAS was proposed to activate the kinase activity of Atg1 and facilitate the incorporation of Atg9 vesicles as an initial membrane platform. However, similar observations have not been made in mammalian cells due to the technical difficulties in the purification of the ULK1 complex's components as they contain long IDRs, especially ATG13 (Shi et al., 2020a).

ATG101 is the last component and the least-studied protein in the ULK1 complex. There is no homolog of ATG101 in budding yeast, and for a long time it was only known as a stabilization factor of ATG13 (Hosokawa et al., 2009b). A recent study by Suzuki et al. (2015a) showed that it contains a Trp-Phe (WF) finger motif that is responsible for direct or indirect recruitment of downstream factors, albeit the mechanism remains unknown.

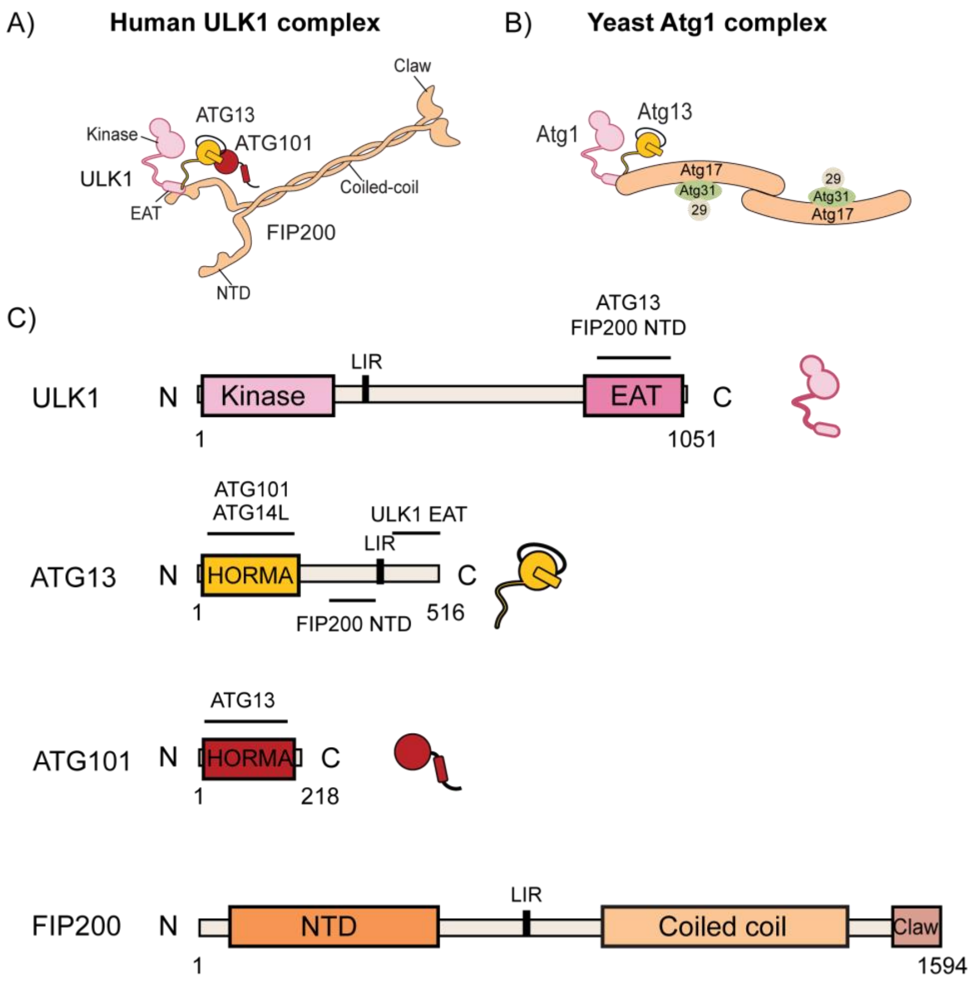

Figure 1.5. Components and organization of the human ULK1 complex. A) and B) Components of the human ULK1 complex, and yeast Atg1 complex, respectively. C) Domain organizations of proteins in the ULK complex. Interaction sites with other subunits are indicated.

1.2.3. ATG9 vesicles

Autophagy is a process that requires extensive membrane remodeling, yet surprisingly, ATG9/Atg9 is the only multi-pass transmembrane protein among the core autophagy machinery. There are two isoforms of ATG9 in mammalian cells: ATG9A and ATG9B, in contrast to only one isoform, Atg9, in yeast (Noda et al., 2000). ATG9A (hereafter ATG9) has been studied more extensively since it is ubiquitously expressed and plays a key role in the autophagy pathway, whereas ATG9B is tissue-specific, which is expressed in certain tissues, e.g., the esophagus mucosa, the cervix, and pituitary gland (Yamada et al., 2005). ATG9/Atg9 is derived from the Golgi apparatus and has been found in a variety of cellular compartments, including early endosomes, recycling endosomes, the plasma membrane, the *trans*-Golgi network (TGN), and large tubulovesicular compartments (also known as Atg9 reservoirs in yeast) (Young et al., 2006, Mari and Reggiori, 2010, Orsi et al., 2012, Puri et al., 2014, Yamamoto et al., 2012). In yeast, the majority of Atg9 is present on cytosolic mobile vesicles of about 30–60 nm in size, each containing approximately 24–32 Atg9 molecules (Yamamoto et al., 2012). Similar characteristics were also observed in mammalian ATG9 (Kakuta et al., 2017). Interestingly, the ATG9 vesicles also contain other membrane proteins such as ATG23 and GTPase Rab1B, yet their roles in autophagy or ATG9 trafficking require further investigation (Backues et al., 2015, Kakuta et al., 2017).

Although ATG9/Atg9 is indispensable for autophagy as demonstrated in several studies (Kuma et al., 2004, Saitoh et al., 2009, Imai et al., 2016, Young et al., 2006, Suzuki et al., 2015b), its role has remained a mystery for a long time because of its complex trafficking in the cytosol and the difficulties in *in vitro* reconstitution. It has long been proposed as a membrane transporter that shuttles lipids and/or proteins from several lipid sources to the growing phagophore because it has some characteristics that are particularly suited for the role. For example, it is highly mobile and can be upregulated when autophagy is induced (Mari et al., 2010, Young et al., 2006, Zhou et al., 2017). In addition to being mobile, it also localizes to various membrane sources in the cytosol, as mentioned above, and especially to the autophagy initiation site in autophagy-inducing conditions. For example, during starvation-induced bulk autophagy in yeast, Atg13 and Atg17 are involved in the Atg9 recruitment to the PAS via their interactions (Suzuki et al., 2015b, Sekito et al., 2009). In mammals, the ULK1 complex first localizes to the ER subdomain enriched in phosphatidylinositol synthase and then translocates to ATG9 vesicles in a manner dependent on both ATG9 and PI3K-C1 (Nishimura and Mizushima, 2017). These observations suggest an early association of ATG9 vesicles with the autophagic membrane and support the putative role of ATG9 as a membrane transporter.

Indeed, the integration of Atg9 vesicles into early autophagic membranes has been shown in several studies, yet some argue that the vesicles may not continue to supply lipids throughout the lifetime of the autophagosome as membrane transporters. Using high-resolution microscopy to track the dynamics of Atg9, Yamamoto et al. (2012) demonstrated that phagophore nucleation in yeast requires about three vesicles of Atg9. They also established that the protein is embedded in the phagophore membrane rather than binding to other proteins on the membrane's surface, thus leaving the possibility for Atg9 membrane integration into the phagophore/autophagosome. However, considering the vesicle size of about 30−60 nm, the amount of membrane supply provided by Atg9 vesicles is far from sufficient for the autophagosome. Therefore, they suggested that Atg9 vesicles may only serve as a seeding membrane rather than a steady supply of membranes. In addition, a study by Judith et al. (2019) demonstrated ATG9-mediated delivery of lipids and cargos to the phagophore for the first time. In this study, the authors showed that ARFIP2, a protein identified using SILAC-based immunoisolation, is a component of the ATG9-positive membranes. Upon starvation, ARFIP2 activates PI4KIIIβ, a phosphatidylinositol-metabolizing enzyme that binds to ATG9, thus mediating PI4P production on the ATG9 vesicles. Both PI4KIIIβ and PI4P are then delivered to the autophagosome initiation site by ATG9 vesicles, followed by the recruitment of the ULK1 complex through ATG13's binding to PI4P. However, the mechanistic detail of the process remains elusive. Moreover, it is notable that ATG9 is only transiently associated with the autophagosome in mammals (Orsi et al., 2012), whereas in yeast, Atg9 becomes an integral part of the phagophore and is recycled before autophagosome closure (Noda et al., 2000).

Meanwhile, the above findings have paved the way for another paradigm in which the fusion of a few ATG9/Atg9 vesicles is supposed to provide the first membrane platform (seeding membrane) instead of a continued supply of lipids in which ATG9 vesicles function as membrane transporters. The nucleated membrane hence requires lipid supply from other sources than ATG9/Atg9 to further expand, which will be discussed in Section 1.3.1. Regarding the fusion of ATG9/Atg9 vesicles, some tethering factors have been investigated. For example, Atg8-PE is proposed by Nakatogawa et al. (2007) as a candidate that mediates the tethering and hemifusion of Atg9 vesicles, since Atg8-PE has been proven to have such activity *in vitro*. Besides, Rao et al. (2016) discovered that Atg17 is another tethering mediator of Atg9 vesicles in bulk autophagy, whereas Matscheko et al. (2019) found that the vesicles are tethered by Atg11 in selective autophagy. Other notable fusion-mediating candidates include SNARE complexes and TRAPP-III tethering machinery (Yu et al., 2018, Lynch-Day et al., 2010). In addition to tethering and fusion, Gomez-Sanchez et al. (2018) also showed that Atg9 recruits the lipid transfer protein Atg2, and its partner Atg18 to establish a contact site between the endoplasmic reticulum (ER) and the phagophore. This is another supportive argument for the role of Atg9 vesicles as seeding membranes, since lipid transfer activity can only occur between two existing membrane platforms, particularly the ER (donor membrane) and Atg9-positive membrane (acceptor membrane). Recently, using purified components involved in the Atg8 lipidation cascades, PI3KC3-C1, and the Atg2-Atg18 complex, Sawa-Makarska et al. (2020) could reproduce the Atg8 lipidation process *in vitro* with Atg9 proteoliposomes or Atg9 vesicles isolated from yeast as a substrate, proving Atg9's role as a platform for the recruitment and subsequent activities of the autophagy machinery.

Aside from the suggested functions, recent structural and biochemical studies have shed light on the functions of ATG9/Atg9. The protein consists of a conserved transmembrane domain (core domain hereafter) and two cytosolic IDRs at both the N and the C terminals, which vary in both length and sequence across species (Tooze, 2010). Structures of the core domain of ATG9/Atg9 have been reported by several groups. Lai et al. (2019) reported the first sub-nanometer cryo-EM structure of Atg9 in *Arabidopsis thaliana,* followed by higher resolution structures of human ATG9A (Guardia et al., 2020, Maeda et al., 2020) and yeast Atg9 (Matoba and Noda, 2021). In general, the data show that ATG9 forms a homotrimer, with each protomer comprising four transmembrane segments and two alpha helices embedded only on the membrane's cytosolic-facing leaflet (Figure 1.6 A and B). The formation of the trimer creates a network of branched cavities within the transmembrane domain of ATG9/Atg9. Those cavities include the vertical pore in the center that connects to the lateral branch opening toward the membrane side and the perpendicular branch facing the cytosolic side (Figure 1.6 C).

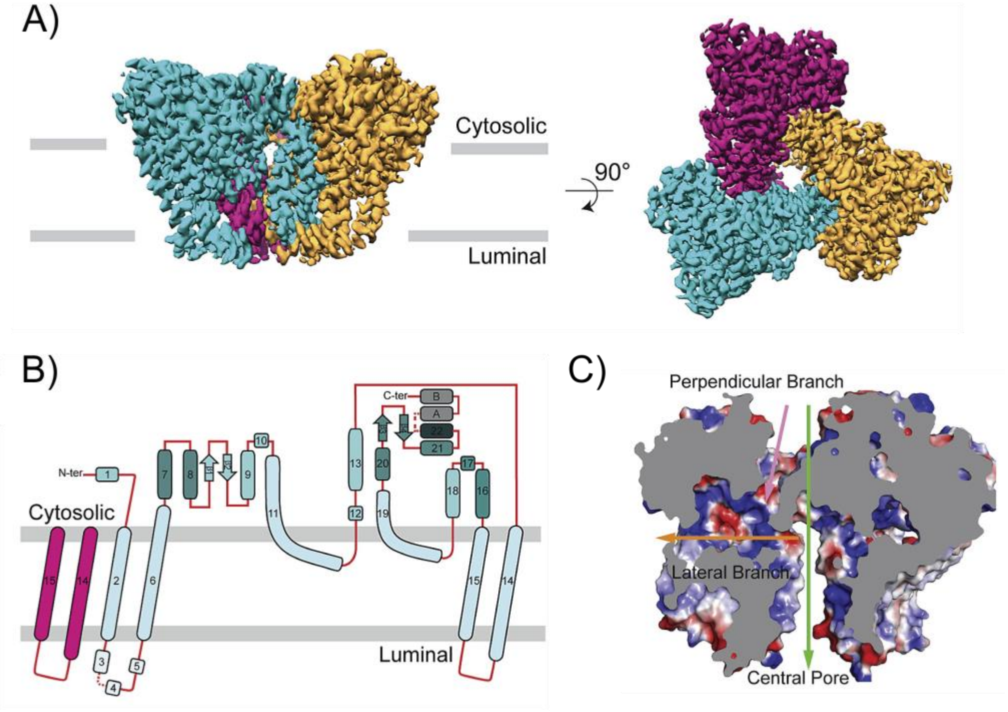

Figure 1.6. Cryo-EM structure of human ATG9A transmembrane domain (PDB: 6WR4). A) Electron density map of ATG9 trimer on lipid bilayer membrane (gray lines), each protomer is colored in purple, yellow and blue, B) Domain organization of ATG9 protomer on lipid bilayer membrane (gray lines), C) A cross-section of ATG9 trimer showing the central pore, lateral branch, and perpendicular branch (green, yellow, and pink arrows, respectively). Figure taken from Guardia et al. (2020).

Biochemical studies of ATG9/Atg9 showed that the cavity is essential for the protein’s function as a scramblase (Matoba et al., 2020, Maeda et al., 2020). Scramblase is a category of lipid transporters that includes flippases, floppases, and scramblases. They change the position of lipid head groups between two leaflets of the lipid bilayer membrane. While flippase and floppase require ATP to transport lipids from the outer leaflet to the inner leaflet and from the inner leaflet to the outer leaflet, respectively, scramblase does not require ATP for its non-specific and bi-directional scrambling of lipid between the two leaflets (Figure 1.7) (Daleke, 2003). This function could be combined with the lipid transfer activity of ATG2/Atg2 to facilitate the elongation of the phagophore, which will be discussed in more detail in Section 1.3.2.

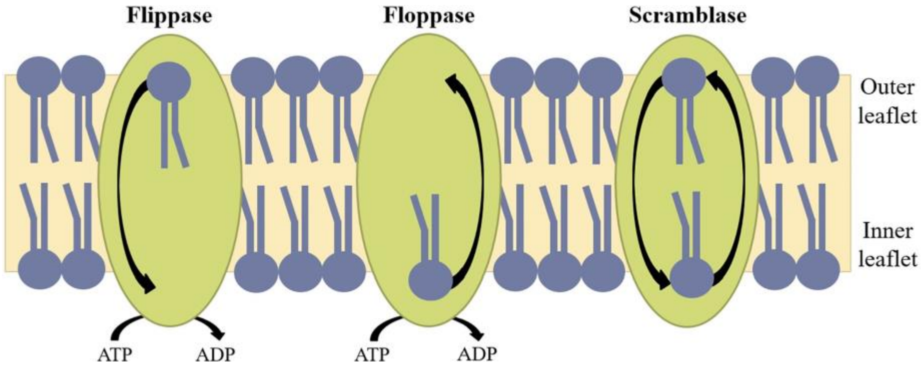

Figure 1.7. A schematic illustration of flippase, floppase and scramblase activity in the lipid bilayer membrane. Figure taken from Clarke et al. (2020).

1.2.4. The class 3 PI3K complex 1

Upon autophagy induction, the ULK1 complex is activated, which subsequently recruits and activates the downstream machinery required for autophagosome formation. It has been shown to directly regulate the class III phosphatidylinositol kinase complex I and II (PI3K-C1 and PI3K-C2), the lipid kinases that exclusively phosphorylate the 3-OH group at the 3’ position of the inositol ring of the lipid molecule PtdIns (PI) to generate PtdIns(3)P (PI3P) (Balla, 2013, Backer, 2016). PI3P has been shown to be a critical element of the autophagic membrane identity and a key secondary messenger in directing the recruitment and activity of downstream effector proteins, as well as intracellular trafficking (Foster et al., 2003, Matsunaga et al., 2010, Axe et al., 2008). Particularly, in autophagosome biogenesis, PI3P recruits WIPI2 (Atg21 in yeast) and WIPI4 (Atg18 in yeast), which are required for LC3 lipidation (discussed in Section 1.2.6) and localization of the lipid transfer machinery (discussed in Section 1.3.2), respectively. Besides PI3P, other PIs produced by other lipid kinase complexes such as PtdIns(4)P (PI4P) and PtsIn(3,5)P_2 (PI(3,5)P_2) are also involved in autophagy and many other cellular functions (Schink et al., 2016). However, PI3P production by PI3K-C1 and the role of PI3P in recruiting downstream effector proteins in autophagy are better characterized.

The PI3K complexes are highly conserved in mammalian cells, the PI3K-C1 consists of Vacuolar Protein Sorting 34 (VPS34), VPS15, BECN1, and ATG14L whereas in the PI3K-C2, ATG14L is replaced by UVRAG. The PI3K-C1 is involved mainly in autophagosome biogenesis by generating PI3P, whereas PI3K-C2 is involved in various intracellular pathways such as endocytic sorting (Liang et al., 2008), autophagosome maturation (Liang et al., 2008), and lysosome recycling (Munson et al., 2015). Cryo-EM structures of the human PI3K-C1 complex have been reported (Ma et al., 2020, Baskaran et al., 2014), which reveal its organization and orientation on the membrane. The complex has a V-shaped structure and a 1:1:1:1 stoichiometry, with VPS34 and VPS15 mainly occupying one arm and ATG14L and BECN1 occupying the other (Figure 1.8). The V-shaped complex binds to membranes with the two arms facing the membrane side, as the tip of each arm contain membrane-binding regions. The kinase domain of VPS34, located at one tip of the V shape, directly binds to the membrane and mediates the conversion of PI to PI3P, making VPS34 the primary lipid kinase in the complex (Schu et al., 1993, Stack and Emr, 1994). VPS34 also has an N-terminal C2 domain and a helical middle domain that are required for the stability of the protein and its interactions with the other subunits, including BECN1 and VPS15 (Rostislavleva et al., 2015, Baskaran et al., 2014) (Figure 1.8 B). VPS15 is a pseudo-kinase that enhances the stability and kinase activity of VPS34 (Panaretou et al., 1997, Stack and Emr, 1994) and serves as a membrane anchor due to its myristoylated N-terminal domain (Herman et al., 1991). The protein interacts with the coiled-coil (CC) domains of BECN1 and ATG14L through its C-terminal WD40 domain, and with the kinase domain of VPS34 through its HEAT domain (Ma et al., 2020, Baskaran et al., 2014) (Figure 1.8 B). BECN1 (the ortholog of yeast Atg6) consists of an N-terminal IDR with multiple phosphorylation sites (residues 1-15) (Lee et al., 2016), a middle CC domain that intertwines with the CC domain of ATG14L (Mei et al., 2016), and a C-terminal β-α autophagy-specific (BARA) domain that targets one arm of the complex to the membrane (Huang et al., 2012) (Figure 1.8 B). ATG14L, the autophagy-specific protein of the PI3K-C1, is also a multi-domain protein. Besides the middle CC domain that binds to BECN1 and VPS34, ATG14L also has an IDR that interacts with ATG13 and a C-terminal BATS domain that has a strong preference for high curvature membranes (Fan et al., 2011, Obara et al., 2006) (Figure 1.8 B).

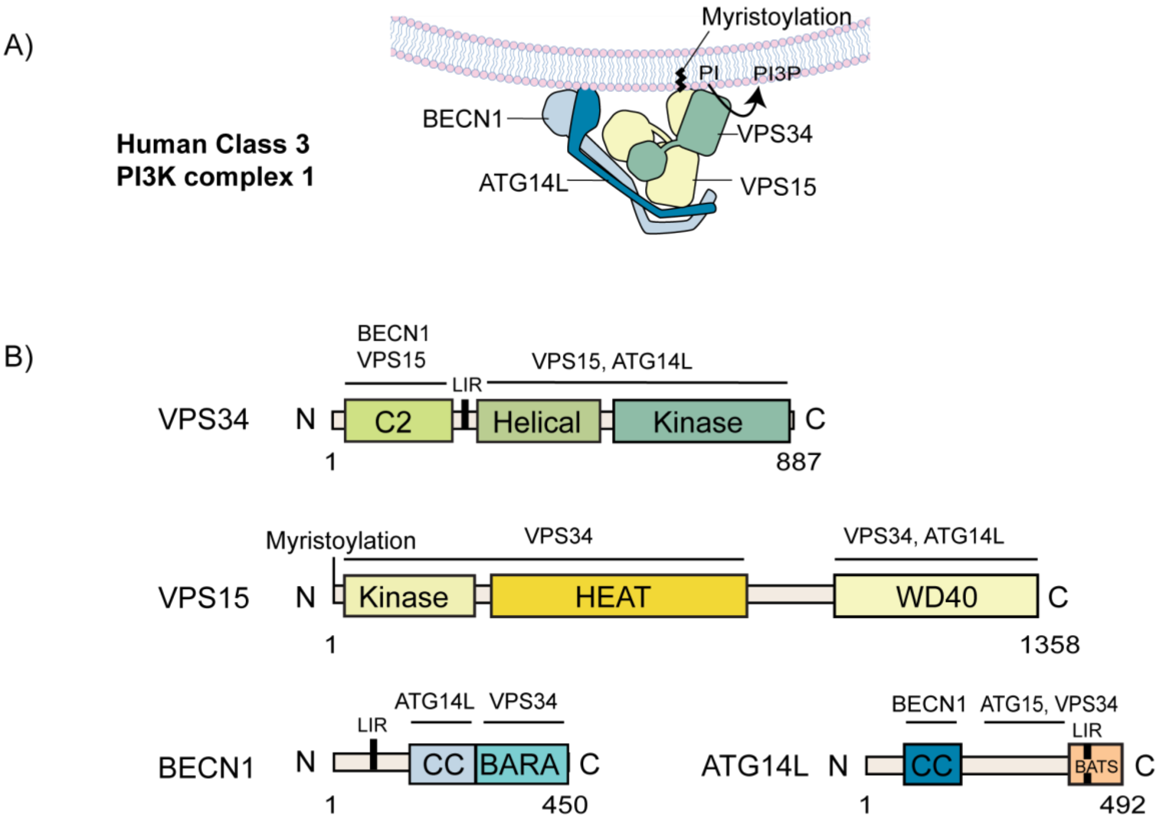

Figure 1.8. Components and organization of the human class 3 PI3K complex 1. A) The orientation of human class 3 PI3K complex on membrane, B) Domain organizations of the PI3K-C1 subunits. Interaction sites with other subunits are indicated.

Regarding the activation and recruitment to the forming autophagosome, PI3K-C1 is known to be regulated by various upstream regulators. Among them, the ULK1/Atg1 complex and the mTOR/TOR complex are the two best characterized. Interestingly, phosphorylations by the ULK1 complex have been reported for all four components of the PI3K-C1 (Mercer et al., 2021, Russell et al., 2013, Wold et al., 2016); however, the consequences of these phosphorylations are unclear. Moreover, at physiological conditions, all phosphorylation happens simultaneously, whereas *in vitro* the phosphorylation of each residue/protein was characterized separately, thus undermining their cooperative effects. Meanwhile, genetic studies have identified some of the most important phosphorylation sites on the PI3K-C1, which are induced by the ULK1 complex. They are S15 and S30 residues on BECN1 (Russell et al., 2013, Park et al., 2018), and S29 on ATG14L (Park et al., 2016). Both phosphorylation of S15 and S30 residues on BECN1 are critical for autophagy induction during amino acid deprivation. Non-phosphorylated mutants of the residues significantly suppress autophagy induction under starvation conditions. S29 phosphorylation on ATG14L occurs after the recruitment of the protein via its binding to a component of the ULK1 complex, ATG13. The interaction allows ULK1 to induce ATG14L's S29 phosphorylation in autophagy-inducing conditions, e.g., nutrient starvation or inhibition of mTOR. This phosphorylation has been shown to subsequently enhance the activity of PI3K-C1, thus facilitating phagophore formation and elongation. Multiple serine/threonine residues on ATG14L were also identified as the targets of mTOR phosphorylation (Yuan et al., 2013). Unlike ULK1-induced phosphorylation, mTOR phosphorylation on ATG14L inhibits PI3K-C1 kinase activity, indicating direct regulation of mTOR in the absence of nutrients and the critical role of ATG14L in the PI3K-C1 activity. In brief, the data indicates that the PI3K-C1 are regulated by both the ULK1 complex and mTOR complex to produce PI3P in the autophagic membrane.

1.2.5. The PI3P-binding proteins

As mentioned previously, PI3P is a key secondary messenger for the recruitment of PI3P-binding proteins to the autophagosome and helps the autophagy pathway progress further. These PI3P-binding proteins are the PROPPINs (β-propellers that bind PtdIns) protein family in yeast, the WIPI (WD-40 repeat containing protein that interacts with PtdIns) protein family, and DFCP1 (double FYVE domain-containing protein 1) in mammals. As the name implies, the PROPPINs and WIPIs' structures generally consist of a characteristic seven-bladed β propeller and the signature FRRG (Phe-Arg-Arg-Gly)/LRRG (Leu-Arg-Arg-Gly) motif that recognizes PI3P (Krick et al., 2006), whereas the DFCP1 contains two PI3P-binding FYVE domains (Axe et al., 2008). Structures of *Kluyveromyces lactis* Hsv2 (PDB: 4AV8) (Baskaran et al., 2012, Krick et al., 2012), Atg18 (PDB: 6KYB) (Lei et al., 2020), WIPI2 (PDB:7MU2) (Strong et al., 2021), and WIPI3 (PDB:6KLR) (Ren et al., 2020) are representative examples of PI3P-binding capabilities. These proteins adopt a typical configuration of a seven-bladed β propeller, each containing a four-stranded antiparallel β sheet that are numbered from one (N-terminal) to seven (C-terminal). In blades 5 and 6 of the β propeller, the conserved FRRG motif creates two PI3P or PI(3,5)P_2 binding sites. The proteins are further anchored to the membrane by a hydrophobic loop in blade 6 that can insert itself into the membrane bilayer. Such arrangements keep the β propeller proteins tightly bound in a perpendicular orientation to the membrane (Figure 1.9) (Krick et al., 2012, Baskaran et al., 2012). The proteins can thus stabilize its binding partners on the membrane.

In yeast, there are three PROPPINs that are involved in autophagy: Atg18, Atg21, and Hsv2. Hsv2 is poorly characterized but is proposed to function in micronucleophagy (Krick et al., 2008). Atg18 binds to Atg2, which was recently shown to be a lipid transfer protein (Osawa et al., 2019). The two proteins independently bind to the membrane and stabilize each other; therefore, it is not known whether they are recruited to the PAS sequentially or as a complex. Although Atg2 does not have PI3P specificity like Atg18, it prefers to bind to high-curvature membranes *in vitro*, suggesting its localization to the edge of the forming phagophore (Kotani et al., 2018). In addition, Atg18 and Atg2 are both involved in phagophore elongation by tethering the ER to the phagophore and mediating lipid transfer from the ER for phagophore elongation (Osawa and Noda, 2019). This interesting function of Atg2-Atg18 is also conserved in mammalian proteins, ATG2-WIPI4 and will be discussed in detail in Section 1.3.2. Atg21 is another PROPPIN that is responsible for the correct localization of Atg16 to the PAS. Therefore, it is also essential for subsequent Atg8 lipidation since Atg16 is part of the Atg8 conjugation cascades, which are required for the downstream autophagy progression, including phagophore maturation and cargo recruitment (Strømhaug et al., 2004, Meiling-Wesse et al., 2004).

In mammals, DFCP1 resides in the ER and Golgi in nutrient-rich conditions and localizes to the omegasome during starvation due to its ER-targeting domain and PI3P-binding sites. Therefore, DFCP1 is commonly used in the field of autophagy as a robust omegasome marker. However, its function in autophagy is unknown, and the protein is also not essential for autophagy since deletion of the *DCFP1* gene also does not affect the process (Axe et al., 2008).

WIPIs in mammals are poorly understood compared to PROPPINs in yeast, although the WIPIs' functions are not redundant. There are four WIPIs: WIPI1, WIPI2, WIPI3 (WDR45B), and WIPI4 (WDR45). WIPI4 is the functional equivalent of Atg18. WIPI4 forms a complex with ATG2A and was recently found to enhance lipid transfer activity of ATG2 (Maeda et al., 2019). Like WIPI4, WIPI3 was found to interact with ATG2 through ATG2's WIR (WIPI-interacting-region) motif, but the functional relevance of this interaction is unclear (Ren et al., 2020). WIPI2 is the functional equivalent of yeast Atg21, which directly binds to ATG16L and directs the lipidation of LC3 (or Atg8 in yeast) (Dooley et al., 2015) (discussed in the following section, Figure 1.10). WIPI1 might also be involved in LC3 conjugation like WIPI2 since both proteins function upstream of the LC3 and ATG16L conjugation systems (Polson et al., 2010, Gaugel et al., 2012).

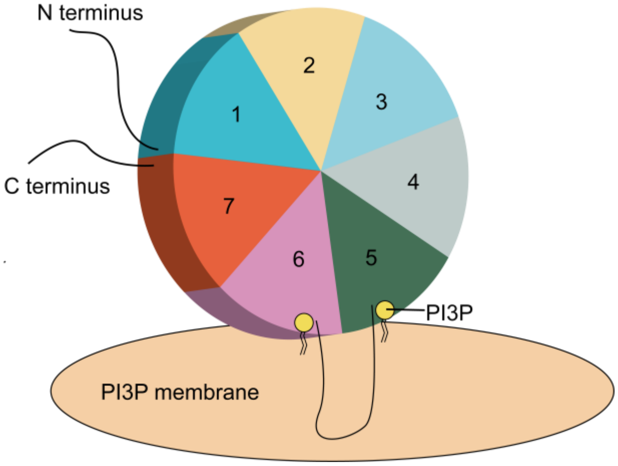

Figure 1.9. The two phosphoinositide-binding sites of PROPPIN and WIPI protein families. These proteins fold into a seven-bladed β propeller with PI3P binding sites in blades 5 and 6. A hydrophobic loop between blades 5 and 6 is inserted into the membrane.

1.2.6. The ubiquitin-like conjugation systems

Microtubule-associated protein light chain 3 (LC3) and GABARAP family proteins are the mammalian orthologs of Atg8 in yeast. LC3/Atg8 are used extensively in the autophagy field as a standard marker for the autophagic membrane since they are specifically conjugated to phosphatidylethanolamine (PE) present on the membrane. They are proposed to be key players in different stages of the autophagy cascades, such as phagophore elongation and closure of the autophagosome (Weidberg et al., 2010). However, their role in cargo recruitment to the autophagosome is the best characterized. As described in

Section 1.1.1, cargos are recognized by corresponding SARs which simultaneously bind to cargos and to Atg8/LC3 thanks to their AIM/LIR motifs, resulting in the sequestration of cargos in the inner membrane of the autophagosome (Xie and Klionsky, 2007, Martens and Behrends, 2020).

The conjugation of the LC3 and GABARAP subfamilies into the autophagosome membrane (also known as LC3 lipidation) is the hallmark of autophagosome membrane biogenesis and the best studied process in autophagy so far. It is a process that resembles ubiquitin conjugation and requires coordination of two ubiquitin-like conjugation cascades, LC3 and ATG12 (Figure 1.10). The conjugation system of ATG12 is processed to generate ATG12~ATG5-ATG16L1 complex, which functions as the RING domain of the ubiquitin E3 ligase in transferring LC3 from the E2-like enzyme ATG3 to PE. The complex is formed in several steps, starting with the activation of ATG12 by the E1-like enzyme ATG7, followed by the covalent conjugation to ATG5 mediated by the E2-like enzyme ATG10. The ATG12~ATG5 conjugate then binds non-covalently to ATG16L1, a dimeric coiled-coil protein, to form a tetrameric complex of ATG12~ATG5-ATG16L1 (Mizushima et al., 1998). On the other hand, the LC3 conjugation cascade begins with the cleaving of LC3 at the C-terminus by the cysteine protease ATG4 to expose a glycine residue required for its conjugation to PE. The processed LC3-I (LC3 with exposed Gly residues) then binds to the E1-like enzyme ATG7. ATG7 subsequently recruits ATG3 and mediates LC3-I transfer to ATG3. ATG3 then recruited the E3-like complex of ATG12~ATG5-ATG16L1 which promotes “protein-to-lipid” conjugation of LC3-I to LC3-II (a lipidated form of LC3) (Kabeya et al., 2000, Ichimura et al., 2000, Hanada et al., 2007). The enzymatic reaction is catalyzed by ATG12~ATG5 (Hanada et al., 2007, Fujioka et al., 2008), while ATG16L1 targets the complex to the autophagosome membrane through its interaction with WIPI2b, the PI3P effector protein on the membrane (Dooley et al., 2014). Lipidation of LC3 is a reversible process in which ATG4 can again cleave PE from LC3-II to release it from the intermediate phagophore membranes. This process allows the phagophore to mature into an enclosed autophagosome while replenishing LC3 levels in the cytosol (Tanida et al., 2004, Satoo et al., 2009).

Downstream of the LC3 conjugation are several molecular machines required for the enclosure of the phagophore and the delivery of the autophagosome to the lysosome for degradation. Comprehensive descriptions of these processes can be found in several excellent reviews (Noda et al., 2009, Jiang et al., 2021, Zhao et al., 2021).

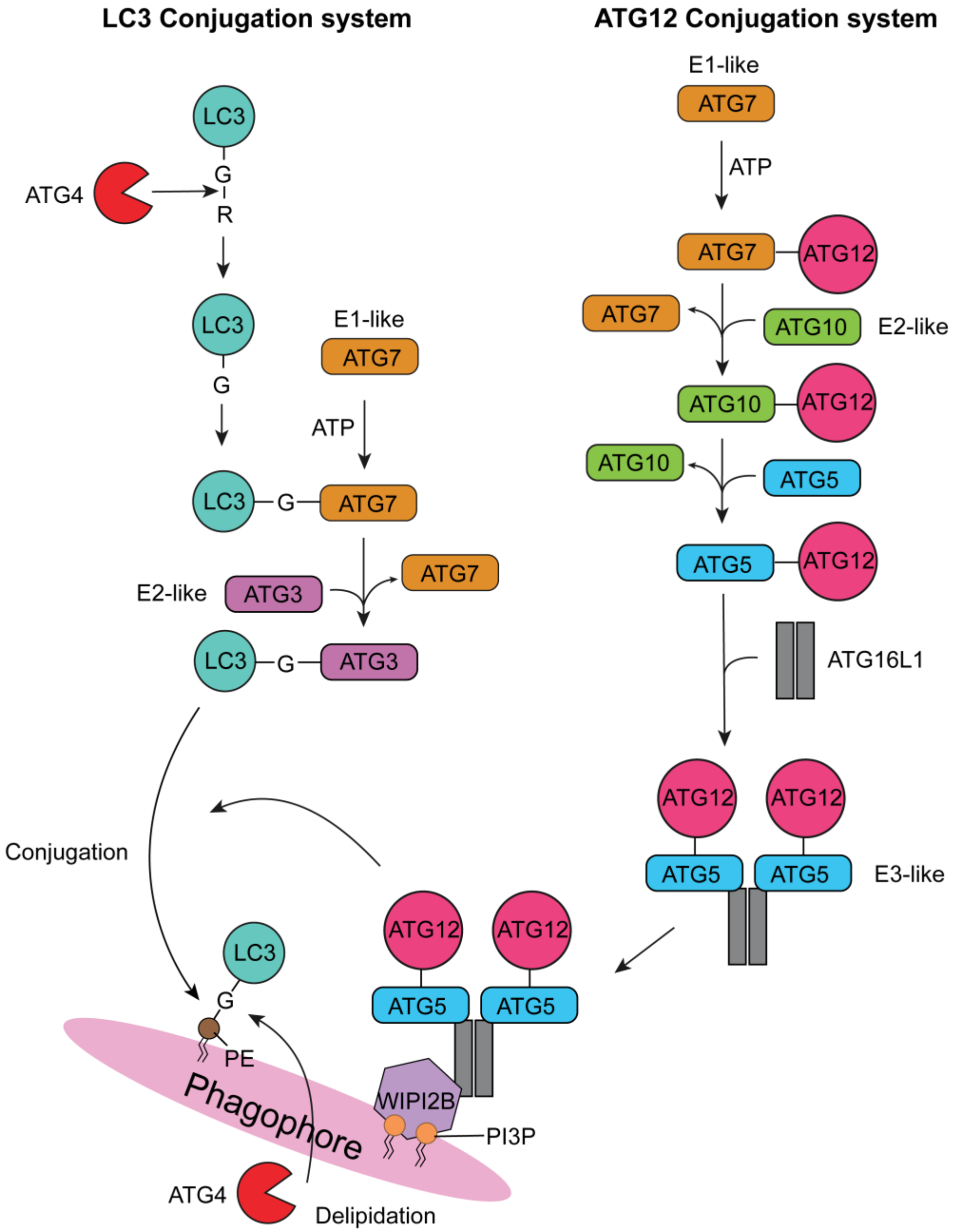

Figure 1.10. LC3 and ATG12 conjugation systems. The two conjugation systems of are interconnected and responsible for the lipidation of LC3 proteins in the phagophore. Details of the process is described in this section.

1.3. Autophagy is a membrane remodeling process

The hallmark of autophagy is the *de novo* formation of an autophagosome, a massive double membrane organelle. The process requires extensive membrane remodeling, which includes changes in the morphology and topology of the autophagic membrane during its lifetime, e.g., transformation of intracellular membranes into autophagic membranes at the PAS/Omegasome, phagophore elongation by lipid transfer and/or vesicle fusion, membrane scission for autophagosome closure, and membrane fusion between autophagosome and lysosome. In the last 50 years, increasing efforts have been put into exploring the basis of these processes. However, one of the most fundamental questions that remains unanswered is: what are the membrane sources of the autophagosome? (Juhasz and Neufeld, 2006). It is partly because the autophagosome is mostly devoid of transmembrane proteins (Baba et al., 1995, Fengsrud et al., 2000), making it challenging to identify the origin of the membrane, different stages in its development, and its trafficking. The following sections will discuss recent research regarding several putative membrane origins of autophagosomes and the corresponding lipid supply mechanisms (Section 1.3.1). In addition, the protein-mediated lipid transfers at the ER-Phagophore membrane contact sites will be discussed in more details since it is the focus of this thesis (Section 1.3.2).

1.3.1. Membrane sources of the autophagosome

Based on previous published data on autophagosome sizes, which can range from a few hundred nanometers to more than a micrometer in diameter depending on the cell type (Jin and Klionsky, 2014, Xie et al., 2008), Melia et al. (2020) estimated that an autophagosome with a diameter of ~400 nm would need about 3.000.000 phospholipid molecules for its maturation. The calculation also takes into account the luminal gap of about 10 to 30 nm between the two lipid bilayers of the double membrane (Nguyen et al., 2017) and the approximate size of a lipid molecule, which is 65 $Å^2$ for the head group area and 20 Å for the length of the molecule (Kucerka et al., 2005). Furthermore, once autophagy is induced, up to 100 autophagosomes can form simultaneously in the cytosol (Fass et al., 2006, Hailey et al., 2010, Guo et al., 2012), thus the amount of lipids needed for autophagosome formation can easily exceed 100.000.000 lipid molecules. Therefore, it is proposed that the autophagosome may receive lipids from several organelles in the cytosol via different routes, as the cell needs to ensure that other essential processes are not compromised and that no single lipid source is depleted. Indeed, recent advances in cellular biology, biochemistry, and imaging techniques have shown that there are several possible routes for lipids to get to the autophagosome. Vesicle-mediated lipid delivery, protein-mediated lipid transfer, and direct extrusion from pre-existing organelles are the most prevalent (Melia et al., 2020, Osawa and Noda, 2019). Along with the postulated lipid supply mechanisms, various cytosolic organelles have been shown to have certain correlations with the autophagosome and could be potential lipid donors. The plasma membrane (Ravikumar et al., 2010), recycling endosomes (Puri et al., 2013), endoplasmic reticulum (ER) (Axe et al., 2008, Hayashi-Nishino et al., 2009), ER-Golgi intermediate compartment (ERGIC)(Appenzeller-Herzog and Hauri, 2006), and mitochondria (Hailey et al., 2010) are among them (Figure 1.11).

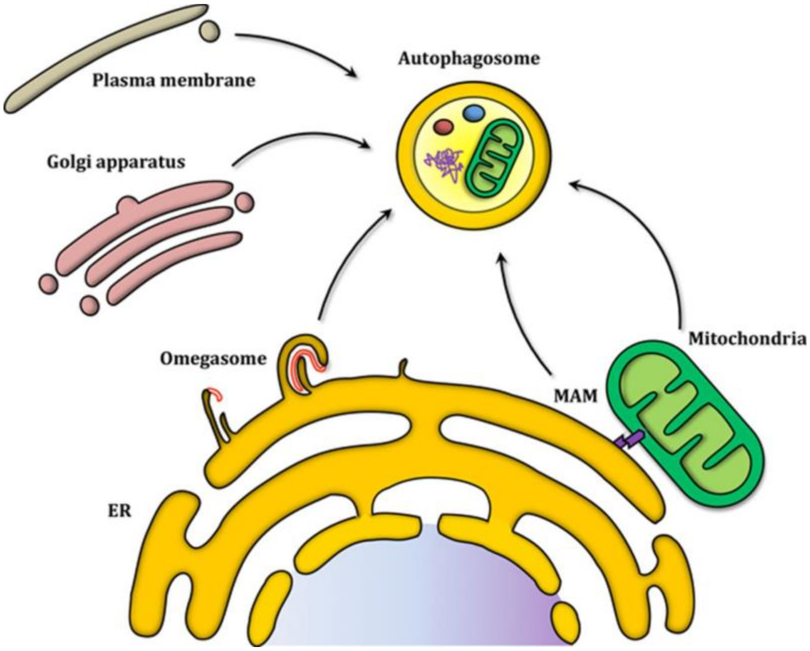

Figure 1.11. Putative membrane sources of the autophagosome. The sources are: the ER, the mitochondria, the plasma membrane, the Golgi apparatus, and MAM (mitochondria-associated ER membrane). Some of these membrane sources are discussed in this section. Figure taken from Gatica et al. (2015).

The ER is the main factory that produces lipids and proteins for the cell. The organelle forms an extensive network throughout the cytoplasm, playing various roles and associating with different cytosolic compartments. Unsurprisingly, it was the first organelle to be suggested as a source of lipids for the autophagosomes (Ericsson, 1969, Arstila and Trump, 1968) (Figure 1.11). Since its discovery by Axe et al. (2008), the omegasome has generally been accepted as the nucleation membrane of the autophagosome. From live-cell imaging experiments, the authors reported the presence of an omega-shaped membrane emerging from a subdomain of the ER (the ERES) enriched in PI3P. The structure was marked by the presence of the PI3P-binding protein DFCP1 and was named “omegasome”. The observation was later confirmed by two other groups using 3D cryo-electron tomography (Hayashi-Nishino et al., 2009, Ylä-Anttila et al., 2009). These findings support the hypothesis that the ER physically connects and supplies lipids to the autophagosome. However, because of the overlap in membrane composition and the absence of distinct markers to differentiate the autophagic membranes at various phases, it is unclear whether the direct connection with the ER persists once the omegasome evolves into the phagophore or autophagosome. Moreover, it is still unclear how the resident proteins in the ER are filtered out in the extruding process, since the autophagosome is mostly devoid of membrane proteins (Baba et al., 1995, Fengsrud et al., 2000).

In addition to the ER, data from Puri et al. (2018) showed that the recycling endosome also supplies the primary membrane platform for the development of the phagophore. Their conclusion was drawn based on several observations. First, they observed that WIPI2 is recruited to RAB11A-positive membranes (RAB11A is the recycling endosome marker), which marks the site for LC3 conjugation on the membranes. They also showed that other core autophagy proteins also localize to this membrane, including DFCP1, ATG14L, and BECN1, and proved that the membrane is indeed a double lipid bilayer. Interestingly, by live-cell imaging, they also showed that the membrane could engulf autophagic substrates such as SQSTM1/p62 or even mitochondria when cells were exposed to a range of autophagy stimuli.

Data from Hailey et al. (2010) also suggest that the outer membrane (cytosolic facing) of mitochondria can also be a site for autophagosome formation (Figure 1.11). They showed that in starved cells, ATG5, a component of the LC3 conjugation machinery, transiently localizes to the mitochondrial outer membrane, followed by LC3s. This indicates that LC3s are conjugated in the membrane after ATG5 recruitment. Using confocal microscopy, they also showed that fluorescently labeled lipids in the mitochondria can be transferred to the autophagosome. In addition, other studies also reveal that the autophagosome nucleates at the ER-mitochondria contact site, where ATG9 vesicles are also recruited during starvation-induced autophagy, suggesting the interplay of different membrane sources in autophagy (Hamasaki et al., 2013, Karanasios et al., 2013, Karanasios et al., 2016).

The plasma membrane is another unexpected source of lipids for the autophagosome. By labeling and monitoring the movement of lipids in the plasma membrane of living cells, Ravikumar et al. (2010) discovered that the labeled lipids can integrate into autophagosomes, suggesting that the plasma membrane is also a lipid donor of the autophagosome. In following studies, ATG9 and ATG16L1 residing on the plasma membrane were shown to be internalized by clathrin-mediated endocytosis and subsequently trafficked to the early endosome and recycling endosome, respectively. ATG9 vesicles then travel from the early endosomes to the recycling endosomes and coalesce with ATG16L in the recycling endosomes. The two subsequently contribute to the establishment of autophagosome precursors through VAMP3 SNARE-mediated heterotypic fusion (Puri et al., 2014, Moreau et al., 2011). These observations are consistent with the proposed function of ATG9 vesicles as a membrane donor via vesicle-mediated delivery. However, the lipid supply from the vesicles is relatively limited given its small size, and the mechanism is still unclear, as discussed earlier in Section 1.2.3.

ER-derived COPII-coated vesicle (COPII vesicle hereafter) is another proposed lipid source since it was observed to accumulate at the PAS when autophagy is inhibited (Tan et al., 2013), and autophagosomes cannot form in mutants that are deficient in COPII vesicle formation (Ishihara et al., 2001).

Furthermore, several complementary studies can be put together to explain how COPII vesicles can possibly deliver lipid to the nascent phagophore, as reviewed in Rabouille (2019) and Li et al. (2020b). The studies have shown that in mammalian cells, COPII vesicles are directed to the ER-Golgi intermediate compartment (ERGIC), and subsequently to the autophagosome in response to starvation. The process is also shown to be partly regulated by FIP200 and ULK1-mediated phosphorylation of COPII vesicle subunits. It is clear from the studies mentioned in the two reviews that COPII is closely related to autophagy; however, direct evidence of COPII vesicle contribution to the phagophore is still needed. One remaining question is how the cells can balance the production of these vesicles for phagophore expansion during nutrient or amino acid deprivation because cells also need to reduce protein secretion due to a lack of resources in such conditions.

In brief, these studies demonstrated that autophagosomes may obtain lipids from various intracellular compartments. Hence, it is of basic interest to learn how the cell regulates these processes and diverse lipid sources in various contexts, as well as whether multiple lipid supplies are contributed to the autophagosome concurrently or sequentially in critical conditions. The next section will discuss protein-mediated lipid transfer from the ER to the phagophore, which happens at the membrane contact site between the two organelles.

1.3.2. Lipid transfer at the ER-phagophore membrane contact site.

In eukaryotic cells, intracellular compartments are typically isolated from the cytosol in the form of membrane-bound organelles. These organelles allow separation of biochemical processes in their dedicated compartments, yet connections between them are often needed to facilitate functional integration of different cellular processes. These connections usually happen at the membrane contacts sites (MSCs), which is defined as small cytosolic gaps of ~10–25 nm between two opposing bi- or monolayer membrane-bound organelles (Scorrano et al., 2019). Additionally, the membranes are not fused at these gaps because the connections are typically established by multiple protein tethers (Pan et al., 2000, Henne et al., 2015, Scorrano et al., 2019). Even though MCSs have been observed by electron microscopy since the early 1950s (Porter, 1953), they were only recently recognized as hubs for the transport of lipids and the exchange of diverse metabolites. MCSs thus plays crucial roles in intracellular signaling, organelle trafficking, and inheritance (Prinz, 2014, Holthuis and Levine, 2005, Helle et al., 2013). Unsurprisingly, increasing data in the last five years has shown that the ER-phagophore MCS is also involved in the regulation of the *de novo* formation of the autophagosome.

MCSs between the ER and the tip of the growing phagophore have been shown to be established by the complex formation of Atg9, Atg2, and Atg18 in yeast (Gomez-Sanchez et al., 2018, Graef et al., 2013). In thier studies, the authors suggested a model in which Atg9 associates with the edge of the phagophore and sequentially targets Atg2 and Atg18 to the site, though Atg2 can bind to the membrane independently of Atg9. Abolishing the complex interactions leads to an abnormal distribution of Atg2 throughout the phagophore surface, severely impairing autophagy as a result of compromising MCSs. In mammals, there are two isoforms of ATG2, ATG2A (ATG2 hereafter) and ATG2B, which share 40% sequence similarity and have redundant functions in autophagy (Velikkakath et al., 2012). Research in the last five years has shown that ATG2/Atg2 is the main factor that mediates both the tethering at the ER-phagophore MCSs and the lipid transfer from the ER to the phagophore. For example, data from several groups show that the protein adopts a rod-shaped structure, with both tips binding and bridging two artificial membranes (liposomes) *in vitro*. The N-terminal tip contains a Pfam-registered conserved domain “Chorein_N” (also called the N tip), and the opposite tip consists of a conserved “ATG2-CAD” domain (also called the CAD tip) (Maeda et al., 2019) (Figure 1.12 A). In addition, binding of ATG2 to the PI3P-effector protein WIPI4 (or yeast Atg2 to Atg18) at the CAD tip facilitates ATG2/Atg2’s heterotypic tethering of PI3P-positive liposomes with PI3P-free liposomes *in vitro* (Zheng et al., 2017, Graef, 2018, Chowdhury et al., 2018, Otomo et al., 2018, Kotani et al., 2018). Although the high-resolution structure of the full length ATG2 has not been reported, sub-nanometer resolution structural data of ATG2A-WIPI4 (Chowdhury et al., 2018), ATG2B-WIPI4 (Zheng et al., 2017) show that the ATG2-WIPI4 complex can bridge a distance of ~ 20 nm, which is a typical gap of MCSs (Figure 1.12 B). The structure also shows a long cavity that runs the length of ATG2, which is thought to act as a lipid channel that transports lipids between membranes (Chowdhury et al., 2018). Moreover, ATG2/Atg2 shares high sequence and structural homology with the vacuolar protein sorting protein VPS13/Vps13, which also functions as a tethering and lipid transfer protein at MCSs of various organelles (Gao and Yang, 2018, Li et al., 2020a, Kumar et al., 2018). Structures of the N-terminal fragments of *Chaetomium thermophilum* (Li et al., 2020a) and *S. cerevisiae* (Kumar et al., 2018) reveal a hydrophobic cavity that can accommodate a large number of lipids with broad specificity. The cavity is predicted to extend to the C-terminal end and create a channel for lipid movement along the protein length, as described for ATG2 (Kumar et al., 2018). Together, these data point to the similarities in the lipid transfer and tethering functions of both proteins. Indeed, the ATP-independent lipid transfer by ATG2/Atg2, like that of Vps13, was later proven in several biochemical studies (Maeda et al., 2019, Otomo and Maeda, 2019, Valverde et al., 2019, Osawa et al., 2019). Yet another question arises: whether the lipid transfer activity of ATG2 is sufficient for phagophore expansion. As noted in Section 1.3.1, an autophagosome of ~ 400 nm to 1 µm in size would need a supply of ~ 3 to 25 million phospholipids to reach its size in ~ 5 to 10 min (Mizushima et al., 2001, Fujita et al., 2008), implying a total transfer rate of more than 5000 lipids/autophagosome/second. The apparent transfer rate of ATG2 *in vitro* is estimated to be about 115 lipid molecules/second/ATG2A molecule and 750 lipid molecules/second/yeast Atg2 molecule (von Bülow and Hummer, 2020, Maeda et al., 2019, Osawa et al., 2019). Therefore, multiple copies of ATG2 at the ER-phagophore contact site in physiological conditions might supply a significant amount of lipids for the autophagosome, although supply from other sources should not be overlooked. Moreover, since ATG2/Atg2 is a peripheral membrane protein, lipid transfer only happens at the cytosolic leaflets of the donor organelle (the ER) and the acceptor organelle (the phagophore), leading to an asymmetry in the lipid bilayer of both organelles. Therefore, factors that equilibrate the two opposing leaflets of the membrane are required. As mentioned in Section 1.2.3, ATG9/Atg9 is a lipid scramblase protein that is ideal for this task. Interestingly, interactions between ATG2/Atg2 and ATG9/Atg9 have also been demonstrated in several studies (Gomez-Sanchez et al., 2018, Ghanbarpour et al., 2021, Tang et al., 2019), supporting their cooperative roles in delivering and equilibrating lipid between the two leaflets of the growing phagophore. Meanwhile, two integral membrane proteins required for the phagophore expansion on the ER side, TMEM41B and VMP1, are also the two scramblase proteins that have recently been shown to interact with ATG2 (Ghanbarpour et al., 2021, Shoemaker et al., 2019, Reinisch et al., 2021, Morita et al., 2018, Wang et al., 2020). Ghanbarpour et al. (2021) also propose a model in which the three scramblases TMEM41B, VMP1 and ATG9 bind to opposite tips of ATG2 and support its lipid transfer activity by equilibrating lipids between the two leaflets of both the ER and the phagophore at the established MCS (Figure 1.12 C). However, the impact of their collaborative activities on lipid transfer efficiency remains to be seen. In this thesis, one of the main goals is to validate this hypothesis using biochemical reconstitution approach.

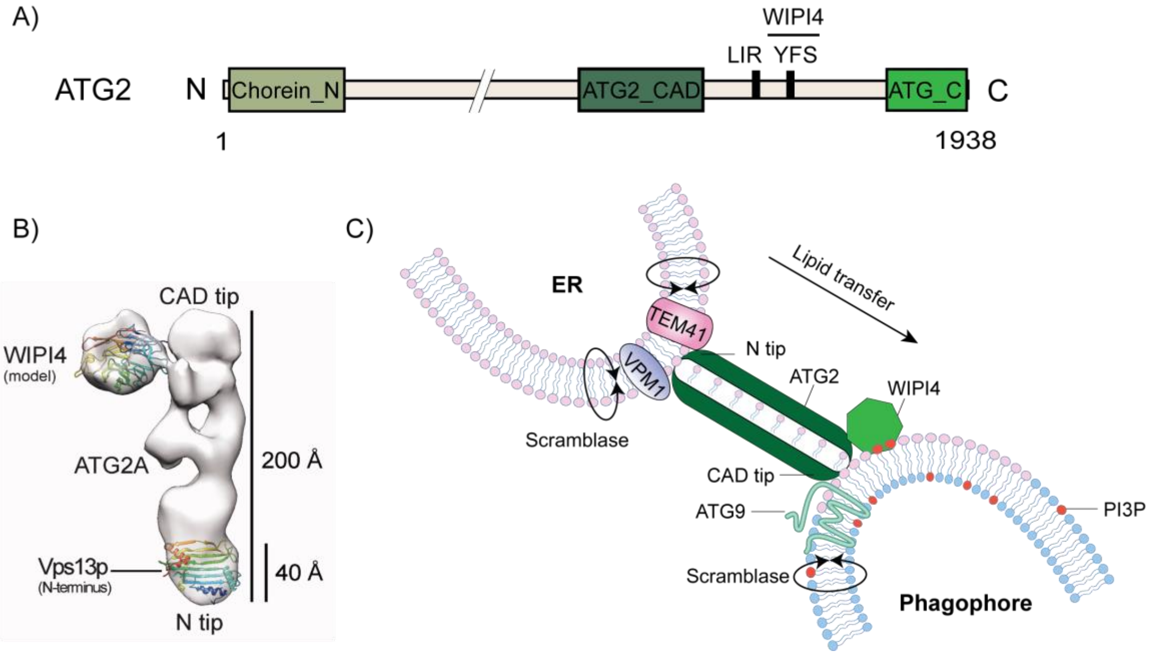

Figure 1.12. Proposed model for lipid transfer at the ER-Phagophore MCS. A) Domain organization of human ATG2A. B) Negative-stain electron microscope structure of the ATG2-WIPI4 complex (EMD-8899), with a docked N-terminal domain of Vps13p (PDB: 6CBC), and WIPI4 homology model (Figure **1.12** B is taken from Otomo et al. (2018)). C) Model for ATG2-mediated lipid transfer at the ER-Phagophore MCS.

1.4. Regulation of autophagy and the potential role of metamorphic proteins

It is estimated that an autophagosome's lifespan from initiation to degradation takes about 4–5 min in yeast (Geng et al., 2008), and 5–10 min in mammals (Mizushima et al., 2001, Fujita et al., 2008). However, little is known about the molecular switch that speeds up or slows down the process in response to environmental conditions. Considering that the formation of the autophagosome is mainly a membrane biogenesis process that requires a large amount of lipid supply via various sources, the assembly of the lipid supply mechanisms might be the rate-limiting step for autophagosome biogenesis. As described previously, the nucleation of the omegasome/phagophore, the production of PI3P, and the recruitment of downstream effector proteins are sequential events that lead to the establishment of the lipid supply mechanism at the MCS between the ER and the phagophore. Those events required cooperative functions of upstream proteins/complexes in the core ATG machinery, including the ULK1 complex, PI3K-C1, and ATG9. The assembly of these complexes at the autophagy initiation site, therefore, dictates autophagosome biogenesis in space and time. Thus, understanding the spatiotemporal regulation of this assembly can provide useful information on how autophagy is regulated in cells.

ATG13, a component of the ULK1 complex, has been shown in several studies to play an important role in interactions between the different subunits within the ULK1 complex (ATG13 interacts with all three subunits: FIP200, ULK1, and ATG101) as well as interactions with other proteins/complexes. Besides, interactions between ATG13 and ATG14L (a component of the PI3K-C1) as well as ATG9 have been reported (Suzuki et al., 2015b, Kannangara et al., 2021, Park et al., 2016). However, the formation of a larger complex including components of the ULK1 complex, PI3K-C1, and ATG9 has not been investigated. If this "super-complex" exists, ATG13 might be positioned at the center of the assembly, linking the other components. In addition, ATG101 forms a stable heterodimer with ATG13, but functional studies of ATG101 are limited partly due to its absence in budding yeast. Disruption of the ATG13-ATG101 heterodimer resulted in a strong autophagy-inhibitory effect, suggesting the central role of the dimer (Wallot-Hieke et al., 2018, Alers et al., 2014, Suzuki et al., 2015a). However, it is unclear whether ATG101 regulates ATG13 activity beyond simply stabilizing it (Suzuki et al., 2015a). Other aspects of ATG13 and ATG101 that have been overlooked are their potential regulatory roles since part of their structures fold into a HORMA domain, a structural feature that may allow interconversion of the protein's native states for its distinct functions. Such an intriguing property was identified in research about metamorphic proteins, which were defined by Murzin (2008) as amino acid sequences that can interconvert between multiple distinct native states to perform different functions. Metamorphosis is a concept that extends the "one sequence - one structure - one function" paradigm perceived from Anfinsen's thermodynamic principle (Figure 1.13). About 100 literature-validated examples of metamorphic proteins that switch their states have been identified, resulting in various functional consequences (Kim and Porter, 2021).

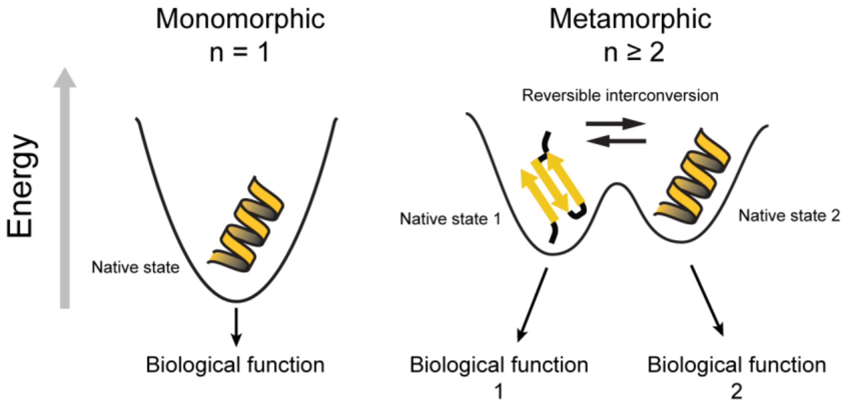

Figure 1.13. Thermodynamic landscape of monomorphic versus metamorphic proteins. Left: Monomorphic proteins fold into one native structure for a particular function. Right: Metamorphic proteins fold into two or more distinct native structures to perform more than one biological functions. Intrinsically disordered proteins are not considered metamorphic because they do not have a folded state. Figure adapted from Dishman and Volkman (2018).

MAD2, a close homolog of ATG13 and ATG101, is the prime example in which the metamorphic states of the protein's HORMA domain serve as a signaling node for the assembly of the mitotic checkpoint complex (MCC) (Figure 1.14) (Gu et al., 2022). The MCC is a part of the mitotic surveillance system called spindle assembly checkpoint (SAC), which ensures that all kinetochores are attached to the mitotic spindle so that the two daughter cells receive a complete set of chromosomes. Thus, the SAC plays a crucial role in safeguarding genome integrity (reviewed in Musacchio (2015b)). When a kinetochore remains unattached, SAC is activated, and MAD2 is recruited to unattached kinetochores in its inactive metamorphic state (open-MAD2). Open-MAD2 then switches to its active metamorphic state (closed-MAD2), which can bind to a consensus motif of CDC20, a component of the MCC, leading to the subsequent formation of the MCC (Figure 1.14). In isolation, MAD2 binding to CDC20 takes several hours due to the slow metamorphic conversion from open-MAD2 to closed-MAD2 (Simonetta et al., 2009, Vink et al., 2006). However, in cells, this conversion is accelerated by catalysts present at unattached kinetochores. The accelerated conversion of MAD2 metamorphic states thus allows the MCC formation in a matter of minutes, resulting in an inhibition of mitotic progression in a timely manner until all kinetochores are properly attached (reviewed in Musacchio and Desai (2017)). In other words, the obligatory conversion of MAD2 metamorphic states presents an important rate-limiting step in MCC assembly, which is only accelerated “on demand” when the kinetochores are unattached.

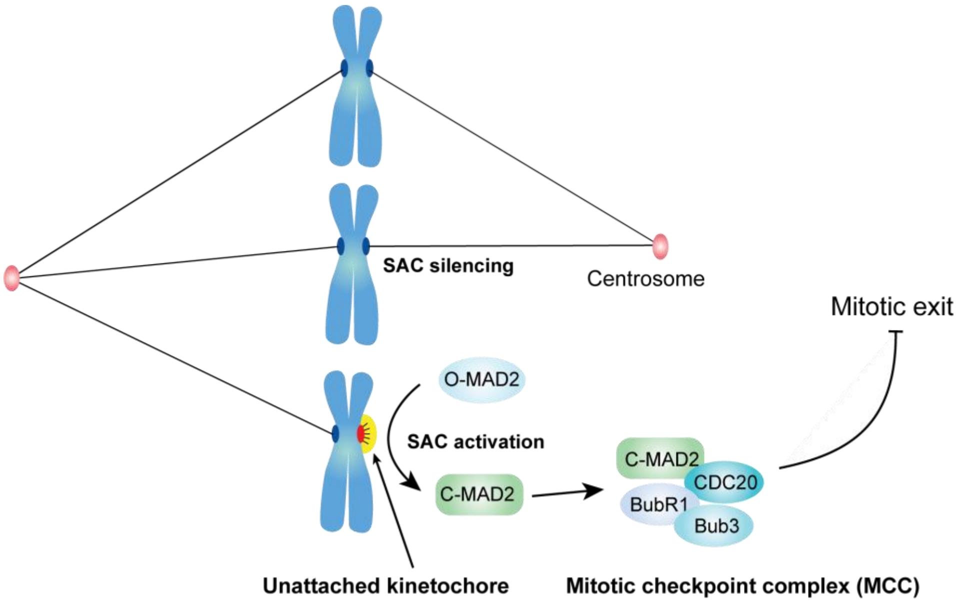

Figure 1.14. Model for metamorphosis of MAD2 during mitosis. When kinetochore is unattached, SAC is activated. This catalyzes the conversion of open-MAD2 to closed-MAD2. Closed-MAD2 can bind to CDC20, resulting in formation of MCC which blocks mitotic exit until all kinetochores are attached. Figure adapted from Musacchio (2015a).

Like the mitotic surveillance system, autophagy also needs to be regulated in a timely manner. Whether a similar regulatory mechanism is also employed by the cells in the case of the two HORMA domain proteins in autophagy remains to be investigated. Are ATG13 and ATG101 metamorphic proteins? Do ATG13 and ATG101 create a rate-limiting step in the assembly of their effector complex(es)? Are they part of a regulatory mechanism of autophagy initiation? Answering these questions would greatly contribute to the current knowledge of how metamorphic proteins are employed for various cellular functions, particularly in autophagy. In addition, it is useful for the development of therapeutic strategies that utilize fold-switching proteins as molecular switches for self-assembling molecular machinery.

1.5. Aims and thesis outline

Autophagy research has made tremendous progress in the last 50 years. However, it is still unclear how autophagy is initiated and how the autophagosome obtains lipids from various sources for expansion. One of the proposed mechanisms is the protein-mediated lipid transfer at the MCS between the ER and the phagophore (Figure 1.12 C). Recently, studies of ATG proteins using biochemical reconstitution have emerged, gradually revealing the mystery of autophagosome biogenesis. This minimalist methodology significantly simplifies the complicated cellular context by allowing each component of interest to be studied separately with maximal control. Thus, using recombinant proteins and artificial membranes, I aim to reconstitute an *in vitro* MCS that recapitulates the ER-phagophore MCS. This would provide the basis for further investigation into the architectural and functional aspects of the ER-phagophore MCS, especially the protein-mediated lipid transfer mechanism and the potential regulatory factors in the assembly of the MCS. I specifically aim to address the following questions (illustrated in Figure 1.15):

1. How do autophagy initiation complexes, including the ULK1 complex, PI3K-C1, and ATG9 assemble at the MCS for autophagosome biogenesis? Is there any regulatory mechanism involved? Are ATG13 and ATG101 part of the regulatory machinery?

2. What is the role of ATG2 and its associated partners in modulating its lipid transfer function at the MCS?

The first step is to establish purification protocols for the proteins involved, which were mostly not available when the project started (Section 3.1). Then, efforts to reconstitute a MCS recapitulating the ER-phagophore's MCS will be presented (Section 3.2). Lastly, Section 3.3 will show our investigation into the functional aspects of the proteins/complexes at the MCS, with a specific focus on ATG2-mediated lipid transfer.

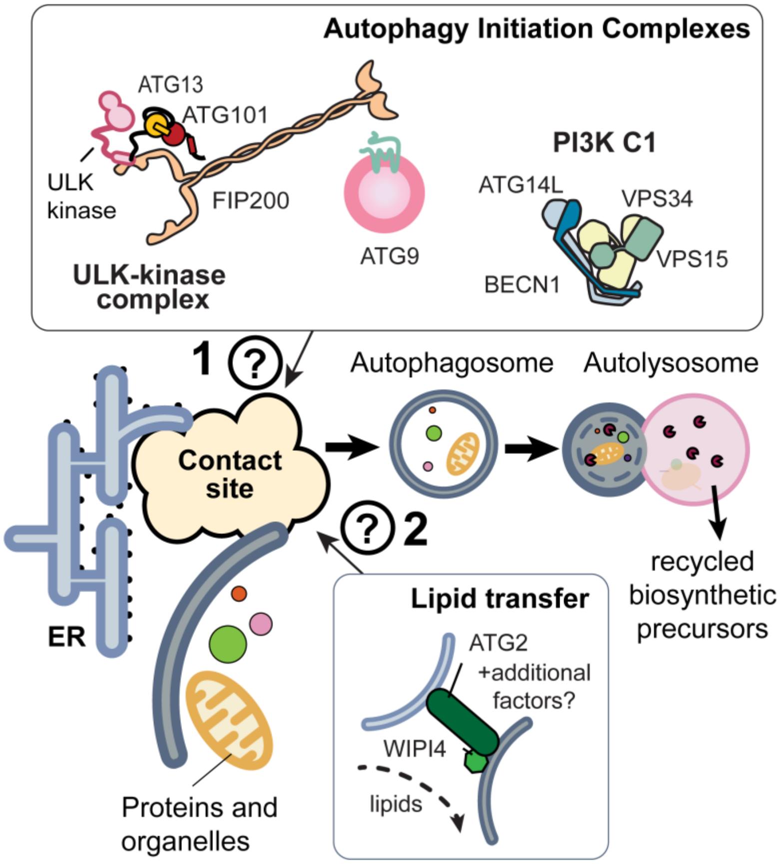

Figure 1.15. Open questions in autophagy initiation. 1) How do autophagy initiation complexes assemble at the MCS for autophagosome biogenesis? Is there any regulatory mechanism involved? Are ATG13 and ATG101 part of the regulatory machinery? 2) What is the role of ATG2 and its associated partners in modulating its lipid transfer function at the MCS?

2. Materials and Methods

All methods used were standard microbiology, molecular biology, or biochemical techniques; changes in standard procedures or manufacturer instructions and non-standard methods are described in more detail below.

2.1. Materials

The following sections lists materials used in this thesis.

2.1.1. Chemicals

Standard chemicals used in this study were obtained from AppliChem (Darmstadt, Germany), BD (Heidelberg, Germany), Roche (Mannheim, Germany), Merck, Novagen and Calbiochem (Darmstadt, Germany), Roth (Karlsruhe, Germany), Serva (Heidelberg, Germany) and Sigma-Aldrich (Taufkirchen, Germany). Special chemicals and materials are listed in the following Tables.

Table 2.1: Special chemicals and materials

Name	Company	Catalog Number
Amylose resin	NEB	E8021L
Pierce™ Glutathione Agarose	Thermo Fisher Scientific	16101
Pierce™ Detergent Removal Resin	Thermo Fisher Scientific	87780
Strep-Tactin Superflow Plus	Qiagen	30004
HisPur™ Cobalt Resin	Thermo Fisher Scientific	89964
Natriumhypodisulfit (Dithionite)	Sigma Aldrich	7775-14-6
Nycodenz®	Alere Technologies	AXS-1002424
Slide-A-Lyzer™ Dialysekassetten, 10 K MWCO, 12 ml	Thermo Fisher Scientific	66807
SERVA FastLoad 1 kb DNA Ladder	SERVA	39317.01
SERVA Fastload 100 bp DNA Ladder	SERVA	39316.01

Name	Company	Catalog Number
SERVA DNA Stain G	SERVA	39803
All Blue Prestained Protein Standards	BioRad	1610373
Protein Dual Color Standards	BioRad	1610374
Gel Loading Dye, Purple (6X)	NEB	B7024S
BS3 (Bis(sulfosuccinimidyl)suberat)	Thermo Fisher Scientific	21580
Maltose Monohydrat	Merck	6363-53-7
L-Glutathion	Merck	70-18-8
X-TREMEGENE 9 DNA Tranfection	Merck	6365779001
Polycarbonate Membranes 0.4µm	Avanti	610007
Polycarbonate Membranes 0.1µm	Avanti	610005
10mm Filter Supports	Avanti	610014
Mini-PROTEAN® TGX Stain-Free™ Protein Gels	BioRad	4568034
4–15% Mini-PROTEAN® TGX™ Precast Protein Gels	BioRad	4561083
96-well microplate (non-binding)	Greiner Bio-one	655906
0.45um Syringe Filter	AMSTAT	C0000629
Amicon® Ultra-15 concentrator 100 kDa	Milipore	UFC910024
Amicon® Ultra-15 concentrator 30 kDa	Milipore	UFC903024

Table 2.2: Enzymes used in this study

Name	Company	Catalog Number
T5 exonuclease	Epicentre	T5E4111K
Phusion® High-Fidelity DNA Polymerase	NEB	M0530
Q5® High-Fidelity DNA Polymerase	NEB	M0491
Taq DNA Polymerase	NEB	M0267
Taq DNA Ligase	NEB	M0208
BamHI	NEB	R0136S
HindIII	NEB	R0104S
Proteinase K	Sigma Alrich	39450-01-6
Benzonase®	Merck	E1014
Dpn1	NEB	R0176S

Table 2.3: Detergents used in this study

Name	Company	Catalog Number	Comments
Dodecyl-β-D-maltoside	Carl Roth	69227-93-6	DDM
n-Decyl β-maltoside	Glycon Biochemical	D322LA	DM
3-[(3-Cholamidopropyl)-dimethylammonio]-1-propansulfonat	Merck	75621-03-3	CHAPS
Triton X-100	Merck	9036-19-5	Triton

Table 2.4: Lipids used in this study

Name	Company	Catalog Number	Comments
1,2-dioleoyl-sn-glycero-3-phosphocholine	Avanti Polar Lipids	850375	DOPC
1,2-dioleoyl-sn-glycero-3-phosphoethanolamine	Avanti Polar Lipids	850725	DOPE
1,2-dioleoyl-sn-glycero-3-phospho-L-serine	Avanti Polar Lipids	840035	DOPS
1,2-dioleoyl-sn-glycero-3-phosphoethanolamine-N-(7-nitro-2-1,3-benzoxadiazol-4-yl)	Avanti Polar Lipids	810145	NBD-PE
1,2-dioleoyl-sn-glycero-3-phosphoethanolamine-N-(lissamine rhodamine B sulfonyl)	Avanti Polar Lipids	810150	Rhod-PE
1,2-dioleoyl-sn-glycero-3-phospho-(1'-myo-inositol-3'-phosphate)	Avanti Polar Lipids	850150	PI3P

2.1.2. Insect cell line and bacterial strain

Table 2.5: Insect cell lines and bacterial strains

Strain	Reference	Purpose
Sf9 insect cells	Invitrogen	transfection, virus production, expression cell line
High5 insect cells	Invitrogen	expression cell line
E. coli DH10EMBacY™	Geneva Biotech	generation of bacmid with genes of interest
E. coli NEB®5-alpha	New England Biolabs	standard cloning strain
E. coli Rosetta (DE3)	New England Biolabs	standard expression strain

2.1.3. Commercially available kits

Ready-to-use kits and commercial solutions listed in Table 2.6 were used according to the manufacturer's instructions unless specified otherwise.

Table 2.6: Commercial kits used in this study

Name	Company	Catalog number
QIAprep Spin Miniprep Kit	Qiagen	27106
Plasmid Mediprep Kit	Invitrogen	K210015
QIAquick PCR purification Kit	Qiagen	28106
HiPPR Detergent Removal Spin Column Kit	Thermo Fisher Scientific	PI88305
Atto 647N Protein Labeling Kit	Jena Bioscience	FP-201-647N
Alexa Fluor™ 488 Protein Labeling Kit	Invitrogen	A10235
Zeba™ Spin-Entsalzungssäulen, 7 K MWCO, 0,5 ml	Thermo Fisher Scientific	89882

2.1.4. Columns for chromatography

All columns listed below in Table 2.7 were used in combination with the appropriate ÄKTA system. The manufacturers' recommendations were followed for handling of the columns, including storage, cleaning, and equilibration.

Table 2.7: Chromatography columns used in this study

Name	Company	Catalog number
MBPTrap™ HP (1 ml; 5 ml)	Cytiva	29048641;28918778
HiTrap TALON crude (1 ml; 5ml)	Cytiva	29048565;28953766
GSTrap™ HP (1 ml; 5 ml)	Cytiva	17528101;17528201
StrepTrap HP (5ml)	Cytiva	28907546
HiLoad 16/600 Superdex 75 pg	Cytiva	28989333
HiLoad 16/600 Superdex 200 pg	Cytiva	28989335
HiLoad 16/600 Superose 6 pg	Cytiva	29323952
Superdex 75 Increase 10/300 GL	Cytiva	29148721
Superdex 200 Increase 5/150 GL	Cytiva	28990945
Superose 6 Increase 10/300 GL	Cytiva	29091596
Superose 6 Increase 5/150 GL	Cytiva	29091597
RESOURCE Q, 6 ml	Cytiva	17117901

2.1.5. Buffers and Media

Table 2.8: Commercially available buffer and media

Name	Company	Catalog number
LB medium	BioChemica	23143289
LB-agar	Roth	X969.2
ESF 921 medium	Expression Systems	96-001-01
Sf-900 medium	Gibco	12658-019

Table 2.9: Homemade buffer and media

Name	Composition
5x ISO buffer (for Gibson master mix)	1M Tris-HCl (pH7.5), 300 µL 1M MgCl2, 60 µL of 100 mM dATP, dCTP, dGTP, dTTP each, 300 µL of 1M DTT, 1.5 g PEG-8000, 300 µL of 100 mM NAD and 1.8 ml ddH_20
CBB staining solution	0.05% Coomassie Blue R250 and 0.05% Coomassie Blue G250 in 10% acetic acid, 50% methanol, and 40% H2O
Destaining solution	40% ethanol, 50%water, 10% acetic acid
Resolving gel (for SDS-PAGE)	10-15% acrylamide, 50% Glycerol, 375 mM Tris-HCl pH 8.8, 0.1% SDS, 0.1% APS, 0.05% TEMED
Laemmli sample loading buffer	10% glycerol, 2% (w/v) SDS, 0.01% bromophenol blue, 60 mM Tris/HCl pH 6.8
SDS running buffer	25 mM Tris, 192 mM glycine, 0.1% (w/v) SDS
Stacking gel (for SDS-PAGE)	4% (w/v) arylamide, 125 mM Tris-HCl pH 6.8, 0.1% (w/v) SDS, 0.1% (w/v) APS, 0.05% TEMED
TAE buffer	40 mM Tris/acetate pH 8.0, 2 mM EDTA

Table 2.10: Buffers for protein purification

Name	Composition
Buffer A	50 mM Hepes (pH 8), 150 mM NaCl, 5 mM MgCl2, 5% (v/v) Glycerol, 0.5 mM TCEP, 1% (w/v) DDM, 0.5 mM PMSF, 10 U/ml Benzonase
Buffer B	50 mM Hepes (pH 8), 150 mM NaCl, 0.5 mM TCEP, 0.03% (w/v) DDM
Buffer C	50 mM Hepes (pH 8), 150 mM NaCl, 0.5 mM TCEP, 0.1% (w/v) DDM
Buffer D	50 mM Hepes (pH 8), 150 mM NaCl, 0.5 mM TCEP
Buffer E	50 mM Hepes (pH 8), 500 mM NaCl, 5 mM MgCl2, 5% (v/v) Glycerol, 0.5 mM DTT, 1% (w/v) DDM, 0.5 mM PMSF, 10 U/ml Benzonase, 100 µM Leupeptin
Buffer F	50 mM Hepes (pH 8), 500 mM NaCl, 5% (v/v) Glycerol, 0.5 mM TCEP, 0.5 mM EDTA, 0.03% (w/v) DDM, 0.5 mM PMSF, 100 µM Leupeptin

Buffer G	50 mM Hepes (pH 8), 500 mM NaCl, 5 mM MgCl2, 5% (v/v) Glycerol, 0.5 mM TCEP, 0.5 mM EDTA, 1% (w/v) DDM, 0.5 mM PMSF, 10 U/ml Benzonase
Buffer H	50 mM Hepes (pH 8), 500 mM NaCl, 5% (v/v) Glycerol, 0.5 mM TCEP, 0.5 mM EDTA, 0.03% (w/v) DDM, 0.5 mM PMSF

2.1.6. Instruments and software

Table 2.11: Instruments used in this study

Name	Manufacturer
ÄKTA pure	Cytiva
ÄKTA start	Cytiva
ÄKTA micro	Cytiva
Sonifier SFX-250	Branson
Amersham Imager 680	GE healthcare
Eppendorf ThermoMixer	Eppendorf
NanoDrop™ One	Thermo Fisher Scientific
Gel Doc 2000 Imaging System	BioRad
UV Transilluminator 2000	BioRad
SI Analytics Lab Benchtop Meter	BioRad
CASY cell counter	Innovatis
Sorvall® MX 150 Plus Micro-Ultracentrifuge	Thermo Fisher Scientific
Sorvall® WX Ultra Centrifuge Series	Thermo Fisher Scientific
Sorvall® LYNX 6000 Superspeed Centrifuge	Thermo Fisher Scientific
Sorvall® Evolution™ RC Superspeed centrifuge	Thermo Fisher Scientific
UV transilluminator Gel DocTM EZ imager	Biorad
Synergy Neo 2 Hybrid Multi-Mode Reader	BioTek
Wide Mini-Sub Cell GT Horizontal Electrophoresis System	Biorad
Mini-PROTEAN® Tetra Vertical Electrophoresis Cell	Biorad
Avanti® Mini-Extruder	Avanti

Table 2.12: Software used in this study

Software (for MAC)	Developer	Version
JalView	Barton Group (University of Dundee)	2.11.1.5
PyMol	Schrödinger, LLC	2.5.2
AlphaFold 2	DeepMind (Alphabet Inc.)	2
Adobe Creative Cloud	Adobe Inc.	5.8.0.592

Graphpad PRISM	GraphPad Software Inc.	8.3.0
ImageJ	NIH, USA	1.53t
ChimeraX 1.4	UCSF	1.4
Snapgene	GSL Biotech	5.3.2
Fiji	Schindelin et al 2012	1.53
Microsoft® Office	Microsoft Corporation	16.64

2.2. General molecular biology methods

2.2.1. Polymerase Chain Reaction (PCR)

Polymerase chain reaction (PCR) was used to amplify DNA fragments for molecular cloning (Mullis et al., 1986). Two appropriate oligonucleotide primers were designed to flank the region of interest, which was amplified by a DNA polymerase during repeated cycles of heating and cooling. The primers used for cloning in this study are listed in Table S2. PCR was done with the Q5 High-Fidelity DNA Polymerase PCR kit (Table 2.2) following the provided protocol for PCR components (Table 2.13). The thermocycler program (Table 2.14) was also adjusted to the length of the amplified fragment (elongation time is 30 sec per 1 kb) and the annealing temperature of the primers.

Table 2.13: PCR Components

Component	25 µl reaction	50 µl reaction	Final concentration
5X Q5 Reaction Buffer	5 µl	10 µl	1X
10 mM dNTPs	0.5 µl	1 µl	200 µM
10 µM Forward Primer	1.25 µl	2.5 µl	0.5 µM
10 µM Reverse Primer	1.25 µl	2.5 µl	0.5 µM
Template DNA	variable	variable	< 1,000 ng
Q5 High-Fidelity DNA Polymerase	0.25 µl	0.5 µl	0.02 U/µl
5X Q5 High GC Enhancer (optional)	(5 µl)	(10 µl)	(1X)
Nuclease-Free Water	to 25 µl	to 50 µl	

Table 2.14: Thermo cycler program

Step	Temperature	Time
Initial Denaturation	98°C	30 seconds
25–35 Cycles	98°C *50–72°C 72°C	5–10 seconds 10–30 seconds 20–30 seconds/kb
Final Extension	72°C	2 minutes
Hold	4–10°C	

2.2.2. DNA purification and concentration determination

For the removal of proteins and other impurities from PCR reactions, the QIAquick PCR purification kit (Table 2.6) was used according to the manufacturer’s protocol. DNA was eluted in 50 µl sterile deionized water. The purified DNAs were stored at -20°C.

The concentration of the purified DNA was assessed photometrically using NanoDrop™ One (Table 2.11) according to the manufacturer’s instructions. Nucleic acids were quantified at 260 nm. The A260/280 ratio was used to check DNA purity. A ratio of ~1.8 was accepted as pure DNA.

2.2.3. Cloning of expression vector by Gibson® assembly

All clonings in this study were done using Gibson assembly (Gibson et al., 2009). Gibson master mix was prepared by adding 320 µl of 5xISO-Buffer, 0.64 µL of 10 U/µl T5 exonuclease, 20 µL of 2 U/µl Phusion HF polymerase, 160 µl of 40 U/µl Taq ligase, and 700 µl of ddH_2O. Aliquots of 15 µl were prepared and stored at -20°C. Insert(s) was amplified using primers with an appropriate 5’-overhang containing overlapping ends of 15-20 bp. Vectors were linearized (~ 1 µg) by incubation with 2 µl of restriction enzymes BamHI® and HindIII® at 37°C overnight in CutSmart® buffer. Vector purification was carried out using PCR purification kit (Table 2.6) according to manufacturer’s protocol. For a typical Gibson assembly reaction, linearized vector was mixed with the insert in 1:5

molar ratio in 15 µl of Gibson master mix. The reaction was incubated at 50°C for 30 minutes. Generally, 2 µl of the reaction mix was used for transformation into *E.coli* NEB 5-alpha.

2.2.4. Transformation of expression vector

For the transformation, approximately 0.5 – 1 µg of plasmid DNA were gently mixed with 15 µl competent cells and incubated on ice for 15 min. The uptake of plasmid DNA was induced by heat shock at 42°C for 60 sec. Heat shock was followed by immediate incubation on ice for 5 min before addition of 100 µl LB media. Finally, the cells were plated on LB-Amp agar plates and incubated at 37°C overnight for plasmid verification.

2.2.5. Plasmid DNA isolation from bacterial cells

For plasmid DNA amplification, a single colony was selected and grown in 5 ml LB media containing ampicillin overnight. The overnight culture was harvested by centrifugation (5000 rpm, 5 min) and further isolated by QIAprep Spin Miniprep Kit (Table 2.6) according to the manufacturer’s instructions. Plasmids were diluted by 50 µl of deionized water and kept at -20°C.

2.2.6. Sequencing of DNA

Newly cloned plasmids were verified by sequencing. The sequencing was performed by Microsynth Seqlab (Göttingen). For each sequencing sample, 12 µl of sample containing 480 – 1200 ng of purified plasmid DNA and 30 pmol of a suitable oligonucleotide primer were sent to Microsynth Seqlab for sequencing. Evaluation of sequencing data was performed using Snapgene (Table 2.12).

2.2.7. Bacmid generation and isolation

Bacmid was generated according to the Tn7 transposition-based method (Trowitzsch et al., 2010). A plasmid carrying the GOI was transformed into E. coli

DH10EMBacY^{TM} by heat shock transformation. Cells were then supplemented with 500 µl LB media and incubated at 37°C for 5h while shaking. After the incubation, 100 µl of transformed cells was plated on LB agar supplemented with 50 µg/ml kanamycin, 10 µg/ml tetracycline and 10 µg/ml gentamycin with 100 µg/ml X-Gal and 1 mM IPTG for blue-white colony screening and incubated at 37°C for 36 h. If the integration of the desired DNA into the bacmid DNA was successful, the colonies would turn white; otherwise, they would turn blue.

To isolate bacmid DNA, a single white colony was picked to inoculate 5 ml of LB medium supplemented with the above-mentioned antibiotics. The culture was incubated at 37°C and 130 rpm overnight and subsequently harvested by centrifugation at 5,000 rpm for 5 min. The supernatant was then removed, and the cells were resuspended in 300 µl of the resuspension buffer P1 (QIAprep Spin Miniprep kit, Table 2.6) in a 2 ml tube. Then, 300 µL of lysis buffer P2 (QIAprep Spin Miniprep kit, Table 2.6) was added, mixed well by inverting the tube. After the incubation, 350 µl of neutralizing buffer N3 (QIAprep Spin Miniprep kit, Table 2.6) was added, followed by a 10 min incubation on ice. The mixture was then centrifuged at 13,000 rpm and 4°C for 10 min. To remove all precipitants, the supernatant was transferred to a fresh 2 ml tube and centrifuged again with the same settings. 700 µl of the clear supernatant was then transferred to a fresh 2 ml tube containing 700 µl cold isopropanol and kept at -20°C overnight to precipitate bacmid DNA. The next day, bacmid DNA was pelleted by centrifugation at 13,000 rpm and 4°C for 30 min. The pellet was washed twice with 500 µl of ice-cold ethanol (70%). The removal of ethanol was carried out under sterile conditions in a hood and the pellet was air dried for 10 to 20 minutes. After removing the ethanol, the pellet was resuspended in 50 µl ddH_2O and kept at -20°C until use.

2.3. Gel electrophoresis

2.3.1. Agarose gel electrophoresis

Agarose gel electrophoresis is a standard method to analyze DNA samples (Lee et al., 2012). In this study, it was used to identify successful amplification of the gene of interest (GOI), and successful insertion of the GOI into the target vector. Agarose gels were produced by boiling 1% (w/v) agarose in an appropriate volume of TAE-buffer until fully dissolved. Agarose solution was then cooled to approximately 50°C and supplemented with 0.1 µl/ml of SERVA DNA Stain G (Table 2.1). A comb was inserted to create a desired number of loading wells. Then the gel was left at room temperature until fully polymerized. Samples were mixed with DNA Loading Dye (Table 2.1) and loaded on the gel together with a standard marker of 1 kb DNA ladder (Table 2.1). Samples were run at 100 V until the desired separation of DNA products was achieved. Gel Doc 2000 Imaging System or UV Transilluminator 2000 (Table 2.11) was used for the final DNA visualization.

2.3.2. SDS-Polyacrylamide Gel Electrophoresis (SDS-PAGE)

SDS-PAGE was developed for the separation of proteins in denatured conditions (Shapiro et al., 1967, Laemmli, 1970). SDS-acrylamide gels were prepared as follows: The resolving gel mixture, containing 10 to 15% acrylamide was loaded into a pre-assembled Mini-PROTEAN 3 multi-casting chamber, immediately followed by a stacking gel mixture. 10- or 15-well combs were then inserted on top, and the gels were allowed to solidify. Alternatively, Mini-PROTEAN® precast gels (Table 2.1) were used according to the supplier's protocols. SDS-PAGE was performed in Mini-PROTEAN® III electrophoresis chambers (Table 2.1) filled with SDS running buffer. Typically, 15 µl to 30 µl of protein sample were mixed with an appropriate amount of 4 x Laemmli sample loading buffer (Table 2.9) and heated for 5 min at 95°C for denaturation. Samples were then loaded together with an appropriate protein molecular weight standard

(Table 2.1) for size determination. Then, the gel was run at 200 V, for approximately 1 hour, until the bromophenol blue front reached the end of the gel. After electrophoresis, SDS gels were incubated for 10 min with Coomassie brilliant blue (CBB) staining solution, subsequently in CBB detaining solution for 5 min, and finally in ddH_2O. Gels were scanned using the Perfection V850 Scanner (Table 2.11).

2.4. Bacteria and insect cell cultivation conditions

2.4.1. Bacteria cultivation

E. coli cultures were grown in lysogeny broth (LB) media or on LB agar plates, supplemented with appropriate antibiotics if required. Liquid cultures were agitated continuously at 37°C and 220 rpm.

2.4.2. Insect cell cultivation

Spodoptera frugiperda (Sf9) cells and *Trichoplusia ni*- derived (Hi5) cells (Table 2.5) were cultured in SF900-III SFM medium and ESF921 medium, respectively (Table 2.8). Sf9 and Hi5 insect cell stocks were constantly maintained in suspension culture, protected from light, at constant temperature (27°C) and agitation (100 rpm). Cells were passaged every 3 to 4 days at a concentration of 0.3×10^6 to 0.5×10^6 cells/ml to maintain their exponential growth phase. Cell concentration, viability, and size were monitored by the CASY cell counter (Table 2.11), according to the manufacturer’s protocol.

2.5. General methods for recombinant protein expression in *E.coli* and insect cell

2.5.1. Expression of protein in *E. coli*

All bacterial expression constructs were expressed in Rosetta cells. A single colony carrying the plasmid of interest was used to inoculate a 100 ml LB-

Amp preculture, which was incubated overnight at 37°C with shaking at 120 rpm. On the following day, two 5-liter flasks containing 1 liter of LB-Amp medium each were inoculated with 50 ml of preculture and agitated at 37°C and 120 rpm until an OD600 of ~ 0.5 – 0.6 was reached. Protein expression was induced by supplementing the culture with 0.5 mM IPTG and further incubation at 18°C with shaking at 120 rpm. On the next day, cells were harvested by centrifugation (20 min, 5000 rpm, 4°C). Cell pellets were flash frozen in liquid nitrogen and stored at -20°C.

2.5.2. Baculovirus generation

The generation of baculovirus was performed by transfecting adherent Sf9 cells with the bacmid. For the preparation of the first virus generation, 3 ml of 10^6 cells/ml Sf9 suspension cell culture was seeded on a 6-well plate. For each transfection, 20 µl of the isolated recombinant bacmid and 5 µl of X-tremeGENE9 (Table 2.1) were mixed in 500 µl SF900-III SFM medium (Table 2.8). The mix was incubated in the hood for at least 30 min at 27°C before being gently distributed into the 6-well plates. The cells were then incubated at 27°C for 3 to 5 days. Cells were then inspected under a fluorescence microscope for YFP expression, which is indicative of successful transfection and resulting virus production. When at least 20% of cells were infected, 3 ml of the virus-containing supernatant was used to infect 12 ml of suspended Sf9 cells at 10^6 cells/ml. The culture was incubated again for 3 to 5 days at 27°C. After that, the supernatant containing the virus stock (V0) was harvested by centrifuging the culture at 500 × *g* for 10 min. To generate more virus particles, 1 ml of V0 was used to infect 50 ml of suspended Sf9 cells at 10^6 cells/ml concentration. After incubation for 3-5 days at 27°C, the intermediate virus stock (V1) was harvested by centrifuging the culture at 500 × *g* for 10 min. Finally, 1 ml of V1 was used to generate 50 ml of the working virus stock (V2) using the same procedure as for V1 production. V2 was directly used to infect Sf9 and Hi5 expression cultures. All virus stocks produced were stored at 4°C, protected from light.

2.5.3. Expression of protein in insect cell

For protein expression, 10 ml of V2 virus stock were used to infect 500 ml of Hi5 cell culture at a density of 10^6 cells/ml. Cells were grown and monitored under cultivation conditions. After the viability dropped to the 80-90% range (usually after 48-72 h), the cells were monitored for YFP expression under a fluorescence microscope. When the YFP expression was positive, the cells were harvested by centrifugation (500 g, 10 min, 4°C). Cells were resuspended in PBS buffer (Table 2.9), then pelleted (500 g, 10 min, 4°C), and stored at -20°C until further use.

2.6. Chromatography methods

To purify the recombinant protein of interest from cellular lysate, different chromatographic methods were employed, which are described below. All columns were stored in 20% (v/v) ethanol, washed with 1 column volume (CV) of ddH_2O, and equilibrated in the appropriate buffer prior to usage. After usage, columns were regenerated, if necessary, and washed with 1 CV of ddH_2O and 1 CV of 20% (v/v) ethanol.

2.6.1. Affinity chromatography

For affinity chromatography, cell pellet was lysed in an appropriate lysis buffer, followed by centrifugation at 20,000 × *g* and 4°C to precipitate large cellular debris. The supernatant was then filtered through a 0.45 µm pore size syringe filter (Table 2.1), and applied to affinity column that was pre-equilibrated with appropriate binding buffer using ÄKTA start (Table 2.11). After this, the column was washed with 10 CV of binding buffer to remove unbound proteins. Bound proteins were eluted from MBP trap, GST trap, and Strep trap affinity columns (Table 2.7) by 4 CV of binding buffer supplemented with either 20 mM maltose, 20 mM reduced glutathione (GSH), or 5 mM desthiobiotin, respectively. For His trap column (Table 2.7), the protein was eluted using a linear gradient (5-300 mM) of Imidazole. Protein eluted in the peak fractions were collected for further purification. Samples from total lysate, supernatant, and peak fractions were collected for SDS-PAGE as described previously to evaluate expression level and protein purity. Protein samples were concentrated if required using the Amicon® Ultra-15 concentrator 100 kDa or Amicon® Ultra-15 concentrator 30 kDa (for WIPI4) (Table 2.1).

2.6.2. Ion exchange chromatography (IEX)

Ion exchange chromatography (IEX) is an additional purification step which separates proteins by their differences in surface charge (Fritz, 2004). For IEX, the protein of interest collected after affinity chromatography was diluted to approximately 50 mM NaCl in an appropriate protein purification buffer. Using ÄKTA pure, the protein solution was then loaded onto a 6 ml Resource Q column (Table 2.7), pre-equilibrated with an appropriate buffer containing 50 mM NaCl. The proteins were then eluted in a salt gradient ranging from 50 mM to 500 mM NaCl. Samples from peak fractions were collected for SDS-PAGE to evaluate the amount and purity.

2.6.3. Size exclusion chromatography (SEC)

The proteins from affinity chromatography or IEX were further purified using size-exclusion chromatography (SEC) methods, which separate proteins by size (Barth et al., 1994). The gel-filtration columns were pre-equilibrated with appropriate running buffer using ÄKTA pure (Table 2.11). Depending on the column and injection loop used, protein sample was concentrated to appropriate amount. Protein sample, prior to loading, was spun down for 10 min at 4°C and 13,000 rpm. The protein was then applied to appropriate size exclusion chromatography column and eluted in the running buffer used. Samples from peak fractions were collect for SDS-PAGE to evaluate the amount and purity of the protein of interest.

2.7. Recombinant protein purification

Recombinant proteins in this study were purified using the chromatography methods described above. Changes appropriate for each specific protein are as follows. All protein constructs used in this study have a PreScission protease cleavage site between the tag and the protein, which allows efficient tag cleavage by PreScission protease.

2.7.1. Expression and purification of ATG9

ATG9A with a tandem N-terminal 6xHis-tag and MBP tag followed by a PreScission protease cleavage site was expressed in Hi5 insect cells using the biGBac expression system as described in Section 2.5.3. Harvested cell pellet was resuspended in lysis buffer A (Table 2.10) and lysed gently on ice for at least 1 hour of stir-mixing. The lysate was then diluted 3 times with DDM-free buffer A and mixed gently for another 30 min before clarifying by centrifugation at 20,000 *g* for 30 min. The proteins in the supernatant were purified by affinity chromatography using MBP trap columns (as described in Section 2.6.1) with Buffer B (Table 2.10) as binding buffer and buffer B supplemented with 20 mM maltose as an elution buffer. The affinity tags were cleaved by PreScission protease treatment at a 1:1000 ratio (PreScission protease : protein) for at least 5 hours at 4°C after affinity chromatography (if required), followed by size exclusion chromatography (as described in Section 2.6.3) using a Superose 6 column (Table 2.7) pre-equilibrated with buffer B. The purified protein was concentrated using the Amicon® Ultra-15 concentrator 100 kDa (Table 2.1), flash frozen in liquid nitrogen, and stored at -80°C.

2.7.2. Expression and purification of ATG9-ATG13-ATG101 complex, ATG9-ATG13 complex, and ATG13-ATG101 complex.

To purify ATG9-ATG13-ATG101 complex, ATG19-ATG13 complex, or ATG13-ATG101 complex. Each protein with a tandem N-terminal 6xHis-tag and

MBP tag followed by a PreScission protease cleavage site was co-expressed in Hi5 cells and purified with the same protocol used for ATG9.

To purify a complex of human ATG9, $ATG13^{HORMA,}$ ATG101. Baculovirus expressing ATG9 was co-expressed with baculovirus expressing a complex of $ATG13^{HORMA}$ and ATG101 in Hi5 cells and purified with the same protocol used for ATG9. Baculovirus expressing the $ATG13^{HORMA}$-ATG101 complex was cloned by F. Lugarini (Research group of Signaling Dynamics, MPI-NAT).

2.7.3. Expression and purification of ATG2

Human ATG2 with a C-terminal StrepII tag expressed in Hi5 cells was purified by affinity chromatography using Strep trap columns (as described in Section 2.6.1) with buffer A as lysis buffer, buffer C (Table 2.10) as binding buffer, and buffer C supplemented with 5 mM desthiobiotin as elution buffer. The proteins were finally purified by size exclusion chromatography using a Superose 6 column pre-equilibrated with Buffer C (as described in Section 2.6.3). The purified protein was concentrated using the Amicon® Ultra-15 concentrator 100 kDa (Table 2.1), flash frozen in liquid nitrogen, and stored at -80°C. For the lipid transfer assay, DDM was subsequently removed by three successive incubations with Pierce detergent removal resin (Table 2.8), pre-equilibrated with buffer D (Table 2.10). Incubation in the detergent removal resin was performed at room temperature for 15 min each.

2.7.4. Expression and purification of WIPI4

WIPI4 with different tag variants were expressed in Hi5 cells and purified similarly by affinity chromatography using appropriate affinity columns. WIPI4 with 6x-His tag was purified by a His trap column, WIPI4 with GST tag was purified by a GST trap column, WIPI4 with MBP tag was purified by a MBP trap column. Cells pellets were lysed by sonication (10 s on, 20 s off, 3 min, 35% amplitude) in buffer D (Table 2.10). Lysate was clarified by centrifugation at 20,000 × *g* for 30 min. Clarified lysate was applied to appropriate affinity chromatography columns using buffer D as a binding buffer and eluted by either 0 to 300 mM linear gradient of imidazole (for His trap column), 10 mM reduced glutathione (for GST trap column), or 20 mM maltose (for MBP trap column). The tag was cleaved if required as described for ATG9, and the proteins were further purified by an optional anion exchange chromatography (as described in Section 2.6.2) with a 50 mM to 100 mM linear gradient of NaCl, and subsequent size exclusion chromatography using Superdex S200 or Superdex S75 column (Table 2.7), pre-equilibrated with buffer D (as described in Section 2.6.3). The purified protein was concentrated using the Amicon® Ultra-15 concentrator 30 kDa (Table 2.1), flash frozen in liquid nitrogen, and stored at -80°C.

2.7.5. Expression and purification of ULK1

ULK1 with an N-terminal GST tag was expressed in Hi5 cells and purified by affinity chromatography using a GST trap column (as described in Section 2.6.1). Cells were stirred gently in lysis buffer E (Table 2.10) on ice for 1 h. The lysate was then diluted 3 times with DDM-free buffer E and mixed gently for another 30 min. The protein was purified by affinity chromatography using a GST trap column (Table 2.7) with binding buffer F (Table 2.10), and buffer F supplemented with 10 mM reduced glutathione as an elution buffer. The protein was subjected to size exclusion chromatography with a Superose 6 column pre-equilibrated with buffer F (as described in Section 2.6.3). The purified protein was concentrated using the Amicon® Ultra-15 concentrator 100 kDa (Table 2.1), flash frozen in liquid nitrogen, and stored at -80°C.

2.7.6. Expression and purification of FIP200

FIP200 with a tandem N-terminal 6xHis-tag and MBP tag followed by a PreScission protease cleavage site was expressed in Hi5 cells and purified by affinity chromatography using a MBP trap column (as described in Section 2.6.1) with buffer G (Table 2.10) as lysis buffer, buffer H (Table 2.10) as binding buffer, and buffer H supplemented with 20 mM maltose as elution buffer. The protein sample was finally purified by size exclusion chromatography using a Superose 6 column pre-equilibrated with Buffer H (as described in Section 2.6.3). The purified proteins were concentrated using the Amicon® Ultra-15 concentrator 100 kDa (Table 2.1), flash frozen in liquid nitrogen, and stored at -80°C.

2.7.7. Expression and purification of ATG14L-BECN1 complex

ATG14L with a tandem N-terminal 6xHis-tag and mCherry tag was co-expressed with BECN1 with a tandem N-terminal 6xHis-tag and MBP tag in Hi5 insect cells using the biGBac expression system. Cell pellets were harvested and purified using the same protocol used for FIP200.

2.8. Generation of LUVs

Large Unilamellar Vesicles (LUVs) were prepared by reversed-phase evaporation as described previously (Hernandez et al., 2012). Briefly, lipids were dissolved in chloroform and mixed at a desired molar ratio (donor LUVs: 46% DOPC, 25% DOPE, 20% DOPS, 2% NBD-PE, and 2% Rh-PE, 5% PI3P; acceptor LUVs: 50% DOPC, 25% DOPE, and 25% DOPS). Chloroform was subsequently removed using a rotary evaporator to allow lipid film formation. The lipid film was then dissolved in 1 ml diethyl ether, followed by 300 µl of buffer D (Table 2.10). The sample was then sonicated for 1 min (10 s on, 20 s off) at 50% amplitude in a bath sonicator at 4°C to create the emulsion. Diethyl ether was initially removed at 500 mbar for 10 min, and 700 µl of buffer D (Table 2.10) was added. The remaining diethyl ether was removed by lowering the pressure stepwise to 100 mbar until diethyl ether was completely removed. The resulting lipid suspension was extruded 11 times through a 0.4-µm polycarbonate filter and then 21 times through a 0.1-µm polycarbonate filter (Mini extruder kit, Avanti Polar Lipids).

2.9. Reconstitution of ATG9 in proteoliposome

To reconstitute ATG9 in proteoliposomes, protein-free LUVs was destabilized by the addition of DM at the concentration described by the R-value (Rigaud and Levy, 2003). ATG9 was added at a protein:lipid ratio of 1:2000 or 1:500, depending on the experiments. The solution was incubated for 1 h at room temperature, and DM was subsequently removed by 3 successive incubations with Pierce detergent removal resin (Table 2.6), pre-equilibrated with buffer D (Table 2.10). Incubations in the detergent removal resin (Table 2.1) were performed at room temperature for 15 minutes each.

2.10. Generation of GUVs

The following protocol for was written by Pouya Hosnani (collaborator at Georg August University of Göttingen, now Heidelberg University Biochemistry Center - BZH), who prepared GUVs for this study.

GUVs were formed by an adapted electroformation protocol as described before (Kroppen et al., 2021, Tarasenko et al., 2017) in the VesiclePrepPro (Nanion). In brief, first a lipid mix with the end concentration of 2 mg/ml was prepared. A rubber ring (Ø28 mm) was slightly coated with silicon and placed carefully on the center of the electrically conductive side of an ITO-plate. The ITO-plate was heated to 50°C on a heating plate. 7.5 µl of the lipid mixture was applied dropwise with a Hamilton syringe on the ITO-plate in the area surrounded by the rubber ring. Following the ITO-plate was placed in a vacuum chamber for 10 min to evaporate the residual organic solvent. The plate was inserted in the chamber and an electroformation buffer (240 mM sucrose, 50 mM HEPES, pH 8, Osm. 380 mOsmol) was added slowly on the lipids. A second ITO-plate was placed on top of the first ITO-plate with the electrically conductive side facing the lipids and the buffer. This way the chamber was sealed.

The electroformation protocol used here consists of three phases: In phase 1 the peak-to-peak amplitude rises linearly from 0 to 2 V. During phase 2 it stays on 2 V for 2 h 55 min. In phase 3 the amplitude decreases to 0 V again in a 20 min period. The frequency is set to 10 Hz in phase 1 and 2. In phase 3 it decreases to 0 Hz linearly. The temperature is set across all three phases to 55°C and as such above the phase-transition temperature of the lipid mix. After finishing the protocol, GUVs were harvested into 1.5 ml Eppendorf tubes. They were used immediately for microscopy.

2.11. Fluorescence microscopy

P. Hosnani and B. Knotkova (collaborators at Georg August University of Göttingen, now Heidelberg University Biochemistry Center - BZH) performed fluorescence microscopy experiments with all protein samples prepared by Anh Nguyen. If required, proteins were labeled with Atto647N Protein Labeling Kit, or Alexa Fluor™ 488 Protein Labeling Kit (Table 6), according to manufacturer's protocol. The following protocol was written by P. Hosnani.

For microscopy the LSM 780 (Carl Zeiss) was used. µ-slides with 8-wells (Ibidi) were coated with BSA by incubating each well with 100 µl 5 mg/ml BSA followed by 3 washing cycles with protein buffer (150 mM NaCl, 50 mM HEPES, 0.5 mM TCEP,1 mM EDTA, pH 8, Osm. 380 mOsm). The wells were prepared for the addition of the GUVs with 200 µl of protein buffer. GUVs were added carefully with a tip-cut pipette. An appropriate window for microscopy was selected and indicated proteins were added to the wells. The pictures were processed with ImageJ-software.

2.12. Cross-linking mass spectrometry (XL-MS)

For $^{\mathrm{MBP}}$ATG9-$^{\mathrm{MBP}}$ATG13$^{\mathrm{HORMA}}$-ATG101 protein–protein crosslinking, 1 uM of the purified complex was incubated with different concentrations of BS3 (Table 2.1). Each of the samples was incubated at 4°C for 60 min and subsequently quenched by adding 50 mM Tris pH8 and incubating for 15 min. Proteins were then separated by SDS-PAGE using a 4–15% Mini-PROTEAN® TGX™ Precast Protein Gels 4–12% gradient gel (Table 2.1).

The following steps were performed and written by I. Parfentev (Research group of Bioanalytical Mass Spectrometry, MPI-NAT). The cross-linked complex was cut out of the gel. Excised gel pieces were then subjected to in-gel tryptic digest (Shevchenko et al., 2006). Samples were reduced with 10 mM dithiotreitol and alkylated with 55 mM iodacetamide and subsequently digested with trypsin (sequencing grade, Promega) at 37°C for 18h. Extracted peptides were dried in a SpeedVac Concentrator and dissolved in loading buffer composed of 4% acetonitrile and 0.05% TFA. Samples were subjected to liquid chromatography mass spectrometry (LC-MS) on a QExactive HF-X (Thermo Scientific). Peptides were loaded onto a Dionex UltiMate 3000 UHPLC+ focused system (Thermo Scientific) equipped with an analytical column (75 µm x 300 mm, ReproSil-Pur 120 C18-AQ, 1.9 µm, Dr. Maisch GmbH, packed in house). Separation by reverse-phase chromatography was done on a 60 min multi-step gradient with a flow rate of 0.3-0.4 µl min^{-1}. MS1 spectra were recorded in profile mode with a resolution of 120 k, maximal injection time was set to 50 ms and AGC target to 1e^{6} to acquire a full MS scan between 380 and 1580 m/z. The top 30 abundant precursor ions (charge state 3-8) were triggered for HCD fragmentation (30% NCE). MS2 spectra were recorded in profile mode with a resolution of 30 k; maximal injection time was set to 128 ms, AGC target to 2e^{5}, isolation window to 1.4 m/z and dynamic exclusion was set to 30s. Raw files were analyzed via pLink2.3.5 to identify cross-linked peptides (Chang et al., 2015). Database was generated based on the protein complex used. FDR was set to 1% and results were filtered by excluding crosslinks supported by only one cross-linked peptide spectrum match. The crosslinks were visualized using the webserver xiNET (Combe et al., 2015).

2.13. Pull-down assay

GST, MBP and Strep pull-down experiments were performed using pre-equilibrated GSH Sepharose beads, MBP beads, or StrepTactin Superflow Plus beads (Table 2.1) in respective pull-down buffers. Protein input samples are prepared by adding approximately 1 µg of each protein or complex into 10 µl Laemmli sample loading buffer. The pull-downs were performed by incubating the indicated amounts of bait and prey in a 1.5 ml tube at specified times and temperatures, as described in the figure legends. To allow binding of the bait to the beads, the mixture was then incubated for 10 min with 30 µl of corresponding beads, pre-equilibrated in pull-down buffer. Beads were then washed twice with 500 µl pull-down buffer and spun down at 500 × *g* for 1 min. After removing the wash buffers, samples were mixed with 10 µl Laemmli sample loading buffer (Table 2.9) and run on a 12% SDS–PAGE gel. Protein bands were visualized with Coomassie brilliant blue staining (Table 2.9)

2.14. Stain-free protein quantification

Stain-Free (SF) is a method of protein visualization and quantification that enables the detection of protein bands in gels without using colorimetric or fluorescent stains (Holzmuller and Kulozik, 2016, Gurtler et al., 2013). In this study, to quantify the relative amount of each protein in a complex, purified protein complexes in increasing amounts (5 µg, 10 µg, 15 µg, 20 µg) were loaded on 12% Mini-PROTEAN® TGX Stain-Free™ Protein Gels (Table 2.1) and separated by electrophoresis. After electrophoresis, protein bands were visualized by placing the gel on the UV transilluminator Gel Doc^{TM} EZ imager (Table 2.11). The intensities of protein bands were then normalized against the number of tryptophan residues in each protein. A linear fit of the band intensities against the amount of protein was fitted to verify that the intensities are proportional to the increase in the amounts of protein loaded (5 µg, 10 µg, 15 µg, 20 µg).

2.15. Flotation assay

Flotation assays were performed as described previously (Krick et al., 2012, Busse et al., 2016) to verify proper reconstitution of ATG9 into protein-free liposomes. Briefly, 50 µl of ATG9 proteoliposomes were mixed with 50 µl 80% (w/v) Nycodenz (Table 2.1) prepared in buffer D (Table 2.10). The mixture was sequentially overlaid with 40 µl of 30% Nycodenz, 40 µl 15% Nycodenz, and 40 µl of buffer D. The density gradient was centrifuged at 50,000 rpm in a S55-S swinging bucket rotor (Table 2.11) for 1 hour at 4°C. Six equal fractions were collected from the top of the gradient and analyzed by SDS-PAGE.

2.16. Protease protection assay

The orientation of ATG9 with an N-terminal MBP tag in liposomes was determined by assessing the accessibility of the N-terminal HRV 3C-cleavage site to PreScission protease. Proteoliposomes were incubated with 1 µM PreScission protease at 4°C for 20 min, 40 min, or overnight. In the control, 1% DDM was added to the proteoliposome and PreScission protease mix. The reactions were stopped by the addition of Laemmli sample loading buffer and samples were analyzed by SDS-PAGE. Gels were quantified using Fiji (ImageJ)(Schindelin et al., 2012)(Table 2.12).

2.17. Dynamic light scattering (DLS)

Dynamic light scattering (DLS) is a method to determine the relative size distribution of particles in solution (Berne, Bruce J., 1940). In this study, DLS was used to measure LUVs tethering activities of ATG2 in the presence or absence of its interacting proteins. The following protocol was written by P. Hosnani (collaborator at BZH).

LUVs were prepared as described above. To mimic the conditions in the lipid transfer experiments, 25 µM lipid concentration of donor liposomes and acceptor liposomes in the presence or absence of the indicated proteins were prepared in 200 µl buffer. A 72-well Terasaki-plate (Greiner bio-one), was prepared with a thin layer of liquid parafinol. 1 µl of each solution was added to the wells. The plate was measured with the spectra light 610 on automatic settings. For creating the diagrams, GraphPad Prism software (Table 2.12) was used.

2.18. Lipid transfer assay

To monitor protein-mediated lipid transfer between liposomes, we performed a FRET-based dequenching assay as described previously (Connerth et al., 2012, Watanabe et al., 2015, Miyata et al., 2016). In brief, a mixture of donor liposomes containing both NBD-PE and fluorescent rhodamine (Rhod)–labeled PE (46% DOPC, 25% DOPE, 20% DOPS, 2% NBD-PE, and 2% Rh-PE, 5% PI3P), and acceptor liposomes without fluorescent lipids were prepared (50% DOPC, 25% DOPE, and 25% DOPS). In our experiments, 25 µM lipid concentration of donor liposomes and acceptor liposomes in the presence or absence of the indicated proteins except ATG2 were prepared in 200 µl buffer D (Table 2.10) in a 96-well microplate (Greiner bio-one). In the sample containing ATG9, the protein was reconstituted into both donor and acceptor liposomes. The microplate was placed in a Synergy Neo 2 Multi-Mode Reader (Table 2.11) and gently shaken for 30 min at 25°C for complex pre-assembly. Subsequently, ATG2 was added at the desired concentrations to start the reaction, and NBD fluorescence intensity (excitation, 485 nm; emission, 528 nm) was monitored for 2 or 3 hours. After the indicated time, triton X-100 was added to the reaction mixture at a 0.5% (v/v) final concentration to solubilize all lipids and therefore maximize NBD fluorescence signals, the signals were then monitored until stabilized. The data was normalized as a percentage of total NBD fluorescence after triton X-100 addition. The transfer rate (k_{obs}) was obtained by fitting the data to a one-phase exponential association equation using GraphPad Prism (Table 2.12).

2.19. Scramblase assay

The scramblase assay was performed as previously reported (Ploier and Menon, 2016, Menon et al., 2011). In our experiments, 50 µM of protein-free liposome or ATG9 PLs containing 2% NBD-PE were prepared in 200 µl buffer D (Table 2.10) in a 96-well microplate (Greiner bio-one). The microplate was placed in a Synergy Neo 2 Multi-Mode Reader (Table 2.11) and NBD fluorescence intensity (excitation, 485 nm; emission, 528 nm) was monitored. After initial signal stabilization, the solution was supplemented with 50 mM sodium dithionite and further supplemented with 50 mM dithionite and triton X-100 0.5% (v/v) after 10 to 15 min of incubation.

2.20. Leakiness control

For the leakiness control, a similar protocol as scramblase assay was used (Ploier and Menon, 2016). PLs were reconstituted as described in Section 2.9, with the exception that the reconstitution buffer was supplemented with 100 uM NBD-glucose and fluorescent lipids were not incorporated into the liposome templates. Liposome templates underwent the same procedure as controls. After reconstitution, NBD-glucose was captured inside the liposome templates and PLs, while extravesicular NBD-glucose was removed by dialysis following the manufacturer’s protocol for Slide-A-Lyzer™ Dialysekassetten (Table 2.1). 50 µM of liposomes or ATG9 PLs containing NBD-glucose were prepared in 200 µl buffer D (Table 2.10) in a 96-well microplate (Greiner bio-one). The microplate was placed in a Synergy Neo 2 Multi-Mode Reader (Table 2.11) and NBD fluorescence intensity (excitation, 485 nm; emission, 528 nm) was monitored. After initial signal stabilization, the solution was supplemented with 50 mM sodium dithionite and further supplemented with 50 mM dithionite and triton X-100 0.5% (v/v) after 10 to 15 min of incubation.

2.21. Mass Photometry

Mass photometry (MP) is a technique to measure molecular weight of biomolecules in solutions (Young et al., 2018). Membrane proteins were reconstituted with amphipols before MP measurements to avoid the noisy background caused by detergent micelles. For amphipol reconstitution, purified ^{MBP}ATG9 or ^{MBP}ATG9-^{MBP}ATG13^{HORMA}-ATG101 complex in buffer containing detergent were incubated with amphipol PMAL-C8 in a protein:amphipol ratio of 1:3 (w/w) for at least 2 hours at 4°C. Detergent and unbound PMAL-C8 were subsequently removed by SEC as described in Section 2.6.3. The ^{MBP}ATG13^{HORMA}-ATG101 complex, amphipol-reconstituted ^{MBP}ATG9, and amphipol-reconstituted ^{MBP}ATG9-^{MBP}ATG13^{HORMA}-ATG101 complex, were then crosslinked by incubating for 1 hour at 4°C with 0,01% glutaraldehyde. The crosslinked samples were then quenched by adding 50 mM Tris pH8 and incubating for 15 min. Quenched samples were used for MP measurements.

MP measurements were performed by A. Patel (Research group of Signaling Dynamics, MPI-NAT) using a OneMP mass photometer (Refeyn Ltd, Oxford, UK). Data was acquired using the AcquireMP software (Refeyn Ltd. v2.3). For the measurement, a drop of immersion oil was first applied on top of the microscope objective. Then, a clean coverslip was placed on the microscope stage. Clean silicon gasket wells to hold the samples were then placed on the cover slip. To find focus, 20 µl of filtered and degassed buffer D was pipetted into one gasket well. The focal point was then identified and locked using the autofocus function. Each sample at an approximate concentration of 20 nM was pipetted into a gasket well, and data were acquired with an acquisition time varying between 60 s and 120 s. The timing was adjusted to get a good number of landing events while avoiding saturation. DiscoverMP software (Refeyn Ltd. v2.3) was used to analyze the data.

2.22. Statistics and reproducibility

All statistical analyses were performed in GraphPad Prism (Table 2.12). Two-tailed student’s t test was used for single comparisons between two groups, and one-way ANOVA (Tukey’s multiple comparisons test) was used for multiple-group comparisons. Statistical relevance is indicated in the graphs as follows: not significant (n.s. or no asterisk) for $p > 0.05$, * for $p < 0.05$, ** for $p < 0.01$, *** for $p < 0.001$ and **** for $p < 0.0001$.

3. Results

3.1. Establishment of purification protocols for autophagy proteins at the ER-phagophore MCS

Efforts made in the last ten years to understand the molecular mechanism of autophagy initiation have been hindered due to the unavailability of purified full-length recombinant proteins of sufficient quality and quantity. This is partly because most of the proteins in the core autophagy machinery are large membrane-associated proteins. Many of them also contain long intrinsically disordered regions (IDR), making them susceptible to degradation and aggregation during purification processes. The reconstitution of autophagy initiation and lipid transfer at the MCS, however, requires the purification of recombinant proteins of the core autophagy initiation complexes (ULK1 complex, PI3K C1, ATG9 vesicles) and lipid transfer complex (ATG2-WIPI4). In this thesis, I have established purification protocols for seven human autophagy proteins, which were mostly not available at the start of this project. The proteins are ULK1, FIP200 (two subunits of the ULK1 complex), ATG14L-BECN1 (two subunits of PI3K C1), ATG9, WIPI4, and ATG2. Purification protocols for ATG13 and ATG101 were also established by my colleagues, and we are currently optimizing the protocols for VPS15 and VPS34, which will complete the list of all proteins required. Domain maps of our purified proteins are illustrated in Figure 3.1.

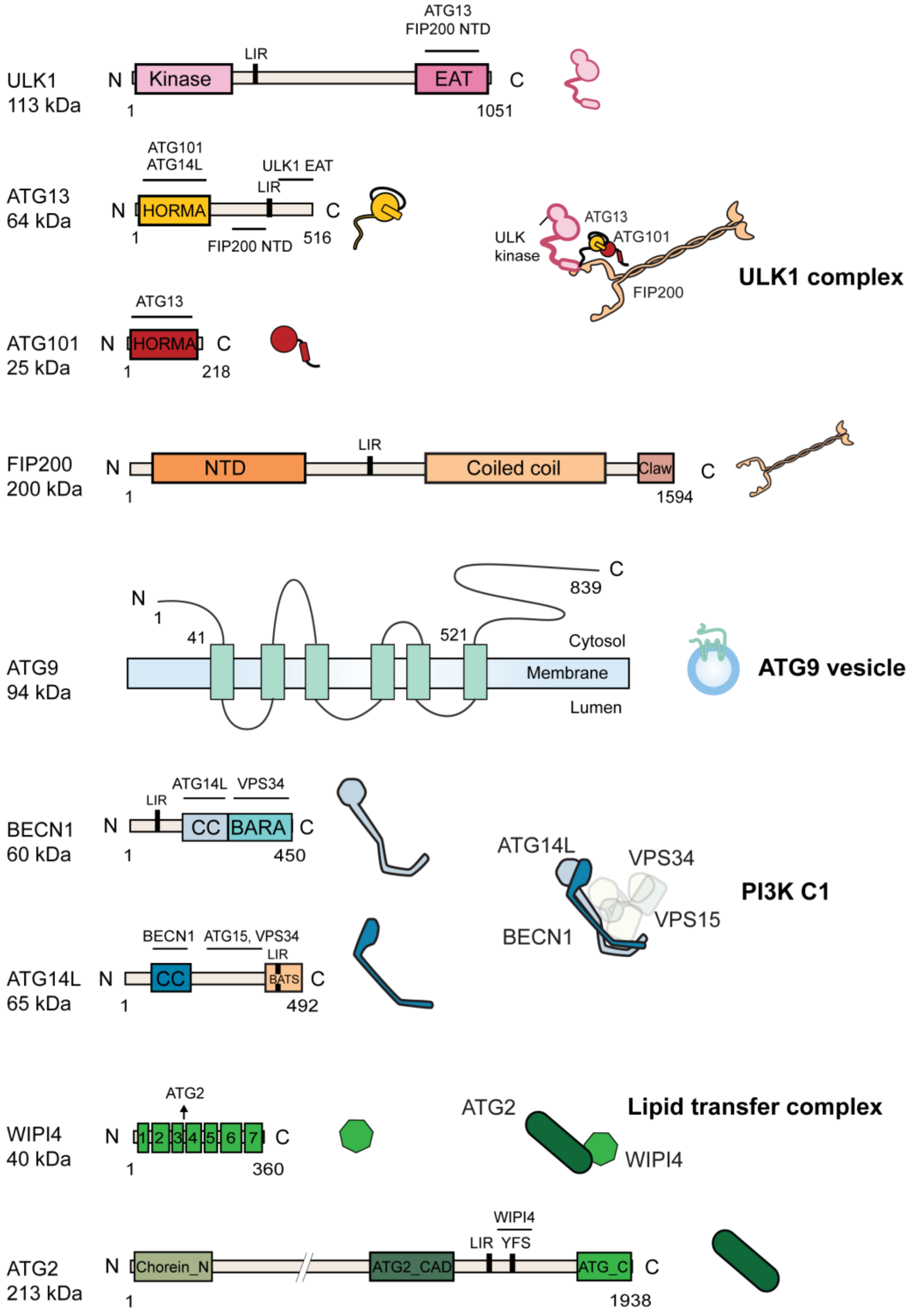

Figure 3.1. Domain architecture of recombinant proteins used in this study. The ULK1 complex includes ULK1, FIP200, ATG13, and ATG101. ATG9 is a transmembrane protein. The PI3K-C1 includes ATG14L, BECN1, VPS34, and VPS15. VPS34 and VPS15 were not used in this study. The lipid transfer complex includes ATG2 and WIPI4.

In general, expression of these large human proteins in bacterial expression systems is challenging. Attempts to recombinantly express these proteins in *E. coli* have been unsuccessful. The MultiBac Baculovirus/Insect Cell Expression System developed by Berger Lab (Sari et al., 2016) is a good alternative. The general advantages of this system are high expression levels driven by the polyhedrin promoter, the ability of the insect cells to perform a variety of post-translational modifications, and the capacity for the expression of large proteins or multi-protein complexes in a single bacmid vector (Trowitzsch et al., 2010, Berger et al., 2004). All proteins/complexes presented in this study are expressed in insect cells using baculovirus, except ATG101. Detailed protocols are described in Materials and Methods. In this section, the optimized protocol for purification of each protein is briefly described along with some deciding factors for successful purification of the proteins, including the choice of tags, detergents, and buffers.

Regarding the ULK1 complex, cloning and the initial buffer screening of ULK1 and FIP200 subunits were done by L. Griese (Research group of Signaling Dynamics, MPI-NAT). ULK1 is a 150 kDa protein containing an N-terminal kinase domain and a C-terminal EAT domain, which are linked by an intrinsically disordered region (IDR) (Figure 3.1). ULK1 is soluble with an N-terminal GST tag (^{GST}ULK1 hereafter). However, insect cells expressing ^{GST}ULK1 tend to die within 48 h post-infection, compared to 60-72 h for most other proteins, suggesting that the protein is toxic to the cells. In addition, the protein is also easily targeted by cellular proteolytic degradation during protein purification, especially at the lysis step. Therefore, harvested cell pellets were lysed immediately with buffer supplemented with 100 µM leupeptin, which was shown to significantly decrease protease activity in Hi5 cells (Martensen and Justesen, 2001). Lysis was done for 1 hour by stir-mixing at 4°C in lysis buffer containing 1% DDM. Lysate was cleared by centrifugation, and the cleared lysate was subjected to affinity chromatography using a GST trap column. The wash buffer and elution buffer should also contain 100 uM leupeptin to prevent proteolytic degradation. The protein was eluted from the GST trap column using 20 mM reduced glutathione

(GSH) in the elution buffer. Eluted ^{GST}ULK1 fractions from affinity chromatography were pooled and subjected to SEC using a Superose 6 column (Figure 3.2 A).

FIP200 (200kDa) is the second largest protein in the core autophagy machinery and contains a long coil-coiled domain (Figure 3.1). The protein is prone to aggregation and was solubilized only with an N-terminal 6x-His-MBP tag (^{MBP}FIP200 hereafter). The protein expression level was low, most likely due to its large size. The purification protocol for ^{MBP}FIP200 is similar to the protocol for ^{GST}ULK1. Cell lysate was subjected to affinity chromatography using an MBP trap column. The protein was eluted from the MBP trap column using 20 mM maltose in the elution buffer. Eluted fractions containing ^{MBP}FIP200 were pooled and subjected to SEC using a Superose 6 column (Figure 3.1 B).

ATG13 (56 kDa) and ATG101 (25 kDa) are the other two subunits of the ULK1 complex. Both of them have a HORMA domain in their structures. (Figure 3.1). The two proteins were found to be unstable when expressed individually; thus, they were purified as a heterodimer (Qi et al., 2015). However, purification protocols for isolated full-length ATG13 and ATG101 have been established by my colleagues L. Griese and A. Patel (Research group of Signaling Dynamics, MPI-NAT), which allow us to characterize them individually *in vitro.* SEC profiles of ATG13 with an N-terminal 6x-His-MBP tag (^{MBP}ATG13 hereafter) and ATG101 with a C-terminal StrepII tag (ATG101^{Strep} hereafter) and corresponding SDS-PAGE analysis of purified proteins are shown in Figure 3.3. ^{MBP}ATG13 eluted in a higher molecular range compared to the theoretical molecular weight of 100 kDa, most likely due to its long C-terminal IDR, whereas ATG101^{Strep} eluted close to its expected size of 26 kDa.

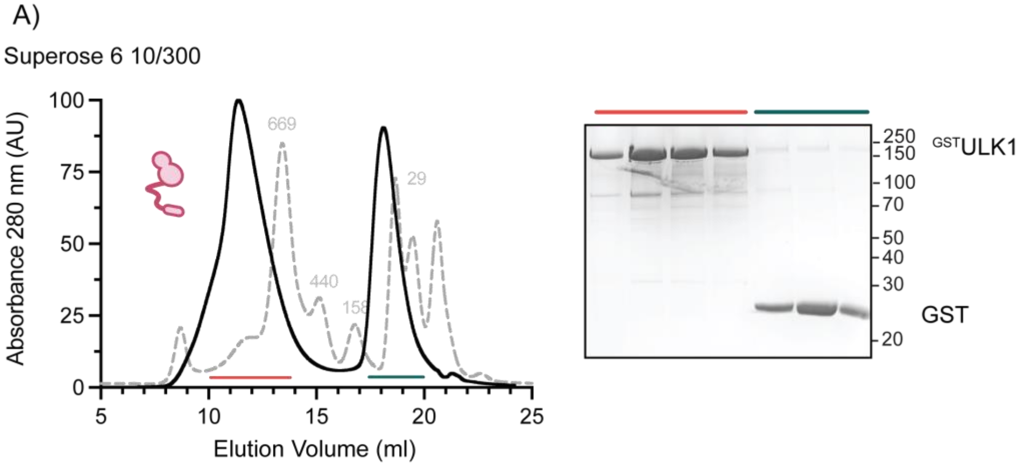

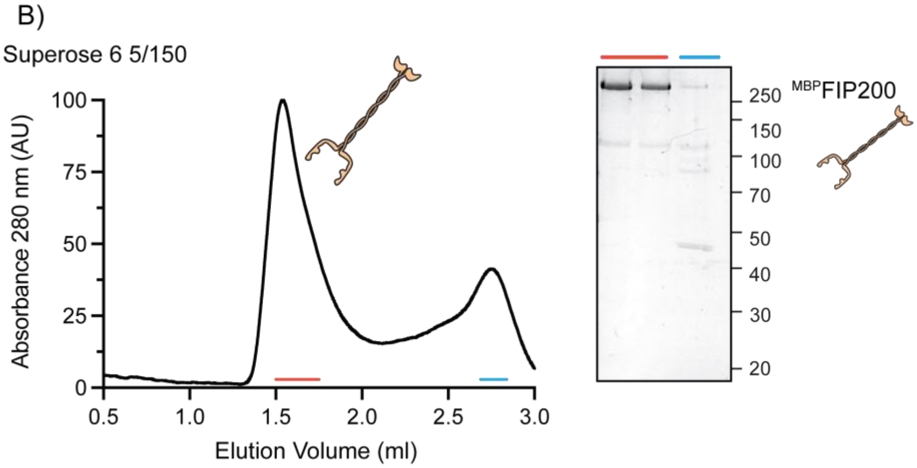

Figure 3.2. Purification of ULK1 and FIP200. A) SEC profile of ^{GST}ULK1 (left) and the corresponding SDS-PAGE analysis of the peak fractions (right). SEC profile of marker proteins is shown in gray-dash line. B) SEC profile of ^{MBP}FIP200 (left) and the corresponding SDS-PAGE analysis of the peak fractions (right).

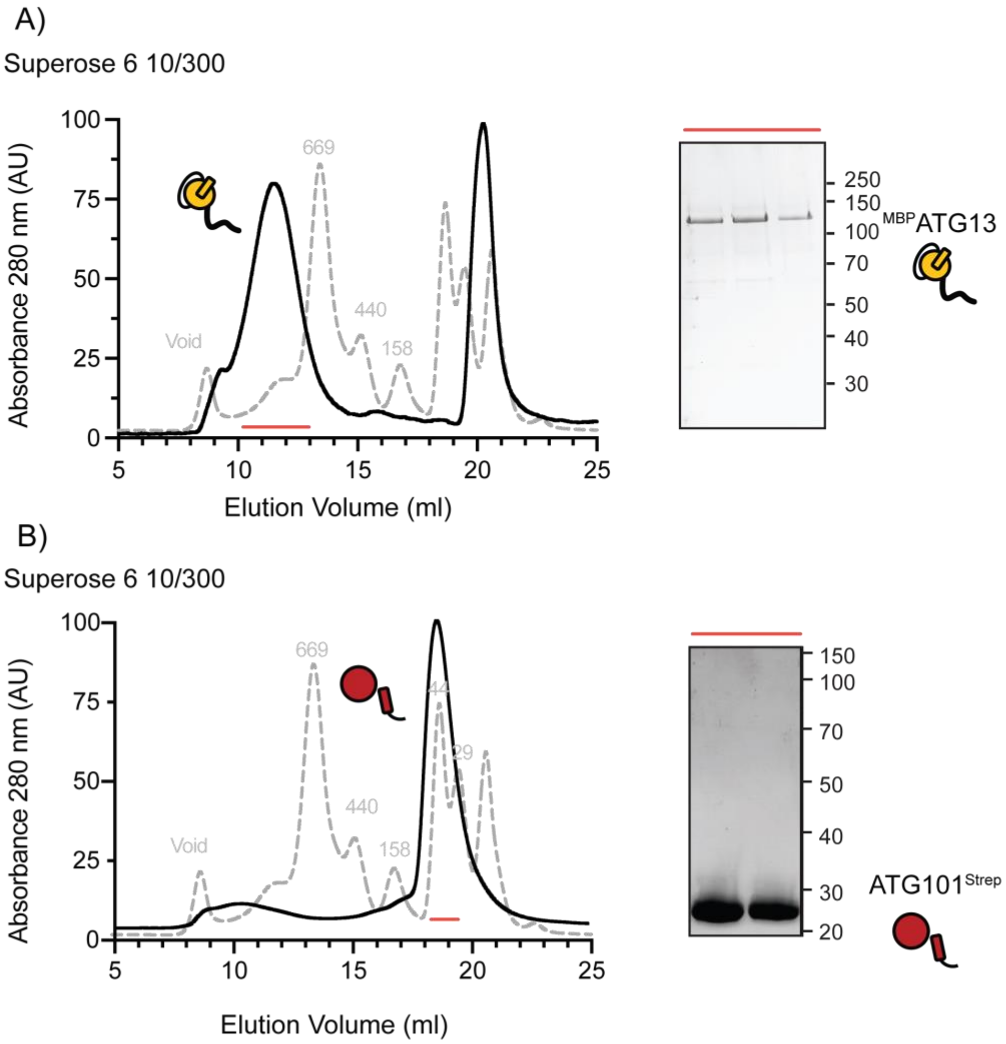

Figure 3.3. Purification of ATG13 and ATG101. A) SEC profile of ^{MBP}ATG13 with markers (gray dashed-line trace trace) (left) and the corresponding SDS-PAGE analysis of the peak fractions (right). Purification of ATG13 was established by L. Griese (MPI-NAT). B) SEC profile of ATG101^{Strep} with markers (gray dashed-line trace) (left) and the corresponding SDS-PAGE analysis of the peak fractions (right). Purification of ATG101^{Strep} was established by A. Patel (MPI-NAT).

ATG9 (94 kDa) is an integral membrane protein consisting of six transmembrane segments (Figure 3.1). The protein is only soluble with an N-terminal MBP tag (^{MBP}ATG9 hereafter). Harvested Hi5 cells expressing ^{MBP}ATG9 were lysed by 1 hour of stir-mixing at 4°C in lysis buffer containing 1% DDM. This condition allows disruption of the plasma membrane as well as extraction of the protein from its bound membrane. Cell lysis by sonication was not performed since it induces protein degradation and aggregation. After lysis, the detergent (DDM) concentration was kept at 0.03% to protect the hydrophobic transmembrane domains of the proteins. The protein was purified using affinity chromatography. After affinity chromatography, eluted fractions containing the protein were pooled, and the tag was cleaved. Samples were further purified by SEC using a Superose 6 column. Figure 3.4 A depicts the SEC profile and corresponding SDS-PAGE analysis of the peak fractions containing ATG9. Protocols for ATG9 purification have since also been established by Guardia et al. (2020) with the HEK cell expression system and Maeda et al. (2020) with expression in Sf9 cells. Both require the preparation of membrane fractions and the subsequent extraction of the protein from the membrane fractions. Here, the protocol offers a cheaper and easier way of purifying ATG9.

The PI3K-C1 is a four-subunit lipid kinase complex containing ATG14L, BECN1, VPS34, and VPS15 (Figure 3.1). ATG14L (55 kDa) and BECN1 (52 kDa) are stable in a complex. Thus, for the purification protocol of ATG14L-BECN1 subcomplex, BECN1 with an N-terminal 6xHis-MBP tag ($^{\text{MBP}}$BECN1 hereafter) and ATG14L with an N-terminal 6xHis-mCherry tag ($^{\text{mCherry}}$ATG14L hereafter) were co-expressed in Hi5 cells. The cell pellet was then harvested and lysed in lysis buffer containing 1% DDM and 500 mM NaCl. Since both proteins have membrane binding regions, DDM was added to solubilize the protein-associated membranes. The subcomplex was then purified by affinity chromatography using an MBP trap column. After affinity chromatography, the eluted fractions containing the complex were then subjected to SEC using a Superose 6 column. SDS-PAGE analysis of the peak fractions shows a purified sample containing a complex of $^{\text{MBP}}$BECN1 and $^{\text{mCherry}}$ATG14L (Figure 3.4 B). The establishment of purification protocols for two other subunits, VPS34 and VPS15, is ongoing.

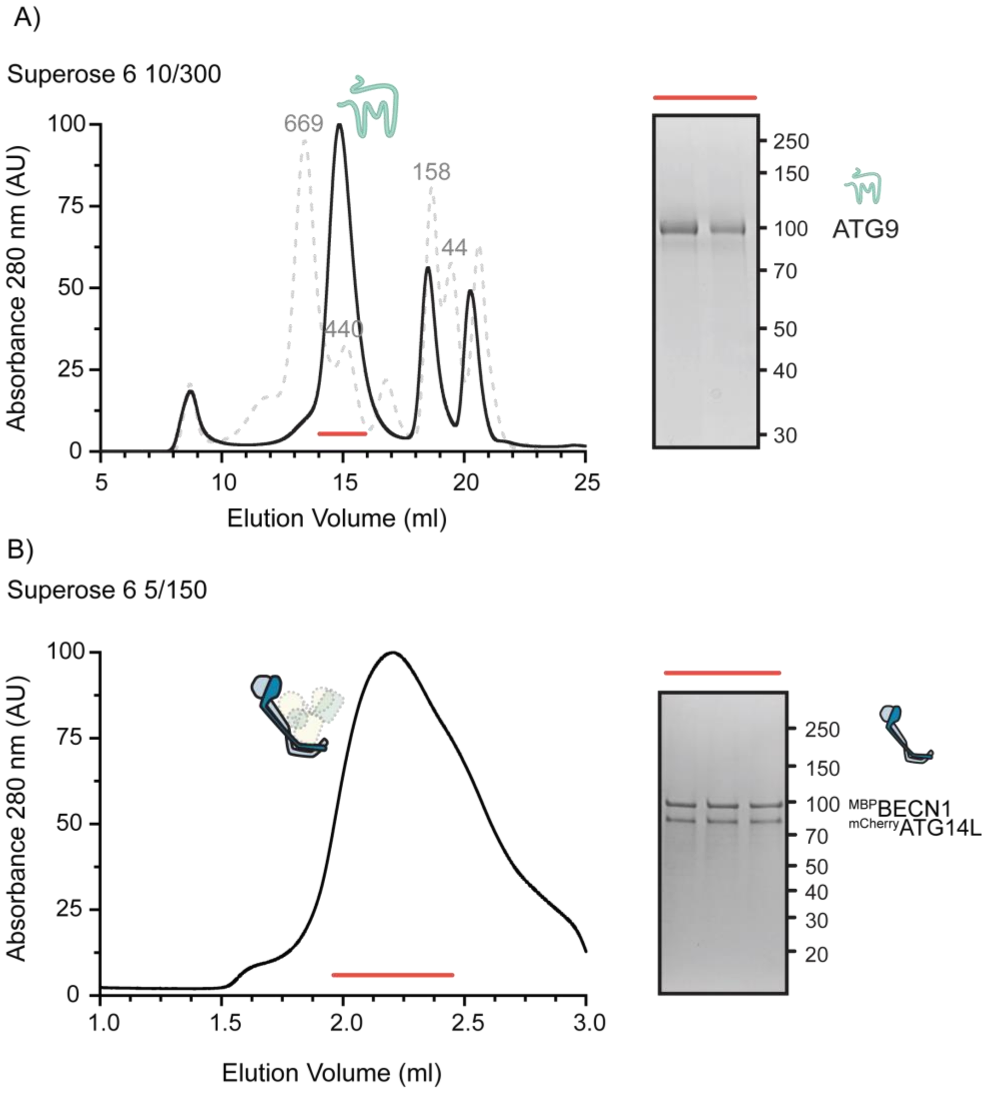

Figure 3.4. Purification of ATG9 and ATG14L-BECN1 complex. A) SEC profile of ^{MBP}ATG9 with markers (gray dashed-line trace trace) (left) and the corresponding SDS-PAGE analysis of the peak fractions (right). B) SEC profile of ^{MBP}BECN1-^{mCherry}ATG14L complex (left) and the corresponding SDS-PAGE analysis of the peak fractions (right).

ATG2 (213 kDa) is the largest among the ATG proteins (Figure 3.1). Because of its extended rod shape and two membrane-bound tips, the protein is prone to aggregation and precipitates with the membrane during lysis. Various combinations of proteins and tags were screened, and the best combination is ATG2 with the C-terminal Strep II tag (ATG2^{Strep} hereafter). The protein was purified with a protocol similar to that of ^{MBP}ATG9, except a high concentration of DDM (0.1%) in both affinity chromatography and SEC buffers is crucial to keep the protein from aggregation. For affinity chromatography, the protein was applied to a Strep trap column and eluted with 5 mM desthiobiotin in elution buffer. Eluted fractions containing the protein were pooled and further purified by SEC using a Superose 6 column. The elution peak corresponds roughly to that of a 669 kDa marker protein because of the elongated shape of the protein (Figure 3.5 A).

WIPI4 (40 kDa) is a PI3P-binding protein that forms a complex with ATG2 (Figure 3.1). It is soluble with various affinity tags, including GFP, mCherry, GST and MBP, making it versatile for various experimental settings. The purification of N-terminal 6xHis-GFP tagged WIPI4 ($^{\text{GFP}}$WIP4) is discussed as an example. The protein was purified by affinity chromatography using a His trap column. Optionally, the protein could be incubated with PreScission protease to cleave the tag. The sample was then subjected to IEX chromatography to remove impurities. The protein was eluted at roughly 300 mM NaCl in IEX chromatography (Figure 3.5 B). Eluted fractions from IEX were pooled and further purified by SEC using a Superdex 75 column. $^{\text{GFP}}$WIP4 eluted at an elution volume roughly corresponding to its theoretical size of 66 kDa (Figure 3.5 C).

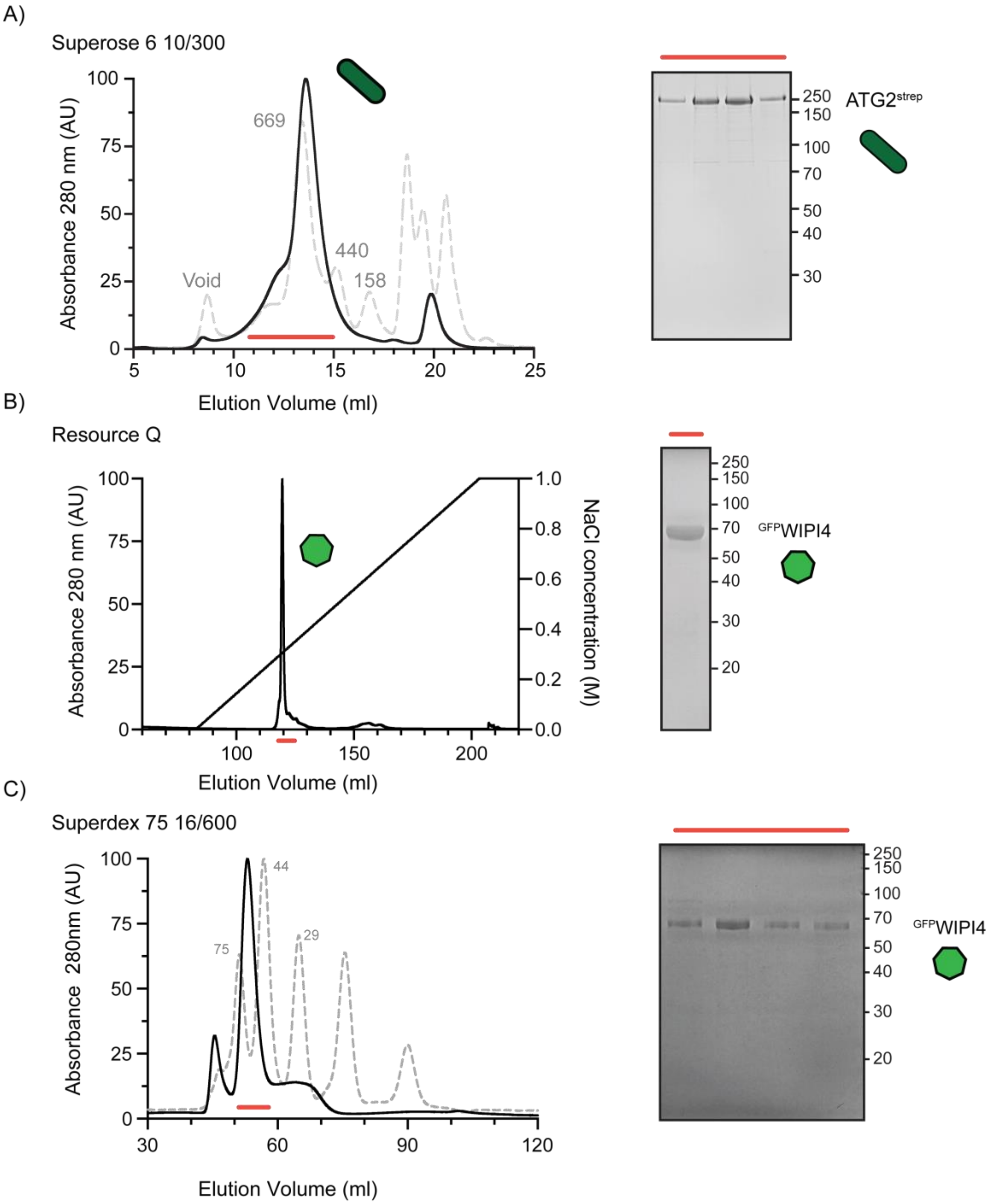

Figure 3.5. Purification of ATG2 and WIPI4. A) SEC profile of ATG2^{Strep} with markers (gray dashed-line trace trace) (left) and the corresponding SDS-PAGE analysis of the peaks' fractions (right). Protein fractions analyzed in SDS-PAGE are indicated by the red line. B) IEX profile of ^{GFP}WIPI4 (left) and the corresponding SDS-PAGE analysis of the peak fractions (right). C) SEC profile of WIPI4 with markers (gray dashed-line trace trace) (left) and the corresponding SDS-PAGE analysis of the peak fractions (right).

3.2. Reconstitution of autophagy initiation complexes and lipid transfer complex

3.2.1. Investigation of complex assemblies

After establishing purification protocols for the recombinant proteins, I started to reconstitute different subcomplexes at the MCS, with the aim of investigating their assemblies and functional significance at the MCS *in vitro*. As mentioned in Section 1.2.2, ULK1 complex is the most upstream complex in autophagy, consisting of ULK1, FIP200, ATG13 and ATG101. To show ULK1 complex formation *in vitro*, a pull-down experiment was performed with ^{GST}ULK1 as bait and the three other subunits as prey. Following a 1-hour pre-incubation at 25°C, the sample was immobilized by incubation with glutathione beads (GST beads) for 10 min and washed twice with 500 µl buffer. Samples, including inputs and controls, were then analyzed by SDS-PAGE (Figure 3.6). This experiment shows that ^{GST}ULK1 can pull down three other subunits of the complex, while protein bands of other subunits are not detected in the absence of ^{GST}ULK1, demonstrating the formation of the ULK1 complex with all full-length subunits.

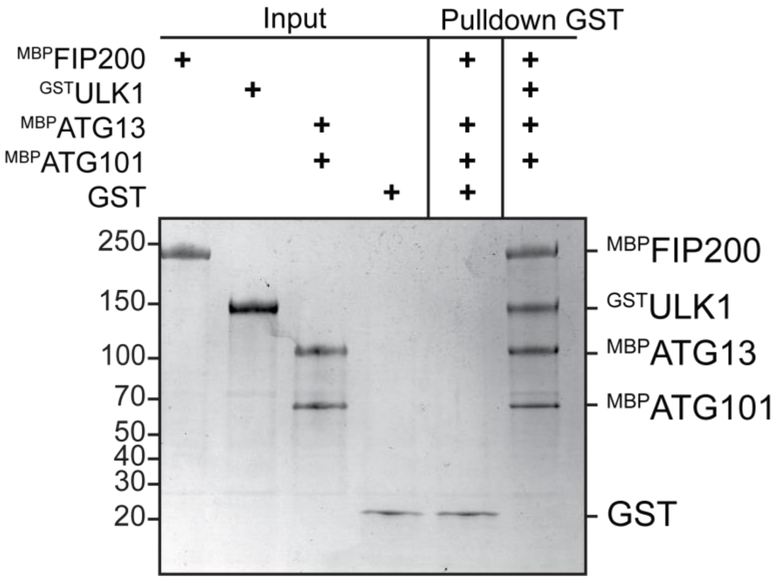

Figure 3.6. *In vitro* pull-down experiment showing the formation of ULK1 complex. The assay was performed with 0.5 µM of bait and 1 µM of prey. Proteins were incubated at 25ºC for 1 h.

Interaction between ULK1/Atg1 complex and ATG9/Atg9 is one of the most upstream events in autophagy and has been observed in both budding yeast and mammals. In yeast, the N-terminal HORMA domain of Atg13 was found to interact with the N-terminal cytoplasmic region of Atg9, and disruption of this interaction leads to severe defects in starvation-induced autophagy (Suzuki et al., 2015b). Using co-IP in mammalian cells, Kannangara et al. (2021) showed that ATG13-ATG101 complex binds to ATG9, and the interaction relies on the HORMA domain of ATG13. Therefore, we used both full-length human ATG13 and a truncation of ATG13 containing only the HORMA domain (Figure 3.7 A) for further characterization of ATG9, ATG13, and ATG101 interactions *in vitro*. Firstly, to confirm ATG13 and ATG101 interactions with ATG9, I co-expressed and purified the complex of ^{MBP}ATG9-^{MBP}ATG13-^{MBP}ATG101 from insect cells. As shown in Figure 3.6 B, ^{MBP}ATG9, ^{MBP}ATG13, and ^{MBP}ATG101 eluted in one peak (brown trace), which corresponds to a larger size than that of ^{MBP}ATG9 (blue trace). This indicates that the three proteins eluted as a complex. When replacing full-length ATG13 with ATG13^{HORMA}, I could also purify the complex of ^{MBP}ATG9-^{MBP}ATG13^{HORMA}-ATG101. As shown in Figure 3.7 C, the ^{MBP}ATG9-

^{MBP}ATG13^{HORMA}-ATG101 complex eluted at roughly 15 ml, while ^{MBP}ATG9 eluted slightly later and the excess ^{MBP}ATG13^{HORMA}-ATG101 complex eluted at roughly 17.5 ml, indicating interactions between the three proteins. This also confirms previous findings that the HORMA domain of ATG13 is sufficient for the interaction with ATG9 (Kannangara et al., 2021). Additionally, compared to the complex of all full-length proteins, the complex of ATG9-ATG13^{HORMA}-ATG101 was less prone to aggregation and easier to purify. Hence, ATG9-ATG13^{HORMA}-ATG101 complex was typically used as an alternative to the full-length complex in this project.

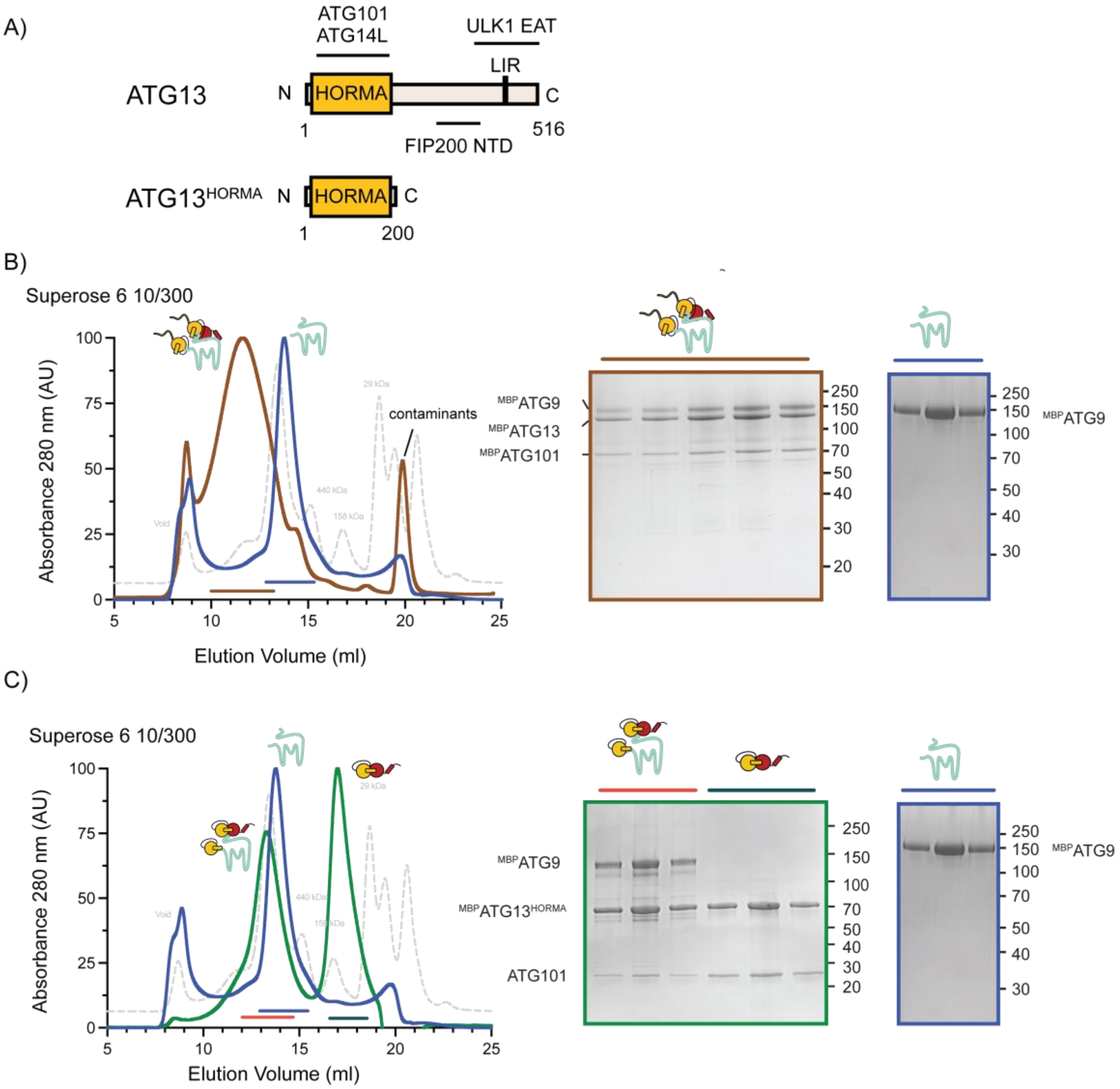

Figure 3.7. Complex of ATG9, ATG13 and ATG101. A) A schematic drawing of full-length ATG13 and a truncation containing only the HORMA domain, ATG13^{HORMA}, B) SEC profiles of full-length ^{MBP}ATG9-^{MBP}ATG13-^{MBP}ATG101 complex (brown trace), ATG9 (blue trace), and markers (gray dashed-line trace trace) (left), and the corresponding SDS-PAGE analysis of the peak fractions (right). C) SEC profiles of ^{MBP}ATG9-^{MBP}ATG13^{HORMA}-^{MBP}ATG101 (green trace), ATG9 (blue trace), and markers (gray dashed-line trace trace) (left), and the corresponding SDS-PAGE analysis of the peak fractions (right).

After purifying the complex, I noticed the increase in intensity of ATG13 and ATG13^{HORMA} bands in SDS-PAGE analysis when they are in a complex with ATG9 (Figure 3.7 C), suggesting that ATG13 is superstoichiometric in the complex. To determine the stoichiometry of the complex, I used mass photometry (MP), an analytical technique that estimates molecular masses of biomolecules by measuring light scattered from single biomolecules in solution (Young et al., 2018). However, the use of MP for membrane proteins or complexes has two disadvantages. First, the use of detergent for membrane proteins creates background noise that adversely affects the results. Second, its optimal detection range is between 5 and 20 nM, which leads to dissociation of low-affinity complexes. To overcome the first problem, I reconstituted ^{MBP}ATG9 and ^{MBP}ATG9-^{MBP}ATG13^{HORMA}-ATG101 complex in amphipols, as described in Section 2.21. Amphipols are a class of amphiphilic polymers that wrap around the hydrophobic transmembrane surface of membrane proteins, making them soluble without the need for detergent (Popot et al., 2011). Detergent can therefore be removed from protein samples after amphipol reconstitution. To work around the low protein concentration required for the optimal detection range of mass photometry, I crosslinked the amphipols-reconstituted ^{MBP}ATG9-^{MBP}ATG13^{HORMA}-ATG101 complex with glutaraldehyde, as described in Section 2.21. The crosslinked products were then used for MP measurements. ^{MBP}ATG13^{HORMA}-ATG101 complex and ^{MBP}ATG9 were first measured as controls. ^{MBP}ATG9, a known trimer, has a theoretical molecular weight (MW) of 537 kDa (including 7 molecules of bound amphipols) compared to the experimental MW of 526 kDa (Figure 3.8 A). ^{MBP}ATG13^{HORMA}-ATG101 complex with a known 1:1 stoichiometry has a theoretical MW of 90 kDa compared to the experimental MW of 100 kDa (Figure 3.8 B). These controls showed that the method is reliable for measuring our protein complexes. The measurement of the ^{MBP}ATG9-^{MBP}ATG13^{HORMA}-ATG101 complex showed an experimental MW of 998 kDa, compared to a theoretical MW of 1007 kDa for a 3:6:3 (^{MBP}ATG9:^{MBP}ATG13^{HORMA}:ATG101) stoichiometry complex.

In addition to mass photometry, I used stain-free (SF) method as a complementary approach to quantify the stoichiometry of ^{MBP}ATG9-^{MBP}ATG13^{HORMA}-ATG101 complex. The method was developed for visualizing and quantifying protein bands in Stain-Free™ SDS-PAGE gels, which does not require the use of colorimetric or fluorescent stains (Gurtler et al., 2013, Holzmuller and Kulozik, 2016). The method takes advantage of an ultraviolet light-induced reaction between tryptophan residues in protein sequences and the trihalo compound supplemented in the gel matrix, which causes the protein band to fluoresce after a brief photoactivation. The intensity of the protein band is thus proportional to the number of tryptophan residues in each protein and can be quantified using the light-induced signals of tryptophan. To determine the stoichiometry by the SF method, the purified ^{MBP}ATG9-^{MBP}ATG13^{HORMA}-ATG101 complex was separated on a Stain-Free™ Gel and quantified as described in Section 2.14. The ^{MBP}ATG13^{HORMA}-ATG101 complex with a known stoichiometry of 1:1 was used as a control. As shown in Figure 3.8 D and E, the normalized intensities of protein bands scale linearly with the amount of protein loaded in both the control and the ^{MBP}ATG9-^{MBP}ATG13^{HORMA}-ATG101 complex. The ratio of normalized band intensities of ATG9:ATG13:ATG101 is 3:6:3 (Figure 3.8 F), which is consistent regardless of the four different amounts of protein loaded, indicating that the complex has a 3:6:3 stoichiometry in solution. This result is consistent with the 3:6:3 stoichiometry obtained from mass photometry of the ATG9-ATG13-ATG101 complex (Figure 3.8 C). Overall, the stoichiometry suggests an interesting assembly mechanism where ATG13 might have one or more binding sites on ATG9, which would be explored in detail in Section 3.2.2.

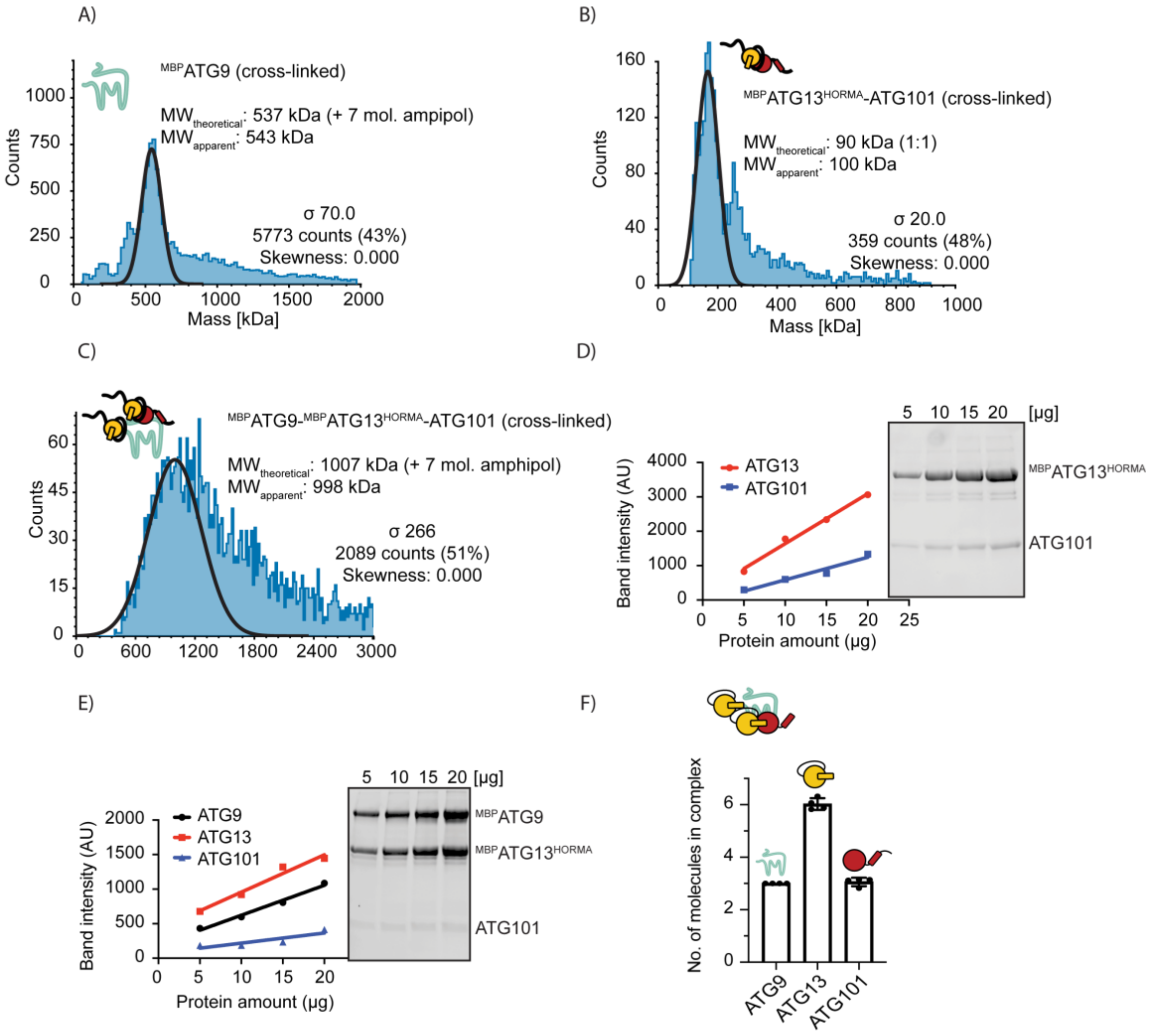

Figure 3.8. Stoichiometry of ATG9-ATG13-ATG101. A) Mass photometry profile of cross-linked $^{\text{MBP}}$ATG9 reconstituted in amphipols shows an apparent MW of 543 kDa compared to a theoretical MW of 537 kDa ($^{\text{MBP}}$ATG9 is a known trimer, each $^{\text{MBP}}$ATG9 monomer has a MW of 137 kDa, including approximately 7 molecules of amphipols of 18 kDa), B) Mass photometry profile of cross-linked $^{\text{MBP}}$ATG13$^{\text{HORMA}}$-ATG101 complex shows an apparent MW of 100 kDa compared to a theoretical trimer MW of a 1:1 stoicheometry complex of 90 kDa (theoretical MW of $^{\text{MBP}}$ATG13$^{\text{HORMA}}$ and ATG101 is 65 kDa and 25 kDa, respectively), C) Mass photometry profile of cross-linked $^{\text{MBP}}$ATG9-$^{\text{MBP}}$ATG13$^{\text{HORMA}}$-ATG101 reconstituted in amphipols shows an apparent MW of 998 kDa compared to a theoretical MW of 1007 kDa of a 3:6:3 stoicheometry complex. σ, standard deviation of the fitted Gaussian. Mass photometry experiments were performed by A. Patel (MPI-NAT), D) Stoichiometry analysis of $^{\text{MBP}}$ATG13$^{\text{HOMRA}}$-ATG101 complex by stain-free method, E) Stoichiometry analysis of $^{\text{MBP}}$ATG9-$^{\text{MBP}}$ATG13$^{\text{HOMRA}}$-ATG101 complex by stain-free method. In D and E, indicated amount of proteins was loaded on stain free gels. Gels were

visualized as described in Section 2.14, and bands intensities were normalized against the number of tryptophan residues in each protein. The signal scales linearly with the protein amount. Ratio between protein band intensities does not change regardless of protein amount loaded. $^{\text{MBP}}$ATG13$^{\text{HOMRA}}$-ATG101 complex has known stoichiometry of 1 to 1 was used as a reference for quantification. F) Quantification of band intensities in E shows a 3:6:3 soicheometry of the ATG9-ATG13-ATG101 complex.

As ATG13-ATG101 is part of the ULK1 complex, the assembly of the ATG9-ATG13-ATG101 complex supports the previous hypothesis that the coalescence of the ULK1 complex with ATG9 promotes phagophore nucleation (Karanasios et al., 2016). Additionally, studies have shown that ULK1 is required for the regulation of ATG9 vesicles' trafficking to the autophagy initiation site (Young et al., 2006, Zhou et al., 2017, Chan et al., 2009), and subsequent regulation of the PI3K-C1 lipid kinase activity via ATG13-ATG14 interaction (Park et al., 2016). Similarly, it has been proposed that Atg9 association with Atg1 complex through Atg9-Atg13 interaction is required for the recruitment of the Atg9-containing vesicle to the PAS, followed by the PI3K complex 1 to facilitate the progression of autophagy (Suzuki et al., 2015b). Hence, I wondered if other subunits of the ULK1 complex and PI3K complex would coalesce with the ATG9-ATG13-ATG101 complex to form a super-complex at the autophagy initiation site. To test this hypothesis, I first investigated interactions between ATG13-ATG101 complex and a subcomplex of PI3K-C1 consisting of ATG14L and BECN1 using SEC. The two purified subcomplexes were mixed in a 1:1 ratio and incubated at 25°C for 1 hour. The mixture was then applied to a Superose 6 5/150 column for SEC. The SEC profile and corresponding SDS-PAGE analysis showed that the four proteins eluted together in one peak (Figure 3.9, blue trace). The complex of ATG13-ATG101-ATG14L-BECN1 has a lower elution volume compared to $^{\text{MBP}}$ATG13-$^{\text{MBP}}$ATG101 subcomplex (brown trace) or $^{\text{mCherry}}$ATG14L-$^{\text{MBP}}$BECN1 subcomplex (green trace), confirming the formation of a four-protein complex. The result is supported by a pull-down experiment by F. Lugarini (MPI-NAT), in which she used $^{\text{GST}}$ATG13$^{\text{HORMA}}$-ATG101 subcomplex as a bait to successfully precipitate the other subcomplex (Figure 3.10).

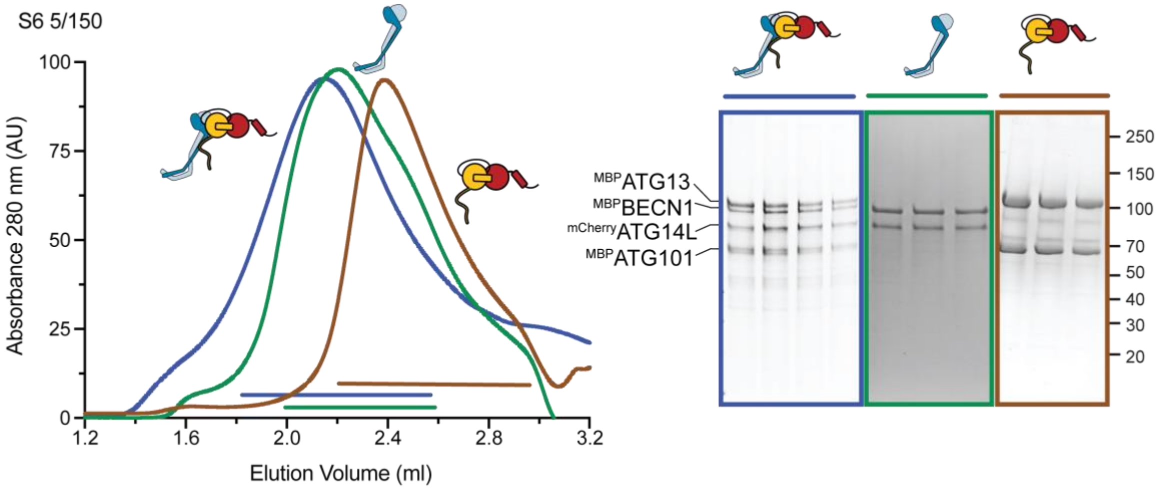

Figure 3.9. Complex of ATG13, ATG101, ATG14L and BECN1. A) SEC profiles of ^{MBP}ATG13-^{MBP}ATG101-^{MBP}BECN1-^{mCherry}ATG14L complex (blue trace), ^{MBP}ATG13-^{MBP}ATG101 (brown trace), and ^{MBP}BECN1-^{mCherry}ATG14L complex (green trace). B) SDS-PAGE analysis of the peak fractions shown in A), showing co-elution of the subunits.

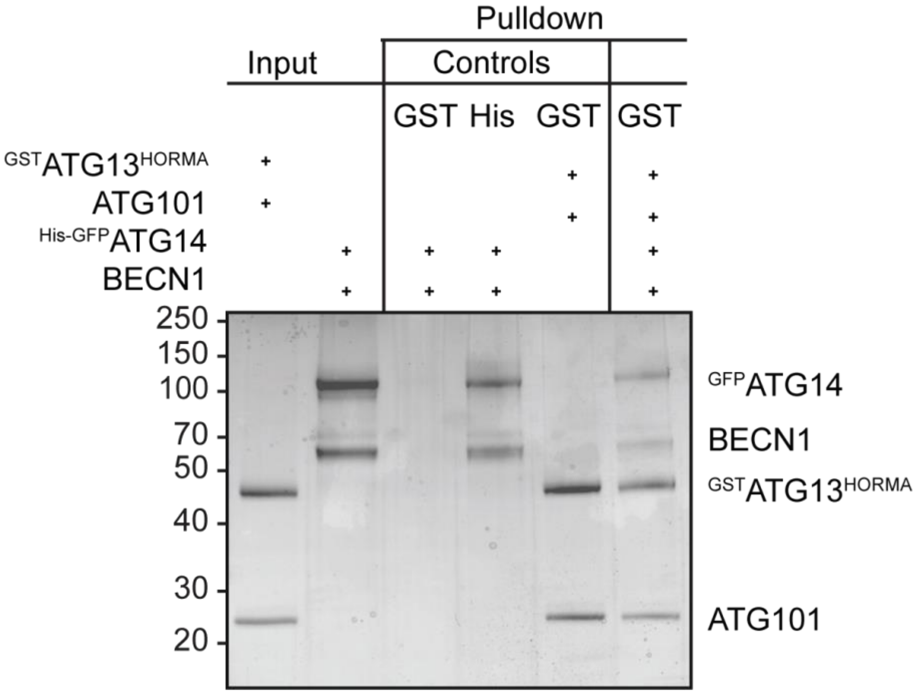

Figure 3.10. *In vitro* pull-down experiment showing that ATG14-BECN1 interacts with ATG13^{HORMA}-ATG101. Pull-down was performed using 1 μM bait (^{GST}ATG13^{HORMA}-ATG101) and 3 μM prey (^{GFP}ATG14-BECN1). Proteins were incubated at 4°C for 1h. The experiment was done by F. Lugarini.

After confirming the interactions between ULK1 and PI3K-C1 subcomplexes, I examined the possibility of a super-complex assembly in which the core complex brings together the subunits of ULK1 complex and PI3K-C1. For that, I performed a pull-down experiment using $^{\text{GST}}$ULK1 as a bait to pull down $^{\text{MBP}}$FIP200, $^{\text{MBP}}$ATG9-$^{\text{MBP}}$13-$^{\text{MBP}}$101 complex, and $^{\text{mCherry}}$ATG14-$^{\text{MBP}}$BECN1 complex. As shown in Figure 3.11, immobilization of $^{\text{GST}}$ULK1 on GST beads could specifically precipitate the other six proteins, confirming the existence of a seven-subunit super-complex.

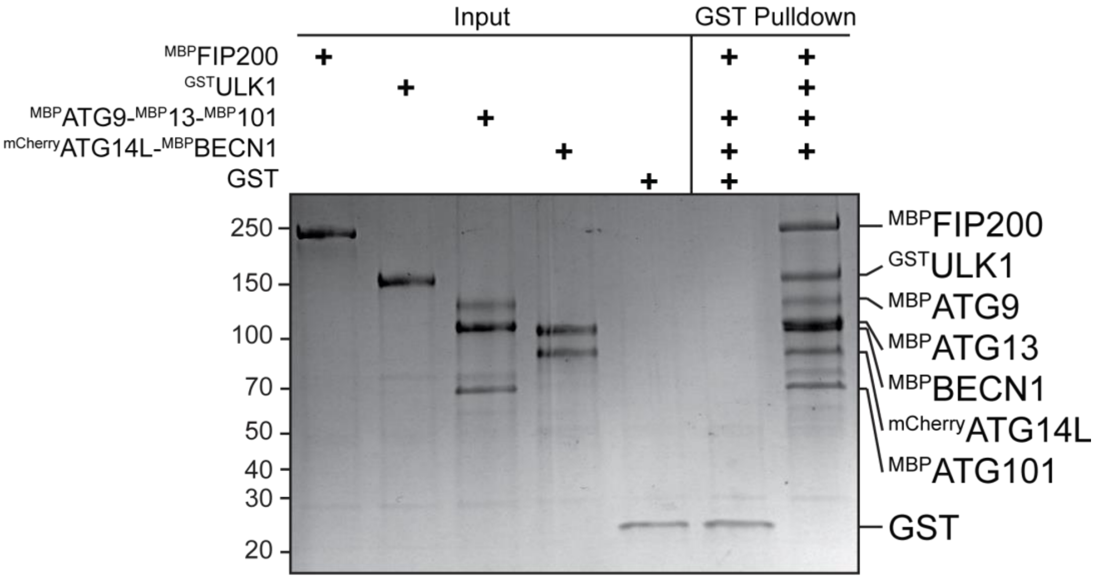

Figure 3.11. *In vitro* pull-down experiment showing a seven-subunit super-complex of the human autophagy proteins. The super-complex includes ATG9, ATG13, ATG101, FIP200, ULK1, ATG14L and BECN1. Pull-down experiment was performed using 1 μM bait and 3 μM prey. Proteins were incubated at 25ºC for 1h.

To determine whether the core complex plays a central role in the super-complex assembly, the pull-down was repeated with a control in which the ATG9-ATG13-ATG101 complex was omitted. As shown in Figure 3.12, when the $^{\text{MBP}}$ATG9-$^{\text{MBP}}$13-$^{\text{MBP}}$101 complex was omitted, the super-complex did not form, suggesting it plays a coordinating role in the assembly of the super-complex. It is thus called the core complex.

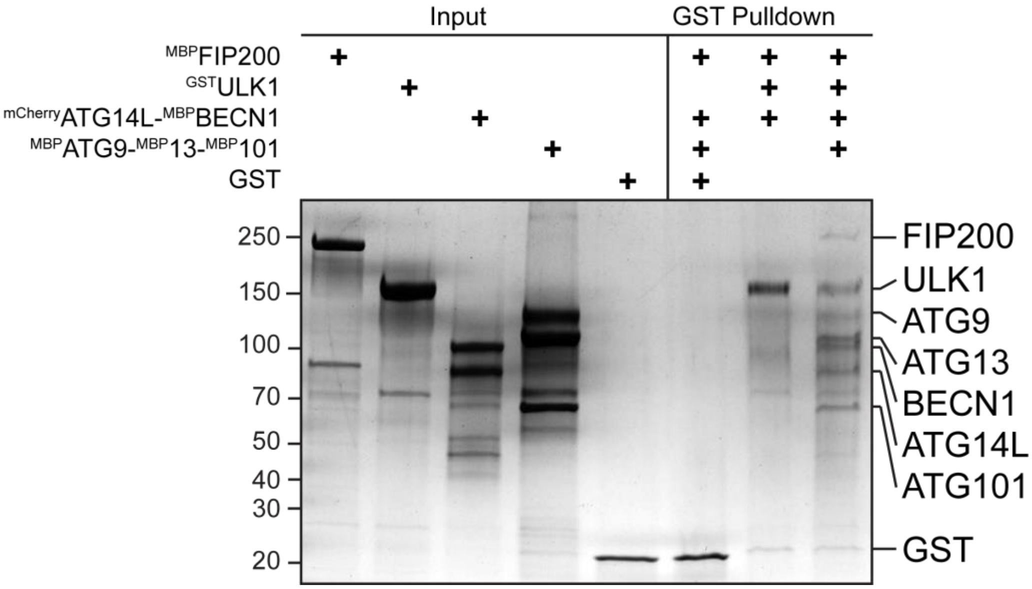

Figure 3.12. *In vitro* pull-down experiment showing ATG9-ATG13-ATG101 complex is required for the formation of the super-complex. When ATG9-ATG13-ATG101 complex was removed, the super-complex could not be pulled by ULK1. 1 μM bait and 3 μM prey were used. Proteins were incubated at 25°C for 1h. The pull-down experiment was performed by F. Lugarini.

The assembly of the super-complex likely leads to the nucleation of the phagophore membrane, which is subsequently expanded by various lipid supply pathways, including the lipid transfer activity of the ATG2-WIPI4 lipid transfer unit. As mentioned in Section 1.3.2, the lipid transfer unit is required for the establishment of the ER-phagophore MCS. Moreover, ATG2 and ATG9 were hypothesized to cooperatively transport lipids from the ER to the two leaflets of the phagophore via their lipid transfer and scramblase activities. In yeast, Atg2 interacts with Atg9, and this interaction is required for the subsequent recruitment of Atg18 via Atg2-Atg18 interaction (Gomez-Sanchez et al., 2018). Here, using a pull-down experiment, I found that ATG2 independently interacts with both ATG9 and WIPI4. As shown in Figure 3.13 A, ATG2^{Strep} immobilized on Strep tactin beads could pull down either ^{MBP}ATG9, ^{GFP}WIPI4 or both, indicating that ATG9 and WIPI4 directly interact with ATG2, and the interactions are not mutually exclusive. In addition, ^{MBP}ATG9 immobilized on MBP beads could not pull down ^{GFP}WIPI4, indicating no interaction between ATG9 and WIPI4. Consistent with the pull-down experiment, the SEC profile of a pre-incubated mixture of ATG2^{Strep}

and ^{GFP}WIPI4 showed co-elution of ATG2^{Strep}-^{GFP}WIPI4 complex independent of ATG9 (Figure 3.13 B, green trace). The addition of ATG9 resulted in a reduction in elution volume to roughly 13 ml, indicating the formation of ATG9-ATG2-WIPI4 complex (Figure 3.13 B, orange trace). The SEC profile of a preincubated mixture of ^{MBP}ATG9 and ^{GFP}WIPI4 showed two distinct peaks of ^{MBP}ATG9 and ^{GFP}WIPI4, indicating no interaction (Figure 3.13 C). The assembly of ATG2-WIPI4-ATG9 suggests cooperative roles of intermembrane and interleaflet transporters through direct interactions, which will be further investigated in Section 3.3.

After showing that ATG9 forms a complex with ATG2-WIPI4, I wondered if the ATG9-ATG13-ATG101 complex could accommodate the ATG2-WIPI4 complex and whether there are any mutually exclusive interactions between the proteins. To test that, I performed a pull-down experiment in which I used ATG2^{Strep} as a bait to pull down ATG9, ^{GFP}WIPI4, and ^{MBP}ATG13^{HORMA}-ATG101. As shown in Figure 3.14, ATG2^{Strep} could pull down four other proteins, indicating the formation of a five-subunit complex. Besides, the increased intensity of ATG9 compared to ATG2^{Strep} suggests that one ATG2 molecule likely interacts with an ATG9 trimer. The formation of the five-subunit complex also suggests that the super-complex likely accommodates with the lipid transfer subcomplex through ATG2-WIPI4 interaction with the core complex.

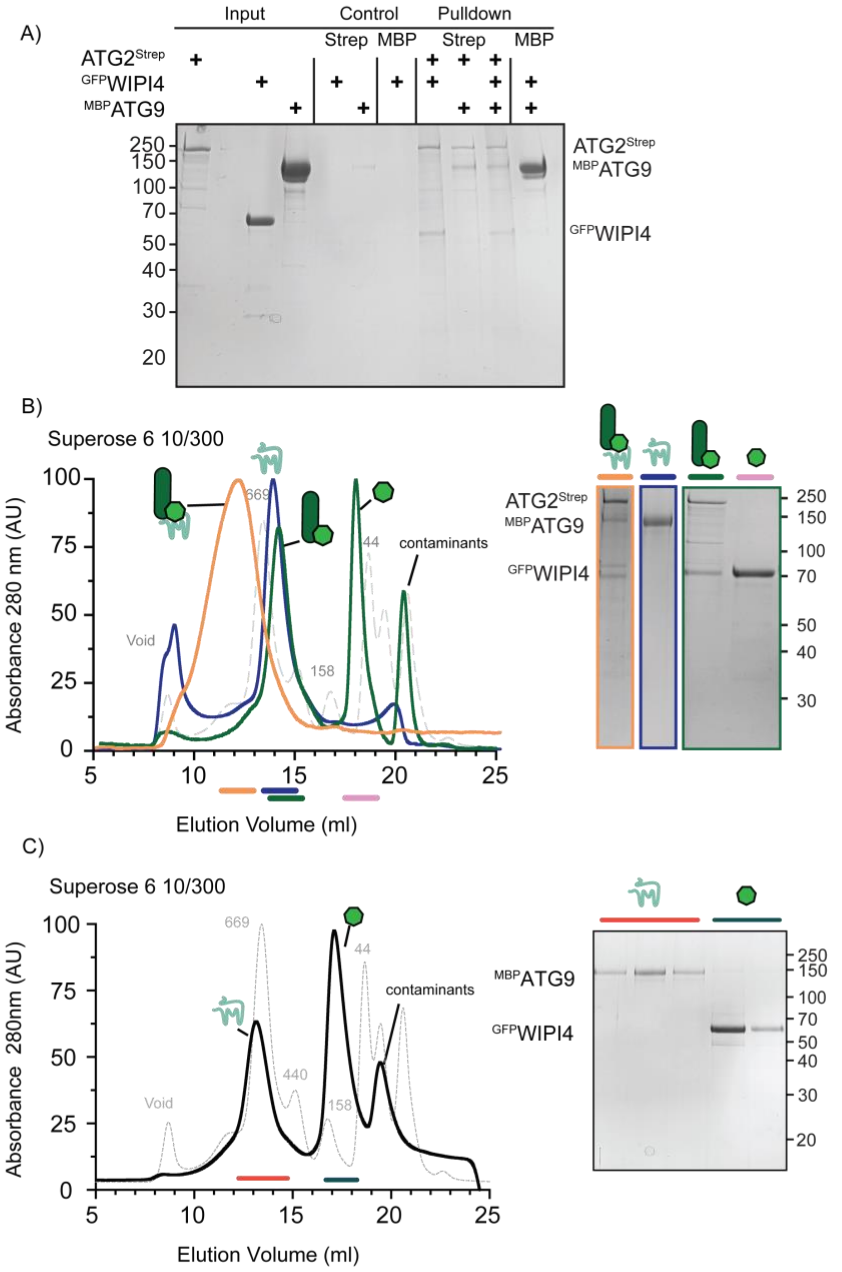

Figure 3.13. Complex of ATG9, ATG2 and WIPI4. A) *In vitro* Strep and MBP pull-down experiment showing interactions between ATG9, ATG2, and WIPI4. ATG2 interacted with both ATG9 and WIPI4, and there was no interaction between WIPI4 and ATG9. Pull-down was performed using 1 µM bait and 3 µM prey. B) SEC profiles of $^{\mathrm{MBP}}$ATG9-ATG2$^{\mathrm{Strep}}$-$^{\mathrm{GFP}}$WIPI4 complex (orange trace), ATG2$^{\mathrm{Strep}}$-$^{\mathrm{GFP}}$WIPI4 complex (green trace), $^{\mathrm{MBP}}$ATG9 (blue trace), and marker proteins (gray dashed-line trace trace) (left). Analysis of corresponding peak fractions demonstrates co-elution of the subunits (right). C) SEC profiles of a pre-incubated mixture of $^{\mathrm{MBP}}$ATG9 and $^{\mathrm{GFP}}$WIPI4 (black trace)(left) and corresponding peak fractions analyzed by SDS–PAGE (right). The two proteins did not co-elute, indicating no interaction.

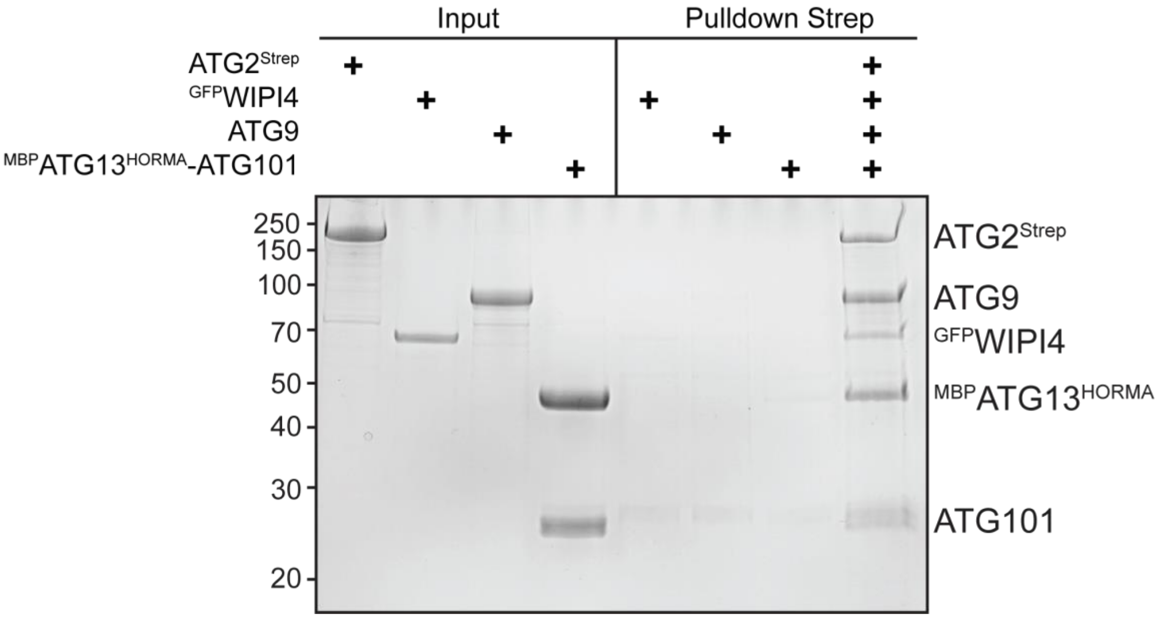

Figure 3.14. *In vitro* pull-down experiment showing a five-subunit complex of ATG2-WIPI4 and ATG9-13-10. Pull-down was performed using 1 µM bait and 3 µM prey. Proteins were incubated at 25°C for 1h.

3.2.2. The core complex's assembly creates a kinetic bottleneck for the super-complex's assembly.

In Section 1.4, we hypothesized the existence of a super-complex in which ATG13 and ATG101 are proposed as factors that might be involved in the regulation of the super-complex assembly. I have also established that the ATG9-ATG13-ATG101 complex plays a central role in the assembly of the super-complex and has an unusual stoichiometry of 3:6:3. Therefore, the next step is to investigate how the ATG9-ATG13-ATG101 complex assembles, with a special focus on the putative regulatory roles of ATG13 and ATG101. First, I used cross-linking mass spectrometry (XL-MS) to examine the basis of protein-protein interaction within the complex. Purified ^{MBP}ATG9-^{MBP}ATG13^{HORMA}-ATG101 complex were crosslinked with different concentrations of crosslinker BS3, as described in Section 2.12. Crosslinked samples were then analyzed by SDS-PAGE (Figure S2). Crosslinked bands appearing in BS3 concentrations of 0.2, 0.5, and 1 mM were cut and digested for XL-MS analysis as described in Section

2.21. Cross-linking analysis showed extensive crosslinks between ATG9 and both ATG13 and ATG101, suggesting that ATG13 or ATG101 independently interact with ATG9 (Figure 3.15). However, interactions of ATG13 or ATG101 with ATG9 have not been investigated since they were found to be stable only in the heterodimer form (Qi et al., 2015). Here, I could show that ATG13 interacts with ATG9 by co-expressing and purifying the complex from insect cells. As shown in Figure 3.16 A, the SEC profile of ^{MBP}ATG9-^{MBP}ATG13 complex (black trace) showed a shift in elution volume compared to the SEC profiles of ^{MBP}ATG9 (light blue trace) and ^{MBP}ATG13 (yellow trace), indicating a complex formation. A. Patel (MPI-NAT) did a similar SEC experiment for ^{MBP}ATG9 and ATG101^{Strep} and found that the two proteins did form a complex. As shown in Figure 3.16 A, ^{MBP}ATG9 and ATG101^{Strep} eluted together in one peak (black trace), which corresponds to a larger size compared to the peak of ^{MBP}ATG9 (light blue trace) or ATG101 (red trace), suggesting that they form a complex.

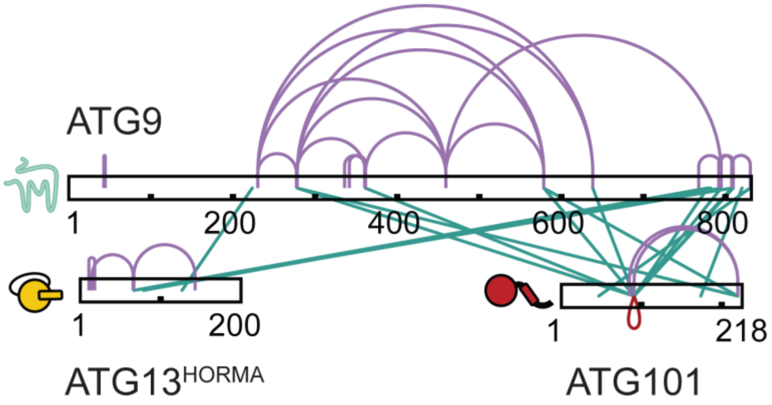

Figure 3.15. XL-MS analysis of the complex of ^{MBP}ATG9-^{MBP}ATG13^{HORMA}-ATG101. Intra-protein cross-links (purple), interprotein cross-links (blue), and homomultimeric links (red) at residue level were visualized by xiNET (Combe et al., 2015). XL-MS was performed and analyzed by I. Pafentef (Research group of Bioanalytical Mass Spectrometry, MPI-NAT).

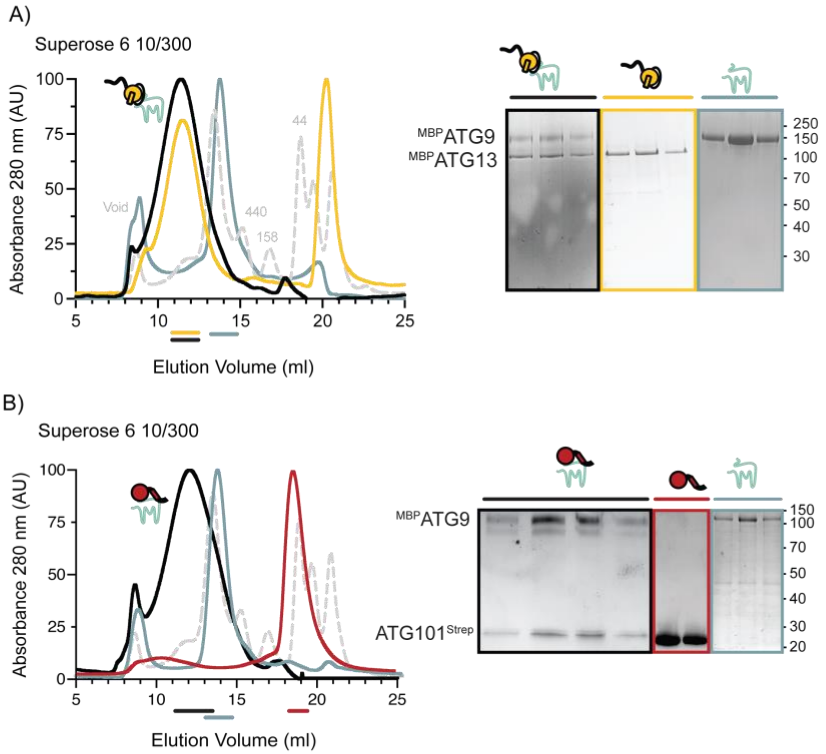

Figure 3.16. ATG13 and ATG101 bind to ATG9 independently. A) SEC profiles of ^{MBP}ATG9-^{MBP}ATG13 complex (black trace), ^{MBP}ATG13 (yellow trace), ^{MBP}ATG9 (light blue trace), and marker proteins (gray dashed-line trace trace) (left), and the corresponding SDS-PAGE analysis of the peak fractions (right). B) SEC profiles of ^{MBP}ATG9-ATG101^{Strep} complex (black trace), ATG101^{Strep} (red trace), ^{MBP}ATG9 (light blue trace), and marker proteins (gray dashed-line trace trace) (left), and the corresponding SDS-PAGE analysis of the peaks fractions (right). The experiment in B) was done by A.Patel (MPI-NAT).

By using different truncations of ATG9, F. Lugarini (Research group of Signaling Dynamics, MPI-NAT) identified the interaction sites of both ATG13 and ATG101 on ATG9. ATG13 and ATG101 bind to ATG9 at the very end of its C-terminal (residues 831 to 839) (ATG9^{C}) which contains two conserved residues, P833 and P834. As shown in Figure 3.17 B, ^{GST}ATG9^{C} immobilized on GST beads could pull down ^{MBP}ATG13^{HORMA} and ATG101 (lane 1), while mutation of the conserved residues P833 and P834 in ATG9^{C} abolished the binding (lane 2), indicating that the residues are essential for ATG13 and ATG101 interactions with ATG9^{C}. Although crosslinks between ATG13 and ATG101 with ATG9^{N} were not detected (Figure 3.15), ATG13 does interact stoichiometrically with the Nterminus of ATG9 (ATG9^{N}) (data not shown). Surprisingly, once bound to ATG9^{N}, ATG13 lost its ability to bind to ATG101 despite a prolonged incubation in an excess amount of ATG101. As shown in Figure 3.17 C, ^{GST}ATG13^{HORMA} immobilized on GST beads could pull down ATG101 (lane 1), but a pre-formed complex of ^{GST}ATG13^{HORMA}-^{mCherry}ATG9^{N} could not (lane 2). This finding contradicts a canonical competitive interaction in which an excess amount of ATG101 would be able to compete with ATG9^{N} for its interaction with ATG13. Since HORMA domain proteins are known to change their interaction spectra by switching between different metamorphic states (Gu et al., 2022), it is likely that ATG13 and ATG101 adopt distinct conformations when interacting with ATG9^{N} and ATG9^{C}.

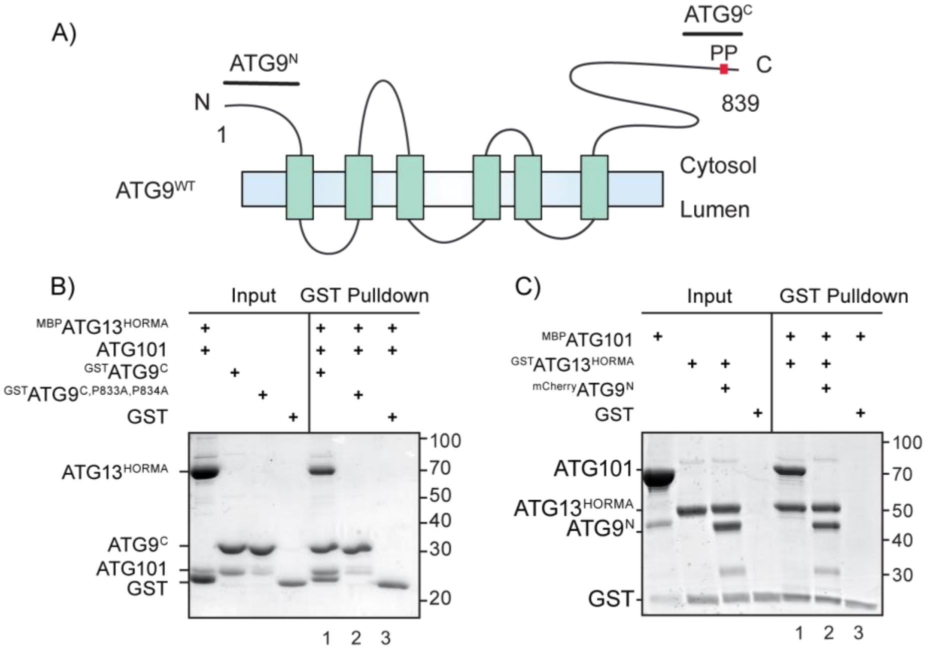

Figure 3.17. Characterization of ATG13 and ATG101 interactions with ATG9. A) A schematic representation of ATG9 truncations, ATG9^{N} and ATG9^{C}. The two conserved residues, P833 and P834, are marked by the red dot. B) ATG13-ATG101 interacts with ATG9^{C}. Point mutations P833A and P834A disrupt the ability of ATG9^{C} to interact with ATG13-ATG101. Pull-down experiment using ^{GST}ATG9^{C} or ^{GST}ATG9^{C,P833A,P834A} as bait. C) ATG101 does not interact with the ATG9^{N}-ATG13^{HORMA} complex. Pull-down experiment using preformed ^{GST}ATG13^{HORMA}-^{mCherry}ATG9^{N}, ^{GST}ATG13^{HORMA} as bait. The assay was performed with 6 µM ^{MBP}ATG101 and 2 µM of bait. Proteins were incubated at 4°C for 1 h. The experiments were done by F. Lugarini.

Interestingly, the interactions of either ATG13^{HORMA} or ATG101 with ATG9 are incredibly slow (18–24 hours) (Figure 3.18 A). The slow interaction kinetics of ATG13 and ATG101 with ATG9 suggest that the two HORMA domain proteins continue the trend of other HORMA domain proteins that default to an inactive conformer that does not readily interact with its partner proteins (Gu et al., 2022). However, the default conformer state may be changed by removing the mobile elements (also known as “seatbelt”) in the HORMA domains (Mapelli et al., 2007). To confirm that ATG13 can indeed adopt two states with distinct binding capabilities, ATG13^{WT} and ATG13 constructs with mutated mobile elements (Figure 3.18 B) were tested for their preferable bindings to either ATG9^{N} or ATG101 (Figure 3.18 D). Although ATG13^{WT} preferentially bound to ATG101 (top panel, lane 5), the ATG13 constructs with mutated mobile elements favoured ATG9^{N} (top panel, lane 2 and 3). Following a strategy previously employed for other HORMA domain proteins, ATG13 constructs were incubated at varying temperatures to induce transitions between stable conformer states. Here, ATG13 constructs were incubated overnight at 4°C in the absence of binding partners to allow for any slow spontaneous conversion between the states (Figure 3.18 D, bottom panel). Indeed, the mutants did switch preference from ATG9^{N} to ATG101 (bottom panel, lane 2 and 3), while the preference of ATG13^{WT} did not change (bottom panel, lane 5). Taken together, the results demonstrate that the thermodynamically stable conformer of ATG13^{WT} preferentially binds ATG101 and that ATG13^{WT} requires a slow metamorphic switch to a state that can bind to ATG9^{N}. Removing the HORMA domain's mobile elements affects conformer stability, consequently changing the default state and binding preference. Another distinguishing feature of HORMA domains is their ability to form homo- and heterodimers via a canonical interface. When HORMA domains dimerize, they may speed up the rate at which they interact with their client(s) (Gu et al., 2022). Indeed, the interaction of the ATG13^{HORMA}–ATG101 complex with ATG9 was accelerated (30–60 minutes) compared to the interaction of individual proteins with ATG9 (18–24 hours) (Figure 3.18 C), proving that dimerization of ATG13 and ATG101 affects their kinetics to ATG9.

Overall, these results showed that ATG13 and ATG101 have a typical characteristic of HORMA domain proteins, and their slow metamorphic conversion creates a kinetic bottleneck for the assembly of the core complex, which is most likely extended to the assembly of the super-complex.

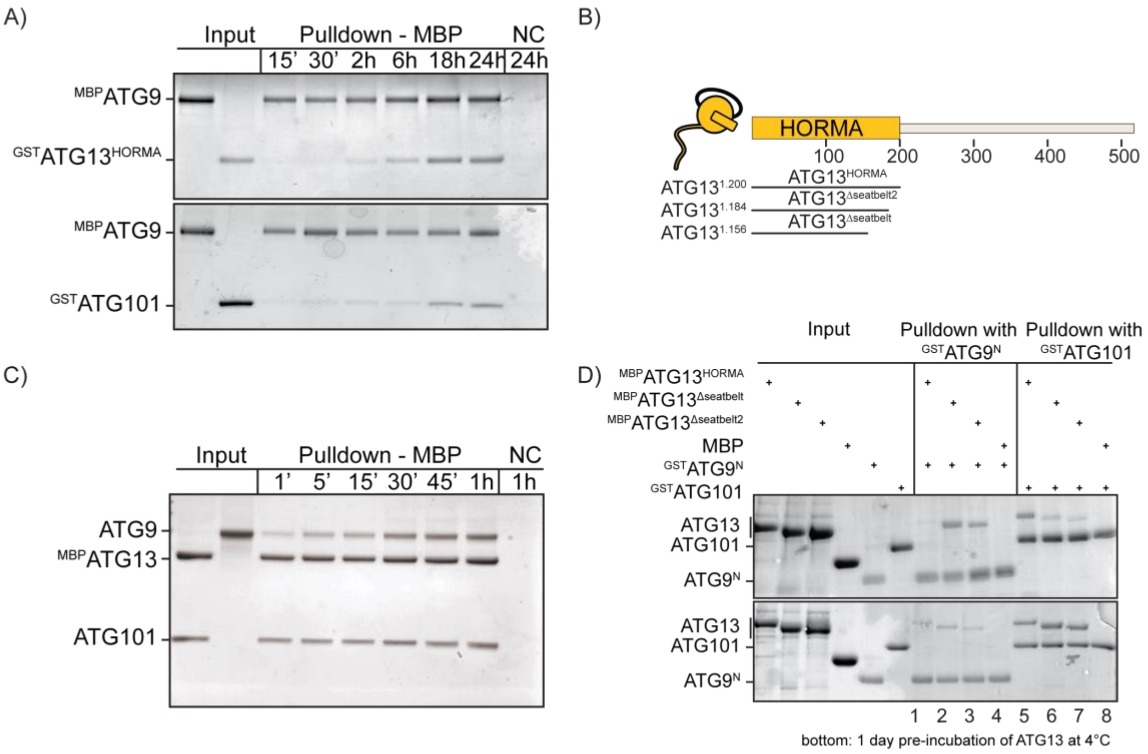

Figure 3.18. The assembly of the core complex is dictated by the metamorphoses of ATG13 and ATG101 conformers. A) Complex formation of ATG9-ATG13 (top) and ATG9-ATG101 (below) takes 18-24 hours. Pull-down experiment was done at 20°C using 2 μM of bait and prey. Proteins were incubated for the time indicated. B) A schematic representation of wild-type ATG13^{HORMA} and its two conformer-mobile element mutants, ATG13$^{\Delta seatbelt1}$ and ATG13$^{\Delta seatbelt2}$. C) Complex formation of ATG9-13-101 takes 30 to 60 minutes. Pull-down experiment was done at 4°C using 0.1 μM bait (^{GST}ATG13^{HORMA}-ATG101) and 0.2 μM ATG9 (ATG9). Proteins were incubated for the time indicated. D) Two distinct conformations of ATG13 exist, each capable of binding either ATG9^{N} or ATG101. Wild-type ATG13^{HORMA} defaults to the ATG101-binding conformer, while ATG13$^{\Delta seatbelt1}$ and ATG13$^{\Delta seatbelt2}$ default to the ATG9-binding conformer (top). However, both ATG13$^{\Delta seatbelt1}$ and ATG13$^{\Delta seatbelt2}$ switch to conformers that bind to ATG101 after being incubated at 4°C for one day in the absence of binding partners (bottom). Pull-down experiment using 1 μM ^{GST}ATG9^{N} or ^{GST}ATG101 as bait and 3 μM ^{MBP}ATG13^{HORMA} or ^{MBP}ATG13$^{\Delta seatbelt}$ mutants. Proteins were incubated at 4°C for 1 h. The experiments were done by F. Lugarini.

3.3. Cooperative functions at the reconstituted MCS

As mentioned in Section 1.3.2, ATG2 is the protein tether at the MCS, which also mediates lipid transfer between membranes. In the following sections, an investigation into the cooperative roles of ATG2's partners in lipid transfer activity at the MCS will be discussed.

3.3.1. Cooperative tethering at the MCS

In collaboration with P.Hosnani and B.Knotkova (Georg August University of Göttingen, now Heidelberg University Biochemistry Center - BZH), we used confocal microscopy to visualize the ATG2-mediated tethering in the presence of its interacting partner, WIPI4. WIPI4 is a known PI3P-binding protein, as previously described in Section 1.2.5. Here, we were able to see the specific binding of WIPI4 to PI3P under a confocal microscope by using giant unilamellar vesicles (GUVs) labelled with Rhod-PE (Rh-GUVs) and ^{GFP}WIPI4. As shown in Figure 3.19, ^{GFP}WIPI4 (green) concentrated at the edges of the PI3P-containing Rh-GUVs (red) (top panel). However, it was not detected on the edge of PI3P-free Rh-GUVs (bottom panel). Next, to visualize the ATG2-mediated contact site between Rh-GUVs, we added ATG2 labelled with ATTO647N (ATG2^{ATTO647N}) to a pre-incubated mixture of WIPI4 labelled with Alexa488 (WIPI4^{Alexa488}) and Rh-GUVs. Images from confocal microscopy shows that multiple Rh-GUVs are tethered together, generating a large cluster of Rh-GUVs (Figure 3.19 B, bottom panel). We also observed an enrichment of ATG2^{ATTO647N} (purple) and WIPI4^{Alexa488} (green) signals along a flat line between two isolated GUVs, which is a typical characteristic of an *in vitro* contact site established by protein tethers (Figure 3.19 B top panel). If the GUVs randomly touched each other, the flat line would not be observed. The appearance of a flat line is in stark contrast to the condition without ATG2, when no tethering was found (Figure 3.19 A). In addition, when we added non-specific proteinase K to samples with ATG2-tethered Rh-GUVs, the Rh-GUVs were slowly separated (video not shown), confirming that the tethering is induced by ATG2. Using dynamic light scattering

(DLS), we observed that the apparent size of LUVs was about 50 nm. The size was increased to about 110 nm in the presence of ATG2 and further increased to about 138 nm upon addition of WIPI4, suggesting that WIPI4 enhances the chance of ATG2-mediated tethering activity via its binding to both ATG2 and the PI3P-positive membrane. Since we also found that ATG2 interacts with ATG9 *in vitro,* we tested ATG2-mediated tethering in the presence of ATG9 (Section 3.2.1). Indeed, when ATG9 was added, we saw a further increase in particle size to about 190 nm, which could be reverted by treatment with non-specific proteinase K (Figure 3.19 C). Other controls are shown in Figure S1. In summary, the experiments using confocal microscopy and DLS show that WIPI4 and ATG9 cooperatively enhance the tethering activity of ATG2, likely by strengthening ATG2 affinity to the membrane through cooperative interactions.

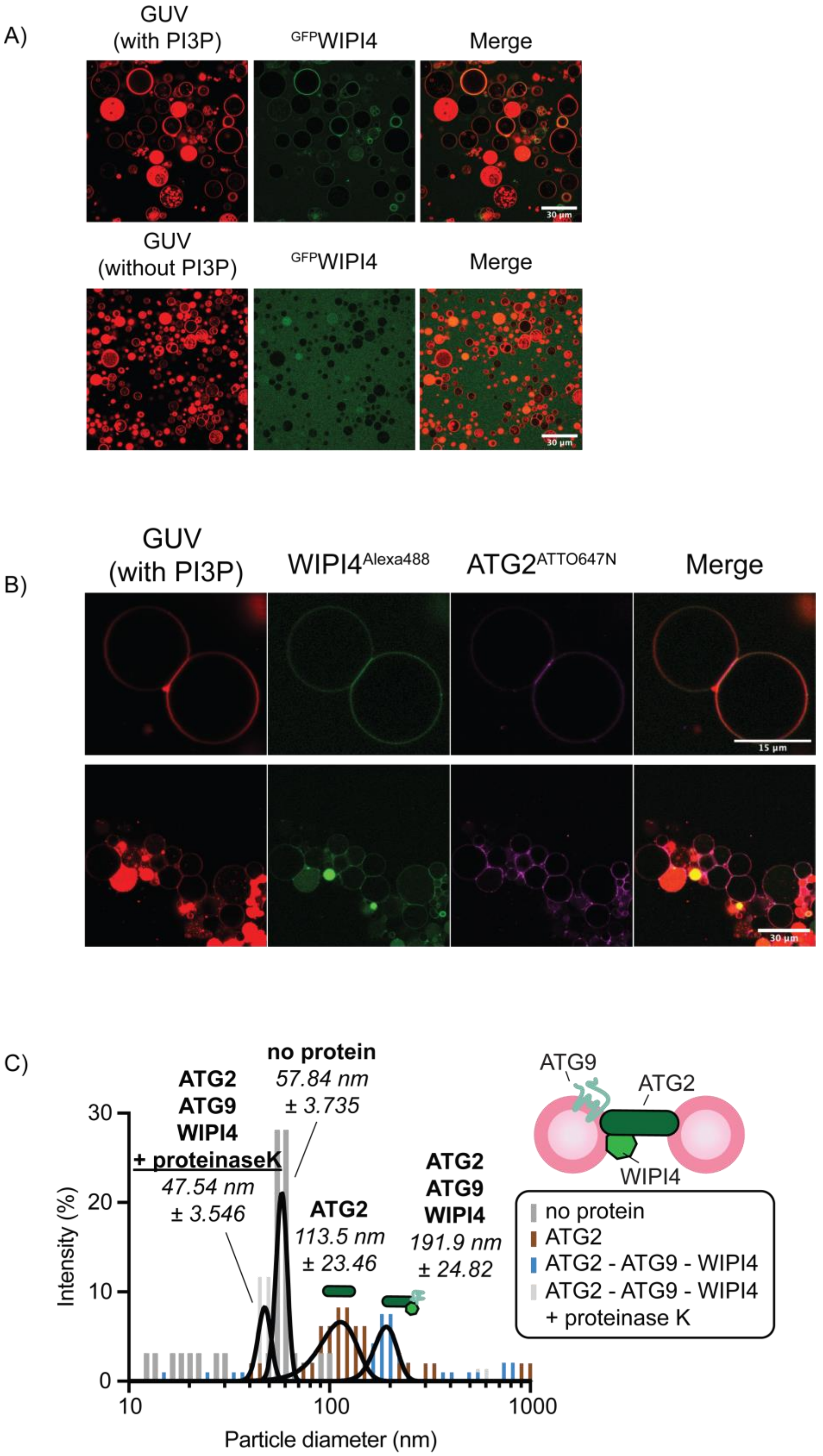
A)
GUV
(with PI3P)
GFPWIPI4
Merge
30 µm
GUV
(without PI3P)
GFPWIPI4
Merge
30 µm
B)
GUV
(with PI3P)
WIPI4Alexa488
ATG2ATTO647N
Merge
15 µm
30 µm
C)
ATG2
ATG9
WIPI4
+ proteinaseK
47.54 nm
± 3.546
no protein
57.84 nm
± 3.735
ATG2
113.5 nm
± 23.46
ATG2
ATG9
WIPI4
191.9 nm
± 24.82
Intensity (%)
0
10
20
30
10
100
1000
Particle diameter (nm)
ATG9
ATG2
WIPI4
no protein
ATG2
ATG2 - ATG9 - WIPI4
ATG2 - ATG9 - WIPI4
+ proteinase K

Figure 3.19. Cooperative tethering at MCS *in vitro*. A) Representative confocal images showing ^{GFP}WIPI4 (200 nM; green) bound to Rh-GUVs (red) in a PI3P-dependent manner. Top panel: WIPI4 bound to PI3P-containing Rh-GUVs; bottom panel: WIPI4 did not bind to PI3P-free Rh-GUVs. Scale bar: 30 µM. B) Alexa488-labeled WIPI4 (200 nM; green) and ATTO647N-labeled ATG2 (200 nM; purple) cooperate to tether Rh-GUVs (red) and form an extensive membrane contact site between two PI3P-containing Rh-GUVs. Representative images show the tethering of two (top panel) or a cluster of GUVs (bottom panel). Scale bar: 15 µM (top panel); Scale bar: 30 µM (bottom panel). C) DLS profiles showing size distribution of LUVs in the presence of ATG2 (brown); ATG2, ATG9, and WIPI4 (blue); no protein (dark gray); or ATG2, ATG9, and WIPI4 after incubation with Proteinase K (dark gray). Tethering activities are indicated by a shift to larger size in the presence of the indicated protein. A shift to smaller size in proteinase K treatment indicates tethering activities are protein-induced and not caused by vesicle fusion. Experiments were done in collaboration with P.Hosnani and B.Knotkova (BZH).

3.3.2. Cooperative lipid transfer at the MCS

During the course of this project, several groups have shown that ATG2 and ATG9 are lipid transfer and scramblase proteins, respectively (Section 1.2.3 and Section 1.3.2). ATG9-mediated scramblase activity is proposed to facilitate lipid transfer efficiency by evenly distributing phospholipids between the two leaflets of the lipid bilayer membrane. In addition, ATG9-containing vesicles may also serve as the autophagosome's seed membrane because ATG2 can only transfer lipid between two existing membranes (the ER and the nascent autophagosome). Since we observed the interaction between human ATG2 and ATG9 (Section 3.2.1) and their cooperative roles in liposome tethering (3.3.1), I decided to include ATG9 in the lipid transfer assay to see if it affects ATG2's lipid transfer efficiency.

First, purified ATG9 needs to be reconstituted into liposomes (also called large unilamellar vesicles, or LUVs) as described in Section 2.9. LUVs are first treated with sufficient detergent so that they swell but do not disintegrate (Section 2.9). ATG9 is then added to the swelling LUVs in the form of protein-detergent micelles, which could integrate into the LUVs and become proteoliposomes (PLs) upon detergent removal. Successful reconstitution was verified by a flotation assay, as described in Section 2.15. In brief, reconstituted PLs were applied to the bottom of a Nycodez step gradient. The gradient was then subjected to ultracentrifugation so that PLs with lower density compared to Nycodez would migrate to the top of the gradient. The gradient was subsequently fractionated into six equal fractions from top to bottom. The fractions are analyzed by SDS-PAGE to identify the presence of PLs (Figure 3.20 A). The protein bands were found in the top three fractions, indicating proper reconstitution of ATG9 in liposomes (Figure 3.20 B). The reconstituted protein also needs to orient properly in the liposome to perform its function. To determine the proper orientation of the protein in the liposome, ^{MBP}ATG9 was first reconstituted into liposomes. The orientation of ^{MBP}ATG9 in liposomes was then tested using a protease protection assay, in which ^{MBP}ATG9 was incubated with PreScission protease. Because the cleavage site is on the (N-terminal) cytosolic facing side of the protein, if the protein is properly oriented, the tag will be removed by the PreScission protease. Conversely, the tag will not be cut if the cleavage site is protected inside the liposome. In the presence of detergent (DDM), the liposome is disrupted, and thus all tags would be cleaved. As shown in Figure 3.20 C, most of the MBP tags were cleaved as compared to complete cleavage of the tag in the presence of DDM, indicating that most of the proteins are properly oriented in PLs.

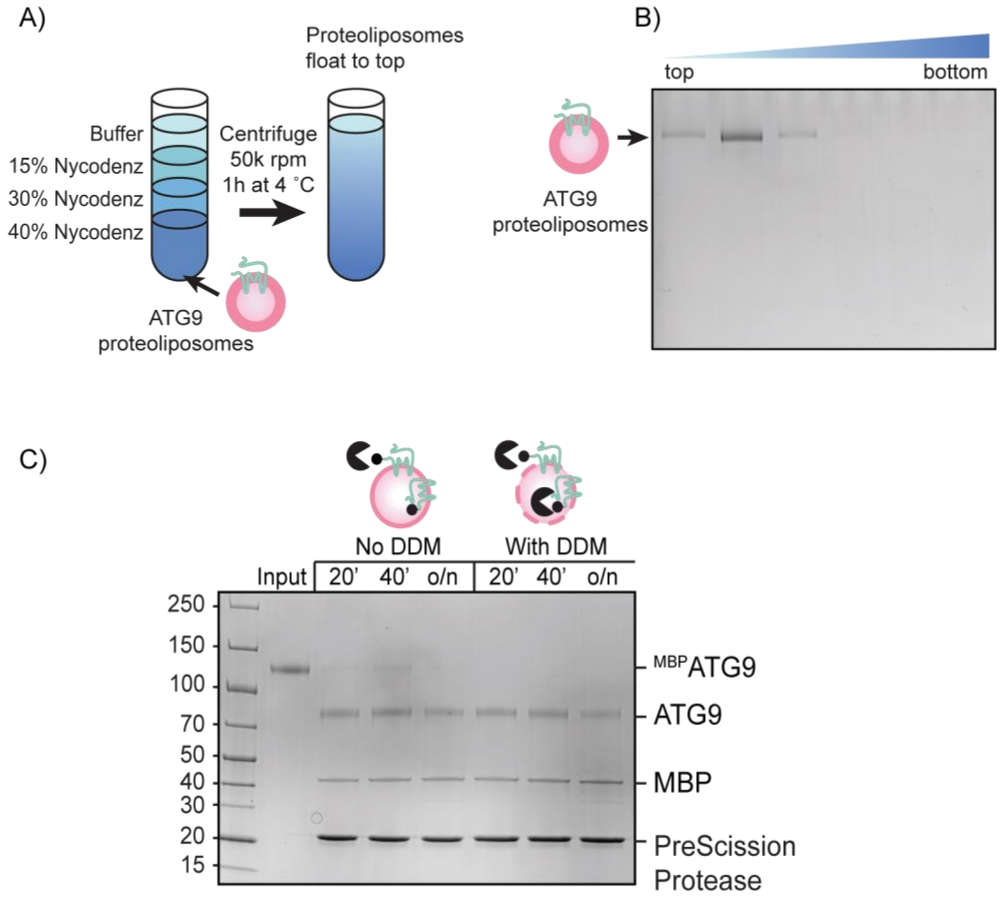

Figure 3.20. ATG9 reconstitution and orientation. A) Schematic of a flotation assay. B) LUVs reconstituted with ATG9 were subjected to a Nycodenz step gradient. After ultracentrifugation, the gradient was fractionated and analyzed by SDS-PAGE. ATG9 proteoliposomes were only found in the top fractions, indicating successful reconstitution. C) Protease protection assay of ^{MBP}ATG9 proteoliposome showed almost complete cleavage of the N-terminal MBP tag of the protein compared to the control in the presence of DDM, indicating that the N-terminal cleavage site of ATG9 was oriented correctly after reconstitution.

Next, I tested the scramblase activity of ATG9 using the fluorescence-based scramblase assay as described in Section 2.19. The principle of scramblase assay is illustrated in Figure 3.21 A. In brief, liposomes containing NBD-PE were prepared. When dithionite ($S_2O_4^{2-}$), a membrane-impermeable quencher, was added, it quenched all of the NBD-PE on the liposome's outer leaflet. This resulted in a 50% reduction of fluorescent signal in the control sample since there was no scrambling of lipids between the two leaflets and fluorescent signals on the inner leaflet were protected from dithionite. Upon reconstitution with ATG9, the addition of dithionite resulted in a total loss of fluorescence (Figure 3.21 C), indicating scramblase activity of ATG9.

Along with the scramblase assay, leakiness control was performed to ensure the quenching effects observed in the scramblase assay were not due to dithionite leaking to the luminal side of the liposomes. A schematic illustration of the leakiness control is shown in Figure 3.21 B. In brief, liposomes and PLs were reconstituted in buffers containing NDB-glucose. Extra vesicular NDB-glucose was then removed by dialysis. Encapsulated NDB-glucose is protected from dithionite if the vesicles are not leaky to dithionite. Conversely, if dithionite gets inside the vesicles, all fluorescent signals of NDB-glucose are quenched. As shown in Figure 3.21 C, addition of dithionite to both liposomes and PLs only slightly decreased the fluorescence, indicating that the vesicles are not leaky to dithionite. These results are consistent with observations from Ghanbarpour et al. (2021).

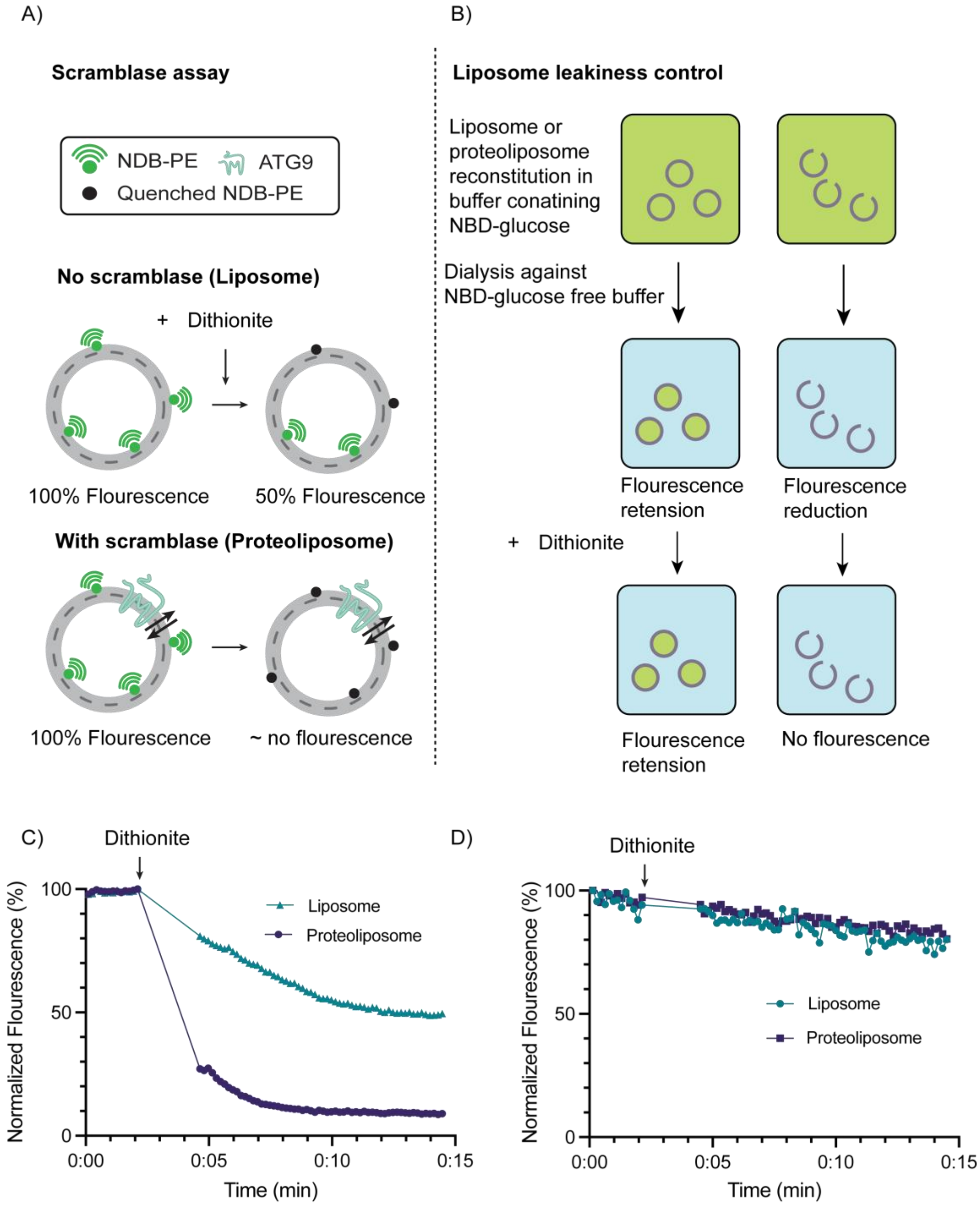

Figure 3.21. ATG9 has scramblase activity. A) A schematic illustration of a scramblase assay. B) A schematic illustration of a leakiness control. C) Scramblase assay showing ATG9 scramblase activity. D) Leakiness control showing that ATG9 proteoliposomes were not leaking. Proteoliposome and protein-free liposome went through the same reconstitution process.

After successfully demonstrating the scramblase function of ATG9, we included ATG9 in the FRET-based lipid transfer assay to test the putative the effects of ATG9 on the lipid transfer activity of ATG2-WIPI4. A schematic illustration of the lipid transfer assay is shown in Figure 3.22 A. In this assay, donor liposomes are prepared with a sufficient concentration of FRET-paired fluorescent lipids (NDB-PE and Rhod-PE) so that NDB-PE fluorescence is quenched by Rhod-PE due to their proximity, while acceptor liposomes are made without fluorescent dye. When lipid transfer proteins are added to a solution containing donor and acceptor liposomes, the lipids may exchange, resulting in dilution and dequenching of NBD flourescence. Hence, the increase in NBD fluorescence can be attributed to lipid transfer activity. In cells, scramblase proteins are present in both the ER (donor membrane) and the phagophore (acceptor membrane) (Ghanbarpour et al., 2021). However, I could not include the two ER-resident scramblases, TMEM41B and VMP1, as their scramblase functions and interactions with ATG2 were reported at a late stage of this project. Therefore, ATG9 was added to both donor and acceptor liposomes to substitute for the two missing scramblases in our experiments. Figure 3.22 B, the addition of ATG9 can increase lipid transfer efficiency by roughly three times compared to that of ATG2 (with k_{obs} of 0.15 h^{-1} and 0.4 h^{-1}, respectively). Adding both ATG9 and WIPI4 further increase the lipid transfer efficiency of ATG2 (with k_{obs} of 0.15 h^{-1} and 0.65 h^{-1}, respectively). In the control, no fluorescence increase is observed in the absence of ATG2. These results show that the scramblase activity of ATG9 can enhance ATG2-mediated lipid transfer, likely by equilibrating the lipid distribution of the tethered liposomes. Since I previously showed that ATG9 formed a complex with ATG13-ATG101, I decided to also test the effect of ATG13-ATG101 on lipid transfer. Surprisingly, the addition of ATG13-ATG101 can increase the lipid transfer efficiency by almost 8 times compared to that of ATG2-ATG9 (with k_{obs} of 1.57 h^{-1} and 0.2 h^{-1}, respectively). Since ATG13 and ATG101 are extensively crosslinked to ATG9 (Figure 3.15), they may likely modulate ATG9 scramblase activity and/or ATG9-ATG2 interaction.

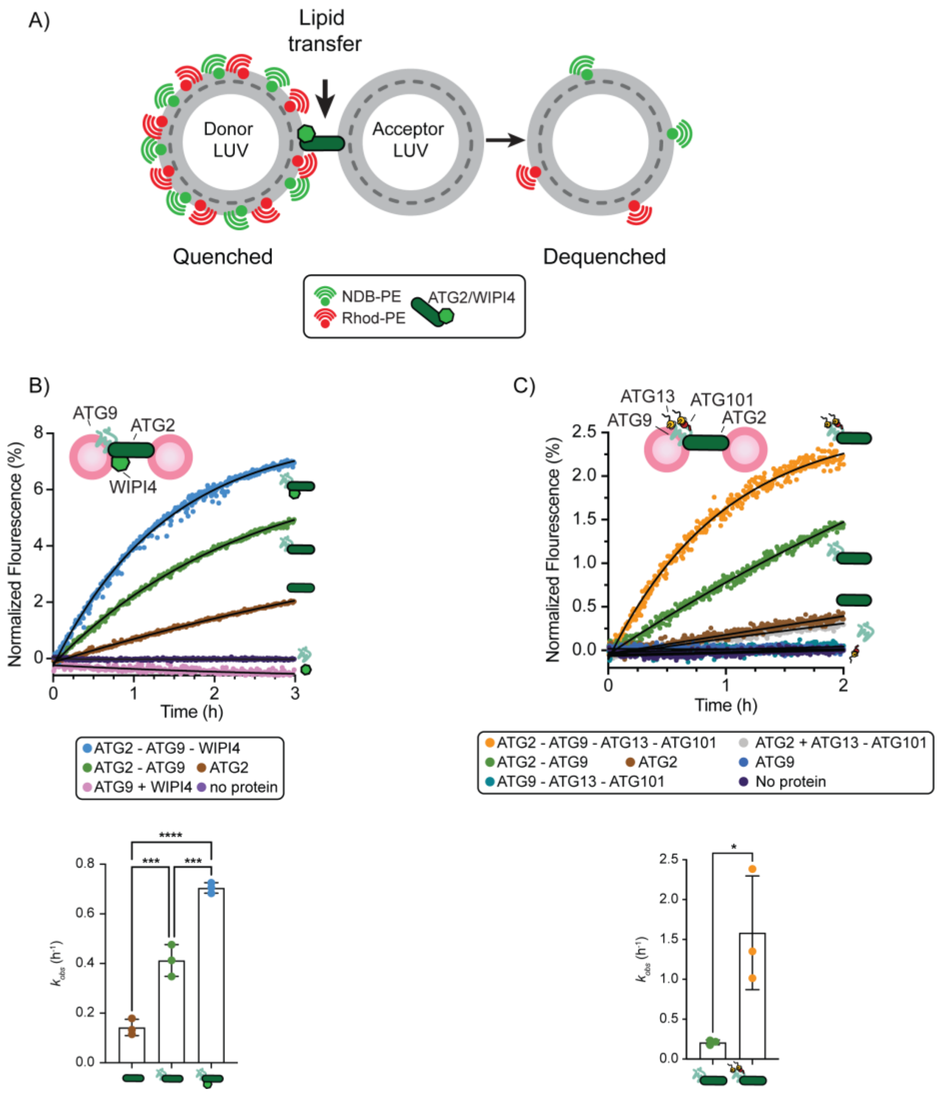

Figure 3.22. Cooperative lipid transfer at *in vitro* MCS. A) A schematic illustration of a FRET-based lipid transfer assay. B) FRET-based lipid transfer assay showing the effects of ATG9 and WIPI4 on the lipid transfer efficiency of ATG2. Concentrations of ATG2, ATG9 and WIPI4 are 33 nM, 100 nM, and 100 nM respectively. Statistical significance was determined by one-way ANOVA followed by Tukey's multiple comparisons test. ***, $P < 0.001$; ****, $P < 0.0001$. The experiments were performed at 25°C with 3 independent technical replicates. A representative dataset is shown. C) FRET-based lipid transfer assay showing the effects of ATG13^{HORMA}-ATG101 and ATG9 on lipid transfer efficiency of ATG2. Concentrations of ATG2, ATG9 and ATG13^{HORMA}-101 complex are 33 nM, 100 nM, and 100 nM respectively. Statistical significance was determined by two-tailed Student's t-test. *, $P \leq 0.05$. The experiments were performed at 25°C with 3 independent technical replicates. A representative dataset is shown. Experiments were done in collaboration with P.Hosnani (BZH). The experiment in C was done with the help of Çağla Alagöz (Research group of Signaling Dynamics, MPI-NAT).

4. Discussion

Research employing genetics and cell biology methods is incredibly effective in providing us insights into the sophisticated autophagy process. However, the complex cellular system makes it difficult to pinpoint the detailed molecular mechanism underlying a certain pathway. Biochemical reconstitution has been proven to be an effective complementary approach for studying the molecular mechanisms of isolated cellular pathways *in vitro*. In this thesis, I aimed to use this approach to understand how autophagy is initiated and how the phagophore expands. To understand how the autophagy initiation process is regulated, I purified the proteins of the core autophagy initiation machinery and investigated their assemblies. To understand factors contributing to the elongation of the phagophore, I used recombinant proteins and an artificial membrane to reconstitute a functional lipid transfer machinery that mimics the lipid transfer process occurring at the MCS between the ER and phagophore in cells. This section will highlight some key results and discuss them in relation to the cellular context, as well as provide some suggestions for further research concerning this topic.

4.1. Partnership between intermembrane and interleaftlet lipid transporter

The biogenesis of autophagosomes requires a large amount of lipid supply from various organelles in the cytosol. Direct connection, vesicular transport, and non-vesicular transport by lipid transfer protein (LTP) are the three pathways that have been proposed for the transfer of lipid from the ER to the phagophore/autophagosome (Figure 4.1) (Melia et al., 2020, Osawa and Noda, 2019). Meanwhile, the lipid composition of the autophagosome, as well as the contribution of each pathway to phagophore expansion have not been quantified.

In addition, it is worth noting that the phagophore is generated in a timely manner as an autophagic response and mostly lacks integral membrane proteins (Baba et al., 1995, Fengsrud et al., 2000). This is in contrast to other cellular membranes, such as the ER or mitochondria, which contain large numbers of integral membrane proteins. The low abundance of transmembrane proteins in the phagophore suggests a mechanism by which lipids are delivered quickly to the phagophore while incorporation of transmembrane proteins is kept to a minimum. Therefore, the direct transport and vesicular transport mechanisms would require a protein-poor vesicle and/or a mechanism for the exclusion of integral membrane proteins present in the source organelles, e.g., the ER. However, such mechanisms have not been reported for autophagy. Meanwhile, the mechanism based on non-vesicular transport can explain the unique characteristics of the autophagosome and might largely contribute to phagophore expansion. In this mode of lipid transport, lipid transfer proteins (LTPs) localize to the MCS between the donor and acceptor membranes and facilitate the lipid transfer between the membranes, while transmembrane proteins are excluded from the process. Most LTPs also act as tethers by forming a bridge between two participating membranes (Holthuis and Menon, 2014, Lahiri et al., 2015). In autophagy, ATG2/Atg2 was initially identified as a tether (Chowdhury et al., 2018, Kotani et al., 2018). Thus, it might also act as a lipid transfer protein. This function was later proven by several groups structurally and biochemically (Maeda et al., 2019, Otomo and Maeda, 2019, Valverde et al., 2019, Osawa et al., 2019), which is a breakthrough in our understanding of how phagophore elongates. As mentioned previously, the lipid transfer activity of ATG2/Atg2 explains why the phagophore does not contain ER’s transmembrane proteins and remains associated with the organelle during its expansion (Yamamoto et al., 1990, Graef et al., 2013, Suzuki et al., 2013, Melia et al., 2020, Osawa and Noda, 2019) (Figure 4.1 right). Furthermore, it explains why the ER-staining lypohilic dye also stained the phagophore (Hirata et al., 2017), which is most likely due to the Atg2-mediated transfer of stained lipids from the ER to the phagophore. In addition, lipid transfer and tethering activities of ATG2 are shown to be enhanced by its adaptor protein, WIPI4 *in vitro.* Chowdhury et al. (2018) demonstrated that ATG2 is a weak tether, but the addition of WIPI4 could significantly increase ATG2-mediated tethering of PI3P-positive liposomes, which could be explained by ATG2's increased affinity to the liposome because WIPI4 simultaneously binds to PI3P moieties on the membrane and ATG2, thus anchoring the ATG2 to the membrane. Similar observations were reported for the yeast Atg2-Atg18 complex (Osawa et al., 2019). Maeda et al. (2019) later confirmed WIPI4's enhancing effect on ATG2 tethering activity and demonstrated that it leads to increased ATG2 lipid transfer efficiency. We also observed a similar effect by visualizing the tethering by ATG2-WIPI4 under confocal microscopy (Figure 3.19) and measuring lipid transfer using the lipid transfer assay (Figure 3.22 B).

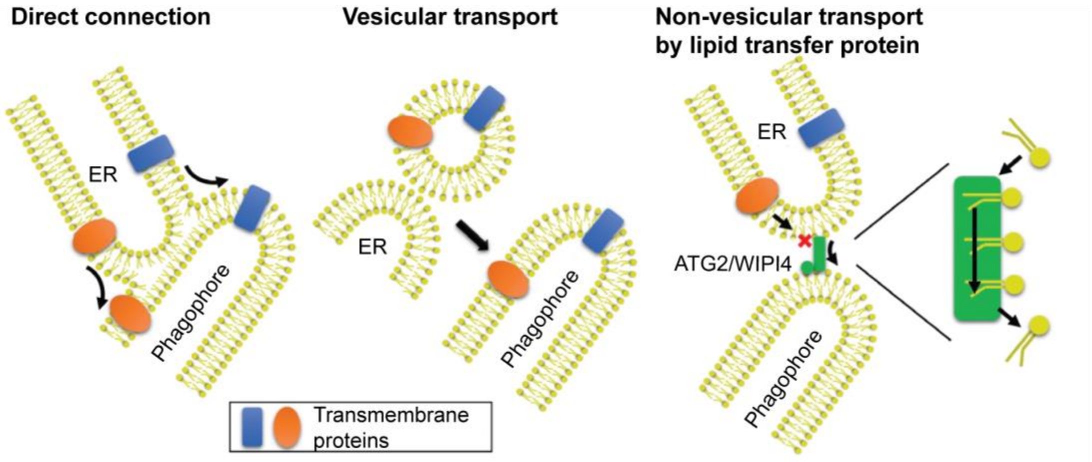

Figure 4.1. Three proposed modes of lipid transfer from the ER to the phagophore. Left: Lipid transport via direct connection between the ER and Phagophore. Middle: Lipid transport via fusion of vesicle originated from the ER with the Phagophore. Right: Non-vesicular lipid transport from the ER to the phagophore by the lipid transfer complex ATG2-WIPI4. Among these models, non-vesicular lipid transport by the lipid transfer complex can transfer lipids while excluding transmembrane proteins, which are abundant in the soure organelles. Figure adapted from Osawa and Noda (2019).

Lipid transfer by the ATG2-WIPI4 complex, however, still presents a problem since ATG2 can only transfer lipids between the cytoplasmic leaflets of the tethered membranes because it is not an integral membrane protein. An additional factor capable of equilibrating lipid between two leaflets of a lipid-bilayer membrane is therefore needed. ATG9 has been proposed as a candidate for the role since it was recently shown to have scramblase activity (Matoba et al., 2020, Maeda et al., 2020). Moreover, ATG2-ATG9 interaction has been shown by co-IP (Tang et al., 2019, Ghanbarpour et al., 2021). Here, we confirmed the interaction using recombinant proteins (Section 3.2.1). We also validated the proposed cooperative activities of ATG2 and ATG9 using the lipid transfer assay, which shows that ATG9 activity can enhance the lipid transfer efficiency of ATG2 by roughly three times (Figure 3.22 B). The enhancement could be attributed to better anchoring of ATG2 to the membrane via its interaction with ATG9, coupled with the scramblase activity of ATG9, which subsequently equilibrates incoming lipids between the two leaflets. It is also worth noting that ATG2's functional homolog, VPS13, interacts with two scramblases, Mcp1 and XK, on the mitochondrial and plasma membranes, respectively (Park et al., 2022, Guillén-Samander et al., 2022, Adlakha et al., 2022). This implies the importance of coupling lipid transfer and scramblase activity for lipid transfer efficiency at different MCSs. Although the physical interaction between lipid transfer and scramblase proteins is not obligatory since they can function independently of each other, this scramblase-transporter complex may have some advantages. For example, by destabilizing the lipid bilayer organization, scramblase protein might reduce the energetic barrier required for the extraction of lipids in the source membrane and the insertion of lipids in the receiving membrane. Indeed, ATG9 has been proposed to promote membrane curvature, which results in lipid packing defects (Guardia et al., 2020, Bigay and Antonny, 2012), while ATG2 preferably binds to high-curvature membranes (Maeda et al., 2019, Chowdhury et al., 2018). In addition, a direct connection between scramblase and lipid transfer proteins may create a continuous hydrophobic cavity for the movement of lipids between opposing membranes. Confirming these hypotheses requires more structural insights into the ATG2-ATG9 complex and detailed characterization of ATG9 and ATG2 mutants that are impaired in protein-protein interaction capabilities. For example, whether these ATG2 and ATG9 binding defect mutants can deliver the same lipid transfer efficiency as the wild type could be examined. Although the high-resolution structure of the complex has not yet been achieved, recent work by van Vliet et al. (2022) reveals some interesting structural insights into the complex. Using mutagenesis coupled with peptide arrays, the authors identified approximate binding regions between ATG2 and ATG9, which span residues 1,760–1,779 at the C-terminal of ATG2 (DS2) and residues 233-252 at the core domains of ATG9 (DC22). The deletion of DS2 and DC22 reduced ATG2-ATG9 interaction by 70% and 50%, respectively. Furthermore, it was shown that the ATG9 DC22 mutant was unable to restore autophagic flux in the *ATG9* KO cell line, most likely due to the impaired ATG2-ATG9 interaction. These mutants could thus be used in the lipid transfer assay to gain more insights into the functional relevance of the ATG2-ATG9 interaction *in vitro.* Based on their experimental data and Alphafold2 prediction, van Vliet et al. (2022) also built a predictive model of the ATG2-ATG9 complex (Figure 4.2). The model shows that ATG2 directly interacts with the core domain of ATG9 at the perpendicular branch formed by the interface of ATG9’s protomers. This is consistent with our preliminary data that one ATG2 monomer interacts with one ATG9 trimer (Figure 3.14). The structure also depicts a continuous hydrophobic cavity from ATG2 to ATG9, which might act as a sliding tube for lipid movement between membranes without exposing them to an aqueous phase. Solving the complex's holostructure with lipids would greatly aid our understanding of the exact molecular mechanism of lipid transfer modulated by the complex.

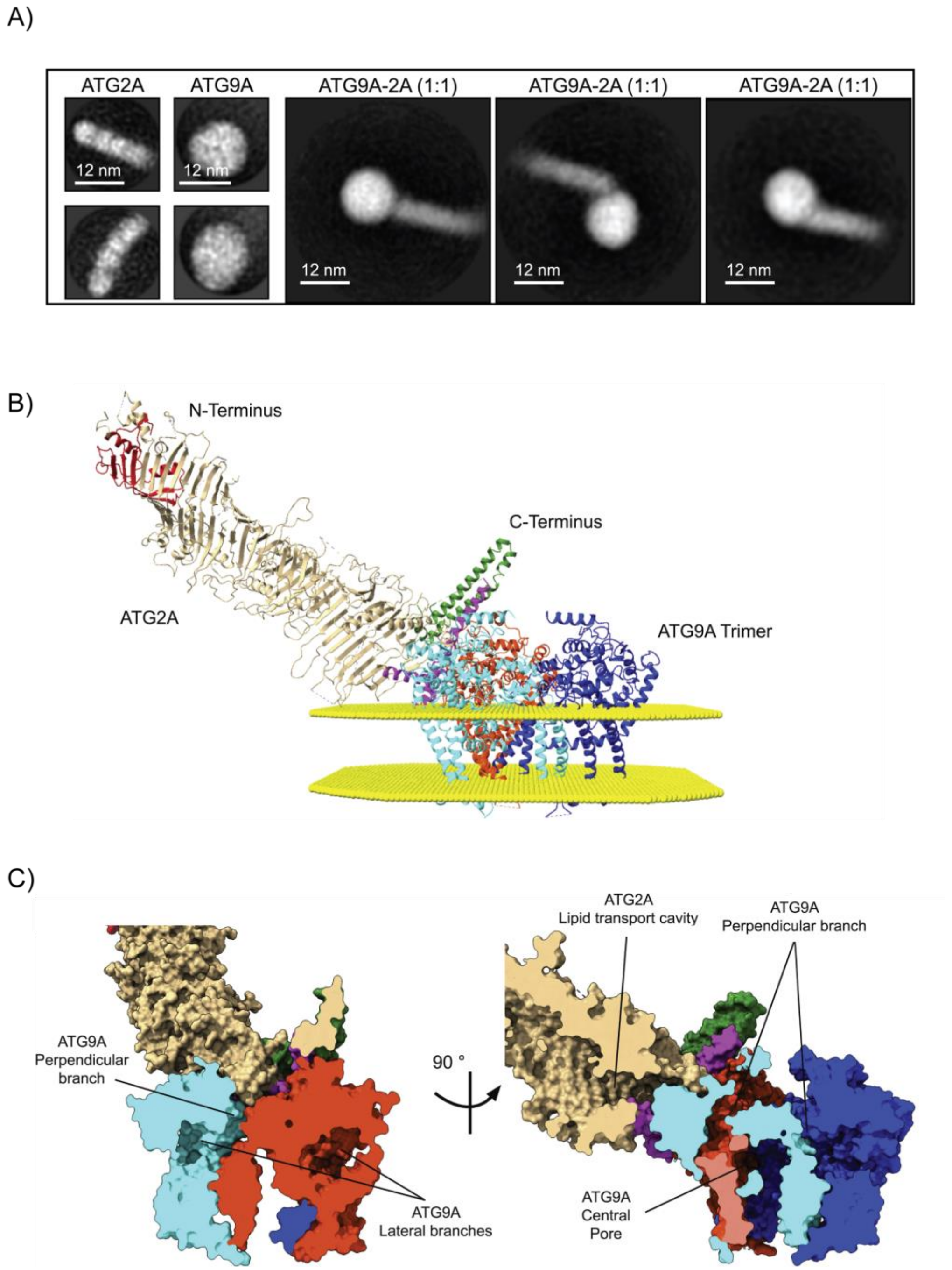

Figure 4.2. Model of ATG2-ATG9 complex. A) 2D class averages from negative stain EM images of the ATG9A, ATG2A, and ATG2A-ATG9A complex B) The predicted structures of the ATG2A-ATG9A complex: ATG2 (tan), ATG9 protomer (orange, cyan, and blue), the Chorein_N, CLR, and ATG_C domains of ATG2 are shown in red, magenta, and green, respectively. C) A vertical section of the complex isosurface showing the cavity of ATG2 and its proximity to the perpendicular branch of ATG9. Figure taken from van Vliet et al. (2022).

After showing that the ATG13-ATG101 complex also interacts directly with ATG9, we wondered whether it had any influence on the lipid transfer. Surprisingly, the addition of ATG13-ATG101 leads to a nearly eight-fold increase in lipid transfer efficiency, as shown in Figure 3.22 C. It is the first time that ATG13-ATG101 has been shown to affect the activity of other proteins. This finding may explain the fast dynamics of the autophagic response, in which the autophagosome needs to form in roughly 10 minutes. Meanwhile, the surprising effect of ATG13-ATG101 may be due to an enhanced scramble activity of ATG9 upon ATG13-ATG101 binding since ATG13-ATG101 is crosslinked to the core domain of ATG9 as shown in Figure 3.15. However, the effects of ATG13-ATG101 on ATG9 scramblase activity could not be shown using the scramblase assay because it is an endpoint assay that can only determine whether a protein has scramblase activity rather than the scrambling rate (Malvezzi et al., 2013, Lee et al., 2018, Malvezzi et al., 2018, Falzone and Accardi, 2020). Another possibility is that ATG13-ATG101 binding induces conformational changes in ATG2 and/or ATG9. These changes could enhance their lipid transporting activity or interactions with the membrane. Further structural investigations and characterization of the five-subunit complex ATG2-WIPI4-ATG9-ATG13-ATG101 might help us determine if these hypotheses are correct.

Another aspect that is typically overlooked is whether ATG2-mediated lipid transport follows the bridge model or the ferry model (Figure 4.3). In the bridge model, ATG2 serves as a bridge that binds to the ER at its N-terminal Chorein_N domain (N-tip), and to the phagophore at its CAD tip. The bridge (tube) is thus able to facilitate lipid movement through its internal cavity. In the ferry model, lipids are first loaded onto one end of the protein. Then, the protein dynamically swings to the other side, where lipids can be unloaded onto the recipient membrane. The tethering factor in this case could be nearby ATG2 molecules or other unidentified tethering factors at the ER-phagophore MCS. In both models, the protein is still anchored to the phagophore through binding at the CAD tip to its partners in the phagophore. However, in analogy to bridge and ferry transportation, the ferry model presents a slower transfer rate than the bridge model. Although we are in support of the bridge model, our current data cannot rule out the other possibility, which was implied in previous studies. For instance, Valverde et al. (2019) reported that the N tip of ATG2 alone (residue 1–345), consisting of the Chorein_N domain, is able to mediate lipid transfer between artificially tethered liposomes *in vitro*. Besides, 10-fold overexpression of this fragment can rescue autophagosome biogenesis deficiency in ATG2A/B double-KO cells. Similarly, Osawa et al. (2019) demonstrated that the N-terminal of yeast Atg2 (residues 21-240) can transfer lipids *in vitro*, albeit at a much lower activity than full-length Atg2. Since tethering between vesicles cannot be established when the CAD tip is removed, these findings imply that ATG2/Atg2 may act according to the ferry model, in which ATG2 dynamically swings between two membranes for lipid transportation (Figure 4.3). It should also be noted that in this model, the interaction of ATG2 with its partners (WIPI4 and ATG9) must be flexible enough to allow ATG2's dynamic movement. In fact, ATG2 has been shown to interact with WIPI3/WIPI4 at a 20-residue WIPI-interacting-region (WIR) motif of ATG2 (Chowdhury et al., 2018, Ren et al., 2020), whereas the ATG2-ATG9 interaction appears to be more rigid in the predicted model of van Vliet et al. (2022). Another argument against the ferry model is the recently identified interaction between the Chorein_N domain of ATG2 and two ER-resident proteins, TMEM41B and VMP1 (Ghanbarpour et al., 2021). The binding of ATG2 to its partners at both the ER and phagophore sides would restrict its movement, as suggested in the ferry model. Therefore, lipid transfer of the ATG2 N-terminal constructs could be re-evaluated in the presence of TMEM41B and VMP1 to determine whether the two models are mutually exclusive.

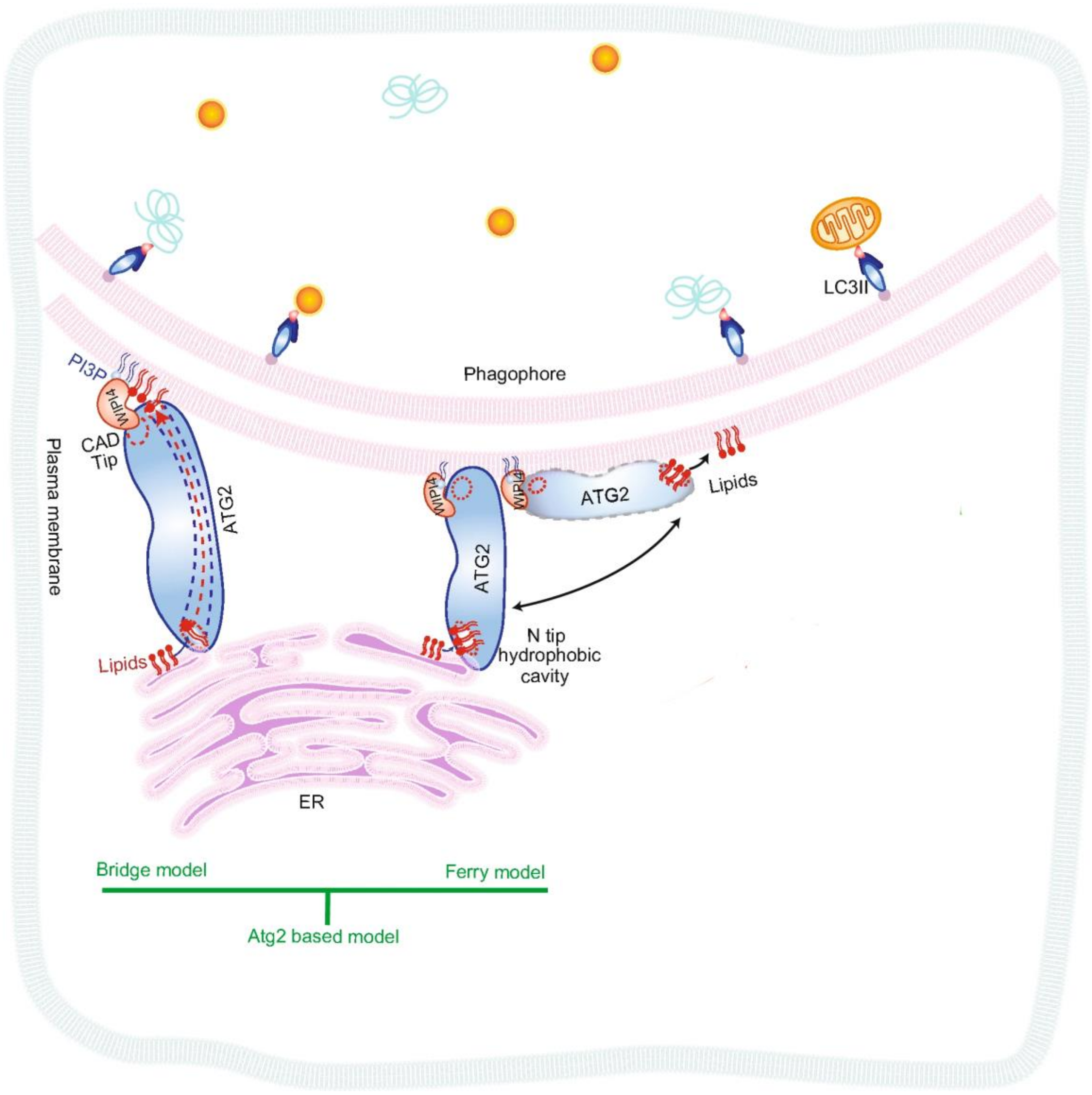

Figure 4.3. Two models of ATG2-mediated lipid transfer. In the bridge model (left), ATG2 is stable and tethered between the ER and phagophore, where lipids can be transferred through its hydrophobic cavity. In the ferry model (right), the proteins dynamically swing between the two membranes to pick up lipids from the ER and deliver them to the phagophore. Figure taken from Li et al. (2021a)

In summary, data obtained from this thesis has proven the partnership between the lipid transfer by ATG2-WIPI4 and the scramblase activity of ATG9 *in vitro*. In addition, we also see a surprising effect of the ATG13-ATG101 complex in enhancing lipid transfer efficiency. Although we cannot exclude the possibility that ATG2 may act as a ferry in lipid transfer, it is highly likely that the protein functions as a bridge between the ER and the phagophore since its binding partners are found on both membranes. If that is the case, we can validate the hypothesis stated in Figure 1.12 C and suggest a revised model that incorporates newly identified modulators, ATG13 and ATG101 (Figure 4.4). Compared to the cellular system, however, our model still requires some additional factors which will be discussed in the following section.

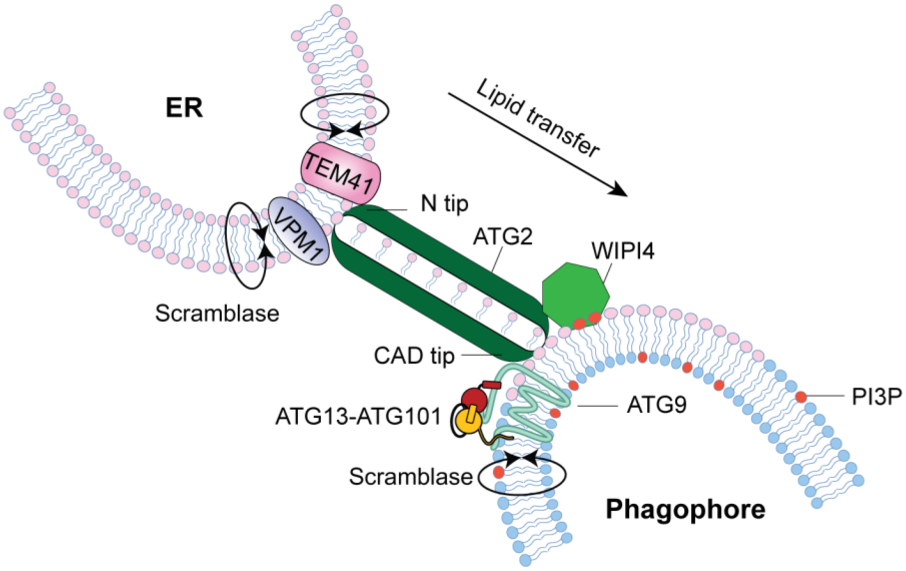

Figure 4.4. A model for partnership between intermembrane and interleaflet lipid transporters. Our data has demonstrated the cooperative functions of ATG9, ATG13, and ATG101 in enhancing the lipid transfer efficiency of the lipid transfer unit ATG2-WIPI4.

4.2. Lipid transfer in cells vs. in the reconstituted system

Consistent with previous observations, our experiments showed that both ATG9 and ATG2 can exert their inter-leaflet and inter-membrane lipid transfer activities in a bidirectional manner independent of energy consumption. This raises a very important question about what other factor(s) and mechanism(s) might be needed to support net lipid transfer into the phagophore. The factor(s) can be associated protein partners, lipid properties, membrane composition, or ATP hydrolysis. Currently, there are five types of directional transport mechanisms that have been reported for other membrane proteins, including lipid consumption, domain formation, ATP-driven, counter exchange, and local lipid synthesis at MCSs (reviewed in Reinisch and Prinz (2021)). Some examples of these mechanisms are illustrated in Figure 4.5. Firstly, unidirectional transfer can be achieved by enzymatically altering lipid molecules when they arrive in the recipient membrane. For instance, ceramide is converted into sphingomyelin (Figure 4.5 A). In another case, lipid molecules become clustered in the recipient membrane (Figure 4.5 B). These two mechanisms rely on changes in the characteristics of lipid molecules to prevent them from returning to the donor membrane. Besides, local lipid synthesis can also be a driving factor for directional transfer (Figure 4.5 C). One example is the lipid transfer at the ER-mitochondria MCS in budding yeast, where local PS synthesis on the ER membrane drives transport of newly synthesized PS to the mitochondria. Directional transport is also possible with the consumption of ATP. As shown in Figure 4.5 D, the trigalactosyldiacylglycerol complex in *Arabidopsis thaliana* uses energy from ATP hydrolysis for the transfer of lipid from the ER to the chloroplast. Besides, mechanisms by which LTPs can transport two different types of lipids in opposite directions have been reported (Figure 4.5 E). A well-known example is OSBP protein, which can counter-exchange ER-derived sterols for PI4Ps in the Golgi. Once PI4Ps arrive at the ER membrane, they are converted to PI by a lipid phosphatase (Sac1) to reduce their affinity for OSBP and allow OSBP to pick up another sterol molecule for the next cycle. Regarding ATG2/Atg2-mediated lipid transfer machinery, it is currently unknown whether the machinery can utilize one or more of these modes of directional regulation. Meanwhile, a recent study in budding yeast suggests that the machinery may employ local lipid synthesis mechanism that relies on concerted actions of proteins present in both the phagophore and the ER (Schütter et al., 2020) (Figure 4.6). In this study, the authors demonstrated that Faa1 (long-chain fatty-acid CoA ligase 1), a conserved Acyl-CoA synthetase, localizes to the nucleated phagophore and synthesizes acyl-CoA from CoA and free fatty acid. The acyl-CoA is then used as a substrate for the local synthesis of phospholipids by a PI synthase residing in the ER. The newly synthesized lipids can then be transported back to the phagophore through Atg2, where the direction of transport is thermodynamically driven by the local gradient of lipids at the MCS. Indeed, by tracking isotopically labeled fatty acids, the authors could show that the labeled fatty acids can be incorporated into phospholipids and channeled to the phagophore through Atg2. A similar mechanism has also been shown to drive lipid transfer at the ER–mitochondria MCS (Kannan et al., 2017). In the context of autophagy, energy consumption needs to be kept to a minimum as energy is limited due to starvation. This mechanism is thus well-suited since it allows phagophore expansion with minimal energy expenditure. Nevertheless, more insights about the involvement of other types of directional transport at the ER-phagophore MCS can be investigated. For example, we could use proximity labeling to see if an ATPase localizes to the MCS, and further explore its potential roles in directional transfer. In addition, by using radiolabeled or fluorescently labeled lipids to study the dynamics of the phagophore and ER membrane's composition during autophagosome formation, we could determine the modes of lipid transport that rely on modifications in membrane composition.

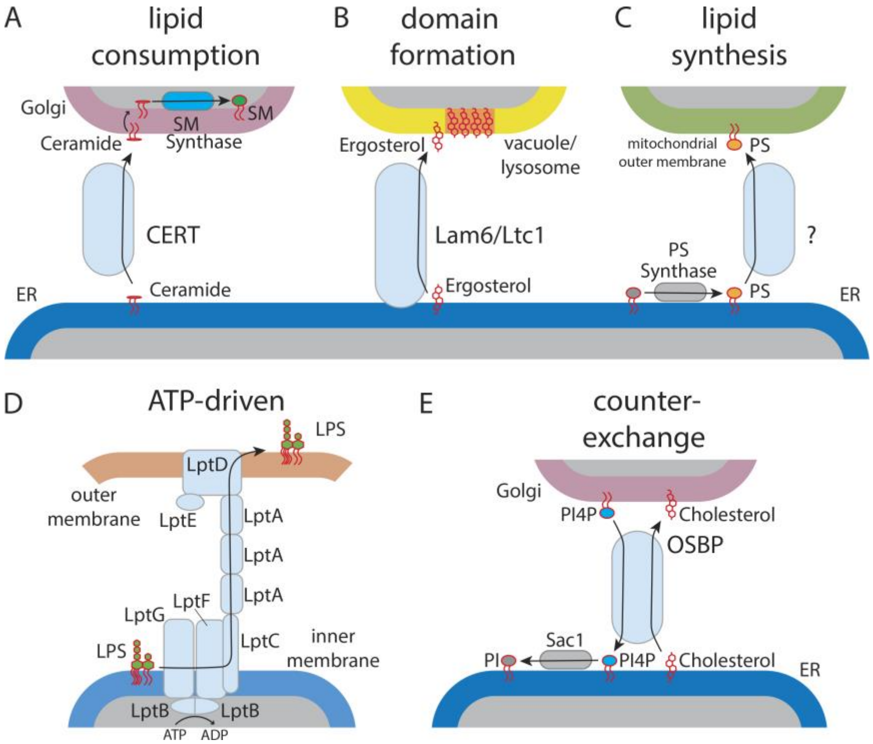

Figure 4.5. Examples of five modes of unidirectional lipid transport. A) Lipid transport driven by lipid consumption. Ceramide is transported by CERT from the ER to the Golgi, where it is converted to sphingomyelin (SM) by SM synthase and cannot be transported back to the ER. B) Lipid transport driven by lipid consumption domain formation. In *S. cerevisiae,* ergosterol is transferred by Lam6/Ltc1 from the donor organelle to the acceptor organelle, where it forms a membrane domain of ergosterol (red) and cannot be returned to the donor organelle. C) Lipid transport driven by lipid synthesis at the MCS. The production of PS at ER–mitochondria MCS in *S. cerevisiae* facilitates PS transport to the mitochondria. The required LTP has not been identified. D) Lipid transport driven by ATP consumption. Trigalactosyldiacylglycerol complex in *Arabidopsis thaliana* consumes ATP for lipid transport from the ER to chloroplasts. E) Lipid transport driven by counter-exchange. The difference in concentration of one type of lipid between two membranes is used to transport a second type of lipid. OSBP uses sterol concentration differences between the ER and the Golgi to counter-exchange for PI4P in the Golgi membrane. Figure taken from Reinisch and Prinz (2021).

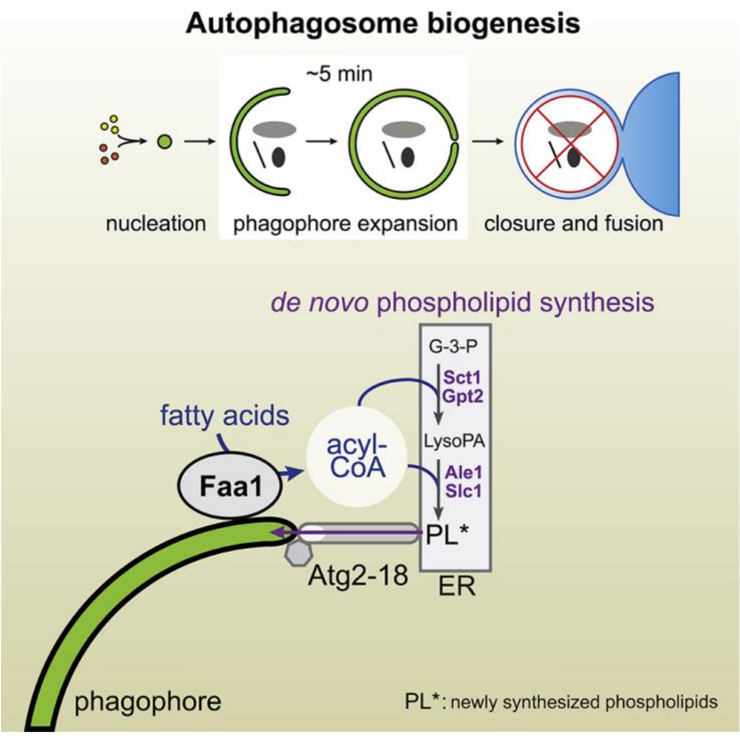

Figure 4.6. Model for unidirectional lipid transfer of Atg2. Fatty acyl-CoA synthetase (Faa1) localizes to the rim of the phagophore to convert fatty acid into acyl-CoA, a phospholipid precursor. Local PI-synthase in the ER synthesizes new phospholipids through several steps, which are then transported to the phagophore thanks to Atg2-Atg18. CoA, coenzyme a; G-3-P,

glycerol-3-phosphate; PA, phosphatidic acid, PL: Phospholipid. Figure taken from Schütter et al. (2020).

Besides the directional regulation, how the CAD tip of ATG2/Atg2 is specifically targeted to the phagophore is currently unknown. While the N-tip is specifically targeted to the ER membrane (lipid donor) via interactions with VMP1 and TMEM41B (Ghanbarpour et al., 2021), the CAD tip might bind to the phagophore (lipid recipient) via interactions with ATG9 and WIPI4. However, ATG9 is not only present in the autophagic membrane but is also ubiquitously present in various cellular organelles, e.g., the TGN or plasma membrane, as mentioned in Section 1.2.3. In addition, although WIPI4/Atg18 specifically binds PI3P, which is enriched in the phagophore, PI3P can also be found on various other membrane structures throughout the endosomal trafficking network (Schink et al., 2013). Furthermore, the significance of ATG2-WIPI4 interaction in cells is unclear, although it clearly results in increased tethering and lipid transfer, at least *in vitro*. Disruption of the ATG2-WIPI4 interaction does not impair autophagy flux (Bozic et al., 2020, Tang et al., 2019) and depletion of WIPI4 does not affect autophagosome maturation only when combined with depletion of WIPI3 (Ji et al., 2021). Meanwhile, the deletions of both WIPI3 and WIPI4 result in reduced autophagosome size, but the phenotype can be rescued by overexpression of ATG2, implying that WIPI3 and WIPI4 play a redundant role in ATG2-mediated lipid transfer/tethering but not in ATG2 specificity to the phagophore (Ji et al., 2021). Taken together, current observations indicate that ATG9 or WIPI4 may not allow specific association of ATG2 with the recipient membrane, thus other factors are required.

Interestingly, research by Bozic et al. (2020) suggests that LC3/GABARAP family proteins may play a role in this specific targeting. As mentioned in Section 1.2.6, LC3/GABARAP family proteins are conjugated to the PE lipid moiety on the phagophore membrane and remain associated with the membrane from early stages until autophagosome maturation. Several core autophagy proteins, including ATG2, also contain a conserved LIR motif that may allow direct interaction with LC3/GABARAP proteins. Indeed, the authors demonstrated that both isoforms of ATG2, ATG2A and ATG2B, interact with GABARAP but not LC3 through the LIR motif, suggesting a distinct role for this interaction in autophagy. Interestingly, the interaction is not mutually exclusive with the ATG2-WIPI4 interaction, which relies on the YFS motif that is located just 30 amino acids from the N-terminal of the LIR motif. The authors also showed that depletion of ATG2 isofoms in double knockout cell lines led to a blockage of autophagosome maturation. The wild-type phenotype could be rescued by ATG2, but not by the ATG2-LIR mutant that lost interaction with GABARAP. This implies that the interaction between ATG2 and GABARAP is essential for autophagy or ATG2 function. In addition, the ATG2-LIR mutant led to the accumulation of open and immature vesicles, suggesting that it might be essential for the proper expansion and closure of the autophagosome. Hence, the interaction could be a promising candidate for additional research regarding ATG2-specific targeting to the phagophore. Another potential candidate is ATG4, a cysteine protease. The dual roles of ATG4 are described in Section 1.2.6, which are to catalyze the C-terminal cleavage of LC3 prior to its conjugation and the de-lipidation of conjugated LC3 from the autophagic membrane. Recently, Nguyen et al. (2021) suggested that ATG4 interacts directly with ATG9 and is also involved in the regulation of ATG9 trafficking by an unknown mechanism. In addition, using a novel artificial intelligence (AI)-directed analysis technique for focused ion beam-scanning electron microscopy (FIB-SEM) imaging, the authors also showed that ATG4 promotes ER-phagophore contact and drives the expansion of the phagophore during the ATG2-mediated lipid transfer phase of autophagosome formation. Besides, as ATG4 is closely associated with LC3/GABARAP proteins for its canonical functions, it might be possible that these two proteins share a role in ATG2’s specific targeting to the phagophore. In brief, the two proposed factors, GABARAP and ATG4, are promising ones, but the list is not exhaustive since ATG2 may rely on multiple factors for its targeting to recipient membranes. Thus, research focusing on its CAD tip specificity and further interaction-based screening would provide better insights into ATG2's specificity for the phagophore.

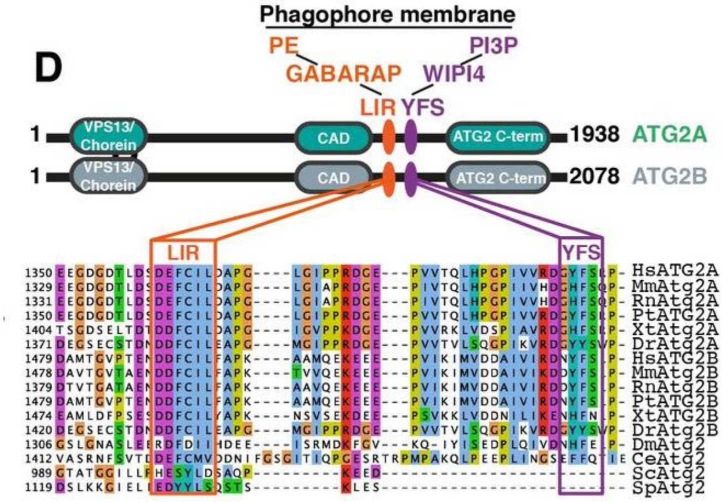

Figure 4.7. Domain structures of two ATG2 isoforms (ATG2A and ATG2B). The LIR motif (organge) for GABARAP interaction is located near the YFS motif (purple) for WIPI4 interaction. The multiple sequence alignment highlights the conservation of these regions. Figure taken from Bozic et al. (2020).

Like ATG2/Atg2 and other members of the bridge-like lipid transfer protein family, VPS13/Vps13 has been predicted to adopt a long rod-shape structure of approximately 300 Å, allowing it to tether and mediate lipid transfer at various MCSs in cells (Figure 4.8). VPS13 has four orthologs in mammals (VPS13A-D) and one in yeast (Vps13) (Lang et al., 2015). The mammalian VPS13A-D localize to ER-mitochondria, ER-lipid droplet, mitochondria-endosome, and ER-peroxisome MCSs (Figure 4.8), while yeast Vps13 localizes to nucleus-vacuole junctions, mitochondria-endosome, and vacuole-mitochondria patch (reviewed in Dziurdzik and Conibear (2021)). Interestingly, Dabrowski et al. (2022) suggested that Vps13 functions in parallel with Atg2 to deliver lipids from the ER to the phagophore. By using time-lapse fluorescence imaging to observe autophagosome biogenesis *in vivo*, the authors found that the duration and size of forming autophagosomes had a strong positive correlation with the number of Atg2 molecules in Vps13-depleted cells, but not in the wild-type cells. The findings suggest that although Vps13 is not essential for autophagy, the presence of Vps13 accelerates the rate of autophagosome formation to a level that is not limited by the number of Atg2 molecules. However, there are still some unknowns. For example, whether Vps13 functions as a tether, a lipid transporter, or both at the ER-phagophore MCS remains elusive. Besides, the lipid transfer function of Vps13, like that of Atg2, should be coupled with scramblase activity on both the ER and phagophore. Thus, Vps13 might directly or indirectly engage with known scramblase proteins at the site, such as Atg9 or other unidentified scramblase proteins dedicated to Vps13. These scramblases thus require further identification. Moreover, since Vps13 is known to function at other MCSs, the parallel activities of Vps13 and Atg2 at the same MCS raise the possibility for a mechanism in which cells can direct Vps13 to the ER-phagophore MCS during starvation. It is unclear whether this mechanism is mutually exclusive with the existing mechanisms that recruited Vps13 to other MCSs. Lastly, the mechanism employed for unidirectional lipid transfer of Vps13 at the ER-phagophore MCS should also be investigated.

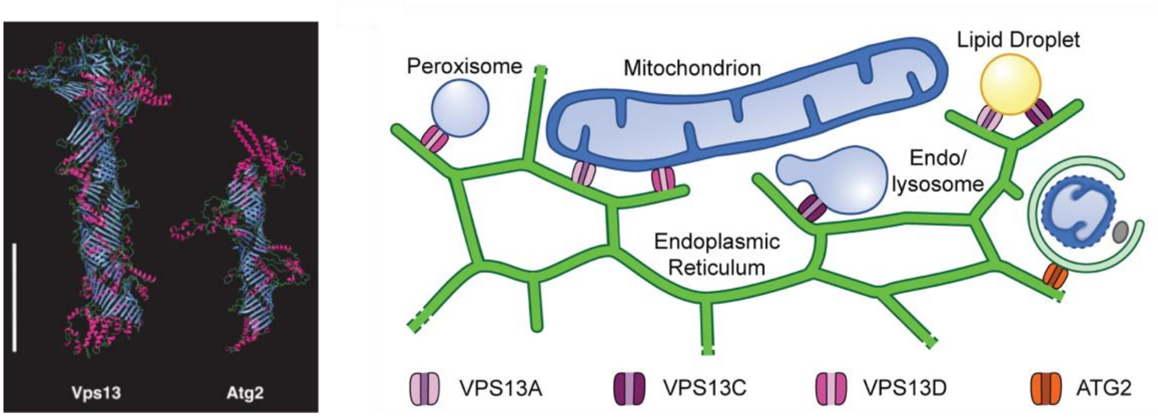

Figure 4.8. Similarities between bridge-like lipid transfer proteins VPS13/Vps13 and ATG2/Atg2. Left : Predicted structures of yeast Vps13 and Atg2 generated with RoseTTAFold. β-sheets (blue), α-helices (red), and coil (green). Bar = 100 Å. Figure taken from Toulmay et al. (2022). Right: Localization of VPS13 at various MCSs and localization of ATG2 at the ER-phagophore MCS. Figure taken from Leonzino et al. (2021).

4.3. Reconstitution of autophagy initiation super-complex

When autophagy is induced, three subcomplexes in the core autophagy initation machinery, including the ULK1 complex, PI3K-C1, and ATG9 are recruited to the inititation site in a hierarchical manner, as described in Section 1.2. Given that the ER is the primary lipid supply with close association with the phagophore and that ATG9-containing vesicles have been hypothesized as the autophagome's seeding membrane, we hypothesized that the three subcomplexes assemble at the MCS between the ER and ATG9-containing membrane to initiate autophagosome biogenesis. Indeed, I was able to reconstitute a seven-subunit super-complex comprising the ULK1 complex, ATG9, and two subunits of the PI3K-C1, ATG14L-BECN1. The remaining two subunits of the PI3K-C1, VPS34 and VPS15 are most likely also assembled into the super-complex to create a larger autophagy initiation super-complex. Interestingly, I found that the super-complex assembles on a core complex, consisting of the integral membrane protein ATG9 and two HORMA domain proteins, ATG13 and ATG101 (Figure 3.12). Besides, I also found that the core complex forms a five-subunit complex with the lipid transfer unit, consisting of ATG2 and WIPI4 (Figure 3.14). Formation of this complex allows tethering of ATG9-containing vesicles for subsequent lipid transfer between the vesicles, supporting the previous hypothesis that ATG9-containing vesicles are the seeding membrane of the autophagosome. Studies in yeast have shown that Atg9-containing vesicles are first recruited to the PAS via their interaction with the Atg1 complex, followed by the phosphatidylinositol 3-phosphate kinase complex, the lipid transfer complex and the Atg8 lipidation cascades (Suzuki et al., 2015b, Sawa-Makarska et al., 2020). These observations suggest that the autophagy initiation machinery assembles directly on Atg9-containg vesicles and subsequently induces its expansion into the phagophore via the recruitment of the lipid transfer unit. Similarly, a recent study by Olivas et al. (2022) demonstrated that ATG9-containing vesicles are the membrane from which mammalian phagophores form. Therefore, it is likely that the lipid transfer unit may also be incoporated into the super-complex through its interaction with the core complex. Overall, the results suggested that the core complex may function as an interaction hub for other functional subcomplexes at the MCS between the ER and the nucleated phagophore in cells. The resulting proximity of the supercomplex subunits allows them to locally modulate the functions of other subunits, implying inherent advantages of their spatial connections. Examples include ULK1 modulation of PI3K-C1 through protein-protein interactions and phosphorylation, as described in Section 1.2.4, or the coupling of scramblase and lipid transfer activity.

Regarding the assembly of the super-complex, we proposed that it self-assembles in cells in the absence of a regulated rate-limiting step. Meanwhile, autophagy should be tightly regulated to prevent premature initiation in basal conditions. As discussed in Section 1.4, we suspect that ATG13 and ATG101 may create a rate-limiting step in the assembly of their effector complexes. Indeed, the data presented in Section 3.2.2 has shown that the metamorphoses of ATG13 and ATG101 results in remarkably slow interactions of the proteins with ATG9. The slow interaction kinetics is attributed to the incredibly slow conversion of ATG13 and ATG101 from their default metamorphic states, which do not interact with the partner protein unless they switch to active metamorphic states. This follows the pattern observed in other HORMA domains, including MAD2 (Gu et al., 2022). MAD2 does not interact with CDC20 in its open state (O-MAD2) but does in its closed state (C-MAD2). The switching between states is slow (typically taking hours to days) unless catalyzed due to a significant activation energy required for the unfolding and refolding during metamorphosis. Overall, the data has shown that ATG13 and ATG101 metamorphoses dictate the kinetics of the core complex assembly, which can be summarized in a "hand-over model" (Figure 4.9). ATG13 (yellow) and ATG101 (red) are by default present in a conformer that allows them to bind each other instantaneously but requires a slow conformer switch to bind to ATG9 (Figure 4.9 A and B). Upon dimerization, they bind quickly to the C terminal of ATG9 ($ATG9^C$) (Figure 4.9 C, Step 1), where ATG13 can switch to another conformer that no longer interacts with ATG101 but can interact with the N terminal of ATG9 (ATG9^{N}). The protein is therefore “handed over” from the C-terminal to the N-terminal of ATG9 (Figure 4.9 C, Step 2). ATG101 can subsequently recruit another ATG13 to saturate the three protomers of ATG9, resulting in a 3:6:3 stoichiometric complex (Figure 4.9 C, Step 3).

The results give us the first fundamental piece of evidence that ATG13 and ATG101 are metamorphic proteins and that the formation of the core complex is a rate-limiting step in the assembly of the super-complex since the core complex serves as an interaction hub for the assembly of the super-complex. Furthermore, it is important to note that metamorphic conversions of the HORMA domains can be catalyzed in both directions, assembly or disassembly (De Antoni et al., 2005, Faesen et al., 2017, Gu et al., 2022). In cells, this implies the possibility of an on-demand acceleration of the assembly or disassembly of the autophagy initiation machinery by a regulatory mechanism that can dynamically control the metamorphic states of HORMA domains. Detailed characterization of such a mechanism requires identification of catalysts in cells, which could be achieved through a quantitative kinetic framework of ATG13 and ATG101 both *in vitro* and *in vivo*.

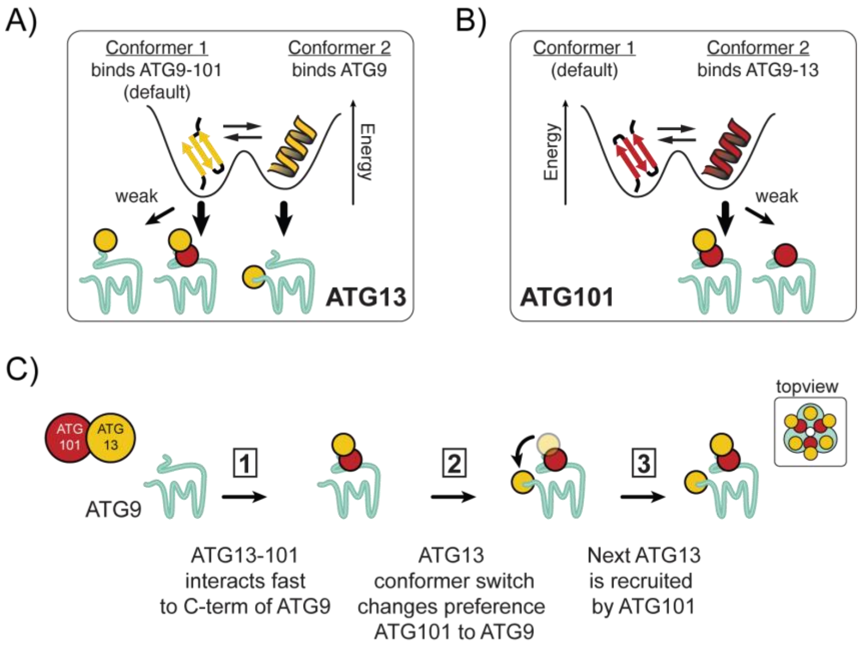

Figure 4.9. Proposed hand-over model for the assembly of ATG9-ATG13-ATG101 complex. Both ATG13 (A, yellow) and ATG101 (B, red) can adopt two conformers, each with an exclusive interaction spectrum. C) Hand-over model for the assembly of the ATG9-ATG13-ATG101 complex.

4.4. Summary and outlook

The goal of this thesis was to build a biochemically well-defined reconstitution system in which the dynamics and functions of the core autophagy proteins at the MCS between the ER and the phagophore could be studied. Up until now, I have shown the assembly of a 7-subunit super-complex, which is built on the core complex of ATG9-ATG13-ATG101 (Figure 4.10). This core complex serves three functions. Firstly, it serves as an obligatory rate-limiting step in the assembly of the super-complex due to the metamorphic behavior of ATG13 and ATG101. Secondly, it coordinates the coincidence of other functional subunits in supporting the initiation of autophagosome growth. Lastly, it interacts with and modulates the activity of the lipid transfer units, ATG2-WIPI4. Although progress has been made, many fundamental questions remain.

Regarding the assemblies of the super-complex at the ER-phagophore MCS, we have now identified the rate-limiting step created by ATG13 and

ATG101 metamorphoses. The next important step is to identify internal or external factor(s) that can accelerate the metamorphic conversion of the proteins and consequently regulate the assemblies of the MCS in space and time. The identification of these factor(s) as well as a mechanistic understanding of how the kinetic bottleneck created by ATG13 and ATG101 could be accelerated, would allow us to conditionally assemble or disassemble a functional MCS *in vitro*. The outcome of these studies is extremely valuable for the future development of novel therapies that take advantage of autophagy modulation. Investigations can start with detailed quantification of the interaction kinetics and thermodynamics of the reconstituted complexes. Then, those interactions can be investigated in the presence of potential factor(s). Since autophagy is regulated by various stress stimuli, the factor(s) could come from the signaling cascade that senses these stress stimuli or from a stress sensor within the complex, e.g., ULK1 kinase. The investigations would be a challenging yet rewarding task for the coming years.

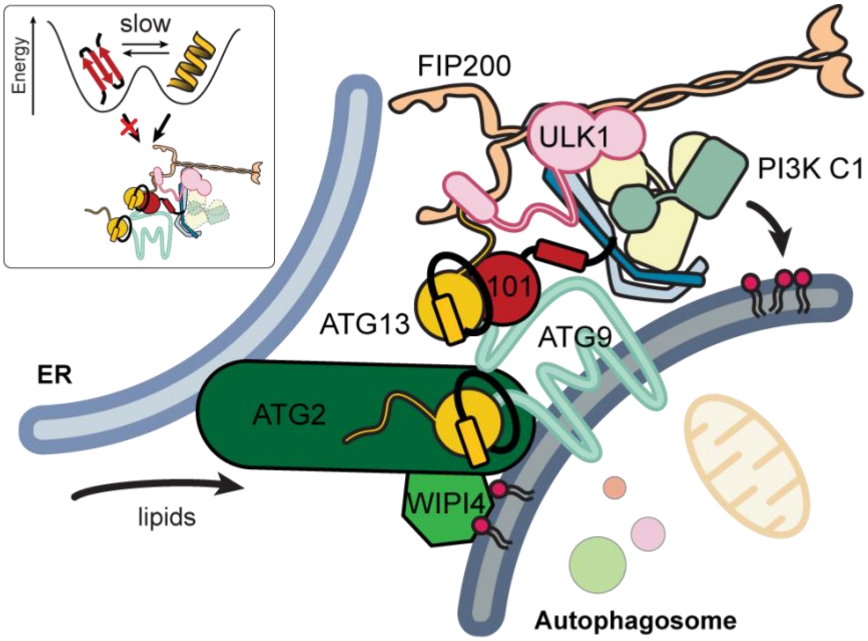

Figure 4.10. Model for complex assembly at the MCS. All functional subcomplexes converge to generate a defined super-complex. The slow conversion between distinct the metamorphic states of ATG13 and ATG101 leads to a slow assembly of the core complex (inset), which presents an onligatory intermediate step in the assembly of the super-complex.

Regarding lipid transfer activity at the MCS, it would be interesting to confirm whether the lipid transfer unit of ATG2-WIPI4 can be incorporated into the current 7-subunit super-complex and the functional consequences thereof. In case it stably incorporates into a larger complex, it would be interesting to see how the lipid transfer unit disassembles when the autophagosome reaches its maturation. Since ATG2-WIPI4 is also connected to the core complex, it may also disassemble with other subcomplexes once the core complex disassembles. Moreover, we must get more insights about the microenvironments at the MCS to build a better system recapitulating physiological conditions. Factors that regulate the directional transfer of ATG2 should be identified, and the mode of lipid transport by ATG2 should also be confirmed, as suggested in Section 4.2. Mechanistic and energetic details of protein factors that enhance lipid transfer efficiency, e.g., ATG13-ATG101 also require detailed characterization.

Mechanistic and functional studies of complexes at the MCS would also greatly benefit from structural insights. For example, a high-resolution structure of the core complex with the lipid transfer unit would provide unprecedented insights into how lipids can be transferred within protein cavities and how the lipid transfer rate can be modulated. Hence, the reconstituted contact site presented in this thesis may provide essential materials and attract future structural characterization of the human autophagy initiation machinery.

5. Reference

ADLAKHA, J., HONG, Z., LI, P. & REINISCH, K. M. 2022. Structural and biochemical insights into lipid transport by VPS13 proteins. *J Cell Biol,* 221.

AHLBERG, J. & GLAUMANN, H. 1985. Uptake microautophagy and degradation of exogenous proteins by isolated rat liver lysosomes. Effects of pH, ATP, and inhibitors of proteolysis. *Exp Mol Pathol,* 42**,** 78-88.

AHLBERG, J., MARZELLA, L. & GLAUMANN, H. 1982. Uptake and degradation of proteins by isolated rat liver lysosomes. Suggestion of a microautophagic pathway of proteolysis. *Lab Invest,* 47**,** 523-32.

AITA, V. M., LIANG, X. H., MURTY, V. V. V. S., PINCUS, D. L., YU, W., CAYANIS, E., KALACHIKOV, S., GILLIAM, T. C. & LEVINE, B. 1999. Cloning and Genomic Organization of Beclin 1, a Candidate Tumor Suppressor Gene on Chromosome 17q21. *Genomics,* 59**,** 59-65.

ALEMU, E. A., LAMARK, T., TORGERSEN, K. M., BIRGISDOTTIR, A. B., LARSEN, K. B., JAIN, A., OLSVIK, H., ØVERVATN, A., KIRKIN, V. & JOHANSEN, T. 2012. ATG8 family proteins act as scaffolds for assembly of the ULK complex: sequence requirements for LC3-interacting region (LIR) motifs. *J Biol Chem,* 287**,** 39275-90.

ALERS, S., WESSELBORG, S. & STORK, B. 2014. ATG13 Just a companion, or an executor of the autophagic program? *Autophagy,* 10**,** 944-956.

APPENZELLER-HERZOG, C. & HAURI, H.-P. 2006. The ER-Golgi intermediate compartment (ERGIC): in search of its identity and function. *Journal of Cell Science,* 119**,** 2173-2183.

ARSTILA, A. U. & TRUMP, B. F. 1968. Studies on cellular autophagocytosis. The formation of autophagic vacuoles in the liver after glucagon administration. *Am J Pathol,* 53**,** 687-733.

ASHFORD, T. P. & PORTER, K. R. 1962. Cytoplasmic components in hepatic cell lysosomes. *J Cell Biol,* 12**,** 198-202.

ASHRAFI, G. & SCHWARZ, T. L. 2013. The pathways of mitophagy for quality control and clearance of mitochondria. *Cell Death Differ,* 20**,** 31-42.

AXE, E. L., WALKER, S. A., MANIFAVA, M., CHANDRA, P., RODERICK, H. L., HABERMANN, A., GRIFFITHS, G. & KTISTAKIS, N. T. 2008. Autophagosome formation from membrane compartments enriched in phosphatidylinositol 3-phosphate and dynamically connected to the endoplasmic reticulum. *J Cell Biol,* 182**,** 685-701.

BABA, M., OSUMI, M. & OHSUMI, Y. 1995. Analysis of the membrane structures involved in autophagy in yeast by freeze-replica method. *Cell Struct Funct,* 20**,** 465-71.

BABA, M., TAKESHIGE, K., BABA, N. & OHSUMI, Y. 1994. Ultrastructural analysis of the autophagic process in yeast: detection of autophagosomes and their characterization. *J Cell Biol,* 124**,** 903-13.

BACKER, J. M. 2016. The intricate regulation and complex functions of the Class III phosphoinositide 3-kinase Vps34. *Biochem J,* 473**,** 2251-71.

BACKUES, S. K., ORBAN, D. P., BERNARD, A., SINGH, K., CAO, Y. & KLIONSKY, D. J. 2015. Atg23 and Atg27 Act at the Early Stages of Atg9 Trafficking in S. cerevisiae. *Traffic,* 16**,** 172-190.

BALLA, T. 2013. Phosphoinositides: tiny lipids with giant impact on cell regulation. *Physiol Rev,* 93**,** 1019-137.

BANDYOPADHYAY, U., KAUSHIK, S., VARTICOVSKI, L. & CUERVO, A. M. 2008. The chaperone-mediated autophagy receptor organizes in dynamic protein complexes at the lysosomal membrane. *Mol Cell Biol,* 28**,** 5747-63.

BARTH, H. G., JACKSON, C. & BOYES, B. E. 1994. Size Exclusion Chromatography. *Analytical Chemistry,* 66**,** 595-620.

BASKARAN, S., CARLSON, L. A., STJEPANOVIC, G., YOUNG, L. N., KIM, D. J., GROB, P., STANLEY, R. E., NOGALES, E. & HURLEY, J. H. 2014. Architecture and dynamics of the autophagic phosphatidylinositol 3-kinase complex. *Elife,* 3.

BASKARAN, S., RAGUSA, M. J., BOURA, E. & HURLEY, J. H. 2012. Two-site recognition of phosphatidylinositol 3-phosphate by PROPPINs in autophagy. *Mol Cell,* 47**,** 339-48.

BERGER, I., FITZGERALD, D. J. & RICHMOND, T. J. 2004. Baculovirus expression system for heterologous multiprotein complexes. *Nat Biotechnol,* 22**,** 1583-7.

BIGAY, J. & ANTONNY, B. 2012. Curvature, lipid packing, and electrostatics of membrane organelles: defining cellular territories in determining specificity. *Dev Cell,* 23**,** 886-95.

BOZIC, M., VAN DEN BEKEROM, L., MILNE, B. A., GOODMAN, N., ROBERSTON, L., PRESCOTT, A. R., MACARTNEY, T. J., DAWE, N. & MCEWAN, D. G. 2020. A conserved ATG2-GABARAP family interaction is critical for phagophore formation. *EMBO Rep,* 21**,** e48412.

BUSSE, R. A., SCACIOC, A., SCHALK, A. M., KRICK, R., THUMM, M. & KUHNEL, K. 2016. Analyzing Protein-Phosphoinositide Interactions with Liposome Flotation Assays. *Methods Mol Biol,* 1376**,** 155-62.

CAMPBELL, C. L. & THORSNESS, P. E. 1998. Escape of mitochondrial DNA to the nucleus in yme1 yeast is mediated by vacuolar-dependent turnover of abnormal mitochondrial compartments. *Journal of Cell Science,* 111**,** 2455-2464.

CHAN, E. Y., LONGATTI, A., MCKNIGHT, N. C. & TOOZE, S. A. 2009. Kinase-inactivated ULK proteins inhibit autophagy via their conserved C-terminal domains using an Atg13-independent mechanism. *Mol Cell Biol,* 29**,** 157-71.

CHANG, C. C., CHOW, C. C., TELLIER, L. C., VATTIKUTI, S., PURCELL, S. M. & LEE, J. J. 2015. Second-generation PLINK: rising to the challenge of larger and richer datasets. *Gigascience,* 4**,** 7.

CHAVEZ-DOMINGUEZ, R., PEREZ-MEDINA, M., LOPEZ-GONZALEZ, J. S., GALICIA-VELASCO, M. & AGUILAR-CAZARES, D. 2020. The Double-Edge Sword of Autophagy in Cancer: From Tumor Suppression to Pro-tumor Activity. *Front Oncol,* 10**,** 578418.

CHEN, S., WANG, C., YEO, S., LIANG, C. C., OKAMOTO, T., SUN, S., WEN, J. & GUAN, J. L. 2016. Distinct roles of autophagy-dependent and -independent functions of FIP200 revealed by generation and analysis of a mutant knock-in mouse model. *Genes Dev,* 30**,** 856-69.

CHEONG, H., LINDSTEN, T., WU, J. M., LU, C. & THOMPSON, C. B. 2011. Ammonia-induced autophagy is independent of ULK1/ULK2 kinases (vol 108, pg 11121, 2011). *Proceedings of the National Academy of Sciences of the United States of America,* 108**,** 17856-17856.

CHEONG, H., NAIR, U., GENG, J. F. & KLIONSKY, D. J. 2008. The Atg1 kinase complex is involved in the regulation of protein recruitment to initiate sequestering vesicle formation for nonspecific autophagy in Saccharomyces cerevisiae. *Molecular Biology of the Cell,* 19**,** 668-681.

CHIANG, H. L., TERLECKY, S. R., PLANT, C. P. & DICE, J. F. 1989. A role for a 70-kilodalton heat shock protein in lysosomal degradation of intracellular proteins. *Science,* 246**,** 382-5.

CHOWDHURY, S., OTOMO, C., LEITNER, A., OHASHI, K., AEBERSOLD, R., LANDER, G. C. & OTOMO, T. 2018. Insights into autophagosome biogenesis from structural and biochemical analyses of the ATG2A-WIPI4 complex. *Proc Natl Acad Sci U S A,* 115**,** E9792-e9801.

CLARKE, R. J., HOSSAIN, K. R. & CAO, K. 2020. Physiological roles of transverse lipid asymmetry of animal membranes. *Biochim Biophys Acta Biomembr,* 1862**,** 183382.

COMBE, C. W., FISCHER, L. & RAPPSILBER, J. 2015. xiNET: cross-link network maps with residue resolution. *Mol Cell Proteomics,* 14**,** 1137-47.

CONNERTH, M., TATSUTA, T., HAAG, M., KLECKER, T., WESTERMANN, B. & LANGER, T. 2012. Intramitochondrial transport of phosphatidic acid in yeast by a lipid transfer protein. *Science,* 338**,** 815-8.

CUERVO, A. M. & DICE, J. F. 1996. A receptor for the selective uptake and degradation of proteins by lysosomes. *Science,* 273**,** 501-3.

CUFI, S., VAZQUEZ-MARTIN, A., OLIVERAS-FERRAROS, C., MARTIN-CASTILLO, B., VELLON, L. & MENENDEZ, J. A. 2011. Autophagy positively regulates the CD44(+) CD24(-/low) breast cancer stem-like phenotype. *Cell Cycle,* 10**,** 3871-85.

DABROWSKI, R., TULLI, S. & GRAEF, M. 2022. Parallel phospholipid transfer by Vps13 and Atg2 determines autophagosome biogenesis dynamics. *bioRxiv***,** 2022.11.10.516013.

DALEKE, D. L. 2003. Regulation of transbilayer plasma membrane phospholipid asymmetry. *J Lipid Res,* 44**,** 233-42.

DE ANTONI, A., PEARSON, C. G., CIMINI, D., CANMAN, J. C., SALA, V., NEZI, L., MAPELLI, M., SIRONI, L., FARETTA, M., SALMON, E. D. & MUSACCHIO, A. 2005. The Mad1/Mad2 complex as a template for Mad2 activation in the spindle assembly checkpoint. *Current Biology,* 15**,** 214-225.

DE DUVE, C. & WATTIAUX, R. 1966. Functions of Lysosomes. *Annual Review of Physiology,* 28**,** 435-492.

DICE, J. F. 1990. Peptide Sequences That Target Cytosolic Proteins for Lysosomal Proteolysis. *Trends in Biochemical Sciences,* 15**,** 305-309.

DING, Y. & CHOI, M. E. 2015. Autophagy in diabetic nephropathy. *Journal of Endocrinology,* 224**,** R15-R30.

DISHMAN, A. F. & VOLKMAN, B. F. 2018. Unfolding the Mysteries of Protein Metamorphosis. *ACS Chem Biol,* 13**,** 1438-1446.

DOOLEY, H. C., RAZI, M., POLSON, H. E., GIRARDIN, S. E., WILSON, M. I. & TOOZE, S. A. 2014. WIPI2 links LC3 conjugation with PI3P, autophagosome formation, and pathogen clearance by recruiting Atg12-5-16L1. *Mol Cell,* 55**,** 238-52.

DOOLEY, H. C., WILSON, M. I. & TOOZE, S. A. 2015. WIPI2B links PtdIns3P to LC3 lipidation through binding ATG16L1. *Autophagy,* 11**,** 190-191.

DZIURDZIK, S. K. & CONIBEAR, E. 2021. The Vps13 Family of Lipid Transporters and Its Role at Membrane Contact Sites. *Int J Mol Sci,* 22.

EGAN, D. F., CHUN, M. G., VAMOS, M., ZOU, H., RONG, J., MILLER, C. J., LOU, H. J., RAVEENDRA-PANICKAR, D., YANG, C. C., SHEFFLER, D. J., TERIETE, P., ASARA, J. M., TURK, B. E., COSFORD, N. D. & SHAW, R. J. 2015. Small Molecule Inhibition of the Autophagy Kinase ULK1 and Identification of ULK1 Substrates. *Mol Cell,* 59**,** 285-97.

EGAN, D. F., SHACKELFORD, D. B., MIHAYLOVA, M. M., GELINO, S., KOHNZ, R. A., MAIR, W., VASQUEZ, D. S., JOSHI, A., GWINN, D. M., TAYLOR, R., ASARA, J. M., FITZPATRICK, J., DILLIN, A., VIOLLET, B., KUNDU, M., HANSEN, M. & SHAW, R. J. 2011. Phosphorylation of ULK1 (hATG1) by AMP-activated protein kinase connects energy sensing to mitophagy. *Science,* 331**,** 456-61.

ERICSSON, J. L. 1969. Studies on induced cellular autophagy. I. Electron microscopy of cells with in vivo labelled lysosomes. *Exp Cell Res,* 55**,** 95-106.

FAESEN, A. C., THANASOULA, M., MAFFINI, S., BREIT, C., MULLER, F., VAN GERWEN, S., BANGE, T. & MUSACCHIO, A. 2017. Basis of catalytic assembly of the mitotic checkpoint complex. *Nature,* 542**,** 498-502.

FALZONE, M. E. & ACCARDI, A. 2020. Reconstitution of Proteoliposomes for Phospholipid Scrambling and Nonselective Channel Assays. *Methods Mol Biol,* 2127**,** 207-225.

FAN, W., NASSIRI, A. & ZHONG, Q. 2011. Autophagosome targeting and membrane curvature sensing by Barkor/Atg14(L). *Proceedings of the National Academy of Sciences,* 108**,** 7769-7774.

FASS, E., SHVETS, E., DEGANI, I., HIRSCHBERG, K. & ELAZAR, Z. 2006. Microtubules support production of starvation-induced autophagosomes but not their targeting and fusion with lysosomes. *J Biol Chem,* 281**,** 36303-16.

FELDWISCH, J., VENTE, A., CAMPOS, N., ZETTL, R. & PALME, K. 1995. Photoaffinity labeling and strategies for plasma membrane protein purification. *Methods Cell Biol,* 50**,** 51-60.

FENGSRUD, M., ERICHSEN, E. S., BERG, T. O., RAIBORG, C. & SEGLEN, P. O. 2000. Ultrastructural characterization of the delimiting membranes of isolated autophagosomes and amphisomes by freeze-fracture electron microscopy. *Eur J Cell Biol,* 79**,** 871-82.

FERREIRA, J. V., SOARES, A. R., RAMALHO, J. S., PEREIRA, P. & GIRAO, H. 2015. K63 linked ubiquitin chain formation is a signal for HIF1A degradation by Chaperone-Mediated Autophagy. *Sci Rep,* 5**,** 10210.

FOSTER, F. M., TRAER, C. J., ABRAHAM, S. M. & FRY, M. J. 2003. The phosphoinositide (PI) 3-kinase family. *J Cell Sci,* 116**,** 3037-40.

FRITZ, J. S. 2004. Early milestones in the development of ion-exchange chromatography: a personal account. *J Chromatogr A,* 1039**,** 3-12.

FUJIOKA, Y., ALAM, J. M., NOSHIRO, D., MOURI, K., ANDO, T., OKADA, Y., MAY, A. I., KNORR, R. L., SUZUKI, K., OHSUMI, Y. & NODA, N. N. 2020. Phase separation organizes the site of autophagosome formation. *Nature,* 578**,** 301-305.

FUJIOKA, Y., NODA, N. N., FUJII, K., YOSHIMOTO, K., OHSUMI, Y. & INAGAKI, F. 2008. In vitro reconstitution of plant Atg8 and Atg12 conjugation systems essential for autophagy. *J Biol Chem,* 283**,** 1921-8.

FUJIOKA, Y., SUZUKI, S. W., YAMAMOTO, H., KONDO-KAKUTA, C., KIMURA, Y., HIRANO, H., AKADA, R., INAGAKI, F., OHSUMI, Y. & NODA, N. N. 2014. Structural basis of starvation-induced assembly of the autophagy initiation complex. *Nat Struct Mol Biol,* 21**,** 513-21.

FUJITA, N., HAYASHI-NISHINO, M., FUKUMOTO, H., OMORI, H., YAMAMOTO, A., NODA, T. & YOSHIMORI, T. 2008. An Atg4B mutant hampers the lipidation of LC3 paralogues and causes defects in autophagosome closure. *Mol Biol Cell,* 19**,** 4651-9.

GANLEY, I. G., LAM DU, H., WANG, J., DING, X., CHEN, S. & JIANG, X. 2009. ULK1.ATG13.FIP200 complex mediates mTOR signaling and is essential for autophagy. *J Biol Chem,* 284**,** 12297-305.

GAO, M. & YANG, H. 2018. VPS13: A lipid transfer protein making contacts at multiple cellular locations. *J Cell Biol,* 217**,** 3322-3324.

GATICA, D., CHIONG, M., LAVANDERO, S. & KLIONSKY, D. J. 2015. Molecular mechanisms of autophagy in the cardiovascular system. *Circ Res,* 116**,** 456-67.

GATICA, D., LAHIRI, V. & KLIONSKY, D. J. 2018. Cargo recognition and degradation by selective autophagy. *Nat Cell Biol,* 20**,** 233-242.

GAUGEL, A., BAKULA, D., HOFFMANN, A. & PROIKAS-CEZANNE, T. 2012. Defining regulatory and phosphoinositide-binding sites in the human WIPI-1 beta-propeller responsible for autophagosomal membrane localization downstream of mTORC1 inhibition. *J Mol Signal,* 7**,** 16.

GENG, J., BABA, M., NAIR, U. & KLIONSKY, D. J. 2008. Quantitative analysis of autophagy-related protein stoichiometry by fluorescence microscopy. *J Cell Biol,* 182**,** 129-40.

GHANBARPOUR, A., VALVERDE, D. P., MELIA, T. J. & REINISCH, K. M. 2021. A model for a partnership of lipid transfer proteins and scramblases in membrane expansion and organelle biogenesis. *Proc Natl Acad Sci U S A,* 118.

GIBSON, D. G., YOUNG, L., CHUANG, R. Y., VENTER, J. C., HUTCHISON, C. A., 3RD & SMITH, H. O. 2009. Enzymatic assembly of DNA molecules up to several hundred kilobases. *Nat Methods,* 6**,** 343-5.

GOMEZ-SANCHEZ, R., ROSE, J., GUIMARAES, R., MARI, M., PAPINSKI, D., RIETER, E., GEERTS, W. J., HARDENBERG, R., KRAFT, C., UNGERMANN, C. & REGGIORI, F. 2018. Atg9 establishes Atg2-dependent contact sites between the endoplasmic reticulum and phagophores. *J Cell Biol,* 217**,** 2743-2763.

GRAEF, M. 2018. Membrane tethering by the autophagy ATG2A-WIPI4 complex. *Proceedings of the National Academy of Sciences,* 115**,** 10540.

GRAEF, M., FRIEDMAN, J. R., GRAHAM, C., BABU, M. & NUNNARI, J. 2013. ER exit sites are physical and functional core autophagosome biogenesis components. *Mol Biol Cell,* 24**,** 2918-31.

GU, Y., DESAI, A. & CORBETT, K. D. 2022. Evolutionary Dynamics and Molecular Mechanisms of HORMA Domain Protein Signaling. *Annu Rev Biochem,* 91**,** 541-569.

GUARDIA, C. M., TAN, X. F., LIAN, T., RANA, M. S., ZHOU, W., CHRISTENSON, E. T., LOWRY, A. J., FARALDO-GOMEZ, J. D., BONIFACINO, J. S., JIANG, J. & BANERJEE, A. 2020. Structure of Human ATG9A, the Only Transmembrane Protein of the Core Autophagy Machinery. *Cell Rep,* 31**,** 107837.

GUILLÉN-SAMANDER, A., WU, Y., PINEDA, S. S., GARCÍA, F. J., EISEN, J. N., LEONZINO, M., UGUR, B., KELLIS, M., HEIMAN, M. & DE CAMILLI, P. 2022. A partnership between the lipid scramblase XK and the lipid transfer protein VPS13A at the plasma membrane. *Proceedings of the National Academy of Sciences,* 119**,** e2205425119.

GUO, Y., CHANG, C., HUANG, R., LIU, B., BAO, L. & LIU, W. 2012. AP1 is essential for generation of autophagosomes from the trans-Golgi network. *J Cell Sci,* 125**,** 1706-15.

GURTLER, A., KUNZ, N., GOMOLKA, M., HORNHARDT, S., FRIEDL, A. A., MCDONALD, K., KOHN, J. E. & POSCH, A. 2013. Stain-Free technology as a normalization tool in Western blot analysis. *Anal Biochem,* 433**,** 105-11.

HAILEY, D. W., RAMBOLD, A. S., SATPUTE-KRISHNAN, P., MITRA, K., SOUGRAT, R., KIM, P. K. & LIPPINCOTT-SCHWARTZ, J. 2010. Mitochondria supply membranes for autophagosome biogenesis during starvation. *Cell,* 141**,** 656-67.

HAMASAKI, M., FURUTA, N., MATSUDA, A., NEZU, A., YAMAMOTO, A., FUJITA, N., OOMORI, H., NODA, T., HARAGUCHI, T., HIRAOKA, Y., AMANO, A. & YOSHIMORI, T. 2013. Autophagosomes form at ER-mitochondria contact sites. *Nature,* 495**,** 389-93.

HANADA, T., NODA, N. N., SATOMI, Y., ICHIMURA, Y., FUJIOKA, Y., TAKAO, T., INAGAKI, F. & OHSUMI, Y. 2007. The Atg12-Atg5 conjugate has a novel E3-like activity for protein lipidation in autophagy. *J Biol Chem,* 282**,** 37298-302.

HARA, T. & MIZUSHIMA, N. 2009. Role of ULK-FIP200 complex in mammalian autophagy: FIP200, a counterpart of yeast Atg17? *Autophagy,* 5**,** 85-7.

HAYASHI-NISHINO, M., FUJITA, N., NODA, T., YAMAGUCHI, A., YOSHIMORI, T. & YAMAMOTO, A. 2009. A subdomain of the endoplasmic reticulum forms a cradle for autophagosome formation. *Nat Cell Biol,* 11**,** 1433-7.

HELLE, S. C., KANFER, G., KOLAR, K., LANG, A., MICHEL, A. H. & KORNMANN, B. 2013. Organization and function of membrane contact sites. *Biochim Biophys Acta,* 1833**,** 2526-41.

HENNE, W. M., ZHU, L., BALOGI, Z., STEFAN, C., PLEISS, J. A. & EMR, S. D. 2015. Mdm1/Snx13 is a novel ER-endolysosomal interorganelle tethering protein. *J Cell Biol,* 210**,** 541-51.

HERMAN, P. K., STACK, J. H., DEMODENA, J. A. & EMR, S. D. 1991. A novel protein kinase homolog essential for protein sorting to the yeast lysosome-like vacuole. *Cell,* 64**,** 425-37.

HERNANDEZ, J. M., STEIN, A., BEHRMANN, E., RIEDEL, D., CYPIONKA, A., FARSI, Z., WALLA, P. J., RAUNSER, S. & JAHN, R. 2012. Membrane fusion intermediates via directional and full assembly of the SNARE complex. *Science,* 336**,** 1581-4.

HIEKE, N., LÖFFLER, A. S., KAIZUKA, T., BERLETH, N., BÖHLER, P., DRIESSE, S., STUHLDREIER, F., FRIESEN, O., ASSANI, K., SCHMITZ, K., PETER, C., DIEDRICH, B., DENGJEL, J., HOLLAND, P., SIMONSEN, A., WESSELBORG, S., MIZUSHIMA, N. & STORK, B. 2015. Expression of a ULK1/2 binding-deficient ATG13 variant can partially restore autophagic activity in ATG13-deficient cells. *Autophagy,* 11**,** 1471-1483.

HIRATA, E., OHYA, Y. & SUZUKI, K. 2017. Atg4 plays an important role in efficient expansion of autophagic isolation membranes by cleaving lipidated Atg8 in Saccharomyces cerevisiae. *PLoS One,* 12**,** e0181047.

HOLTHUIS, J. C. & LEVINE, T. P. 2005. Lipid traffic: floppy drives and a superhighway. *Nat Rev Mol Cell Biol,* 6**,** 209-20.

HOLTHUIS, J. C. & MENON, A. K. 2014. Lipid landscapes and pipelines in membrane homeostasis. *Nature,* 510**,** 48-57.

HOLZMULLER, W. & KULOZIK, U. 2016. Protein quantification by means of a stain-free SDS-PAGE technology without the need for analytical standards: Verification and validation of the method. *Journal of Food Composition and Analysis,* 48**,** 128-134.

HOSOKAWA, N., HARA, T., KAIZUKA, T., KISHI, C., TAKAMURA, A., MIURA, Y., IEMURA, S., NATSUME, T., TAKEHANA, K., YAMADA, N., GUAN, J. L., OSHIRO, N. & MIZUSHIMA, N. 2009a. Nutrient-dependent mTORC1 association with the ULK1-Atg13-FIP200 complex required for autophagy. *Mol Biol Cell,* 20**,** 1981-91.

HOSOKAWA, N., SASAKI, T., IEMURA, S., NATSUME, T., HARA, T. & MIZUSHIMA, N. 2009b. Atg101, a novel mammalian autophagy protein interacting with Atg13. *Autophagy,* 5**,** 973-9.

HUANG, W., CHOI, W., HU, W., MI, N., GUO, Q., MA, M., LIU, M., TIAN, Y., LU, P., WANG, F.-L., DENG, H., LIU, L., GAO, N., YU, L. & SHI, Y. 2012. Crystal structure and biochemical analyses reveal Beclin 1 as a novel membrane binding protein. *Cell Research,* 22**,** 473-489.

HUTCHINS, M. U., VEENHUIS, M. & KLIONSKY, D. J. 1999. Peroxisome degradation in Saccharomyces cerevisiae is dependent on machinery of macroautophagy and the Cvt pathway. *J Cell Sci,* 112 (Pt 22)**,** 4079-87.

ICHIMURA, Y., KIRISAKO, T., TAKAO, T., SATOMI, Y., SHIMONISHI, Y., ISHIHARA, N., MIZUSHIMA, N., TANIDA, I., KOMINAMI, E., OHSUMI, M., NODA, T. & OHSUMI, Y. 2000. A ubiquitin-like system mediates protein lipidation. *Nature,* 408**,** 488-92.

IMAI, K., HAO, F., FUJITA, N., TSUJI, Y., OE, Y., ARAKI, Y., HAMASAKI, M., NODA, T. & YOSHIMORI, T. 2016. Atg9A trafficking through the recycling endosomes is required for autophagosome formation. *J Cell Sci,* 129**,** 3781-3791.

ISHIHARA, N., HAMASAKI, M., YOKOTA, S., SUZUKI, K., KAMADA, Y., KIHARA, A., YOSHIMORI, T., NODA, T. & OHSUMI, Y. 2001. Autophagosome requires specific early Sec proteins for its formation and NSF/SNARE for vacuolar fusion. *Mol Biol Cell,* 12**,** 3690-702.

ITAKURA, E. & MIZUSHIMA, N. 2010. Characterization of autophagosome formation site by a hierarchical analysis of mammalian Atg proteins. *Autophagy,* 6**,** 764-776.

JAO, C. C., RAGUSA, M. J., STANLEY, R. E. & HURLEY, J. H. 2013. A HORMA domain in Atg13 mediates PI 3-kinase recruitment in autophagy. *Proc Natl Acad Sci U S A,* 110**,** 5486-91.

JI, C. C., ZHAO, H. Y., CHEN, D., ZHANG, H. & ZHAO, Y. G. 2021. beta-propeller proteins WDR45 and WDR45B regulate autophagosome maturation into autolysosomes in neural cells. *Current Biology,* 31**,** 1666-+.

JIANG, W., CHEN, X., JI, C., ZHANG, W., SONG, J., LI, J. & WANG, J. 2021. Key Regulators of Autophagosome Closure. *Cells,* 10.

JIN, M. & KLIONSKY, D. J. 2014. Regulation of autophagy: modulation of the size and number of autophagosomes. *FEBS Lett,* 588**,** 2457-63.

JUDITH, D., JEFFERIES, H. B. J., BOEING, S., FRITH, D., SNIJDERS, A. P. & TOOZE, S. A. 2019. ATG9A shapes the forming autophagosome through Arfaptin 2 and phosphatidylinositol 4-kinase IIIbeta. *J Cell Biol,* 218**,** 1634-1652.

JUHASZ, G. & NEUFELD, T. P. 2006. Autophagy: a forty-year search for a missing membrane source. *PLoS Biol,* 4**,** e36.

JUNG, C. H., JUN, C. B., RO, S. H., KIM, Y. M., OTTO, N. M., CAO, J., KUNDU, M. & KIM, D. H. 2009. ULK-Atg13-FIP200 complexes mediate mTOR signaling to the autophagy machinery. *Mol Biol Cell,* 20**,** 1992-2003.

KABEYA, Y., MIZUSHIMA, N., UENO, T., YAMAMOTO, A., KIRISAKO, T., NODA, T., KOMINAMI, E., OHSUMI, Y. & YOSHIMORI, T. 2000. LC3, a mammalian homologue of yeast Apg8p, is localized in autophagosome membranes after processing. *EMBO J,* 19**,** 5720-8.

KABUTA, T., FURUTA, A., AOKI, S., FURUTA, K. & WADA, K. 2008. Aberrant interaction between Parkinson disease-associated mutant UCH-L1 and the lysosomal receptor for chaperone-mediated autophagy. *J Biol Chem,* 283**,** 23731-8.

KAKUTA, S., YAMAGUCHI, J., SUZUKI, C., SASAKI, M., KAZUNO, S. & UCHIYAMA, Y. 2017. Small GTPase Rab1B is associated with ATG9A vesicles and regulates autophagosome formation. *Faseb j,* 31**,** 3757-3773.

KANG, M. R., KIM, M. S., OH, J. E., KIM, Y. R., SONG, S. Y., KIM, S. S., AHN, C. H., YOO, N. J. & LEE, S. H. 2009. Frameshift mutations of autophagy-related genes ATG2B, ATG5, ATG9B and ATG12 in gastric and colorectal cancers with microsatellite instability. *J Pathol,* 217**,** 702-6.

KANNAN, M., LAHIRI, S., LIU, L. K., CHOUDHARY, V. & PRINZ, W. A. 2017. Phosphatidylserine synthesis at membrane contact sites promotes its transport out of the ER. *Journal of Lipid Research,* 58**,** 553-562.

KANNANGARA, A. R., POOLE, D. M., MCEWAN, C. M., YOUNGS, J. C., WEERASEKARA, V. K., THORNOCK, A. M., LAZARO, M. T., BALASOORIYA, E. R., OH, L. M., SODERBLOM, E. J., LEE, J. J., SIMMONS, D. L. & ANDERSEN, J. L. 2021. BioID reveals an ATG9A interaction with ATG13-ATG101 in the degradation of p62/SQSTM1-ubiquitin clusters. *EMBO Rep***,** e51136.

KARANASIOS, E., STAPLETON, E., MANIFAVA, M., KAIZUKA, T., MIZUSHIMA, N., WALKER, S. A. & KTISTAKIS, N. T. 2013. Dynamic association of the ULK1 complex with omegasomes during autophagy induction. *J Cell Sci,* 126**,** 5224-38.

KARANASIOS, E., WALKER, S. A., OKKENHAUG, H., MANIFAVA, M., HUMMEL, E., ZIMMERMANN, H., AHMED, Q., DOMART, M. C., COLLINSON, L. & KTISTAKIS, N. T. 2016. Autophagy initiation by ULK complex assembly on ER tubulovesicular regions marked by ATG9 vesicles. *Nat Commun,* 7**,** 12420.

KIM, A. K. & PORTER, L. L. 2021. Functional and Regulatory Roles of Fold-Switching Proteins. *Structure,* 29**,** 6-14.

KIM, J., KUNDU, M., VIOLLET, B. & GUAN, K.-L. 2011a. AMPK and mTOR regulate autophagy through direct phosphorylation of Ulk1. *Nature Cell Biology,* 13**,** 132-141.

KIM, J., KUNDU, M., VIOLLET, B. & GUAN, K. L. 2011b. AMPK and mTOR regulate autophagy through direct phosphorylation of Ulk1. *Nat Cell Biol,* 13**,** 132-41.

KOCATURK, N. M., AKKOC, Y., KIG, C., BAYRAKTAR, O., GOZUACIK, D. & KUTLU, O. 2019. Autophagy as a molecular target for cancer treatment. *European Journal of Pharmaceutical Sciences,* 134**,** 116-137.

KOTANI, T., KIRISAKO, H., KOIZUMI, M., OHSUMI, Y. & NAKATOGAWA, H. 2018. The Atg2-Atg18 complex tethers pre-autophagosomal membranes to the endoplasmic reticulum for autophagosome formation. *Proc Natl Acad Sci U S A,* 115**,** 10363-10368.

KRAFT, C., KIJANSKA, M., KALIE, E., SIERGIEJUK, E., LEE, S. S., SEMPLICIO, G., STOFFEL, I., BREZOVICH, A., VERMA, M., HANSMANN, I., AMMERER, G., HOFMANN, K., TOOZE, S. & PETER, M. 2012. Binding of the Atg1/ULK1 kinase to the ubiquitin-like protein Atg8 regulates autophagy. *EMBO J,* 31**,** 3691-703.

KRICK, R., BUSSE, R. A., SCACIOC, A., STEPHAN, M., JANSHOFF, A., THUMM, M. & KUHNEL, K. 2012. Structural and functional characterization of the two phosphoinositide binding sites of PROPPINs, a beta-propeller protein family. *Proc Natl Acad Sci U S A,* 109**,** E2042-9.

KRICK, R., HENKE, S., TOLSTRUP, J. & THUMM, M. 2008. Dissecting the localization and function of Atg18, Atg21 and Ygr223c. *Autophagy,* 4**,** 896-910.

KRICK, R., TOLSTRUP, J., APPELLES, A., HENKE, S. & THUMM, M. 2006. The relevance of the phosphatidylinositolphosphat-binding motif FRRGT of Atg18 and Atg21 for the Cvt pathway and autophagy. *Febs Letters,* 580**,** 4632-4638.

KROEMER, G., MARINO, G. & LEVINE, B. 2010. Autophagy and the integrated stress response. *Mol Cell,* 40**,** 280-93.

KROPPEN, B., TESKE, N., YAMBIRE, K. F., DENKERT, N., MUKHERJEE, I., TARASENKO, D., JAIPURIA, G., ZWECKSTETTER, M., MILOSEVIC, I., STEINEM, C. & MEINECKE, M. 2021. Cooperativity of membrane-protein and protein-protein interactions control membrane remodeling by epsin 1 and affects clathrin-mediated endocytosis. *Cell Mol Life Sci,* 78**,** 2355-2370.

KUCERKA, N., TRISTRAM-NAGLE, S. & NAGLE, J. F. 2005. Structure of fully hydrated fluid phase lipid bilayers with monounsaturated chains. *J Membr Biol,* 208**,** 193-202.

KUMA, A., HATANO, M., MATSUI, M., YAMAMOTO, A., NAKAYA, H., YOSHIMORI, T., OHSUMI, Y., TOKUHISA, T. & MIZUSHIMA, N. 2004. The role of autophagy during the early neonatal starvation period. *Nature,* 432**,** 1032-6.

KUMAR, N., LEONZINO, M., HANCOCK-CERUTTI, W., HORENKAMP, F. A., LI, P., LEES, J. A., WHEELER, H., REINISCH, K. M. & DE CAMILLI, P. 2018. VPS13A and VPS13C are lipid transport proteins differentially localized at ER contact sites. *J Cell Biol,* 217**,** 3625-3639.

LAEMMLI, U. K. 1970. Cleavage of structural proteins during the assembly of the head of bacteriophage T4. *Nature,* 227**,** 680-5.

LAHIRI, S., TOULMAY, A. & PRINZ, W. A. 2015. Membrane contact sites, gateways for lipid homeostasis. *Curr Opin Cell Biol,* 33**,** 82-87.

LAI, L. T. F., YU, C., WONG, J. S. K., LO, H. S., BENLEKBIR, S., JIANG, L. & LAU, W. C. Y. 2019. Subnanometer resolution cryo-EM structure of Arabidopsis thaliana ATG9. *Autophagy***,** 1-9.

LANG, A. B., PETER, A. T. J., WALTER, P. & KORNMANN, B. 2015. ER-mitochondrial junctions can be bypassed by dominant mutations in the endosomal protein Vps13. *Journal of Cell Biology,* 210**,** 883-890.

LAZARUS, M. B., NOVOTNY, C. J. & SHOKAT, K. M. 2015. Structure of the human autophagy initiating kinase ULK1 in complex with potent inhibitors. *ACS Chem Biol,* 10**,** 257-61.

LEE, B. C., KHELASHVILI, G., FALZONE, M., MENON, A. K., WEINSTEIN, H. & ACCARDI, A. 2018. Gating mechanism of the extracellular entry to the lipid pathway in a TMEM16 scramblase. *Nat Commun,* 9**,** 3251.

LEE, E. F., PERUGINI, M. A., PETTIKIRIARACHCHI, A., EVANGELISTA, M., KEIZER, D. W., YAO, S. & FAIRLIE, W. D. 2016. The BECN1 N-terminal domain is intrinsically disordered. *Autophagy,* 12**,** 460-71.

LEE, E. J. & TOURNIER, C. 2011. The requirement of uncoordinated 51-like kinase 1 (ULK1) and ULK2 in the regulation of autophagy. *Autophagy,* 7**,** 689-95.

LEE, P. Y., COSTUMBRADO, J., HSU, C. Y. & KIM, Y. H. 2012. Agarose gel electrophoresis for the separation of DNA fragments. *J Vis Exp*.

LEI, Y., TANG, D., LIAO, G., XU, L., LIU, S., CHEN, Q., LI, C., DUAN, J., WANG, K., WANG, J., SUN, B., LI, Z., DAI, L., CHENG, W., QI, S. & LU, K. 2020. The crystal structure of Atg18 reveals a new binding site for Atg2 in Saccharomyces cerevisiae. *Cell Mol Life Sci*.

LEONZINO, M., REINISCH, K. M. & DE CAMILLI, P. 2021. Insights into VPS13 properties and function reveal a new mechanism of eukaryotic lipid transport. *Biochimica Et Biophysica Acta-Molecular and Cell Biology of Lipids,* 1866.

LI, L. S., TONG, M. D., FU, Y. H., CHEN, F., ZHANG, S., CHEN, H. M., MA, X., LI, D. F., LIU, X. X. & ZHONG, Q. 2021a. Lipids and membrane-associated proteins in autophagy. *Protein & Cell,* 12**,** 520-544.

LI, P., LEES, J. A., LUSK, C. P. & REINISCH, K. M. 2020a. Cryo-EM reconstruction of a VPS13 fragment reveals a long groove to channel lipids between membranes. *J Cell Biol,* 219.

LI, W., HE, P., HUANG, Y., LI, Y. F., LU, J., LI, M., KURIHARA, H., LUO, Z., MENG, T., ONISHI, M., MA, C., JIANG, L., HU, Y., GONG, Q., ZHU, D., XU, Y., LIU, R., LIU, L., YI, C., ZHU, Y., MA, N., OKAMOTO, K., XIE, Z., LIU, J., HE, R. R. & FENG, D. 2021b. Selective autophagy of intracellular organelles: recent research advances. *Theranostics,* 11**,** 222-256.

LI, Z., HUANG, W. & WANG, W. 2020b. Multifaceted roles of COPII subunits in autophagy. *Biochim Biophys Acta Mol Cell Res,* 1867**,** 118627.

LIANG, C., LEE, J. S., INN, K. S., GACK, M. U., LI, Q., ROBERTS, E. A., VERGNE, I., DERETIC, V., FENG, P., AKAZAWA, C. & JUNG, J. U. 2008. Beclin1-binding UVRAG targets the class C Vps complex to coordinate autophagosome maturation and endocytic trafficking. *Nat Cell Biol,* 10**,** 776-87.

LIANG, X. H., JACKSON, S., SEAMAN, M., BROWN, K., KEMPKES, B., HIBSHOOSH, H. & LEVINE, B. 1999. Induction of autophagy and inhibition of tumorigenesis by beclin 1. *Nature,* 402**,** 672-6.

LORIN, S., HAMAI, A., MEHRPOUR, M. & CODOGNO, P. 2013. Autophagy regulation and its role in cancer. *Semin Cancer Biol,* 23**,** 361-79.

LYNCH-DAY, M. A., BHANDARI, D., MENON, S., HUANG, J., CAI, H., BARTHOLOMEW, C. R., BRUMELL, J. H., FERRO-NOVICK, S. & KLIONSKY, D. J. 2010. Trs85 directs a Ypt1 GEF, TRAPPIII, to the phagophore to promote autophagy. *Proc Natl Acad Sci U S A,* 107**,** 7811-6.

MA, M., LIU, J. J., LI, Y., HUANG, Y., TA, N., CHEN, Y., FU, H., YE, M. D., DING, Y., HUANG, W., WANG, J., DONG, M. Q., YU, L. & WANG, H. W. 2020. Author Correction: Cryo-EM structure and biochemical analysis reveal the basis of the functional difference between human PI3KC3-C1 and -C2. *Cell Res,* 30**,** 551-552.

MAEDA, S., OTOMO, C. & OTOMO, T. 2019. The autophagic membrane tether ATG2A transfers lipids between membranes. *bioRxiv***,** 555441.

MAEDA, S., YAMAMOTO, H., KINCH, L. N., GARZA, C. M., TAKAHASHI, S., OTOMO, C., GRISHIN, N. V., FORLI, S., MIZUSHIMA, N. & OTOMO, T. 2020. Structure, lipid scrambling activity and role in autophagosome formation of ATG9A. *Nature Structural & Molecular Biology*.

MALVEZZI, M., ANDRA, K. K., PANDEY, K., LEE, B. C., FALZONE, M. E., BROWN, A., IQBAL, R., MENON, A. K. & ACCARDI, A. 2018. Out-of-the-groove transport of lipids by TMEM16 and GPCR scramblases. *Proc Natl Acad Sci U S A,* 115**,** E7033-E7042.

MALVEZZI, M., CHALAT, M., JANJUSEVIC, R., PICOLLO, A., TERASHIMA, H., MENON, A. K. & ACCARDI, A. 2013. Ca2+-dependent phospholipid scrambling by a reconstituted TMEM16 ion channel. *Nat Commun,* 4**,** 2367.

MAPELLI, M., MASSIMILIANO, L., SANTAGUIDA, S. & MUSACCHIO, A. 2007. The Mad2 conformational dimer: structure and implications for the spindle assembly checkpoint. *Cell,* 131**,** 730-43.

MARI, M., GRIFFITH, J., RIETER, E., KRISHNAPPA, L., KLIONSKY, D. J. & REGGIORI, F. 2010. An Atg9-containing compartment that functions in the early steps of autophagosome biogenesis. *Journal of Cell Biology,* 190**,** 1005-1022.

MARI, M. & REGGIORI, F. 2010. Atg9 reservoirs, a new organelle of the yeast endomembrane system? *Autophagy,* 6**,** 1221-1223.

MARTENS, S. & BEHRENDS, C. 2020. Molecular Mechanisms of Selective Autophagy. *J Mol Biol,* 432**,** 1-2.

MARTENSEN, P. M. & JUSTESEN, J. 2001. Specific inhibitors prevent proteolytic degradation of recombinant proteins expressed in High Five cells. *Biotechniques,* 30**,** 782-4, 786, 788 passim.

MARZELLA, L., AHLBERG, J. & GLAUMANN, H. 1981. Autophagy, heterophagy, microautophagy and crinophagy as the means for intracellular degradation. *Virchows Arch B Cell Pathol Incl Mol Pathol,* 36**,** 219-34.

MATOBA, K., KOTANI, T., TSUTSUMI, A., TSUJI, T., MORI, T., NOSHIRO, D., SUGITA, Y., NOMURA, N., IWATA, S., OHSUMI, Y., FUJIMOTO, T.,

NAKATOGAWA, H., KIKKAWA, M. & NODA, N. N. 2020. Atg9 is a lipid scramblase that mediates autophagosomal membrane expansion. *Nature Structural & Molecular Biology*.

MATOBA, K. & NODA, N. N. 2021. Structural catalog of core Atg proteins opens new era of autophagy research. *Journal of Biochemistry,* 169**,** 517-525.

MATSCHEKO, N., MAYRHOFER, P., RAO, Y. J., BEIER, V. & WOLLERT, T. 2019. Atg11 tethers Atg9 vesicles to initiate selective autophagy. *Plos Biology,* 17.

MATSUNAGA, K., MORITA, E., SAITOH, T., AKIRA, S., KTISTAKIS, N. T., IZUMI, T., NODA, T. & YOSHIMORI, T. 2010. Autophagy requires endoplasmic reticulum targeting of the PI3-kinase complex via Atg14L. *J Cell Biol,* 190**,** 511-21.

MAYCOTTE, P., JONES, K. L., GOODALL, M. L., THORBURN, J. & THORBURN, A. 2015. Autophagy Supports Breast Cancer Stem Cell Maintenance by Regulating IL6 Secretion. *Mol Cancer Res,* 13**,** 651-8.

MEI, Y., SU, M., SANISHVILI, R., CHAKRAVARTHY, S., COLBERT, C. L. & SINHA, S. C. 2016. Identification of BECN1 and ATG14 Coiled-Coil Interface Residues That Are Important for Starvation-Induced Autophagy. *Biochemistry,* 55**,** 4239-53.

MEILING-WESSE, K., BARTH, H., VOSS, C., ESKELINEN, E. L., EPPLE, U. D. & THUMM, M. 2004. Atg21 is required for effective recruitment of Atg8 to the preautophagosomal structure during the Cvt pathway. *J Biol Chem,* 279**,** 37741-50.

MELIA, T. J., LYSTAD, A. H. & SIMONSEN, A. 2020. Autophagosome biogenesis: From membrane growth to closure. *J Cell Biol,* 219.

MENON, I., HUBER, T., SANYAL, S., BANERJEE, S., BARRE, P., CANIS, S., WARREN, J. D., HWA, J., SAKMAR, T. P. & MENON, A. K. 2011. Opsin Is a Phospholipid Flippase. *Current Biology,* 21**,** 149-153.

MERCER, T. J., OHASHI, Y., BOEING, S., JEFFERIES, H. B. J., DE TITO, S., FLYNN, H., TREMEL, S., ZHANG, W., WIRTH, M., FRITH, D., SNIJDERS, A. P., WILLIAMS, R. L. & TOOZE, S. A. 2021. Phosphoproteomic identification of ULK substrates reveals VPS15-dependent ULK/VPS34 interplay in the regulation of autophagy. *EMBO J,* 40**,** e105985.

MIYATA, N., WATANABE, Y., TAMURA, Y., ENDO, T. & KUGE, O. 2016. Phosphatidylserine transport by Ups2-Mdm35 in respiration-active mitochondria. *J Cell Biol,* 214**,** 77-88.

MIZUSHIMA, N., LEVINE, B., CUERVO, A. M. & KLIONSKY, D. J. 2008. Autophagy fights disease through cellular self-digestion. *Nature,* 451**,** 1069-1075.

MIZUSHIMA, N., SUGITA, H., YOSHIMORI, T. & OHSUMI, Y. 1998. A new protein conjugation system in human. The counterpart of the yeast Apg12p conjugation system essential for autophagy. *J Biol Chem,* 273**,** 33889-92.

MIZUSHIMA, N., YAMAMOTO, A., HATANO, M., KOBAYASHI, Y., KABEYA, Y., SUZUKI, K., TOKUHISA, T., OHSUMI, Y. & YOSHIMORI, T. 2001.

Dissection of autophagosome formation using Apg5-deficient mouse embryonic stem cells. *J Cell Biol,* 152**,** 657-68.

MIZUSHIMA, N., YOSHIMORI, T. & OHSUMI, Y. 2011. The role of Atg proteins in autophagosome formation. *Annu Rev Cell Dev Biol,* 27**,** 107-32.

MOREAU, K., RAVIKUMAR, B., RENNA, M., PURI, C. & RUBINSZTEIN, D. C. 2011. Autophagosome precursor maturation requires homotypic fusion. *Cell,* 146**,** 303-17.

MORITA, K., HAMA, Y., IZUME, T., TAMURA, N., UENO, T., YAMASHITA, Y., SAKAMAKI, Y., MIMURA, K., MORISHITA, H., SHIHOYA, W., NUREKI, O., MANO, H. & MIZUSHIMA, N. 2018. Genome-wide CRISPR screen identifies TMEM41B as a gene required for autophagosome formation. *J Cell Biol,* 217**,** 3817-3828.

MRAKOVCIC, M. & FROHLICH, L. F. 2018. p53-Mediated Molecular Control of Autophagy in Tumor Cells. *Biomolecules,* 8.

MULLER, O., SATTLER, T., FLOTENMEYER, M., SCHWARZ, H., PLATTNER, H. & MAYER, A. 2000. Autophagic tubes: vacuolar invaginations involved in lateral membrane sorting and inverse vesicle budding. *J Cell Biol,* 151**,** 519-28.

MULLIS, K., FALOONA, F., SCHARF, S., SAIKI, R., HORN, G. & ERLICH, H. 1986. Specific enzymatic amplification of DNA in vitro: the polymerase chain reaction. *Cold Spring Harb Symp Quant Biol,* 51 Pt 1**,** 263-73.

MUNSON, M. J., ALLEN, G. F., TOTH, R., CAMPBELL, D. G., LUCOCQ, J. M. & GANLEY, I. G. 2015. mTOR activates the VPS34-UVRAG complex to regulate autolysosomal tubulation and cell survival. *EMBO J,* 34**,** 2272-90.

MURZIN, A. G. 2008. Biochemistry. Metamorphic proteins. *Science,* 320**,** 1725-6.

MUSACCHIO, A. 2015a. Closing the Mad2 cycle. *eLife,* 4**,** e08283.

MUSACCHIO, A. 2015b. The Molecular Biology of Spindle Assembly Checkpoint Signaling Dynamics. *Curr Biol,* 25**,** R1002-18.

MUSACCHIO, A. & DESAI, A. 2017. A Molecular View of Kinetochore Assembly and Function. *Biology (Basel),* 6.

NAKATOGAWA, H. 2020. Mechanisms governing autophagosome biogenesis. *Nat Rev Mol Cell Biol,* 21**,** 439-458.

NAKATOGAWA, H., ICHIMURA, Y. & OHSUMI, Y. 2007. Atg8, a ubiquitin-like protein required for autophagosome formation, mediates membrane tethering and hemifusion. *Cell,* 130**,** 165-78.

NAKATOGAWA, H. & MOCHIDA, K. 2015. Reticulophagy and nucleophagy: New findings and unsolved issues. *Autophagy,* 11**,** 2377-8.

NGUYEN, N., SHTEYN, V. & MELIA, T. J. 2017. Sensing Membrane Curvature in Macroautophagy. *J Mol Biol,* 429**,** 457-472.

NGUYEN, T. N., PADMAN, B. S., ZELLNER, S., KHUU, G., UOSELIS, L., LAM, W. K., SKULSUPPAISARN, M., LINDBLOM, R. S. J., WATTS, E. M., BEHRENDS, C. & LAZAROU, M. 2021. ATG4 family proteins drive phagophore growth independently of the LC3/GABARAP lipidation system. *Mol Cell,* 81**,** 2013-2030 e9.

NISHIMURA, T. & MIZUSHIMA, N. 2017. The ULK complex initiates autophagosome formation at phosphatidylinositol synthase-enriched ER subdomains. *Autophagy,* 13**,** 1795-1796.

NIXON, R. A. & CATALDO, A. M. 2006. Lysosomal system pathways: genes to neurodegeneration in Alzheimer's disease. *J Alzheimers Dis,* 9**,** 277-89.

NODA, T., FUJITA, N. & YOSHIMORI, T. 2009. The late stages of autophagy: how does the end begin? *Cell Death & Differentiation,* 16**,** 984-990.

NODA, T., KIM, J., HUANG, W. P., BABA, M., TOKUNAGA, C., OHSUMI, Y. & KLIONSKY, D. J. 2000. Apg9p/Cvt7p is an integral membrane protein required for transport vesicle formation in the Cvt and autophagy pathways. *J Cell Biol,* 148**,** 465-80.

OBARA, K., SEKITO, T. & OHSUMI, Y. 2006. Assortment of Phosphatidylinositol 3-Kinase Complexes—Atg14p Directs Association of Complex I to the Pre-autophagosomal Structure in Saccharomyces cerevisiae. *Molecular Biology of the Cell,* 17**,** 1527-1539.

OLIVAS, T. J., WU, Y., YU, S., LUAN, L., CHOI, P., NAG, S., DE CAMILLI, P., GUPTA, K. & MELIA, T. J. 2022. ATG9 vesicles comprise the seed membrane of mammalian autophagosomes. *bioRxiv***,** 2022.08.16.504143.

ORENSTEIN, S. J. & CUERVO, A. M. 2010. Chaperone-mediated autophagy: molecular mechanisms and physiological relevance. *Semin Cell Dev Biol,* 21**,** 719-26.

ORSI, A., RAZI, M., DOOLEY, H. C., ROBINSON, D., WESTON, A. E., COLLINSON, L. M. & TOOZE, S. A. 2012. Dynamic and transient interactions of Atg9 with autophagosomes, but not membrane integration, are required for autophagy. *Molecular Biology of the Cell,* 23**,** 1860-1873.

OSAWA, T., KOTANI, T., KAWAOKA, T., HIRATA, E., SUZUKI, K., NAKATOGAWA, H., OHSUMI, Y. & NODA, N. N. 2019. Atg2 mediates direct lipid transfer between membranes for autophagosome formation. *Nat Struct Mol Biol,* 26**,** 281-288.

OSAWA, T. & NODA, N. N. 2019. Atg2: A novel phospholipid transfer protein that mediates de novo autophagosome biogenesis. *Protein Sci*.

OTOMO, T., CHOWDHURY, S. & LANDER, G. C. 2018. The rod-shaped ATG2A-WIPI4 complex tethers membranes in vitro. *Contact (Thousand Oaks),* 1.

OTOMO, T. & MAEDA, S. 2019. ATG2A transfers lipids between membranes in vitro. *Autophagy,* 15**,** 2031-2032.

PAN, X., ROBERTS, P., CHEN, Y., KVAM, E., SHULGA, N., HUANG, K., LEMMON, S. & GOLDFARB, D. S. 2000. Nucleus-vacuole junctions in Saccharomyces cerevisiae are formed through the direct interaction of Vac8p with Nvj1p. *Mol Biol Cell,* 11**,** 2445-57.

PANARETOU, C., DOMIN, J., COCKCROFT, S. & WATERFIELD, M. D. 1997. Characterization of p150, an adaptor protein for the human phosphatidylinositol (PtdIns) 3-kinase. Substrate presentation by phosphatidylinositol transfer protein to the p150.Ptdins 3-kinase complex. *J Biol Chem,* 272**,** 2477-85.

PARK, J. M., JUNG, C. H., SEO, M., OTTO, N. M., GRUNWALD, D., KIM, K. H., MORIARITY, B., KIM, Y. M., STARKER, C., NHO, R. S., VOYTAS, D. & KIM, D. H. 2016. The ULK1 complex mediates MTORC1 signaling to the autophagy initiation machinery via binding and phosphorylating ATG14. *Autophagy,* 12**,** 547-64.

PARK, J. M., SEO, M., JUNG, C. H., GRUNWALD, D., STONE, M., OTTO, N. M., TOSO, E., AHN, Y., KYBA, M., GRIFFIN, T. J., HIGGINS, L. & KIM, D. H. 2018. ULK1 phosphorylates Ser30 of BECN1 in association with ATG14 to stimulate autophagy induction. *Autophagy,* 14**,** 584-597.

PARK, J. S., HU, Y., HOLLINGSWORTH, N. M., MILTENBERGER-MILTENYI, G. & NEIMAN, A. M. 2022. Interaction between VPS13A and the XK scramblase is important for VPS13A function in humans. *J Cell Sci,* 135.

PETHERICK, K. J., CONWAY, O. J., MPAMHANGA, C., OSBORNE, S. A., KAMAL, A., SAXTY, B. & GANLEY, I. G. 2015. Pharmacological inhibition of ULK1 kinase blocks mammalian target of rapamycin (mTOR)-dependent autophagy. *J Biol Chem,* 290**,** 11376-83.

PLOIER, B. & MENON, A. K. 2016. A Fluorescence-based Assay of Phospholipid Scramblase Activity. *J Vis Exp*.

POLSON, H. E., DE LARTIGUE, J., RIGDEN, D. J., REEDIJK, M., URBE, S., CLAGUE, M. J. & TOOZE, S. A. 2010. Mammalian Atg18 (WIPI2) localizes to omegasome-anchored phagophores and positively regulates LC3 lipidation. *Autophagy,* 6**,** 506-22.

POPOT, J. L., ALTHOFF, T., BAGNARD, D., BANERES, J. L., BAZZACCO, P., BILLON-DENIS, E., CATOIRE, L. J., CHAMPEIL, P., CHARVOLIN, D., COCCO, M. J., CREMEL, G., DAHMANE, T., DE LA MAZA, L. M., EBEL, C., GABEL, F., GIUSTI, F., GOHON, Y., GOORMAGHTIGH, E., GUITTET, E., KLEINSCHMIDT, J. H., KUHLBRANDT, W., LE BON, C., MARTINEZ, K. L., PICARD, M., PUCCI, B., SACHS, J. N., TRIBET, C., VAN HEIJENOORT, C., WIEN, F., ZITO, F. & ZOONENS, M. 2011. Amphipols from A to Z. *Annu Rev Biophys,* 40**,** 379-408.

PORTER, K. R. 1953. Observations on a submicroscopic basophilic component of cytoplasm. *J Exp Med,* 97**,** 727-50.

PRINZ, W. A. 2014. Bridging the gap: membrane contact sites in signaling, metabolism, and organelle dynamics. *J Cell Biol,* 205**,** 759-69.

PURI, C., RENNA, M., BENTO, C. F., MOREAU, K. & RUBINSZTEIN, D. C. 2013. Diverse autophagosome membrane sources coalesce in recycling endosomes. *Cell,* 154**,** 1285-99.

PURI, C., RENNA, M., BENTO, C. F., MOREAU, K. & RUBINSZTEIN, D. C. 2014. ATG16L1 meets ATG9 in recycling endosomes Additional roles for the plasma membrane and endocytosis in autophagosome biogenesis. *Autophagy,* 10**,** 182-184.

PURI, C., VICINANZA, M., ASHKENAZI, A., GRATIAN, M. J., ZHANG, Q., BENTO, C. F., RENNA, M., MENZIES, F. M. & RUBINSZTEIN, D. C. 2018. The RAB11A-Positive Compartment Is a Primary Platform for Autophagosome Assembly Mediated by WIPI2 Recognition of PI3P-RAB11A. *Dev Cell,* 45**,** 114-131 e8.

QI, S. Q., KIM, D. J., STJEPANOVIC, G. & HURLEY, J. H. 2015. Structure of the Human Atg13-Atg101 HORMA Heterodimer: an Interaction Hub within the ULK1 Complex. *Structure,* 23**,** 1848-1857.

QUINTAVALLE, C., DI COSTANZO, S., ZANCA, C., TASSET, I., FRALDI, A., INCORONATO, M., MIRABELLI, P., MONTI, M., BALLABIO, A., PUCCI, P., CUERVO, A. M. & CONDORELLI, G. 2014. Phosphorylation-regulated degradation of the tumor-suppressor form of PED by chaperone-mediated autophagy in lung cancer cells. *J Cell Physiol,* 229**,** 1359-68.

RABOUILLE, C. 2019. COPII vesicles and the expansion of the phagophore. *Elife,* 8.

RAGUSA, M. J., STANLEY, R. E. & HURLEY, J. H. 2012. Architecture of the Atg17 complex as a scaffold for autophagosome biogenesis. *Cell,* 151**,** 1501-1512.

RAO, Y., PERNA, M. G., HOFMANN, B., BEIER, V. & WOLLERT, T. 2016. The Atg1-kinase complex tethers Atg9-vesicles to initiate autophagy. *Nat Commun,* 7**,** 10338.

RAVIKUMAR, B., MOREAU, K., JAHREISS, L., PURI, C. & RUBINSZTEIN, D. C. 2010. Plasma membrane contributes to the formation of pre-autophagosomal structures. *Nat Cell Biol,* 12**,** 747-57.

REINISCH, K. M., CHEN, X. W. & MELIA, T. J. 2021. "VTT"-domain proteins VMP1 and TMEM41B function in lipid homeostasis globally and locally as ER scramblases. *Contact (Thousand Oaks),* 4.

REINISCH, K. M. & PRINZ, W. A. 2021. Mechanisms of nonvesicular lipid transport. *Journal of Cell Biology,* 220.

REN, J., LIANG, R., WANG, W., ZHANG, D., YU, L. & FENG, W. 2020. Multi-site-mediated entwining of the linear WIR-motif around WIPI beta-propellers for autophagy. *Nat Commun,* 11**,** 2702.

RIGAUD, J. L. & LEVY, D. 2003. Reconstitution of membrane proteins into liposomes. *Methods Enzymol,* 372**,** 65-86.

ROSTISLAVLEVA, K., SOLER, N., OHASHI, Y., ZHANG, L., PARDON, E., BURKE, J. E., MASSON, G. R., JOHNSON, C., STEYAERT, J., KTISTAKIS, N. T. & WILLIAMS, R. L. 2015. Structure and flexibility of the endosomal Vps34 complex reveals the basis of its function on membranes. *Science,* 350**,** aac7365.

RUSSELL, R. C., TIAN, Y., YUAN, H., PARK, H. W., CHANG, Y. Y., KIM, J., KIM, H., NEUFELD, T. P., DILLIN, A. & GUAN, K. L. 2013. ULK1 induces autophagy by phosphorylating Beclin-1 and activating VPS34 lipid kinase. *Nat Cell Biol,* 15**,** 741-50.

SAITOH, T., FUJITA, N., HAYASHI, T., TAKAHARA, K., SATOH, T., LEE, H., MATSUNAGA, K., KAGEYAMA, S., OMORI, H., NODA, T., YAMAMOTO, N., KAWAI, T., ISHII, K., TAKEUCHI, O., YOSHIMORI, T. & AKIRA, S. 2009. Atg9a controls dsDNA-driven dynamic translocation of STING and the innate immune response. *Proc Natl Acad Sci U S A,* 106**,** 20842-6.

SARI, D., GUPTA, K., THIMIRI GOVINDA RAJ, D. B., AUBERT, A., DRNCOVA, P., GARZONI, F., FITZGERALD, D. & BERGER, I. 2016. The MultiBac

Baculovirus/Insect Cell Expression Vector System for Producing Complex Protein Biologics. *Adv Exp Med Biol,* 896**,** 199-215.

SARKAR, S., DAVIES, J. E., HUANG, Z., TUNNACLIFFE, A. & RUBINSZTEIN, D. C. 2007. Trehalose, a novel mTOR-independent autophagy enhancer, accelerates the clearance of mutant huntingtin and alpha-synuclein. *J Biol Chem,* 282**,** 5641-52.

SATOO, K., NODA, N. N., KUMETA, H., FUJIOKA, Y., MIZUSHIMA, N., OHSUMI, Y. & INAGAKI, F. 2009. The structure of Atg4B-LC3 complex reveals the mechanism of LC3 processing and delipidation during autophagy. *EMBO J,* 28**,** 1341-50.

SAWA-MAKARSKA, J., BAUMANN, V., COUDEVYLLE, N., VON BÜLOW, S., NOGELLOVA, V., ABERT, C., SCHUSCHNIG, M., GRAEF, M., HUMMER, G. & MARTENS, S. 2020. Reconstitution of autophagosome nucleation defines Atg9 vesicles as seeds for membrane formation. *Science,* 369**,** eaaz7714.

SAXTON, R. A. & SABATINI, D. M. 2017. mTOR Signaling in Growth, Metabolism, and Disease. *Cell,* 169**,** 361-371.

SCHINDELIN, J., ARGANDA-CARRERAS, I., FRISE, E., KAYNIG, V., LONGAIR, M., PIETZSCH, T., PREIBISCH, S., RUEDEN, C., SAALFELD, S., SCHMID, B., TINEVEZ, J. Y., WHITE, D. J., HARTENSTEIN, V., ELICEIRI, K., TOMANCAK, P. & CARDONA, A. 2012. Fiji: an open-source platform for biological-image analysis. *Nat Methods,* 9**,** 676-82.

SCHINK, K. O., RAIBORG, C. & STENMARK, H. 2013. Phosphatidylinositol 3-phosphate, a lipid that regulates membrane dynamics, protein sorting and cell signalling. *Bioessays,* 35**,** 900-912.

SCHINK, K. O., TAN, K. W. & STENMARK, H. 2016. Phosphoinositides in Control of Membrane Dynamics. *Annu Rev Cell Dev Biol,* 32**,** 143-171.

SCHU, P. V., TAKEGAWA, K., FRY, M. J., STACK, J. H., WATERFIELD, M. D. & EMR, S. D. 1993. Phosphatidylinositol 3-kinase encoded by yeast VPS34 gene essential for protein sorting. *Science,* 260**,** 88-91.

SCHUCK, S. 2020. Microautophagy - distinct molecular mechanisms handle cargoes of many sizes. *J Cell Sci,* 133.

SCHUCK, S., GALLAGHER, C. M. & WALTER, P. 2014. ER-phagy mediates selective degradation of endoplasmic reticulum independently of the core autophagy machinery. *J Cell Sci,* 127**,** 4078-88.

SCHÜTTER, M., GIAVALISCO, P., BRODESSER, S. & GRAEF, M. 2020. Local Fatty Acid Channeling into Phospholipid Synthesis Drives Phagophore Expansion during Autophagy. *Cell,* 180**,** 135-149.e14.

SCORRANO, L., DE MATTEIS, M. A., EMR, S., GIORDANO, F., HAJNOCZKY, G., KORNMANN, B., LACKNER, L. L., LEVINE, T. P., PELLEGRINI, L., REINISCH, K., RIZZUTO, R., SIMMEN, T., STENMARK, H., UNGERMANN, C. & SCHULDINER, M. 2019. Coming together to define membrane contact sites. *Nat Commun,* 10**,** 1287.

SCOTT, J. W., NORMAN, D. G., HAWLEY, S. A., KONTOGIANNIS, L. & HARDIE, D. G. 2002. Protein kinase substrate recognition studied using the recombinant catalytic domain of AMP-activated protein kinase and a model substrate11Edited by J. Karn. *Journal of Molecular Biology,* 317**,** 309-323.

SEKITO, T., KAWAMATA, T., ICHIKAWA, R., SUZUKI, K. & OHSUMI, Y. 2009. Atg17 recruits Atg9 to organize the pre-autophagosomal structure. *Genes to Cells,* 14**,** 525-538.

SETO, B. 2012. Rapamycin and mTOR: a serendipitous discovery and implications for breast cancer. *Clin Transl Med,* 1**,** 29.

SHAPIRO, A. L., VINUELA, E. & MAIZEL, J. V., JR. 1967. Molecular weight estimation of polypeptide chains by electrophoresis in SDS-polyacrylamide gels. *Biochem Biophys Res Commun,* 28**,** 815-20.

SHEVCHENKO, A., TOMAS, H., HAVLIS, J., OLSEN, J. V. & MANN, M. 2006. In-gel digestion for mass spectrometric characterization of proteins and proteomes. *Nat Protoc,* 1**,** 2856-60.

SHI, X., CHANG, C., YOKOM, A. L., JENSEN, L. E. & HURLEY, J. H. 2020a. The autophagy adaptor NDP52 and the FIP200 coiled-coil allosterically activate ULK1 complex membrane recruitment. *Elife,* 9.

SHI, X., YOKOM, A. L., WANG, C., YOUNG, L. N., YOULE, R. J. & HURLEY, J. H. 2020b. ULK complex organization in autophagy by a C-shaped FIP200 N-terminal domain dimer. *J Cell Biol,* 219.

SHOEMAKER, C. J., HUANG, T. Q., WEIR, N. R., POLYAKOV, N. J., SCHULTZ, S. W. & DENIC, V. 2019. CRISPR screening using an expanded toolkit of autophagy reporters identifies TMEM41B as a novel autophagy factor. *PLoS Biol,* 17**,** e2007044.

SIMONETTA, M., MANZONI, R., MOSCA, R., MAPELLI, M., MASSIMILIANO, L., VINK, M., NOVAK, B., MUSACCHIO, A. & CILIBERTO, A. 2009. The influence of catalysis on mad2 activation dynamics. *PLoS Biol,* 7**,** e10.

STACK, J. H. & EMR, S. D. 1994. Vps34p required for yeast vacuolar protein sorting is a multiple specificity kinase that exhibits both protein kinase and phosphatidylinositol-specific PI 3-kinase activities. *J Biol Chem,* 269**,** 31552-62.

STJEPANOVIC, G., DAVIES, C. W., STANLEY, R. E., RAGUSA, M. J., KIM, D. J. & HURLEY, J. H. 2014. Assembly and dynamics of the autophagy-initiating Atg1 complex. *Proc Natl Acad Sci U S A,* 111**,** 12793-8.

STRØMHAUG, P. E., REGGIORI, F., GUAN, J., WANG, C. W. & KLIONSKY, D. J. 2004. Atg21 is a phosphoinositide binding protein required for efficient lipidation and localization of Atg8 during uptake of aminopeptidase I by selective autophagy. *Mol Biol Cell,* 15**,** 3553-66.

STRONG, L. M., CHANG, C., RILEY, J. F., BOECKER, C. A., FLOWER, T. G., BUFFALO, C. Z., REN, X., STAVOE, A. K., HOLZBAUR, E. L. & HURLEY, J. H. 2021. Structural basis for membrane recruitment of ATG16L1 by WIPI2 in autophagy. *Elife,* 10.

SUZUKI, H., KAIZUKA, T., MIZUSHIMA, N. & NODA, N. N. 2015a. Structure of the Atg101-Atg13 complex reveals essential roles of Atg101 in autophagy initiation. *Nature Structural & Molecular Biology,* 22**,** 572-+.

SUZUKI, K., AKIOKA, M., KONDO-KAKUTA, C., YAMAMOTO, H. & OHSUMI, Y. 2013. Fine mapping of autophagy-related proteins during autophagosome formation in Saccharomyces cerevisiae. *J Cell Sci,* 126**,** 2534-44.

SUZUKI, K., KUBOTA, Y., SEKITO, T. & OHSUMI, Y. 2007. Hierarchy of Atg proteins in pre-autophagosomal structure organization. *Genes Cells,* 12**,** 209-18.

SUZUKI, K. & OHSUMI, Y. 2010. Current knowledge of the pre-autophagosomal structure (PAS). *FEBS Lett,* 584**,** 1280-6.

SUZUKI, S. W., YAMAMOTO, H., OIKAWA, Y., KONDO-KAKUTA, C., KIMURA, Y., HIRANO, H. & OHSUMI, Y. 2015b. Atg13 HORMA domain recruits Atg9 vesicles during autophagosome formation. *Proceedings of the National Academy of Sciences of the United States of America,* 112**,** 3350-3355.

TAN, D., CAI, Y., WANG, J., ZHANG, J., MENON, S., CHOU, H. T., FERRO-NOVICK, S., REINISCH, K. M. & WALZ, T. 2013. The EM structure of the TRAPPIII complex leads to the identification of a requirement for COPII vesicles on the macroautophagy pathway. *Proc Natl Acad Sci U S A,* 110**,** 19432-7.

TANG, Z., TAKAHASHI, Y., HE, H., HATTORI, T., CHEN, C., LIANG, X., CHEN, H., YOUNG, M. M. & WANG, H. G. 2019. TOM40 Targets Atg2 to Mitochondria-Associated ER Membranes for Phagophore Expansion. *Cell Rep,* 28**,** 1744-1757 e5.

TANIDA, I., SOU, Y. S., EZAKI, J., MINEMATSU-IKEGUCHI, N., UENO, T. & KOMINAMI, E. 2004. HsAtg4B/HsApg4B/autophagin-1 cleaves the carboxyl termini of three human Atg8 homologues and delipidates microtubule-associated protein light chain 3- and GABAA receptor-associated protein-phospholipid conjugates. *J Biol Chem,* 279**,** 36268-76.

TARASENKO, D., BARBOT, M., JANS, D. C., KROPPEN, B., SADOWSKI, B., HEIM, G., MOBIUS, W., JAKOBS, S. & MEINECKE, M. 2017. The MICOS component Mic60 displays a conserved membrane-bending activity that is necessary for normal cristae morphology. *J Cell Biol,* 216**,** 889-899.

THUMM, M., EGNER, R., KOCH, B., SCHLUMPBERGER, M., STRAUB, M., VEENHUIS, M. & WOLF, D. H. 1994. Isolation of Autophagocytosis Mutants of Saccharomyces-Cerevisiae. *Febs Letters,* 349**,** 275-280.

TOOZE, S. A. 2010. The role of membrane proteins in mammalian autophagy. *Semin Cell Dev Biol,* 21**,** 677-82.

TOOZE, S. A. & SCHIAVO, G. 2008. Liaisons dangereuses: autophagy, neuronal survival and neurodegeneration. *Curr Opin Neurobiol,* 18**,** 504-15.

TROWITZSCH, S., BIENIOSSEK, C., NIE, Y., GARZONI, F. & BERGER, I. 2010. New baculovirus expression tools for recombinant protein complex production. *J Struct Biol,* 172**,** 45-54.

TSUKADA, M. & OHSUMI, Y. 1993. Isolation and characterization of autophagy-defective mutants of Saccharomyces cerevisiae. *FEBS Lett,* 333**,** 169-74.

TURCO, E., WITT, M., ABERT, C., BOCK-BIERBAUM, T., SU, M. Y., TRAPANNONE, R., SZTACHO, M., DANIELI, A., SHI, X., ZAFFAGNINI, G., GAMPER, A., SCHUSCHNIG, M., FRACCHIOLLA, D., BERNKLAU,

D., ROMANOV, J., HARTL, M., HURLEY, J. H., DAUMKE, O. & MARTENS, S. 2019. FIP200 Claw Domain Binding to p62 Promotes Autophagosome Formation at Ubiquitin Condensates. *Mol Cell,* 74**,** 330-346 e11.

UTTENWEILER, A. & MAYER, A. 2008. Microautophagy in the yeast Saccharomyces cerevisiae. *Methods Mol Biol,* 445**,** 245-59.

VALVERDE, D. P., YU, S. L., BOGGAVARAPU, V., KUMAR, N., LEES, J. A., WALZ, T., REINISCH, K. M. & MELIA, T. J. 2019. ATG2 transports lipids to promote autophagosome biogenesis. *Journal of Cell Biology,* 218**,** 1787-1798.

VAN VLIET, A. R., CHIDUZA, G. N., MASLEN, S. L., PYE, V. E., JOSHI, D., DE TITO, S., JEFFERIES, H. B. J., CHRISTODOULOU, E., ROUSTAN, C., PUNCH, E., HERVAS, J. H., O'REILLY, N., SKEHEL, J. M., CHEREPANOV, P. & TOOZE, S. A. 2022. ATG9A and ATG2A form a heteromeric complex essential for autophagosome formation. *Mol Cell,* 82**,** 4324-4339 e8.

VELIKKAKATH, A. K. G., NISHIMURA, T., OITA, E., ISHIHARA, N. & MIZUSHIMA, N. 2012. Mammalian Atg2 proteins are essential for autophagosome formation and important for regulation of size and distribution of lipid droplets. *Molecular Biology of the Cell,* 23**,** 896-909.

VINK, M., SIMONETTA, M., TRANSIDICO, P., FERRARI, K., MAPELLI, M., DE ANTONI, A., MASSIMILIANO, L., CILIBERTO, A., FARETTA, M., SALMON, E. D. & MUSACCHIO, A. 2006. In vitro FRAP identifies the minimal requirements for Mad2 kinetochore dynamics. *Curr Biol,* 16**,** 755-66.

VON BÜLOW, S. & HUMMER, G. 2020. Kinetics of Atg2-mediated lipid transfer from the ER can account for phagophore expansion. *bioRxiv***,** 2020.05.12.090977.

WALLOT-HIEKE, N., VERMA, N., SCHLUTERMANN, D., BERLETH, N., DEITERSEN, J., BOHLER, P., STUHLDREIER, F., WU, W., SEGGEWISS, S., PETER, C., GOHLKE, H., MIZUSHIMA, N. & STORK, B. 2018. Systematic analysis of ATG13 domain requirements for autophagy induction. *Autophagy,* 14**,** 743-763.

WANG, P., KOU, D. & LE, W. 2020. Roles of VMP1 in Autophagy and ER-Membrane Contact: Potential Implications in Neurodegenerative Disorders. *Front Mol Neurosci,* 13**,** 42.

WATANABE, Y., TAMURA, Y., KAWANO, S. & ENDO, T. 2015. Structural and mechanistic insights into phospholipid transfer by Ups1-Mdm35 in mitochondria. *Nat Commun,* 6**,** 7922.

WEIDBERG, H., SHVETS, E., SHPILKA, T., SHIMRON, F., SHINDER, V. & ELAZAR, Z. 2010. LC3 and GATE-16/GABARAP subfamilies are both essential yet act differently in autophagosome biogenesis. *EMBO J,* 29**,** 1792-802.

WEN, X. & KLIONSKY, D. J. 2016. An overview of macroautophagy in yeast. *J Mol Biol,* 428**,** 1681-99.

WHITE, E. 2012. Deconvoluting the context-dependent role for autophagy in cancer. *Nat Rev Cancer,* 12**,** 401-10.

WOLD, M. S., LIM, J., LACHANCE, V., DENG, Z. & YUE, Z. 2016. ULK1-mediated phosphorylation of ATG14 promotes autophagy and is impaired in Huntington’s disease models. *Molecular Neurodegeneration,* 11**,** 76.

XIE, Z. & KLIONSKY, D. J. 2007. Autophagosome formation: core machinery and adaptations. *Nat Cell Biol,* 9**,** 1102-9.

XIE, Z., NAIR, U. & KLIONSKY, D. J. 2008. Atg8 controls phagophore expansion during autophagosome formation. *Mol Biol Cell,* 19**,** 3290-8.

YAMADA, T., CARSON, A. R., CANIGGIA, I., UMEBAYASHI, K., YOSHIMORI, T., NAKABAYASHI, K. & SCHERER, S. W. 2005. Endothelial nitric-oxide synthase antisense (NOS3AS) gene encodes an autophagy-related protein (APG9-like2) highly expressed in trophoblast. *J Biol Chem,* 280**,** 18283-90.

YAMAMOTO, A., MASAKI, R. & TASHIRO, Y. 1990. Characterization of the isolation membranes and the limiting membranes of autophagosomes in rat hepatocytes by lectin cytochemistry. *J Histochem Cytochem,* 38**,** 573-80.

YAMAMOTO, H., KAKUTA, S., WATANABE, T. M., KITAMURA, A., SEKITO, T., KONDO-KAKUTA, C., ICHIKAWA, R., KINJO, M. & OHSUMI, Y. 2012. Atg9 vesicles are an important membrane source during early steps of autophagosome formation. *J Cell Biol,* 198**,** 219-33.

YAN, J., KUROYANAGI, H., KUROIWA, A., MATSUDA, Y., TOKUMITSU, H., TOMODA, T., SHIRASAWA, T. & MURAMATSU, M. 1998. Identification of mouse ULK1, a novel protein kinase structurally related to C. elegans UNC-51. *Biochem Biophys Res Commun,* 246**,** 222-7.

YAN, J., KUROYANAGI, H., TOMEMORI, T., OKAZAKI, N., ASATO, K., MATSUDA, Y., SUZUKI, Y., OHSHIMA, Y., MITANI, S., MASUHO, Y., SHIRASAWA, T. & MURAMATSU, M. 1999. Mouse ULK2, a novel member of the UNC-51-like protein kinases: unique features of functional domains. *Oncogene,* 18**,** 5850-9.

YANG, Y. & KLIONSKY, D. J. 2020. Autophagy and disease: unanswered questions. *Cell Death Differ,* 27**,** 858-871.

YEH, Y. Y., SHAH, K. H. & HERMAN, P. K. 2011. An Atg13 protein-mediated self-association of the Atg1 protein kinase is important for the induction of autophagy. *J Biol Chem,* 286**,** 28931-28939.

YLÄ-ANTTILA, P., VIHINEN, H., JOKITALO, E. & ESKELINEN, E.-L. 2009. 3D tomography reveals connections between the phagophore and endoplasmic reticulum. *Autophagy,* 5**,** 1180-1185.

YORIMITSU, T. & KLIONSKY, D. J. 2005. Autophagy: molecular machinery for self-eating. *Cell Death Differ,* 12 Suppl 2**,** 1542-52.

YOUNG, A. R. J., CHAN, E. Y. W., HU, X. W., KOCH, R., CRAWSHAW, S. G., HIGH, S., HAILEY, D. W., LIPPINCOTT-SCHWARTZ, J. & TOOZE, S. A. 2006. Starvation and ULK1-dependent cycling of mammalian Atg9 between the TGN and endosomes. *Journal of Cell Science,* 119**,** 3888-3900.

YOUNG, G., HUNDT, N., COLE, D., FINEBERG, A., ANDRECKA, J., TYLER, A., OLERINYOVA, A., ANSARI, A., MARKLUND, E. G., COLLIER, M. P., CHANDLER, S. A., TKACHENKO, O., ALLEN, J., CRISPIN, M., BILLINGTON, N., TAKAGI, Y., SELLERS, J. R., EICHMANN, C., SELENKO, P., FREY, L., RIEK, R., GALPIN, M. R., STRUWE, W. B., BENESCH, J. L. P. & KUKURA, P. 2018. Quantitative mass imaging of single biological macromolecules. *Science,* 360**,** 423-+.

YU, L., CHEN, Y. & TOOZE, S. A. 2018. Autophagy pathway: Cellular and molecular mechanisms. *Autophagy,* 14**,** 207-215.

YUAN, H. X., RUSSELL, R. C. & GUAN, K. L. 2013. Regulation of PIK3C3/VPS34 complexes by MTOR in nutrient stress-induced autophagy. *Autophagy,* 9**,** 1983-95.

ZACHARI, M. & GANLEY, I. G. 2017. The mammalian ULK1 complex and autophagy initiation. *Essays Biochem,* 61**,** 585-596.

ZHAO, Y. G., CODOGNO, P. & ZHANG, H. 2021. Machinery, regulation and pathophysiological implications of autophagosome maturation. *Nat Rev Mol Cell Biol,* 22**,** 733-750.

ZHENG, J. X., LI, Y., DING, Y. H., LIU, J. J., ZHANG, M. J., DONG, M. Q., WANG, H. W. & YU, L. 2017. Architecture of the ATG2B-WDR45 complex and an aromatic Y/HF motif crucial for complex formation. *Autophagy,* 13**,** 1870-1883.

ZHOU, C., MA, K., GAO, R., MU, C., CHEN, L., LIU, Q., LUO, Q., FENG, D., ZHU, Y. & CHEN, Q. 2017. Regulation of mATG9 trafficking by Src- and ULK1-mediated phosphorylation in basal and starvation-induced autophagy. *Cell Res,* 27**,** 184-201.

Supplement

Table S1. Plasmids used in this thesis

Vector	Affinity tag	Cleavage site	Cloning done by
pLIB-6x-His-MBP-ATG9	N terminal 6x-His-MBP	PreScission	A. Nguyen
pLIB-ATG2-Strep	C terminal StrepII	PreScission	A. Nguyen
pLIB-6xHis-GFP-WIPI4	N terminal 6xHis-GFP	PreScission	A. Nguyen
pLIB-6xHis-mCherry-WIPI4	N terminal 6xHis-mCherry	PreScission	A. Nguyen
pLIB-GST-WIPI4	N terminal GST	PreScission	A. Nguyen
pLIB-ATG101-Strep	C terminal StrepII	PreScission	A. Patel
pLIB-6x-His-MBP-ATG101	N terminal 6x-His-MBP	PreScission	F. Lugarini
pBIG-6x-His-MBP-ATG13^{HORMA}-ATG101	N terminal 6x-His-MBP	PreScission	F. Lugarini
pBIG-GST-ATG13^{HORMA}-ATG101	N terminal GST	PreScission	F. Lugarini
pLIB-6x-His-MBP-FIP200	N terminal 6x-His-MBP	PreScission	L. Griese
pLIB-6x-His-MBP-ATG13	N terminal 6x-His-MBP	PreScission	L. Griese
pLIB-6x-His-MBP-BECN1	N terminal 6x-His-MBP	PreScission	L. Griese
pLIB-GST-ULK1	N terminal GST	PreScission	L. Griese
pLIB-6xHis-mCherry-ATG14	N terminal 6xHis-mCherry	PreScission	L. Griese

Table S2. Primer used in this thesis

Purpose	Forward primer (5' to 3')	Reverse primer (5' to 3')
ATG2 cloning	CCACCATCGGGCGCGGATCCATGTCACGATGGCTG	TCCAGATCCAGATCCGCTTCCGTCTTGGGCACTGTCCGAGC
ATG9 cloning	CTGTTCCAGGGGCCCGGATCCATGGCGCAGTTTGACACTG	TCCTCTAGTACTTCTCGACAAGCTTTTACTATACCTTGTGCACCTGAG
WIPI4 cloning	CTGTTCCAGGGGCCCGGATCCATGACTCAACAGCCACTTCGAG	TCCTCTAGTACTTCTCGACAAGCTTTTAAAAGTCATCATCATCACAG

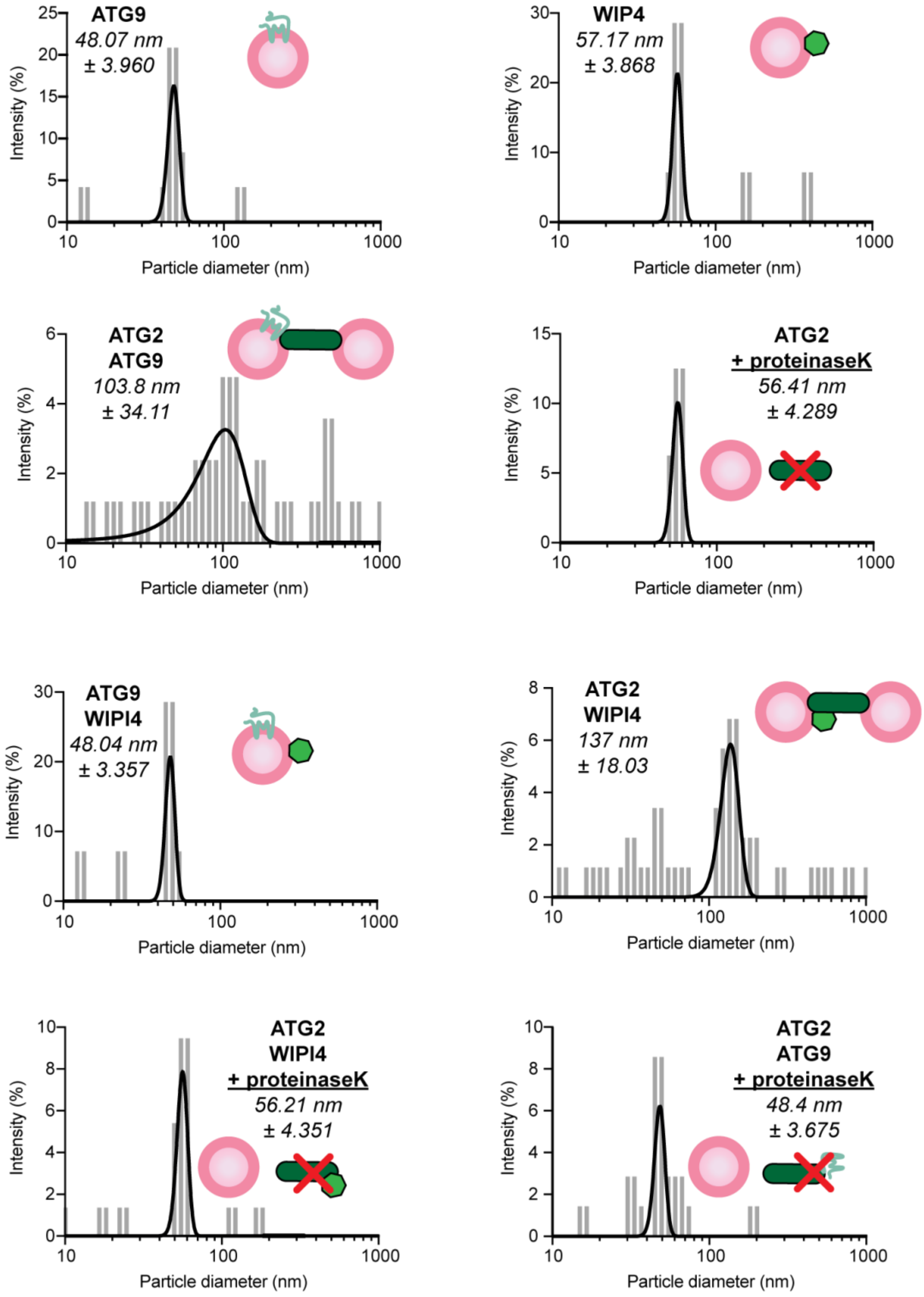

Figure S1. DLS profiles of LUVs in the presence or absence of indicated proteins. The experiment was performed by P. Hosnani.

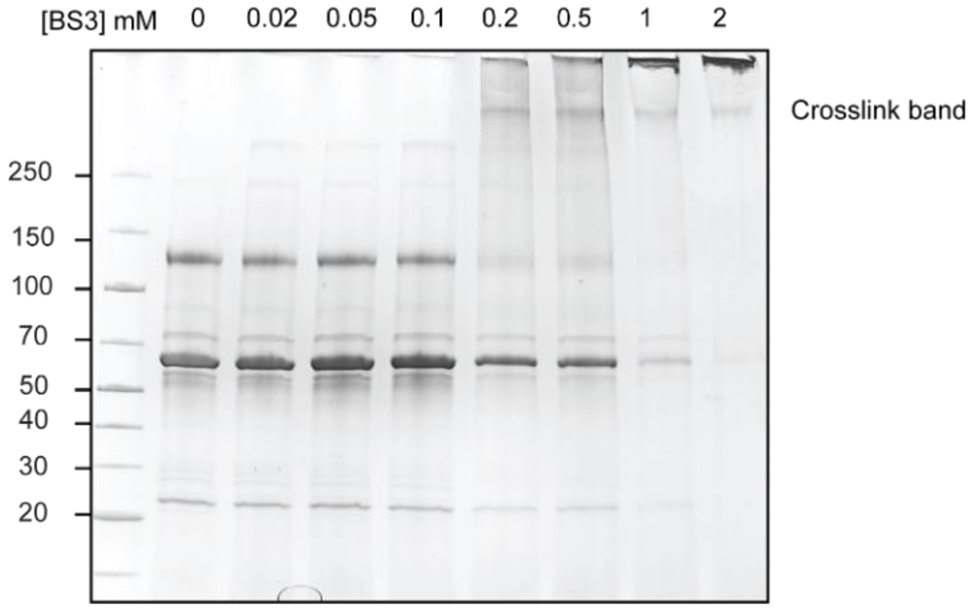

Figure S2. Crosslinking of ^{MBP}ATG9-^{MBP}ATG13^{HOMRA}-ATG101 by BS3. 3 µM of ^{MBP}ATG9-^{MBP}ATG13^{HOMRA}-ATG101 complex was incubated with indicated concentration of BS3 for 1h at 4ºC. Samples were then quenched by 50 mM Tris pH8 for 15 min and analyzed by SDS-PAGE. Crosslinked band of the complex at 0.2 mM BS3 were cut out for XL-MS analysis.

Acknowledgement

I would like to thank my supervisor, Dr. Alex Faesen, for the opportunity to work on this challenging and exciting project, and for his excellent supervision and guidance throughout this project. His passion for science and dedication to this project have given me a lot of motivation during my PhD. I am grateful to my thesis committee members, Prof. Dr. Marina Rodnina and Prof. Dr. Michael Thumm for their input and discussions throughout the course of the project. The TAC meetings were encouraging and helpful. I am thankful to Prof. Dr. Reinhard Jahn, Dr. Alexander Stein, and Prof. Dr. Rubén Fernández-Busnadiego for being part of my examination board. I would also like to thank the GGNB office for organizing the doctoral program and the support they provide throughout the years.

I would like to thank Pouya, Barbora, Prof. Dr. Michael Meinecke, Celine, Anabelle, Prof. Dr. Björn Stork, Dr. Iwan Parfentev, Dr. Olexandr Dybkov, Prof. Dr. Henning Urlaub for the wonderful and productive collaborations, especially for all their work and dedication regarding the publication.

I'm grateful for the help and support of Dr. Christian Dienemann, Ulrich Steuerwald Cryo-EM facilitiy, Dr. Peter Lenart and Antonio Politi at the light microscopy facility.

I would also like to thank members of Stein lab, Jahn lab, Sonia lab for their scientific input over the years. Special thanks to Anuruti and Claudia for their helpful advice and input about membrane proteins.

I would also like to thank Juliane Moses for her excellent administrative support, and Gertrud for a lot of help with the labware.

Thank you Caglalala for your tremendous help with the paper. You saved the last 3 months of my PhD. I cannot imagine doing the revision and writing my

thesis at the same time without your help. Thanks Hong, Florian, Nesil, and Pooja for a lot of help during your time in the lab.

Thanks to Steffarose for her excellent technical support and tremendous help in protein purification. Most of my protein purifications were partly done by her. Thank you, Princess Patel, for tidying up my bench and desk as your hobby, as well as for all your help when I needed it and a lot of distractions when I did not. Your lovely positive energy is spreading not only in our lab but on the whole floor; please don’t lose it. Everybody needs it. Thank you, Laura Griese, for feeding me when I’m hungry and for always helping and caring. Thank the whole lab for sharing inputs, protocols, discussions, and coffee time. Thanks Vivek, Bastina, Caglalala for proofreading my thesis. Importantly, I am grateful to Francesca for her work and contributions to the manuscript.

I would also like to thank Dennis and Britney for all the entertainment and emotional support.

This thesis is dedicated to my parents.